

MICROCOPY RESOLUTION TEST CHART
NATIONAL BUREAU OF STANDARDS 1963-A

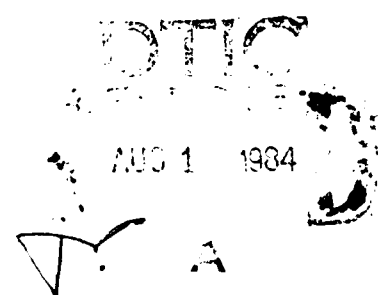
RADC-TR-84-74
Final Technical Report
April 1984



THEORETICAL ANALYSIS OF MICROWAVE PROPAGATION

SIGNATRON, Inc.

S. Parl
A. Malaga



APPROVED FOR PUBLIC RELEASE; DISTRIBUTION UNLIMITED

AD-A143 762

DTIC FILE COPY

ROME AIR DEVELOPMENT CENTER
Air Force Systems Command
Griffiss Air Force Base, NY 13441

82

This report has been reviewed by the RADC Public Affairs Office (PA) and is releasable to the National Technical Information Service (NTIS). At NTIS it will be releasable to the general public, including foreign nations.

RADC-TR-84-74 has been reviewed and is approved for publication.

APPROVED:



JOHN E. RASMUSSEN
Chief, Propagation Branch

APPROVED:



ALLAN C. SCHELL
Chief, Electromagnetic Sciences Division

FOR THE COMMANDER:



JOHN A. RITZ
Acting Chief, Plans Office

If your address has changed or if you wish to be removed from the RADC mailing list, or if the addressee is no longer employed by your organization, please notify RADC (EEPS), Hanscom AFB MA 01731. . This will assist us in maintaining a current mailing list.

Do not return copies of this report unless contractual obligations or notices on a specific document requires that it be returned.

UNCLASSIFIED

SECURITY CLASSIFICATION OF THIS PAGE

REPORT DOCUMENTATION PAGE					
1a. REPORT SECURITY CLASSIFICATION UNCLASSIFIED		1b. RESTRICTIVE MARKINGS N/A			
2a. SECURITY CLASSIFICATION AUTHORITY N/A		3. DISTRIBUTION/AVAILABILITY OF REPORT Approved for public release; Distribution unlimited			
2b. DECLASSIFICATION/DOWNGRADING SCHEDULE N/A					
4. PERFORMING ORGANIZATION REPORT NUMBER(S) N/A		5. MONITORING ORGANIZATION REPORT NUMBER(S) RADC-TR-84-74			
6a. NAME OF PERFORMING ORGANIZATION SIGNATRON, INC.		6b. OFFICE SYMBOL (If applicable)	7a. NAME OF MONITORING ORGANIZATION Rome Air Development Center (EEPS)		
6c. ADDRESS (City, State and ZIP Code) 12 Hartwell Avenue Lexington MA 02173		7b. ADDRESS (City, State and ZIP Code) Hanscom AFB MA 01731			
8a. NAME OF FUNDING/SPONSORING ORGANIZATION Rome Air Development Center		8b. OFFICE SYMBOL (If applicable) EEPS	9. PROCUREMENT INSTRUMENT IDENTIFICATION NUMBER F19628-80-C-0106		
8c. ADDRESS (City, State and ZIP Code) Hanscom AFB MA 01731		10. SOURCE OF FUNDING NOS.			
		PROGRAM ELEMENT NO. 61102F	PROJECT NO. 2305	TASK NO. J6	WORK UNIT NO. 23
11. TITLE (Include Security Classification) THEORETICAL ANALYSIS OF MICROWAVE PROPAGATION					
12. PERSONAL AUTHOR(S) S. Parl & A. Malaga					
13a. TYPE OF REPORT Final		13b. TIME COVERED FROM <u>Sep80</u> TO <u>Sep83</u>	14. DATE OF REPORT (Yr., Mo., Day) April 1984	15. PAGE COUNT 396	
16. SUPPLEMENTARY NOTATION N/A					
17. COSATI CODES			18. SUBJECT TERMS (Continue on reverse if necessary and identify by block number) Line-Of Sight Propagation Path Loss Prediction Delay Spread Troposcatter Propagation Refractive Multipath Diffraction Propagation Atmospheric Scattering		
FIELD	GROUP	SUB. GR.			
17	02				
20	14				
19. ABSTRACT (Continue on reverse if necessary and identify by block number) -This report documents a comprehensive investigation of microwave propagation. The structure of line-of-sight multipath is determined and the impact on practical diversity is discussed. A new model of diffraction propagation for multiple rounded obstacles is developed. A troposcatter model valid at microwave frequencies is described. New results for the power impulse response, and the delay spread and Doppler spread are developed. A 2-component model separating large and small scale scatter effects is proposed. The prediction techniques for diffraction and troposcatter have been implemented in a computer program intended as a tool to analyze propagation experiments.					
20. DISTRIBUTION/AVAILABILITY OF ABSTRACT UNCLASSIFIED/UNLIMITED <input checked="" type="checkbox"/> SAME AS RPT. <input type="checkbox"/> DTIC USERS <input type="checkbox"/>			21. ABSTRACT SECURITY CLASSIFICATION UNCLASSIFIED		
22a. NAME OF RESPONSIBLE INDIVIDUAL Uve H. W. Lammers		22b. TELEPHONE NUMBER (Include Area Code) (617) 861-4239	22c. OFFICE SYMBOL EEPS		

DD FORM 1473, 83 APR

EDITION OF 1 JAN 73 IS OBSOLETE.

UNCLASSIFIED

SECURITY CLASSIFICATION OF THIS PAGE

UNCLASSIFIED

SECURITY CLASSIFICATION OF THIS PAGE

Item #17 Continued

Cosati Codes

Field Group

04 01

DTIC
COPY
INSPECTED
1

711

UNCLASSIFIED

SECURITY CLASSIFICATION OF THIS PAGE

TABLE OF CONTENTS

<u>SECTION</u>	<u>PAGE</u>
1	INTRODUCTION..... 1-1
1.1	BACKGROUND..... 1-2
1.2	SUMMARY OF MAJOR ACCOMPLISHMENTS..... 1-4
1.2.1	Troposcatter Propagation..... 1-4
1.2.2	Diffraction..... 1-13
1.2.3	Line-of-Sight Propagation..... 1-20
1.3	RECOMMENDED FUTURE RESEARCH..... 1-24
1.3.1	Troposcatter..... 1-24
1.3.2	Diffraction..... 1-25
1.3.3	Line-of-Sight..... 1-25
2	CHARACTERISTICS OF THE ATMOSPHERE..... 2-1
2.	THE STANDARD ATMOSPHERE..... 2-1
2.1	VARIABILITY OF THE REFRACTIVITY GRADIENT.... 2-2
2.2	EFFECTS OF REFRACTIVITY GRADIENTS..... 2-4
2.3	DUCTING AND LOS MULTIPATH FADING..... 2-7
2.4	SMALL SCALE IRREGULARITIES..... 2-14
2.4.1	The Structure Constant C_n^2 2-17
2.4.2	The Outer Scale of Turbulence..... 2-26
2.4.3	The Inner Scale of Turbulence..... 2-26
2.5	ATMOSPHERIC ABSORPTION..... 2-26
2.6	RAIN ATTENUATION..... 2-29
3	TROPOSCATTER PROPAGATION..... 3-1
3.1	INTRODUCTION..... 3-1
3.2	THEORIES OF SCATTER PROPAGATION..... 3-2
3.3	PATH GEOMETRY..... 3-4
3.4	CHARACTERIZATION OF THE TROPOSCATTER CHANNEL..... 3-6
3.5	SCATTERING FROM ISOTROPIC TURBULENCE WITH A SCALE SMALL COMPARED TO THE COMMON VOLUME..... 3-9

TABLE OF CONTENTS (Continued)

<u>SECTION</u>	<u>PAGE</u>
3.5.1 Scattering Equation.....	3-10
3.5.2 Path Loss with Widebeam Antennas.....	3-15
3.5.3 Path Loss with Finite Beamwidth Antennas.....	3-19
3.5.4 Horizontal Correlation at the Receiver.....	3-23
3.5.5 Vertical Correlation at the Receiver.....	3-25
3.5.6 A Second Look at Aperture-to-Medium Coupling Loss.....	3-26
3.5.7 Delay Spread.....	3-28
3.5.8 Doppler Spread.....	3-42
3.5.9 Validity of the Uncorrelated Scatterer Assumption.....	3-46
3.6 SCATTERING FROM ANISOTROPIC TURBULENCE.....	3-49
3.6.1 Small Scale Turbulence.....	3-49
3.6.2 Large Scale, Highly Anisotropic Turbulence.....	3-53
3.6.3 Common Volume Dimensions.....	3-56
3.7 LAYER REFLECTION.....	3-57
3.8 RAIN EFFECTS.....	3-63
3.8.1 Pathloss Above C-Band.....	3-63
3.8.2 Rain Scatter.....	3-65
3.9 A PROPOSED 2-COMPONENT MODEL.....	3-68

TABLE OF CONTENTS (Continued)

<u>SECTION</u>	<u>PAGE</u>
4	DIFFRACTION..... 4-1
4.1	BACKGROUND..... 4-1
4.2	APPLICATION OF HUYGHENS' PRINCIPLE..... 4-7
4.2.1	Single Knife Edge..... 4-7
4.2.2	Iterative Computational Technique for Multiple Edges..... 4-14
4.2.3	Numerical Comparison with the Results of Vogler [1982]..... 4-19
4.2.4	The Double-Knife Edge Case, and Other Special Cases..... 4-22
4.2.5	Extension of the Computational Technique to Include Ground Reflections..... 4-32
4.2.6	Diffraction Over a Flat-Top..... 4-39
4.2.7	The Computational Technique with Straight Line Approximations to Rounded Edges..... 4-42
4.3	AD-HOC TECHNIQUES FOR CALCULATION OF MULTIPLE EDGE DIFFRACTION..... 4-47
4.3.1	Bullington Method..... 4-47
4.3.2	Epstein Peterson Method..... 4-47
4.3.3	Japanese Atlas Method..... 4-52
4.3.4	Deygout Method..... 4-53
4.4	UNIFORM GEOMETRICAL THEORY OF DIFFRACTION (UGTD)..... 4-54
4.4.1	Diffraction Coefficient for a Knife-Edge..... 4-63
4.4.2	Diffraction for a Rounded Edge..... 4-68

TABLE OF CONTENTS (Continued)

<u>SECTION</u>	<u>PAGE</u>
4.4.2.1	Transition Region and Shadow Boundary Solutions... 4-76
4.4.2.2	Shadow and Lit Region Solutions..... 4-82
4.4.2.3	Polynomial Approximations... 4-85
4.5	MULTIPLE EDGE DIFFRACTION..... 4-87
4.5.1	Field in the Shadow Zone..... 4-89
4.5.2	Field in the Lit Zone..... 4-93
4.5.3	Comparison with Other Methods..... 4-97
4.6	EDGE PROFILE EFFECTS..... 4-103
4.7	TEMPORAL VARIABILITY IN DIFFRACTION LOSS CALCULATIONS..... 4-116
5	LINE-OF-SIGHT PROPAGATION..... 5-1
5.1	OVERVIEW..... 5-1
5.2	SINGLE RAY PROPAGATION REGIMES..... 5-2
5.3	MULTIPATH FADING FROM AN ELEVATED DUCT..... 5-12
5.3.1	Introduction..... 5-12
5.3.2	Two Layer Refractivity Model..... 5-13
5.3.3	Ray Equations..... 5-18
5.3.4	Examples..... 5-24
5.3.5	Solving the Ray Equations (REAL CASE)..... 5-34
5.3.6	Conditions for Multipath..... 5-40
5.3.7	Angle of Arrival (AOA)..... 5-41
5.3.8	Delay Spread with Equal Height Terminals..... 5-43

TABLE OF CONTENTS (Concluded)

<u>SECTION</u>	<u>PAGE</u>
5.4 ANGLE DIVERSITY FOR LOS MULTIPATH PROTECTION.....	5-47
5.4.1 Introduction.....	5-47
5.4.2 Diversity Combining.....	5-53
5.4.3 Frequency Diversity Considerations...	5-54
5.4.4 Space Diversity Considerations.....	5-54
5.4.5 A Baseline Angle Diversity Multipath Protection System.....	5-56
5.4.6 Conclusions.....	5-61
APPENDIX A DERIVATION OF LOS RAY PARAMETERS	
APPENDIX B DIVERSITY COMBINER PERFORMANCE	
APPENDIX C DERIVATION OF THE SCATTER EQUATION	

LIST OF FIGURES

<u>FIGURE NO.</u>		<u>PAGE</u>
1-1	Total Transmission Loss for $d=200\text{km}$ and Various C_N^2 Values.....	1-5
1-2	RSL vs. Frequency with Rain.....	1-7
1-3	Troposcatter Signal RSL at 5 and 15 GHz as a Function of Path Length for Typical (Median) and Extreme Conditions.....	1-9
1-4	Over-the-Horizon (OTH) Propagation Components.....	1-10
1-5	Summary of Troposcatter Path Loss.....	1-11
1-6	Correlation Distance, Delay and Doppler Spreads.....	1-12
1-7	Modification of $Q(\tau)$ for Long Term Variability of Pathloss and Delay Spread.....	1-14
1-8	Huyghens' Principle for Knife-Edge Diffraction.....	1-15
1-9	Multiple Edge Diffraction Geometries.....	1-17
1-10	Comparison Between UGTD Ray Method and Integral Solution (Huyghens' Principle) for Triple Knife-Edge Geometry Shown (Frequency = 1 GHz).....	1-18
1-11	Comparison Between UGTD, Epstein-Peterson, Japanese-Atlas and Deygout Methods for Triple Knife-Edge Geometry Shown (Frequency = 1 GHz).....	1-19
1-12	Example of Multipath Dependence on Layer Height.....	1-21
1-13	Examples of Ray Paths.....	1-23

LIST OF FIGURES (Continued)

<u>FIGURE NO.</u>		<u>PAGE</u>
2-1	Earth Radius Transformations.....	2-6
2-2	Illustration of a Surface Duct.....	2-8
2-3	Illustration of an Elevated Duct.....	2-10
2-4	Refractive Fading Modeled as a Function of Windspeed (Schiavone, 1983).....	2-11
2-5	Distribution of Duct Thickness at Various Locations (From Bean and Dutton, 1966).....	2-13
2-6	Distribution of Gradient (Sasaki and Akiyama, 1979).....	2-15
2-7	Structure Parameter as Function of Altitude with Sea-Level Water Vapor Pressure as Parameter (From Sirkis, 1971).....	2-21
2-8	Height Profiles of the Structure Constant ($m^{-2/3}$) (From Gossard, 1977).....	2-24
2-9	Atmospheric Attenuation Coefficient.....	2-28
2-10	Rain Attenuation Coefficient.....	2-32
3-1	Path Geometry.....	3-5
3-2	Link with No Coupling Loss.....	3-13
3-3	Link with Significant Coupling Loss.....	3-13
3-4	The Common Volume Integration.....	3-16
3-5	Theoretical and Numerically Integrated Power Impulse Response Function.....	3-35
3-6	Theoretical and Computed Power Impulse Responses for Different Aperture Dimensions....	3-40
3-7	Geometry for Determination of the Uncorrelated Scatter Conditions.....	3-47
3-8	RSL vs. Frequency with Rain.....	3-64

LIST OF FIGURES (Continued)

<u>FIGURE NO.</u>		<u>PAGE</u>
3-9	Troposcatter Signal RSL at 5 and 15 GHz as a Function of Path Length for Typical (Median) and Extreme Conditions.....	3-66
3-10	Transmission Loss of 2 Component Model for $d = 200$ km.....	3-70
3-11	Transmission Loss of 2 Component Model for $d = 500$ km.....	3-71
3-12	Total Transmission Loss for $d = 200$ km and various C_n^2 Values.....	3-72
4-1	Diffraction on an LOS Link.....	4-2
4-2	Mixed Troposcatter/Diffraction Mode.....	4-3
4-3	Huyghens' Principle for Knife-Edge Diffraction.....	4-8
4-4	Finite Opening Approximation.....	4-15
4-5	Multiple Edge Path Integration.....	4-20
4-6	Attenuation vs. Height of Middle Knife-Edge in Vogler's 3-Knife Edge Example.....	4-21
4-7	Attenuation vs. Receiver Heights h_R for a 50 km Path and Various Numbers of Knife Edges on a Line Through the Transmitter.....	4-23
4-8	2-Knife Edge Geometry.....	4-24
4-9	Fields over a Curved Obstacle.....	4-33
4-10	Ground Reflection Geometry.....	4-37
4-11	Reflection Coefficient of a Perfectly Plane Earth with $\epsilon/\epsilon_0 = 10$, $\sigma = 10^{-3}$ mho/m.....	4-40
4-12	Diffraction over Square-Topped Edge.....	4-41

LIST OF FIGURES (Continued)

<u>FIGURE NO.</u>		<u>PAGE</u>
4-13	Flat-Top and Wedge Approximations to a Rounded Edge.....	4-43
4-14	Diffraction Loss over Various Perfectly Reflecting Obstacles Approximating a Rounded Obstacle.....	4-44
4-15	Effect of Ground Reflections on Diffraction....	4-46
4-16	Multiple Diffraction: Construction.....	4-48
4-17	Multiple Edge Diffraction Geometry with Multiple Rays.....	4-51
4-18	Knife-Edge Diffraction Geometry.....	4-56
4-19	Caustics of an Astigmatic Tube of Rays.....	4-57
4-20	Geometry for Knife Edge Diffraction.....	4-65
4-21	Rays and Regions Associated with the Diffraction and Scattering by a Convex Surface.....	4-69
4-22	Shadow Zone (a) and Lit Zone (b) Geometries for the Diffraction by a Rounded Edge.....	4-73
4-23	(a) Real and Imaginary Parts of the Integral $G(X)$ as a Function of X for $q=0$. (b) Real and Imaginary Parts of the Integral $G(X)$ as a Function of X for $q=\infty$	4-78
4-24	Diffraction Loss Due to a Perfectly Conducting Rounded Obstacle.....	4-79
4-25	Permittivity, ϵ , and Conductivity, σ , as a Function of Frequency.....	4-80
4-26	Multiple Edge Diffraction Geometries.....	4-88
4-27	Distances and Scattering Angles for Triple-Edge Diffraction.....	4-92
4-28	Distances and Scattering Angles for Triple-Edge Diffraction.....	4-96

LIST OF FIGURES (Continued)

<u>FIGURE NO.</u>	<u>PAGE</u>
4-29	Comparison Between UGTD Ray Method and Integral Solution (Huyghens' Principle) for Triple Knife-Edge Geometry Shown (Frequency = 1 GHz)..... 4-98
4-30	Comparison Between UGTD Ray Method and Integral Solution (Huyghens' Principle) for Triple Knife-Edge Geometry Shown (Frequency = 1 GHz)..... 4-99
4-31	Comparison Between UGTD Ray Method and Integral Solution (Huyghens' Principle) for Triple Knife-Edge Geometry Shown (Frequency = 1 GHz)..... 4-100
4-32	Comparison Between UGTD Ray Method and Integral Solution (Huyghens' Principle) for Various Triple Knife-Edge Geometries (Frequency = 100 MHz)..... 4-102
4-33	Comparison Between UGTD, Epstein-Peterson, Japanese-Atlas and Deygout Methods for Triple Knife-Edge Geometry Shown (Frequency = 1 GHz)..... 4-104
4-34	Comparison Between UGTD, Epstein-Peterson, Japanese-Atlas and Deygout Methods for Triple Knife-Edge Geometry Shown (Frequency = 1 GHz)..... 4-105
4-35	Comparison Between UGTD, Epstein-Peterson, Japanese-Atlas and Deygout Methods for Triple Knife-Edge Geometry Shown (Frequency = 1 GHz)..... 4-106
4-36	Illustration of Multiple Diffraction Points on a Bilinear Screen..... 4-109
4-37	Magnitude and Phase of the Correction Factor $K(u,v)$ 4-112
4-38	Diffraction Loss Measured on a Cluttered Path with Multiple Diffraction Paths..... 4-114
4-39	Path Profile: LSTF to WILLCOX..... 4-117
4-40	Variability in Diffraction Path Loss as a Function of Refractivity Gradient and Edge Horizontal Extents..... 4-119

LIST OF FIGURES (Concluded)

<u>FIGURE NO.</u>		<u>PAGE</u>
5-1	Regions of Atmospheric Turbulence.....	5-7
5-2	The Function $H_{11/6}(x)$	5-8
5-3	LOS Scintillation.....	5-11
5-4	Refractivity Height Profile.....	5-15
5-5	Path Geometry for Refractive Path.....	5-16
5-6	Ray Parameters Defined.....	5-19
5-7	Example of Multipath Dependence on Layer Height.....	5-25
5-8	Angle-of-Arrival and Relative Delay as a Function of Layer Height above Transmitter for Different Ducting Gradient.....	5-29
5-9	Angle-of-Arrival and Relative Delay and Maximum Ray Height as Function of Height of Layer Above Transmitter.....	5-31
5-10	Total Field Strength Relative to Line-of Sight at Low Frequencies.....	5-32
5-11	Total Field Strength at 4 GHz.....	5-33
5-12	Fading vs. Frequency for a Layer Boundary Height to 0.2 m Intervals near 30 m on a 1-0 km Link with $h_R - h_T = 20$ m.....	5-35
5-13	The Maximum Height Difference that may Support Multipath.....	5-42
5-14	Maximum Delay Spread vs. Distance and Duct Gradient for a Duct of Intensity $\Delta N = -50$ Nu...	5-48
5-15	Principles of Angle Diversity.....	5-50
5-16	Geometry for Dual Space Diversity with Two Rays.....	5-55
5-17	Angle Diversity System Configuration.....	5-57
5-18	Performance as a Function of Height of Duct....	5-59
5-19	Worst Fade Depth with Optimum Combiner.....	5-60
5-20	Typical Angle Diversity Performance.....	5-64

LIST OF TABLES

<u>TABLE NO.</u>		<u>PAGE</u>
3-1	Ratio of Structure Constant and the Squared Refractive Index Gradient.....	3-62
4-1	Radio 60 $\sigma\lambda/\epsilon_r$ vs. Frequency.....	4-81
5-1	Angle Spread of Received Rays (Degrees) Lower Layer Refractivity Gradient -40 Nu/km.....	5-51
5-2	Probability that Both Receivers see Multipath Given that One Does.....	5-62

SECTION 1 INTRODUCTION

This report contains the results of an investigation of microwave propagation prediction techniques for the purpose of designing and maintaining wideband microwave communication links. The work was performed under Contract No. F19628-80-C-0106 for RADC/EEPS, Hanscom AFB, Massachusetts.

The scope of the report includes multipath fading on line-of-sight links, troposcatter signal characterization and diffraction path calculations, all in the frequency range of 1-18 GHz.

The objective of the report is to determine the factors affecting wideband line-of-sight, troposcatter, and diffraction microwave propagation and to develop the necessary prediction techniques. As a result of the work performed under this contract, a number of new results have been obtained.

The background and key results are summarized in this section, followed by a list of future research required to further advance the reliability of propagation prediction techniques. Section 2 contains the background in atmospheric modeling required for the remaining part of the report. Section 3 describes troposcatter communication, the propagation model on which the computer program TRODIF, developed under this program, is based and a number of new useful analytical results. Section 4 describes the theory of diffraction and two new computational techniques developed to overcome the limited applicability of current available techniques. Section 5 develops the theory of LOS propagation, particularly the characterization of refractive multipath.

1.1 BACKGROUND

This study was motivated by the increasing need for high data rate links in a modern tactical environment. Communication links over ranges which are longer than conventional LOS microwave links, and which may reach up to the usual troposcatter path lengths, are of interest to a number of future military applications such as netting of radars over inaccessible terrain (e.g., arctic), in a tactical deployment (netted radar surveillance), or in support of mobile command elements for missile control, strike operations, or air defense. A common feature of such links is that they must have a high likelihood of being operational when deployed. The proper deployment of tactical links in a given climate and time-of-year therefore requires a much better understanding of the atmospheric processes underlying the observed propagation effects.

The system availability (fraction of time that a performance measure such as bit error rate is exceeded) of narrowband systems depends primarily on the yearly distribution of the path loss for the type of propagation mode. Due to the increasing data rate requirements, and spread spectrum usage, there is a need for modeling of channel multipath spreads, fade rates and diversity correlation in addition to path loss because the availability of wideband systems depends strongly on these parameters. Short- and long-term statistics of these parameters are desired, as well as seasonal and geographical variations. A particularly severe multipath condition has been identified, both from theory and measurement, to occur on links with mixed propagation modes (simultaneous troposcatter and double edge diffraction). This effect has often been neglected in past propagation models. Hence a major goal of this study is to provide a unified prediction model of path loss, multipath spread and diversity correlation.

When atmospheric effects are not properly taken into account, it is necessary instead to allow a considerable margin for prediction error. The dB margin depends on the service probability requirement, and can therefore be particularly severe for tactical links. Including correctly the atmospheric effects on the propagation can substantially reduce the dB margin required for a given service probability and in a given geographical location and time-of-year. This saving in dB margin, which could be as much as 10 dB, can then be used to improve other important link parameters such as transmitter power requirements, path lengths of operational over-the-horizon links, interceptability, or ECM vulnerability.

The interest in higher frequencies is a result of spectrum crowding at the lower microwave frequencies combined with a need for additional bandwidth to accommodate spread spectrum waveforms and other ECCM techniques. A side benefit of using higher frequencies would be the feasibility of smaller, more mobile equipment. The analysis in this report therefore includes new propagation results valid up to and beyond the 15-20 GHz range above which rain effects will limit system availability.

The best existing LOS, diffraction, and troposcatter prediction techniques (NBS, CCIR) are not capable of satisfying the requirements of a propagation model for wideband tactical applications. The most important reason for this is that these techniques offer predictions only of the path loss, not of other important parameters such as delay spread, fading rate, and diversity correlations. In addition, the path loss predictions of the existing troposcatter techniques are based on a model developed primarily for frequencies below 1-3 GHz. At these lower frequencies the propagation mechanism can be totally different from that at higher frequencies. Typically, over-the-horizon propagation relies on layer reflection below 1-3 GHz and turbulence scatter above that approximate frequency range. SIGNATRON has developed

a troposcatter model capable of improved path loss prediction as well as multipath characterization. This model, developed for prediction of strategic links in a previous DoD contract [Monsen and Parl, 1980], forms the starting point for the model described in Section 3.

1.2 SUMMARY OF MAJOR ACCOMPLISHMENTS

1.2.1 Troposcatter Propagation

Troposcatter systems are usually evaluated using the NBS technique [Rice, et al., 1967] or an updated version of it [MIL-Handbook 417, CCIR]. The estimates are based on empirical analysis of data mostly below 1 GHz. The predictions do not agree with the well established Kolmogorov-Obhukov turbulence scatter theory. For the NBS model, the scattering cross-section is proportional to f^{-1} , while for turbulent scatter it is proportional to $f^{1/3}$. A general model that includes both of the above is one in which the scattering cross-section of the atmospheric scatterers is proportional to a Von Karman wavenumber spectrum with spectrum slope m , where $m=5$ for the NBS model and $m=11/3$ for the Kolmogorov model. Layer reflection is another possible model. In this report we discuss the fundamental physical processes that make troposcatter systems work and develop analytical expressions for many of the key parameters. Some of the specific new results obtained in Section 3 are:

- A two component model in which radio signals are scattered from two types of atmospheric refractive index irregularities (turbulence and larger scale layers) with different scattering cross-sections and possibly long term statistics is proposed. The model agrees with NBS measurements at low frequencies and with turbulence scatter at high frequencies. Figure 1-1 shows the troposcatter transmission loss for a 200 km path as a function of frequency and for various values of the structure constant of the turbulence.

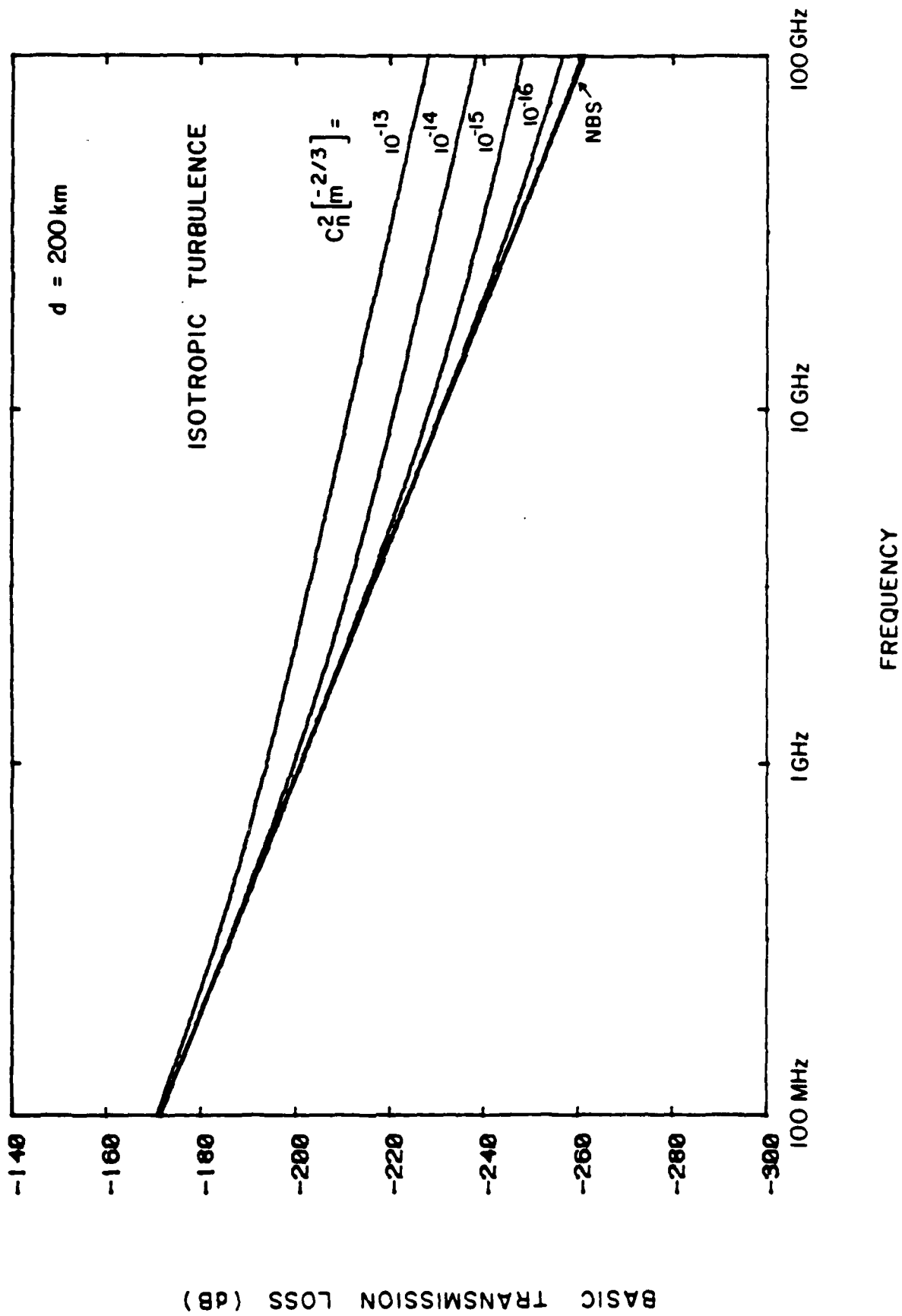


Figure 1-1 Total transmission loss for $d=200\text{km}$ and various C_N^2 values

- The validity of turbulence scatter up to at least 20 GHz is supported theoretically.
- It is shown that turbulence scatter will be stronger than partial layer reflections above a frequency on the order of 1-3 GHz. One reason is that gradual layer transitions appear smooth at higher frequencies. Another is that high strength of the turbulence, measured by the structure constant C_n^2 , is associated with large gradients.
- Anisotropic turbulence primarily affects scatter off the great circle plane. It is similar to layer reflection when the horizontal scales are much larger than the vertical scale. Explicit expressions are derived to demonstrate that
 - Anisotropy causes an enhancement of the forward scattered signal.
 - Anisotropy, defined by the ratio of horizontal to vertical scales reduces the azimuth component of the aperture-to-medium coupling loss.
 - Anisotropy reduces the Doppler spread.
 - Anisotropy increases correlation between horizontally spaced diversity antennas.
- Anisotropy with horizontal scales larger than the common volume reduces the effective spectrum slope parameter by 1 (if only the azimuthal scale is large) or by 2 (if both azimuthal and longitudinal scales are large). Large scale turbulence is likely to be highly anisotropic. Measurements of spectrum slope m can easily be corrupted by anisotropy.
- Since frequencies below approximately 1 GHz are affected mostly by larger scale turbulence, anisotropy should be included in the modeling. The NBS model, with its spectrum slope of 5, could also be explained by large scale turbulence with an anisotropic wave-number spectrum with a slope of 6 or 7. However, the NBS data do not allow determination of the anisotropy.
- At frequencies above 5 GHz, the effects of rain attenuation and atmospheric absorption must be considered. Figure 1-2 shows the troposcatter received signal level (RSL) for a 100 km path as a function of frequency for various values of the water

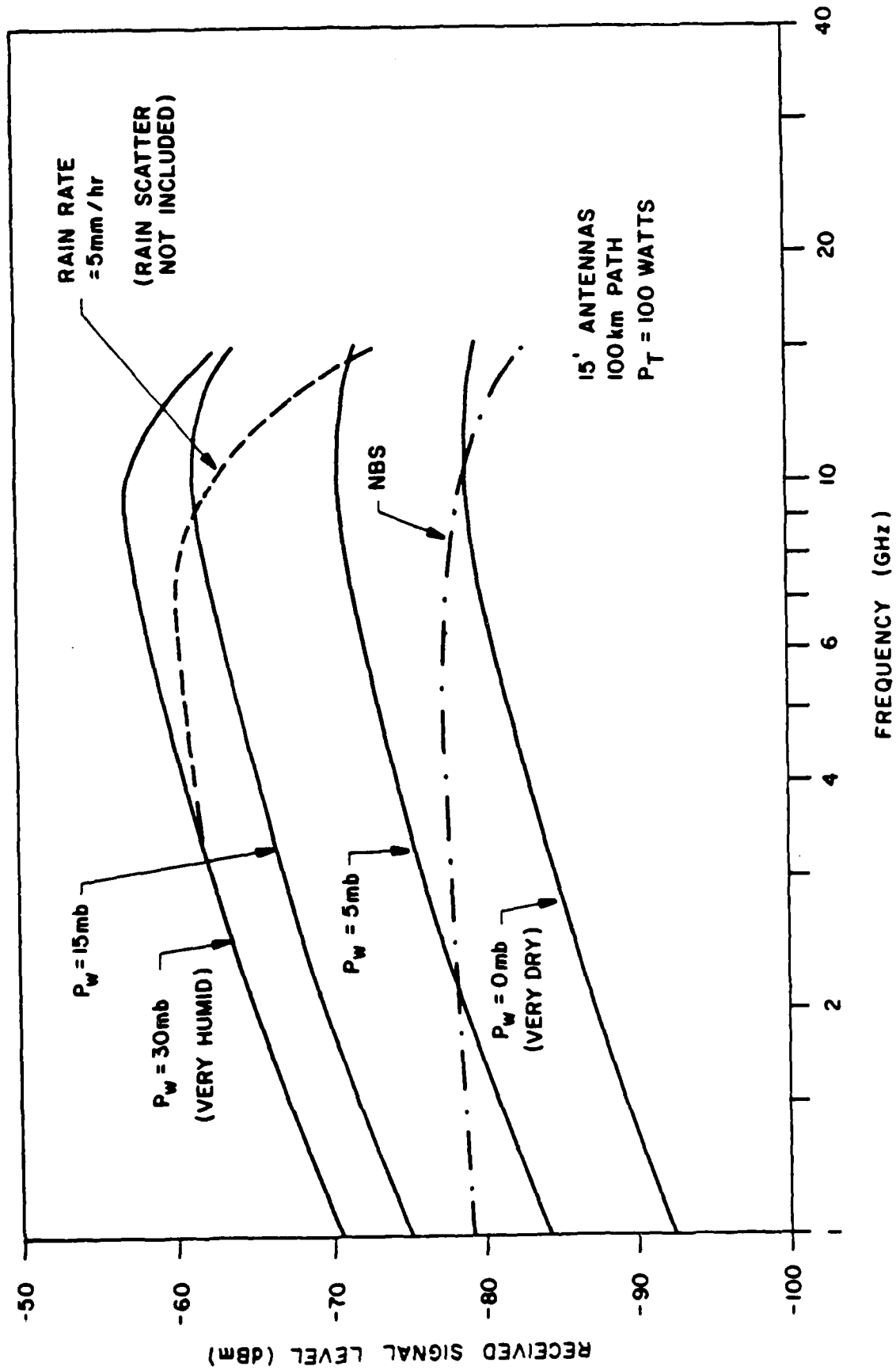


Figure 1-2 RSL vs. Frequency with Rain

vapor pressure at sea level. The curves assume a fixed antenna size. The increase in RSL with frequency is due to the increase in antenna gain. At frequencies above 10 GHz, atmospheric absorption becomes significant. The dashed curve of Figure 1-2 also shows that troposcatter propagation at higher frequencies may be less vulnerable to rain attenuation than line-of-sight propagation. This is due to the fact that the strength of the turbulent scatter signal increases with humidity. Figure 1-2 shows that, for sufficiently short paths, the RSL at 15 GHz assuming a 5mm/hr rain rate is stronger than the RSL assuming dry air. As the path length increases the effects of rain attenuation become more pronounced as shown in Figure 1-3. The curves of Figure 1-2 also indicate that the long-term variability in troposcatter paths is due to changes in the humidity, or more specifically the structure constant of the turbulence.

- A new approximate expression for the power impulse response $Q(\tau)$ is derived. This expression promises to be particularly useful for evaluating the effects of
 - height profile of C_n^2 ,
 - different antenna sizes,
 - long-term variations in path loss,
 - long-term variations in delay spread.
- An integral expression for the frequency coherence function and an expression for the Doppler spread are derived.
- Expressions for spatial correlation distances at the receiver are derived.

Figure 1-4 summarizes the components affecting the over-the-horizon power impulse response (received power per unit delay). Figure 1-5 shows the theoretical expressions for the calculation of the troposcatter path loss. Figure 1-6 shows the expressions for the calculation of other troposcatter parameters such as spatial correlations, R_h , R_v , power impulse response $Q(\tau)$, delay spread σ_τ , and Doppler spread B_c . The results for $Q(\tau)$ can be easily combined with the expression for the Doppler spectrum at a given delay [Birkemeier et al., 1969] to yield an analytical expression for the entire scattering function.

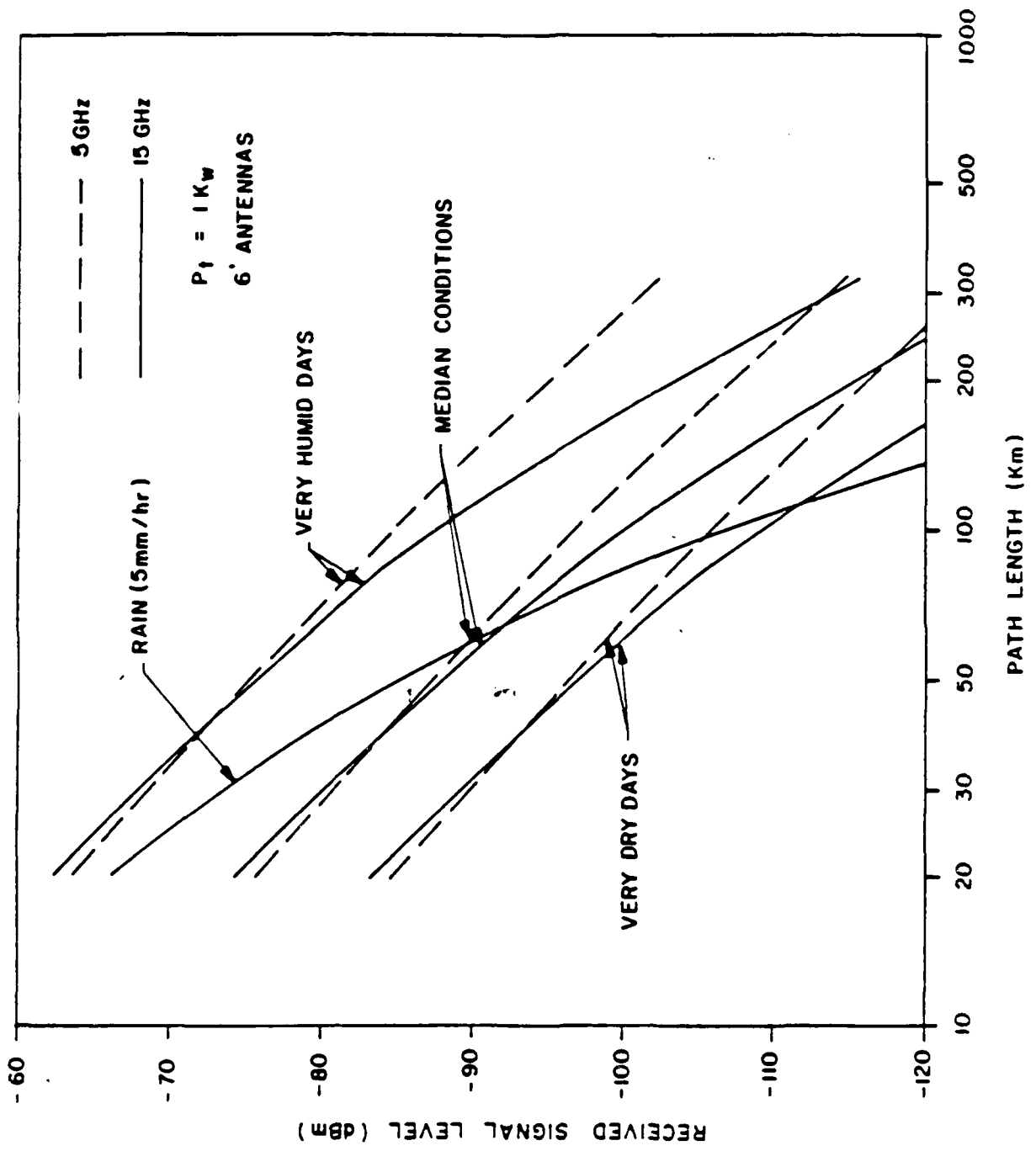


Figure 1-3 Troposcatter signal RSL at 5 and 15 GHz as a function of path length for typical (median) and extreme conditions.

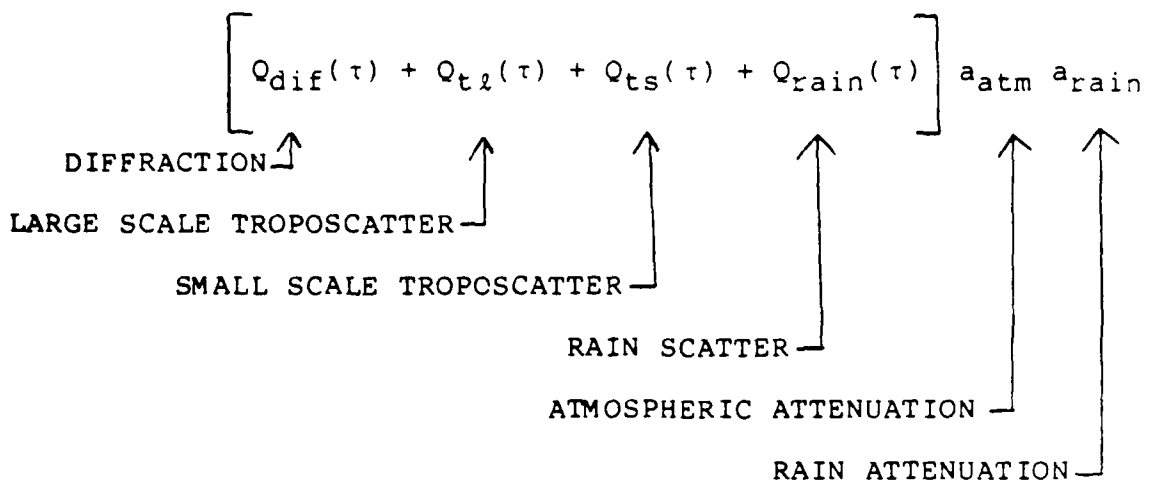


Figure 1-4 Over-the-Horizon (OTH) Propagation Components

	L_t	Total Tropo Transmission Loss (in dB)
=	L_b	(Basic Transmission Loss with Omni directional Antennas)
+	L_h	(Aperture-to-Medium Coupling Loss in Azimuth Direction)
+	L_v	(Aperture-to-Medium Coupling Loss in Vertical and Horizontal Directions)
+	L_a	(Coupling Loss Correction for Asymmetric Links)
-	G_T	(Transmitter Antenna Gain in dB)
-	G_R	(Receiver Antenna Gain in dB)

The following approximate expressions are obtained as a function of spectrum slope m :

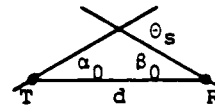
$$L_b = -10 \log [C_1(m) (k\theta_s)^{2-m}/d]; \quad C_1(11/3) = 0.0196 C_n^2 A$$

$$L_h = 10 \log [1 + C_2(m) \theta_s / (A b_h)]; \quad C_2(11/3) = 1.85$$

(equal horizontal beams b_h)

$$L_v = -10 \log [F_{m-1}(b_{Tv}/\theta_s, b_{Rv}/\theta_s)]; \quad F_v(x,y) \approx 1 - (1+x)^{-v} - (x,y)^{-v} + (1+x+y)^{-v}$$

$$L_a = -10 \log [1 + |\alpha_0 - \beta_0| / \theta_s]; \quad \theta_s = \alpha_0 + \beta_0:$$



where

θ_s	=	min. scattering angle
d	=	distance
k	=	$2\pi f/c$ = wavenumber
b_h, b_{Tv}, b_{Rv}	=	horizontal and vertical beamwidths
A	=	Anisotropy factor L_{ov}/L_{oh}

Figure 1-5 Summary of Troposcatter Path Loss

HORIZONTAL CORRELATION DISTANCE

$$R_h \equiv \int \rho_h / \max \rho_h;$$

ρ_h = correlation function in horizontal direction at receiving aperture

$$\sim \frac{A \lambda}{\theta_s} \frac{m \beta_{m-1} (\alpha_0 / \theta_s)}{2(m-1)C_2(m)} [1 + C_2(m) \theta_s / (A b_h)]; \quad \beta_n \text{ defined on page 3-23.}$$

VERTICAL CORRELATION DISTANCE

$$R_v \sim (m-2) \frac{\lambda}{\theta_s}$$

POWER IMPULSE RESPONSE Q(τ) (Wide Beams)

$$Q(\tau) \sim \frac{c}{d} \frac{C_3(m)}{\theta_s^2} P_R(\tau/\tau_0)^{-m/2} \ln\left(\frac{\tau}{\tau_0}\right) \sqrt{1-\tau_0/\tau}, \quad \tau > \tau_0 ;$$

$$C_3(11/3) = 8.89; \quad \tau_0 = \alpha_0 \beta_0 d / 2c \quad \theta_s = \alpha_0 + \beta_0$$

DELAY SPREAD (Wide Beams)

$$\sigma_\tau \equiv \int Q / \max(Q) = C_4(m) d \theta_s^2 / c; \quad C_4(11/3) = 1.78$$

DOPPLER SPREAD

$$B_c \equiv \int B / \max(B) = 2C_2(m) \frac{u \theta_s}{\lambda A} / (1 + C_2(m) \theta_s / (A b_h))$$

u = wind velocity perpendicular to path

Figure 1-6 Correlation Distance, Delay and Doppler Spreads

Figure 1-7 illustrates how the expression for the power impulse response, $Q(\tau)$, obtained assuming wide antenna beams can be modified to account for variability in the turbulence structure constant $C_n^2(h)$ and the effect of finite antenna beamwidths. The key assumption is that height h is essentially constant at a given delay. The finite beam pattern can be included approximately as indicated, or can be calculated using the computer program. Calculations and plots of $Q(\tau)$ for wide and narrow beams are presented in Section 3.5.7.

1.2.2 Diffraction

Diffraction loss calculations are needed on most troposcatter systems, particularly for the evaluation of the long term distributions of the path loss and the delay spread. The delay spread can be unexpectedly large and exhibit a great deal of variability on mixed mode links (troposcatter and diffraction). The analysis of diffraction links is discussed in Section 4. The results include:

- Development of computer techniques using Huyghens' principle to evaluate the loss over knife-edges and shaped edges with arbitrary ground reflection characteristics. Huyghen's principle for a knife-edge is illustrated in Figure 1-8. The field at the observation point, R , is composed of the field radiated from secondary sources in the plane of the knife-edge. The extension to multiple knife-edges consists of treating the field incident on each subsequent semi-infinite aperture (knife-edge) as the superposition of the field re-radiated by each secondary source in the plane above the previous edge.
 - The technique is evaluated with multiple knife-edges, and shows perfect agreement with other multiple knife-edge results [Vogler, 1982].
 - The effect of square, round, and wedge-shaped obstacles is evaluated and shows good agreement with other published results [Hacking, 1970], although the rounded edge results are less accurate and computationally difficult to get.

$$Q_{\text{eff}}(\tau) = Q(\tau) C_n^2(h(\tau)) G_{\text{TR}}(h(\tau))$$

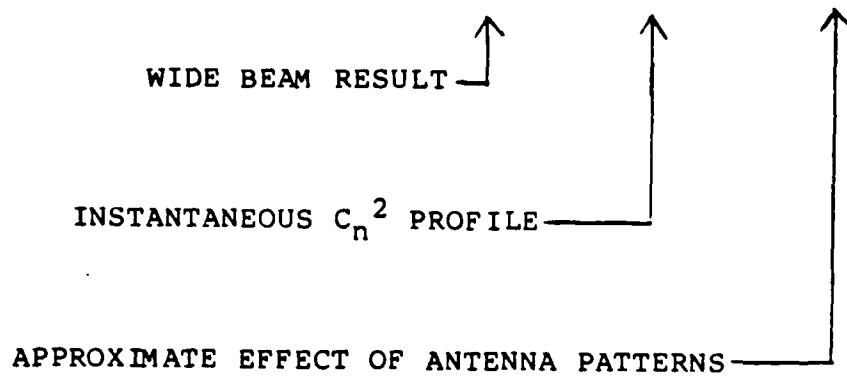


Figure 1-7 Modification of $Q(\tau)$ for long term variability of path loss and delay spread

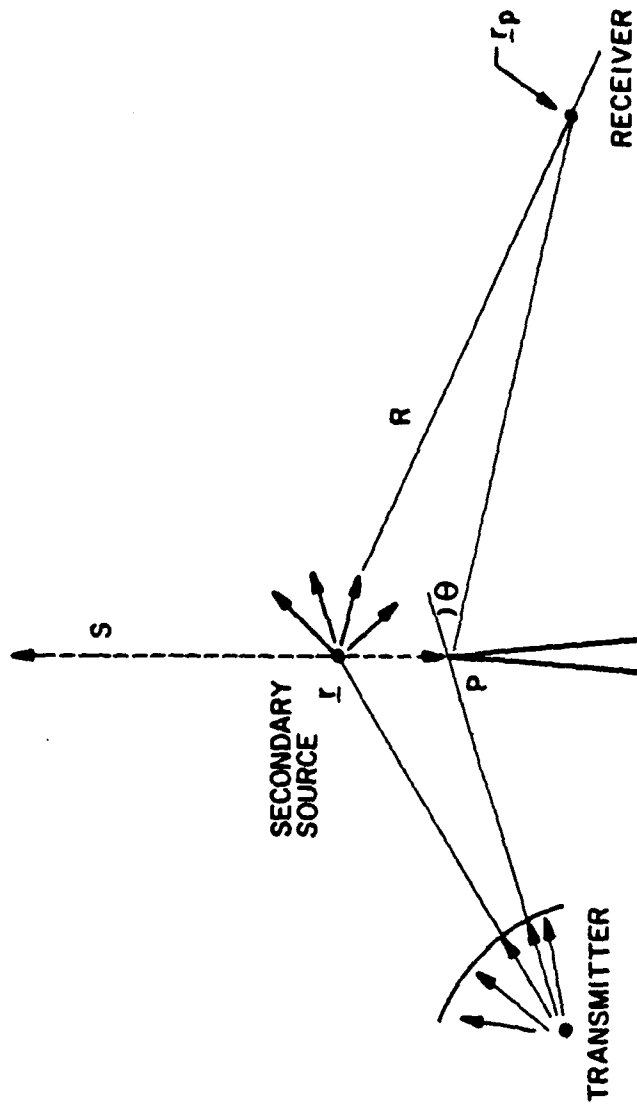


Figure 1-8 Huyghens' Principle for Knife-Edge Diffraction

- It is demonstrated theoretically that the diffraction loss in some cases is reduced by increasing the height of the obstacles.
- A number of existing ad hoc techniques are discussed and a new ray technique is developed which is much simpler to use than the cumbersome integration technique using Huyghens' principle and which is more accurate than the adhoc techniques currently used such as the Deygout [1966] method.
- In the ray technique, the received field consists of the addition of the field due to each ray scattered by the edges as shown in Figure 1-9. The field due to each ray is calculated by using edge diffraction coefficients.
- In order for the field calculated using the ray technique to be continuous as the height of the receiver is increased (or decreased), the edge diffraction coefficients must be determined by treating the previous edge (or transmitter) as the source and the receiver as the observation point (not the next edge). We refer to this technique as the UGTD method for multiple edge diffraction. Figure 1-10 compares the diffraction loss calculated using the UGTD method (dashed line) with that calculated using Huyghens' principle (solid line) for the geometry shown also in the figure. Excellent agreement is seen for receiver heights of less than 140 meters or greater than 270 meters. The UGTD is not as accurate when the receiver is the transition region of two or more edges. Figure 1-11 compare the UGTD ray method with ad-hoc techniques such as the Deygout method [1966], Epstein-Peterson [1953] method and Japanese-Atlas [1957] method. Of these, only the Deygout method is in close agreement for all receiver heights. The Epstein-Peterson and Japanese-Atlas methods break-down whenever there is more than one ray. The Deygout method is not always in as close agreement with the more accurate integral method results (Huyghens' principle or Vogler's results) as is the UGTD method because it includes contributions from non-existent rays in some cases as shown in Section 4.4.
- The UGTD ray technique can be used with rounded edges as described in Section 4.4.

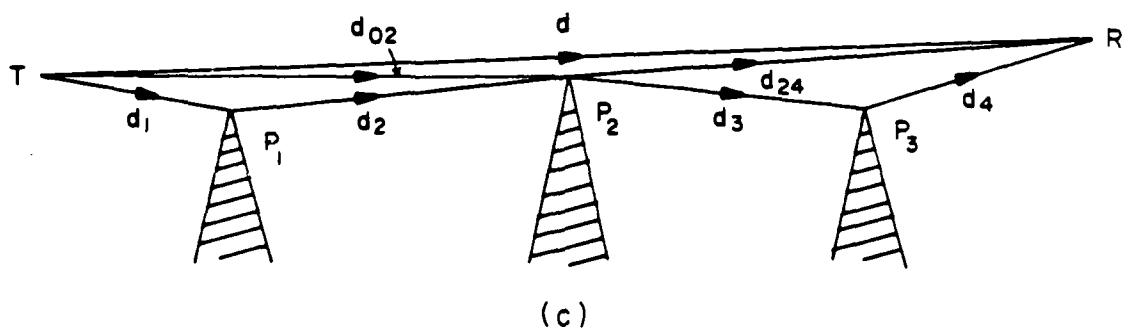
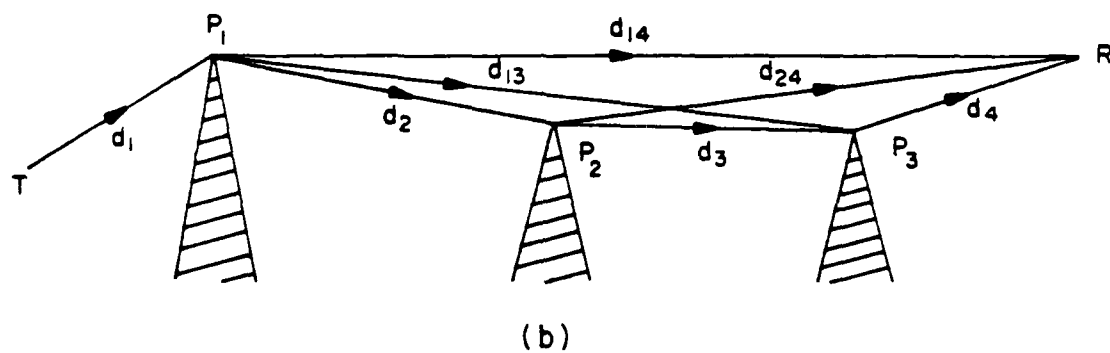
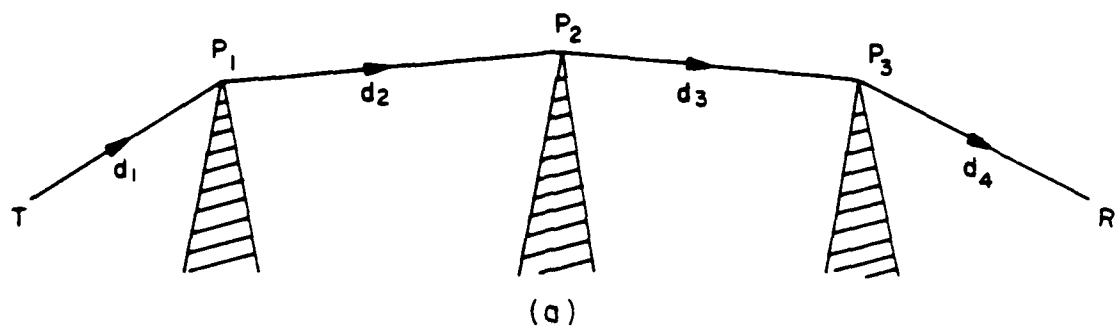


Figure 1-9 Multiple edge diffraction geometries.

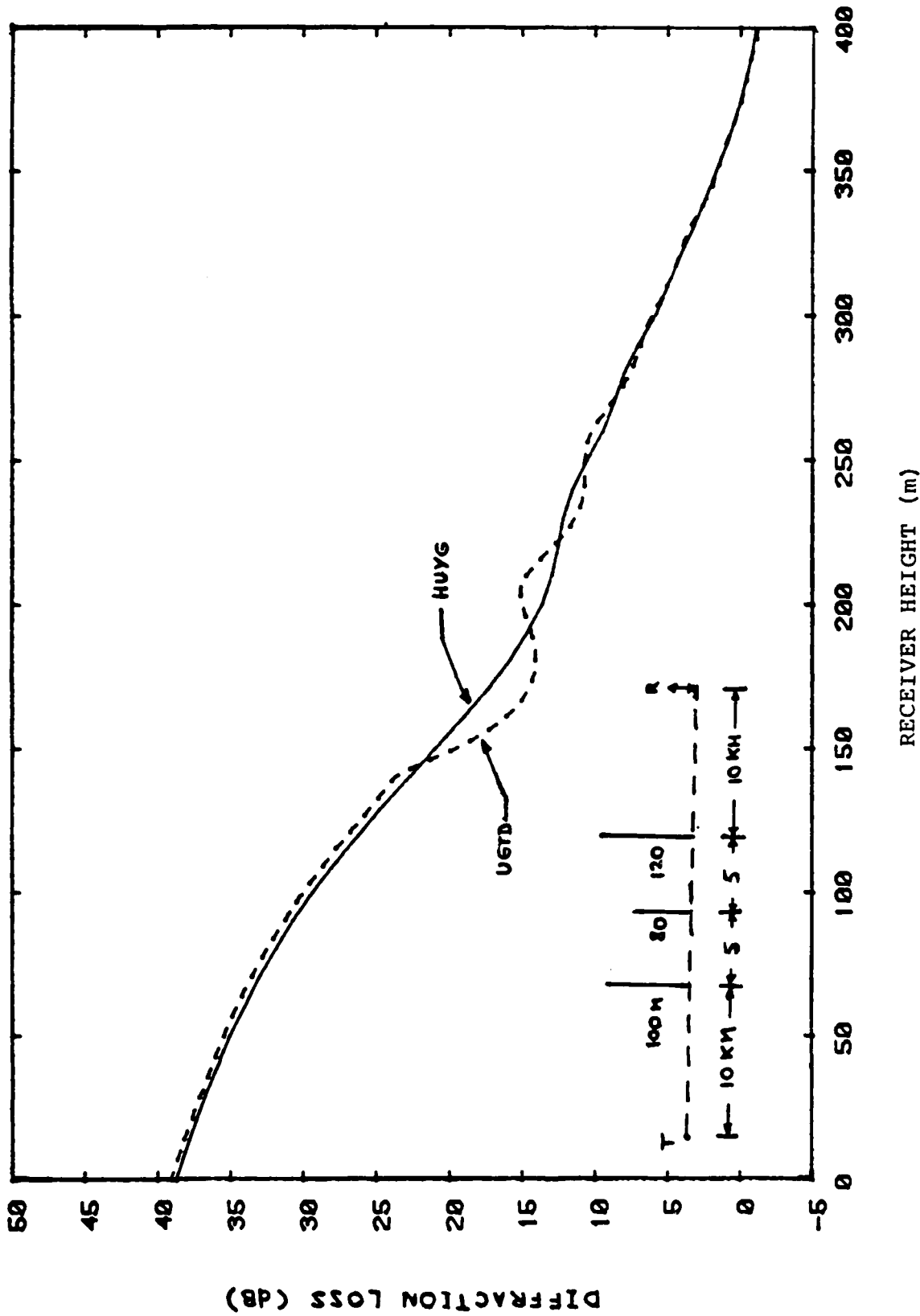
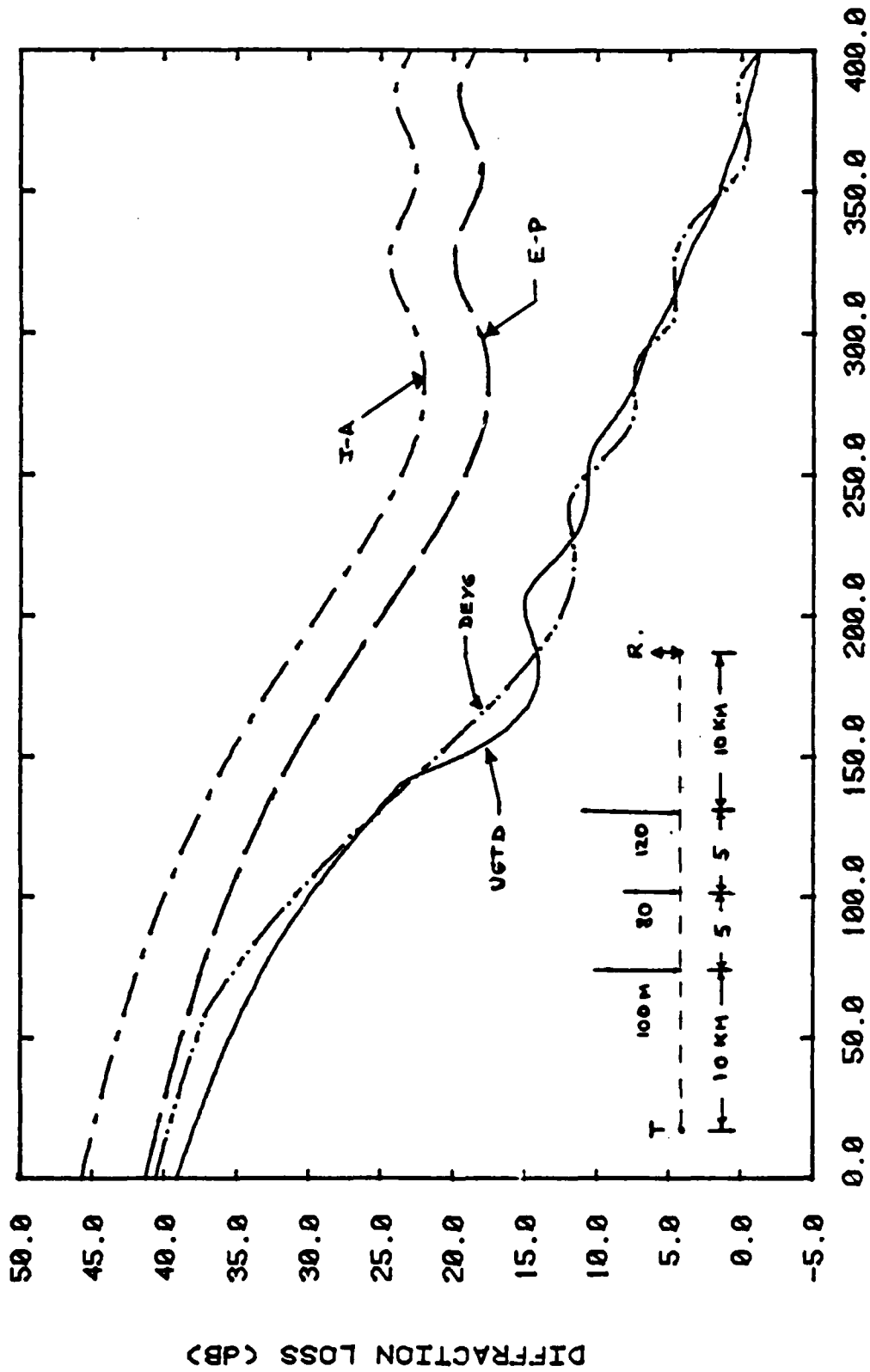


Figure 1-10 Comparison between UGTD ray method and integral solution (Huyghens, principle) for triple knife-edge geometry shown (Frequency = 1 GHz).



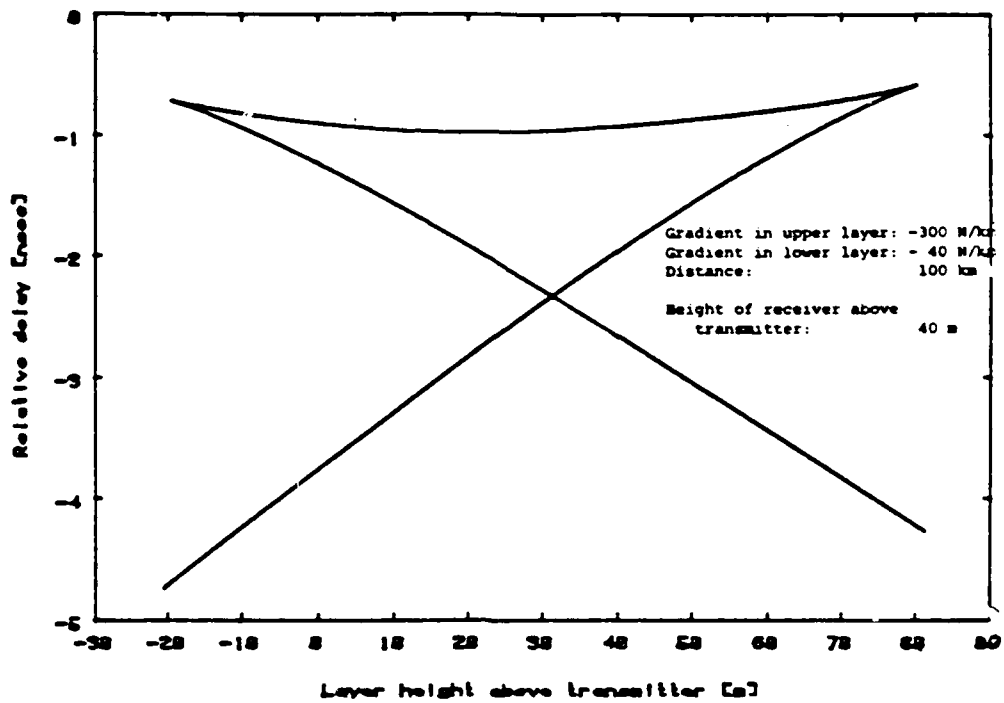
RECEIVER HEIGHT (m)

Figure 1-11 Comparison between UGTD, Epstein-Peterson, Japanese-Atlas and Deygout methods for triple knife-edge geometry shown (Frequency = 1 GHz).

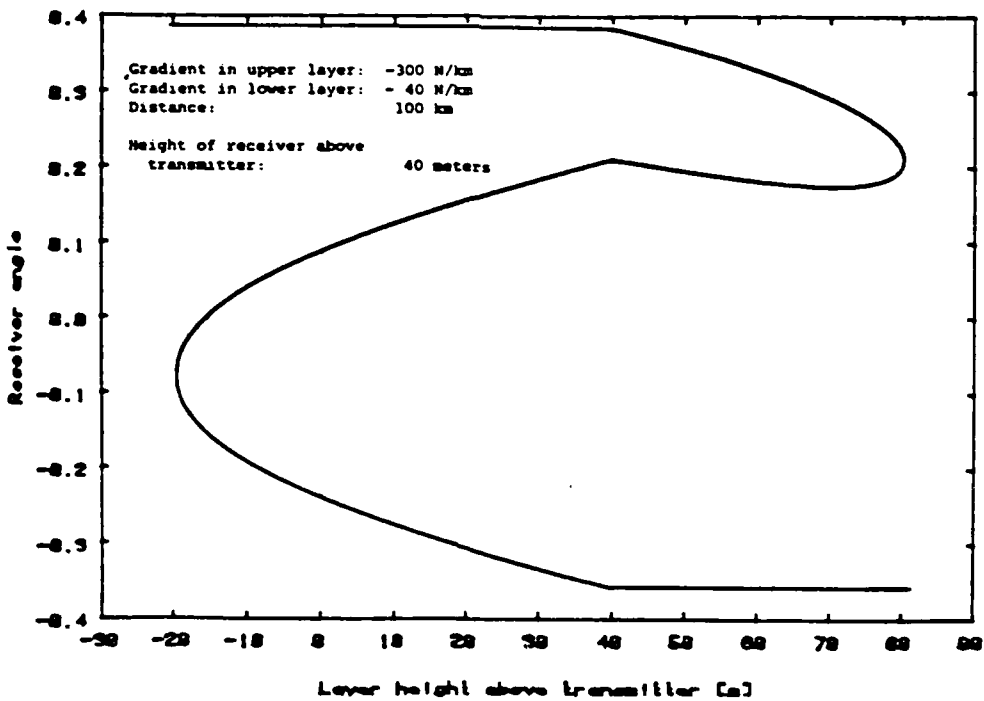
1.2.3 Line-of-Sight Propagation

Refractive multipath is the principal source of frequency selective fading on wideband LOS links. The multipath arises when a ducting layer is formed above a non-ducting layer. In the ducting layer rays are refracted down towards the layer interface, while in the non-ducting layer the rays are effectively turned up towards the layer interface. The multipath characteristics depend strongly on the height profile of the refractivity. Constant gradient layers are commonly observed in the atmosphere and represent an appropriate model for calculating the multipath characteristics. Based on such a model we have obtained analytical results and computed a set of curves characterizing completely the amplitudes and delays of the various multipath rays and their angle-of-arrival. In the neighborhood of caustics a correction factor to the amplitude found from the geometric optics approach is described.

The main conclusion of our investigation is that a three-ray model is necessary to adequately characterize the frequency selective fading. While a modified two-ray model such as that of Rummler [1979] is adequate in a wide range of static multipath conditions only a three ray model can completely characterize the fading on wideband LOS systems. This is particularly true if the dynamic change of the multipath must be characterized, as is required for evaluation of adaptive equalization and synchronization systems. Dynamic changes in the multipath structure occur because the height of the ducting layer above local ground, and relative to the terminals, varies with time of day. As the height of the layer relative to the terminals increases (or decreases), the number of rays, their relative delays and angles of arrival also change. Figure 1-12(a) shows an example of how the delay of the various multipath rays varies as the layer height relative to the transmitter increases from -30 m (transmitter in ducting layer) to +90 m. An important characteristic of the



(a) Delay



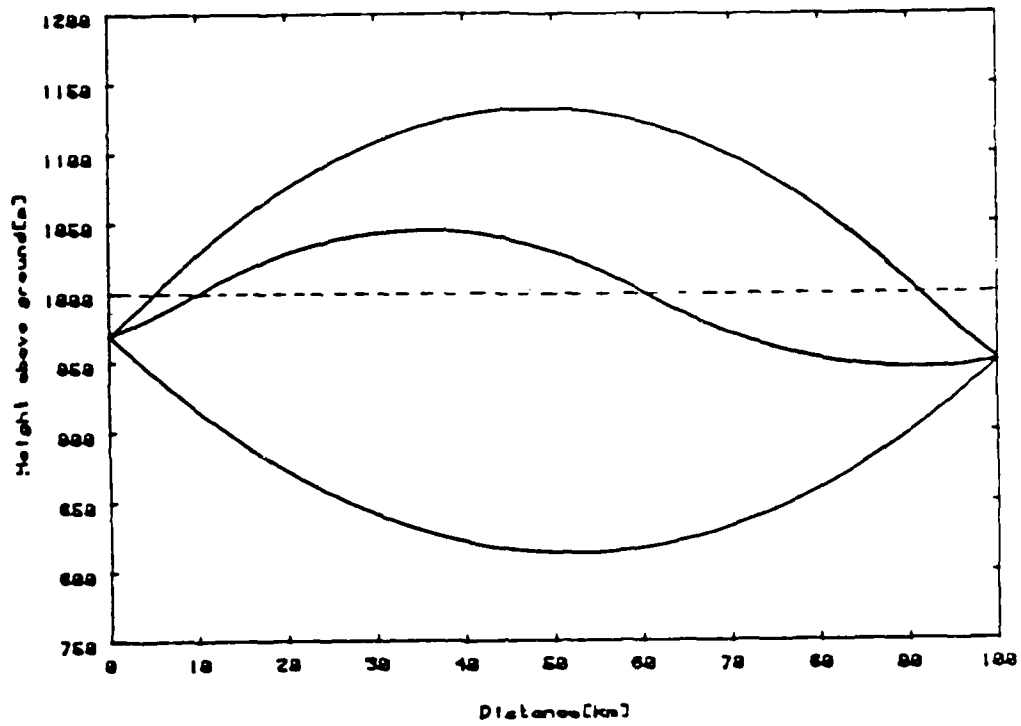
(b) Angle-of-Arrival

Figure 1-12 Example of Multipath Dependence on Layer Height

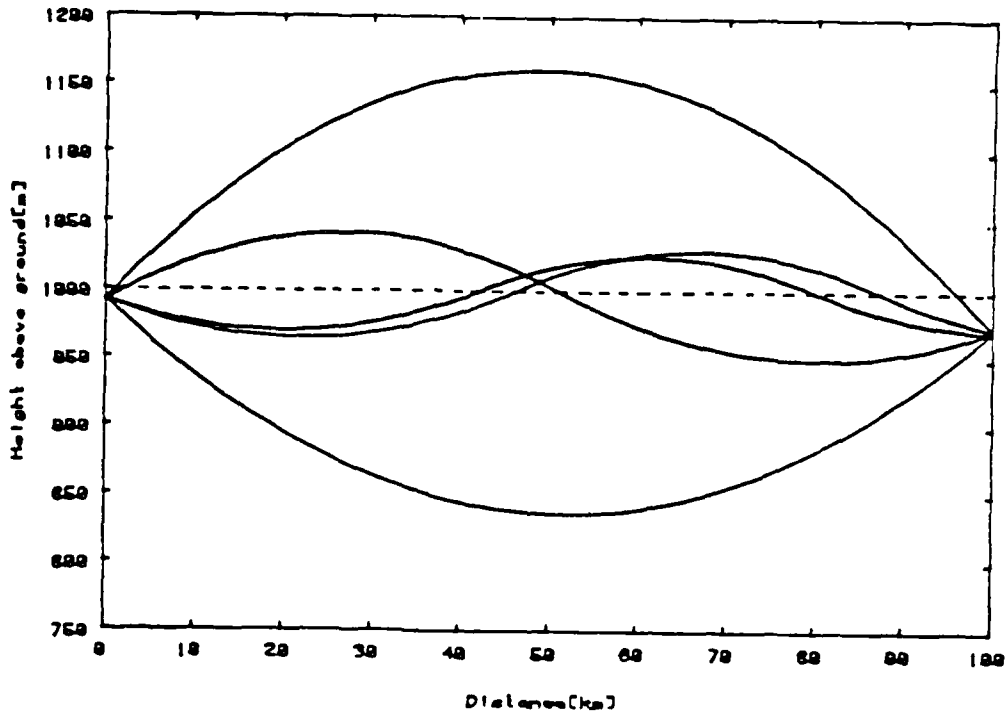
various multipath rays is the angle-of-arrival variation as ducting layer boundary rises up through the terminals. Figure 1-12(b) shows how the angle-of-arrival changes with layer height. It is seen that the angle-of-arrival can change suddenly by an amount which may be comparable to the antenna beamwidth of some systems. This effect is not explicitly included in the Rummler model, which considers only multipath delay dispersion.

Some of the major accomplishments of the LOS research presented in Section 5 are:

1. The effective earth radius transformation has been used to derive multipath equations which are exact for a particular class of refractive index height profiles. The conditions for which the effective earth radius transformation is exact have also been derived. A small-angle approximation to the exact equations leads to a set of quartic equations for the take-off angle or angle of arrival. The quartic equations are equivalent to those obtained by Pickering and DeRosa [1979] using a flat-earth approximation.
2. Three-ray multipath has been found to be typical. Higher order multipath occurs when both terminals are close to the layer interface. The higher order multipath rays show much smaller delay and angle spreads.
3. Multipath rays occur in pairs. Figure 1-13 shows the rays for two different terminal heights relative to the layer and illustrates how two rays appear simultaneously as the layer moves closer to the terminals. That the number of rays is odd can be seen by considering the height of all rays at the distance of the receiver: rays with extremely negative take-off angles will pass well below the receiver and the height of the ray at a fixed horizontal distance will decrease with decreasing take-off angles. Similarly, rays with extremely large positive take-off angles will pass well above the receiver and their height at a fixed receiver distance will increase with increasing take-off angle. For intermediate take-off angles the height of the ray will change continuously. If the height of the ray increases monotonically with the take-off angle there is only one ray, the line-of-sight ray. In general, the continuity of height vs. take-off angle and the asymptotic behavior guarantees an odd number of rays.



(a) Layer 30 m Above Terminal



(b) Layer 10 m Above Terminal

Figure 1-13 Examples of Ray Paths

4. It is shown that the number of rays reflected from an elevated duct for fixed terminal heights and separation distance actually occur in groups of four once the total number of rays (including the direct ray) exceed three, in the following sense: If there are five rays for some layer height, then there is another layer height yielding 7 rays. In general the maximum number of rays is 1, or $3+4p$ where $p>0$.
5. More than three rays occur only when both terminals are close to the layer. This can occur for terminals with unequal heights only when the layer is tilted sufficiently.
6. Multipath rays whose relative delays are indistinguishable may be easily distinguishable based on angle-of-arrival. Modeling angle variations is therefore an important requirement for an LOS multipath model.
7. A possible angle diversity system is described in Section 5. It is shown that angle diversity may be an efficient technique against refractive fading.
8. Equations for calculation of the ray amplitudes have been derived. These are similar to those obtained by Pickering and DeRosa [1979], and are valid everywhere except near caustics. A means of evaluating the field correctly near caustics has also been derived.

1.3 RECOMMENDED FUTURE RESEARCH

1.3.1 Troposcatter

- Evaluate long term path loss and delay spread variations based on the principles outlined in Figure 1-7.
- Develop graphs of path loss and delay spread.
- Modify the computer model to account for anisotropy.
- Compare the model with TRC-170 measurements to determine limitations of the present theory and find empirical or analytical corrections to the theory.

- Compare with world-wide path loss data and atmospheric parameters to determine geographic and seasonal variations of path loss and delay spread. Estimate the physical parameters such as C_n^2 , scale sizes, refractive index, and long term correlations.
- Perform multi-frequency experiment to validate the theoretical model, including anisotropy effects.
- Evaluate experimentally and theoretically the diversity performance of different diversity systems with variable atmospheric parameters.

1.3.2 Diffraction

- Refine the integration techniques in Section 4.2 to speed up the computation.
- Compare the techniques in Section 4.2 with known results for a wedge.

1.3.3 Line-of-Sight

- Evaluate long-term distributions based on atmospheric data. This includes probability of multipath and multipath fading distributions.
- Extend the evaluation of angle diversity techniques by considering more links and antenna patterns.

SECTION 1
REFERENCES

- Atlas of Radio Wave Propagation Curves for Frequencies between 30 and 10,000 Mc/s. Radio Research Laboratory, ministry of Postal Services, Tokyo, Japan, pp. 172-179, 1957.
- Birkemeier, W.P., Duvoisin, P.F., Fontaine, A.B., and Thomson, D.W. (1969), "Indirect atmospheric measurements utilizing RAKE tropospheric scatter techniques - Part II: Radiometeorological interpretation of RAKE channel-sounding observations", Proc. IEEE, Vol. 57, No. 4, pp. 552-559.
- Deygout, J. (1966), "Multiple knife-edge diffraction of microwaves", IEEE Trans. Antennas & Prop., V. AP-14, No. 4, pp. 480-489.
- Epstein, J. and Peterson, A.W. (1953), "An experimental study of wave propagation at 850 Mc/2", Proc. IEEE, V. 41, No. 5, pp. 595-611.
- Hacking, K., (1970) "U.H.F. propagation over rounded hills", Proc. IEE., Vol. 117, No. 3.
- Monsen, P., and Parl, S.A. (1980) Final Report, Adaptive antenna control (AAC) program, CAS-76-8085-6, for U.S. Army, Ft. Monmouth, NJ, March 1980.
- Pickering, L.W. and DeRosa, J.K. (1979), "Refractive multipath model for microwave line-of-sight links", IEEE Trans. Commun., Vol. COM-27, pp. 1174-82.
- Rice, P.L., Longley, A.G., Norton, K.A., and Barsis, A.P. (1965, Rev. 1967), "Transmission loss predictions for tropospheric communications circuits", N.B.S. Tech. Note 101.
- Rummler, W.D. (1979), "A new selective fading model: application to propagation data", BSTJ, Vol. 58, pp. 1037-1071.
- Vogler, L.E., (1982) "An attenuation function for multiple knife-edge diffraction", Radio Science, Vol. 17, No. 6, pp. 1541-1546.

SECTION 2
CHARACTERISTICS OF THE ATMOSPHERE

2. THE STANDARD ATMOSPHERE

Microwave propagation on terrestrial line-of-sight and over-the-horizon links is greatly affected by variability in the mean refractive index of the lower atmosphere and random refractive index fluctuations about the mean. In order to understand and quantify the long term variability in microwave radio links it is important to determine the variability in the atmospheric parameters which affect each mode of propagation.

The mean refractive index in the atmosphere has a value that is near unity. Its departure from unity is so small that it is usually expressed in parts per million, i.e.,

$$n = 1 + N \times 10^6 \quad (2.1)$$

where n is the mean refractive index and N is referred to as the refractivity.

The refractivity N depends on atmospheric pressure, temperature, and humidity as indicated by the formula [Smith and Weintraub, 1953]

$$N = \frac{77.6}{T} \left(p + 4810 \frac{e}{T} \right) \quad (2.2)$$

where p is the atmospheric pressure in millibars, e is the water vapor pressure in millibars and T is the absolute temperature in degrees Kelvin.

Since the atmospheric pressure decreases with height, the mean refractive index under normal conditions decreases exponentially with height, i.e.,

$$n(h) = 1 + N_S \times 10^6 \exp\{-bh\} \quad (2.3)$$

where N_S is the surface refractivity, h is the height in km and b is a parameter with units of inverse kilometers. For sufficiently small heights the decrease in refractive index is approximately linear. The mean refractive index gradient $\Delta N/\Delta h$ in the first kilometer of height is defined as

$$\Delta N/\Delta h = N(1) - N_S = -N_S \{1 - e^{-b}\} \quad (2.4)$$

where ΔN is negative under normal conditions.

Since temperature and humidity vary seasonally and geographically, the surface refractivity N_S and the refractivity gradient also exhibit geographical variations. The average or standard atmosphere is one for which $N_S = 315$ and $b = .136$ [CCIR, 1978] which corresponds to a 1-km refractivity gradient of approximately $\Delta N/\Delta h = -40$ N-units/km.

2.1 VARIABILITY OF THE REFRACTIVITY GRADIENT

The yearly median value of the refractivity gradient in most temperate regions is -40 N-units/km. The variations in the refractivity gradient about the median depend on the height interval over which they are measured. Measurements of refractivity gradients over height intervals of 75m, 150m, 500m, and 1000m conducted in the United Kingdom [Hall and Comer, 1969]

showed that the refractivity gradients measured over the smaller height intervals exhibited more variability than those measured over the greater intervals. In each case, however, the median gradient was found to be -40 N/km. This is significant because the gradients measured over height intervals of 1 km are applicable to over-the-horizon propagation (troposcatter and diffraction) while gradients measured over smaller intervals, say 75 meters or less, are applicable to line-of-sight propagation.

Analysis of measurements of the refractivity gradient over a 1-km height interval have shown $\Delta N/\Delta h$ to be inversely correlated with the surface refractivity. This dependence can be modelled as

$$\Delta N/\Delta h = -A \exp[BN_S] \quad (2.5)$$

where $2.1 < A < 9.3$ and $0.0045 < B < 0.0094$ [Hall, 1979]. In the continental United States the constants A and B have values $A = 7.32$ and $B = .005577$ [Rice, et al., 1967]. World maps of monthly mean values of the 1-km interval refractivity gradient have been prepared by Bean et al., [1966]. Monthly mean values of $\Delta N/\Delta h$ range from -30 N/km in dry climates, to -100 N-/km in the Persian Gulf and West Coast of Africa.

Maps of refractivity gradients in the lowest 100 m of the atmosphere have also been published in the "World Atlas of Atmospheric Radio Refractivity" [Bean, et al., 1966]. The maps give the refractivity gradients not exceeded for 10% and 2% of the time. Complete cumulative time probability distribution of the 100 m gradients at a number of specific locations distributed world wide are available in [Samson, 1975]. The median values of the 100-m gradients are similar to those measured over a 1-km height interval. However, the gradients not exceeded with small

probability tend to be much greater. Large negative gradients which cause ducting ($\Delta N/\Delta h < -157$ N/km) occur with probabilities ranging from the negligible in some dry mountainous regions of the world, to 5% of the time in mild temperate hot humid regions (Charleston, South Carolina), to 40% in tropical maritime climates with mixed wet and dry seasons (Dakar, Senegal).

2.2 EFFECTS OF REFRACTIVITY GRADIENTS

The main effect of refractivity gradients is that radio-waves do not propagate in straight lines. If the height above the surface of the earth over which the radiowave propagates is such that the refractivity gradient can be assumed to be constant, then the bending of the radiowave ray path trajectory can be accounted for by use of an effective earth radius transformation or an earth flattening transformation.

The effective earth radius transformation consists of transforming to a spherical coordinate system in which rays travel in straight lines and the earth (or atmospheric layers in which the rays propagate) is modelled as a sphere with effective radius of curvature, a_e , given by

$$a_e = \frac{a}{1 + a \frac{\Delta N}{\Delta h} \times 10^{-6}} \quad (2-6a)$$

where a is the true earth radius (6370 km). If the refractivity gradient, $\Delta N/\Delta h$ is -40 N/km then $a_e = 8548$ km. The ratio

$$K = \frac{a_e}{a} = (1 + a \frac{\Delta N}{\Delta h} 10^{-6})^{-1} \quad (2.6b)$$

is referred to as the effective earth radius factor.

A second transformation often used is the earth flattening transformation in which rays propagate in arcs of effective radius, r_e , given by the right-hand side of (2-6a) and the earth is flat. Figure 2-1 illustrates the flat-earth and effective earth radius transformations for the case $\Delta N/\Delta h > -157$ N/km. In this case, the ray radius of curvature is positive (rays bend upwards). When $\Delta N/\Delta h < -157$ N/km, the ray radius of curvature (or effective earth radius factor) is negative (rays bend downwards). When $\Delta N/\Delta h = 157$ N/km rays propagate in a straight line ($r_e = \infty$) in the flat-earth model. For this reason it is often convenient to define a modified refractivity M as

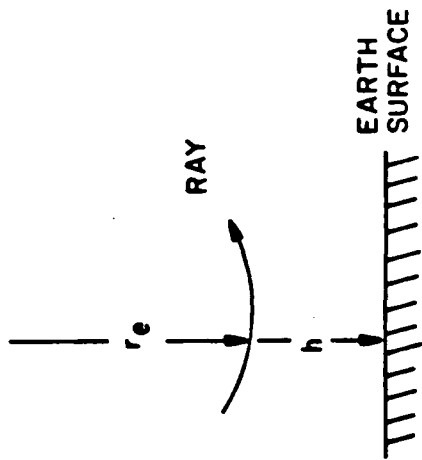
$$M(h) = N(h) + 157 h \quad (2.7a)$$

and the modified refractivity gradient, dM/dh , as

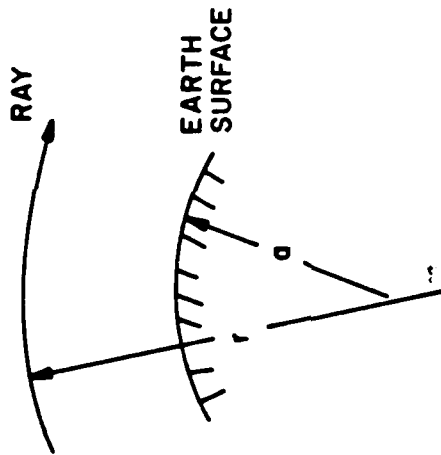
$$\frac{dM}{dh} = \frac{\Delta N}{\Delta h} + 157 . \quad (2.7b)$$

Therefore when $dM/dh > 0$, rays are bent upwards and when $dM/dh < 0$ rays are bent downwards.

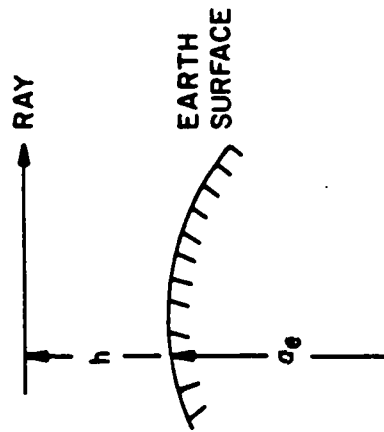
A positive effective earth radius factor, K , (or positive modified refractivity gradient) has the following effects on microwave propagation. In line-of-sight paths, as K increases from its normal value of $4/3$ to ∞ , the earth appears to flatten resulting in greater distances to the horizon for a fixed transmitter height. If K decreases below $4/3$, the horizon distance will also decrease and may result in blockage of the path between two terminals which under normal conditions ($K = 4/3$) have line-of-sight propagation between them. This condition is known as fading due to blockage by the bulge of the earth. In tropo-scatter and diffraction paths, as K increases, the effective



c) FLAT EARTH
EFFECTIVE RAY RADIUS MODEL



b) REAL EARTH
REAL RAY RADIUS



a) EFFECTIVE EARTH RADIUS
STRAIGHT-RAY MODEL

Figure 2-1 Earth Radius Transformations

scattering or diffraction angle decreases because of the earth (or ray curvature) flattening effect resulting in smaller propagation loss and hence stronger signals. Conversely as K decreases below $4/3$ the scattering or diffraction angles increase resulting in weaker signals. Most of the long term variability in microwave (below 10 GHz) diffraction paths can be attributed to variations in the refractivity gradient. In troposcatter paths, it partially accounts for variability in the path loss and multipath spread.

Negative effective earth radius factors (or negative modified refractivity gradients) cause either ducting or multipath fading on line-of-sight paths. These are discussed next. In beyond-the-horizon paths (troposcatter and/or diffraction) negative K factors result in enhanced received signal levels due to ducted propagation.

2.3 DUCTING AND LOS MULTIPATH FADING

Ducting is a meteorological condition in which the modified refractivity M , decreases with height above the surface ($\Delta N/\Delta h < -157$ N/km) rather than increase with height as under normal atmospheric conditions. This condition may persist up to a certain height H above which M may increase at its normal rate ($dM/dh \sim 117$ M/km). If we use the earth flattening transformation, it can be seen that rays leaving the transmitter at an angle θ (measured from the horizontal) smaller than some critical angle, θ_c , are trapped within the duct of thickness H . If the surface is relatively smooth and is a relatively good conductor (e.g., sea water), then the trapped rays may propagate over distances substantially greater than under normal conditions. This situation is illustrated in Figure 2-2.

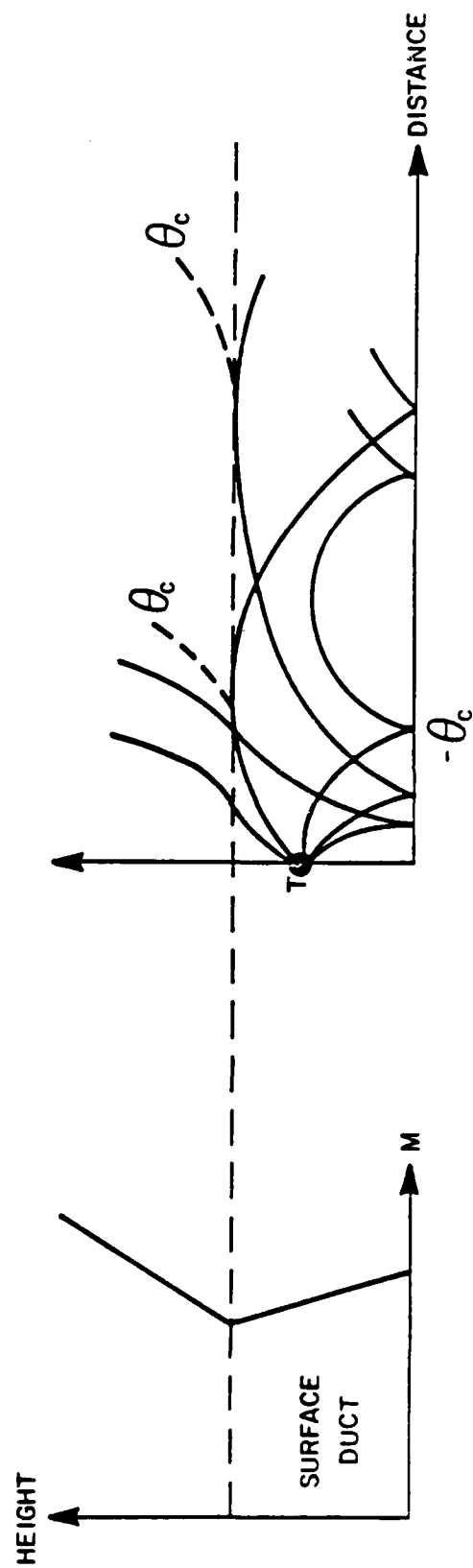
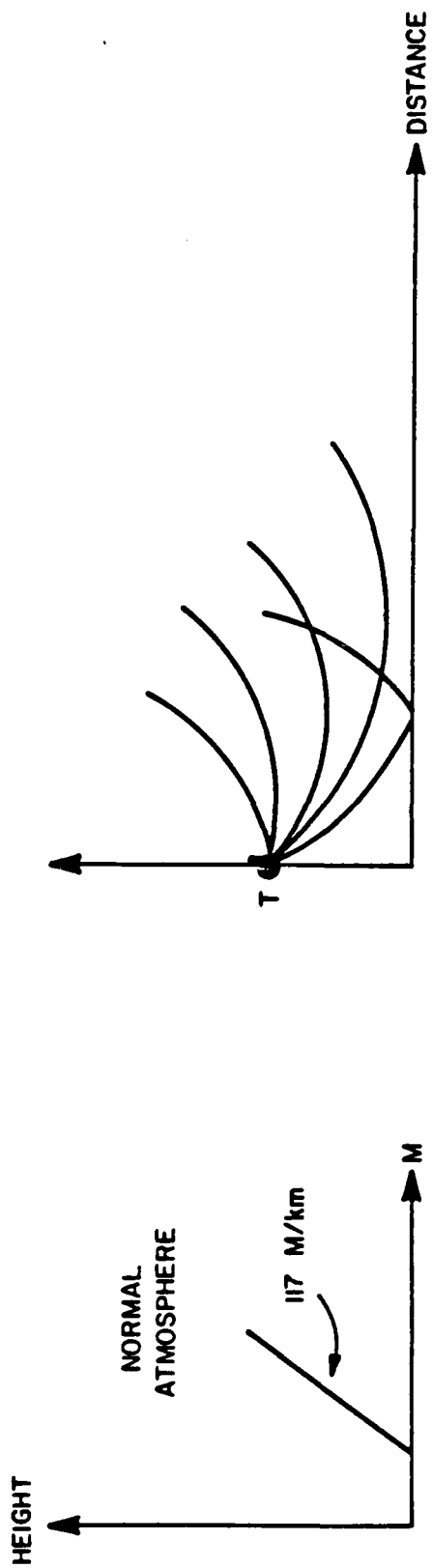


Figure 2-2 Illustration of a Surface Duct

If the layer of thickness H where the modified refractivity decreases with height ($\Delta N/\Delta h < -157 \text{ N/km}$) is elevated, then rays leaving the transmitter with take-off angles, θ , such that $-\theta_c < \theta < \theta_c$ are trapped in the region between the top of the elevated layer and the ground. The angle θ_c is a critical angle which depends on the refractivity gradients of the elevated anomalous layer and the region below the layer, and the location of the transmitter as illustrated in Figure 2-3. If the elevated layer forms a surface duct, then rays trapped within the duct include ground reflections (Figure 2-3a). If the elevated layer forms an elevated duct then ground reflections are not trapped within the duct (Figure 2.3b). At sufficiently long distances or for transmitter and receiver heights sufficiently close to the elevated anomalous layer, multiple ray paths between transmitter and receiver are possible. This condition is known as multipath fading.

Groundbased ducting layers may be formed when the water vapor pressure, e , decreases rapidly with height or if the temperature increases with height or a combination of both (see Eq. 2.2). The movement of a mass of hot dry air over cold wet air (advection) will cause the temperature to increase with height producing a region of low refractive index (ducting layer) above a region of high refractive index. This is most likely to occur in the early evening with the onset of a land breeze. Radiation cooling at night also produces positive temperature gradients. Air next to the ground becomes colder than that higher up creating a surface duct. The duct becomes thicker during the night. In the early morning solar heating of the ground produces an elevated duct. Figure 2-4a shows the number of seconds that refractive fading occurred in a 57 km LOS link during two 3 month periods (summer and fall) for each 1 hour period of the day. These recordings indicate that during the warm summer months advection was the more likely mechanism as fading occurred in the

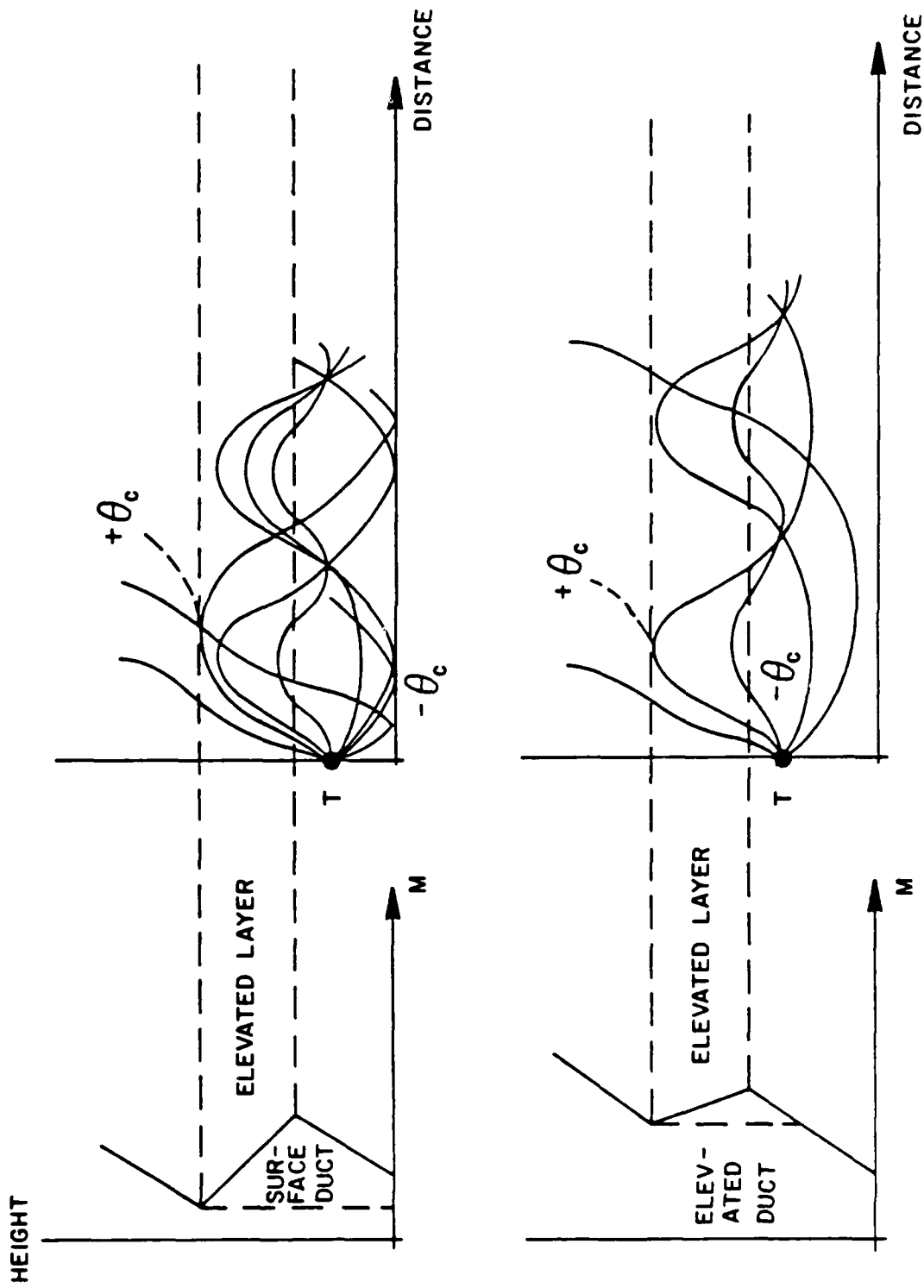
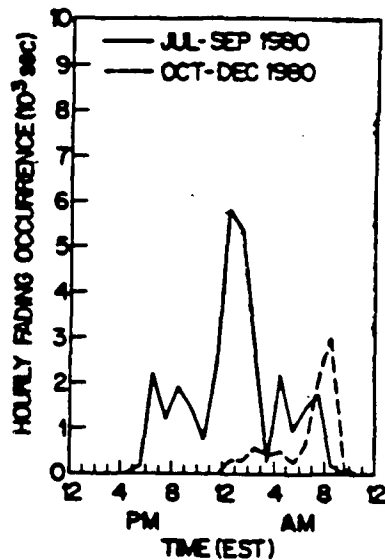
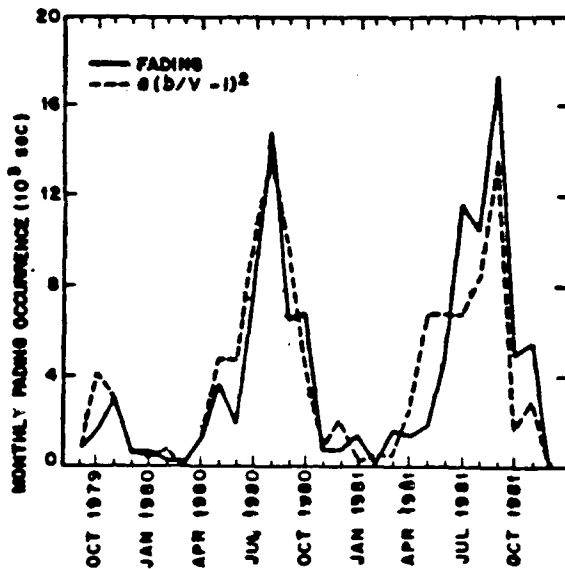


Figure 2-3 Illustration of an Elevated Duct



Diurnal distribution of refractive fading occurrence for two 3-month periods in 1980. Plotted values are total number of seconds that received signal was at least 20 dB below normal level.



Monthly time series of refractive fading occurrence: solid line represents monthly accumulated time that received signal was degraded beyond 20 dB below normal level and broken line represents that predicted by 4 am EST monthly average surface wind speed at Atlanta. Wind speed (V) is in mph, $a = 17600$, and $b = 12$.

Figure 2-4 Refractive Fading Modeled as a Function of Windspeed (Schiavone, 1983)

evening hours. In the fall, however, radiation cooling followed by solar heating of the surface was the probable mechanism as fading was found to occur more often in the early morning hours. In both cases the occurrence of fading, and thus elevated ducting layer formation, was found to be highly correlated with the 4 a.m. monthly average surface wind speed [Schiavone, 1983]. Months having low average 4 a.m. wind speeds are months with frequent occurrence of nonturbulent nocturnal atmospheric boundary layers, a condition which results in fading. Figure 2-4b plots the total number of seconds in a month during which fading occurred for each month in a two year period. The figure also shows that predicted by the relationship

$$t = a (b/v - 1)^2 \quad (2.8)$$

where t is the number of fading seconds in a month, v is the 4 a.m. monthly average surface wind speed in miles per hour, and a and b are parameters which depend on climate zone. For the Palmetto, GA link where the measurements of Figure 2-4 were made they are given by $a = 17600$ and $b = 12$ [Schiavone, 1983]. The plots of Figure 2-4a and 2.4b can be used to generate diurnal and annual statistics of fading occurrence on LOS links.

In addition to the probability of duct occurrence it is useful to know the duct thickness and the refractivity gradient within the duct. Distributions of ducting layer thickness have been compiled by Bean and Dutton [1966] for various regions of the world and are reproduced in Figure 2-5. The layer thickness, ΔH , is seen to vary from 40 to 280 meters. Median values for three climates are

$$\Delta H = \begin{cases} 66 \text{ meters,} & \text{arctic climate} \\ 97 \text{ meters,} & \text{temperate climate} \\ 106 \text{ meters,} & \text{tropical maritime climate} \end{cases} \quad (2-9)$$

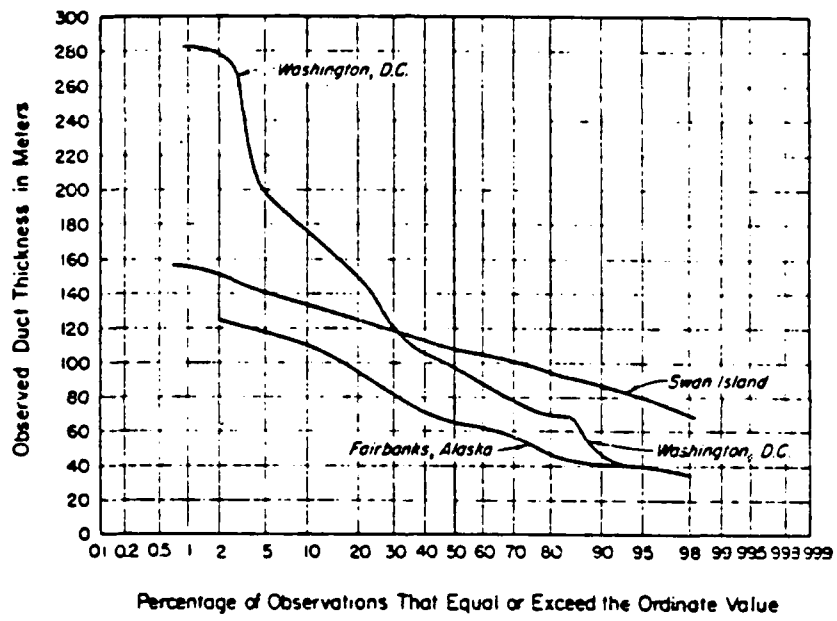


Figure 2-5 Distribution of Duct Thickness at Various Locations (From Bean and Dutton, 1966)

For a given ducting layer thickness, ΔH , the refractivity gradient depends on the duct intensity, defined as the difference in the refractivity (or modified refractivity) at the bottom and top of the layer, $\Delta M = \Delta N$. Meteorological data collected at 6 stations in Japan over a period of 6 years yielded the distributions of duct intensity ΔM and modified refractivity gradient $\alpha_d = -\Delta M/\Delta H$ shown in Figure 2-6 [Sasaki and Akiyama, 1979]. Median values of the modified refractivity gradient within the layer were found to be around -60 M/km which corresponds to refractivity gradients of $\Delta N/\Delta H = -217$ N/km. Modified refractivity gradients of -300 M/km (or $\Delta N/\Delta H = -457$ N/km) were found to occur 1% of the time.

2.4 SMALL SCALE IRREGULARITIES

Small scale turbulent irregularities in the refractive index give rise to forward scatter and scintillation of radio-waves at microwave frequencies. The random fluctuations in the refractive index are usually described in terms of the spatial correlation function, ϕ_n , or by a three-dimensional power spectral density (wavenumber spectrum), ϕ_n , which are defined as

$$\phi_n(\underline{r}_1 - \underline{r}_2) = E\{\delta n(\underline{r}_1) \delta n(\underline{r}_2)\} \quad (2.10a)$$

$$\phi_n(\underline{\kappa}) = \frac{1}{(2\pi)^3} \int \int \int_{-\infty}^{\infty} \phi_n(\underline{r}) e^{j\underline{\kappa} \cdot \underline{r}} d^3 \underline{r} \quad (2.10b)$$

where δn is the refractive index random fluctuations due to turbulence and $\underline{\kappa} = 2\pi/\lambda$ where λ is the scale of the turbulence. When the turbulence fluctuations are isotropic, the correlation function and the three-dimensional wavenumber spectrum are functions of the magnitudes $r = |\underline{r}_1 - \underline{r}_2|$ and κ , respectively.

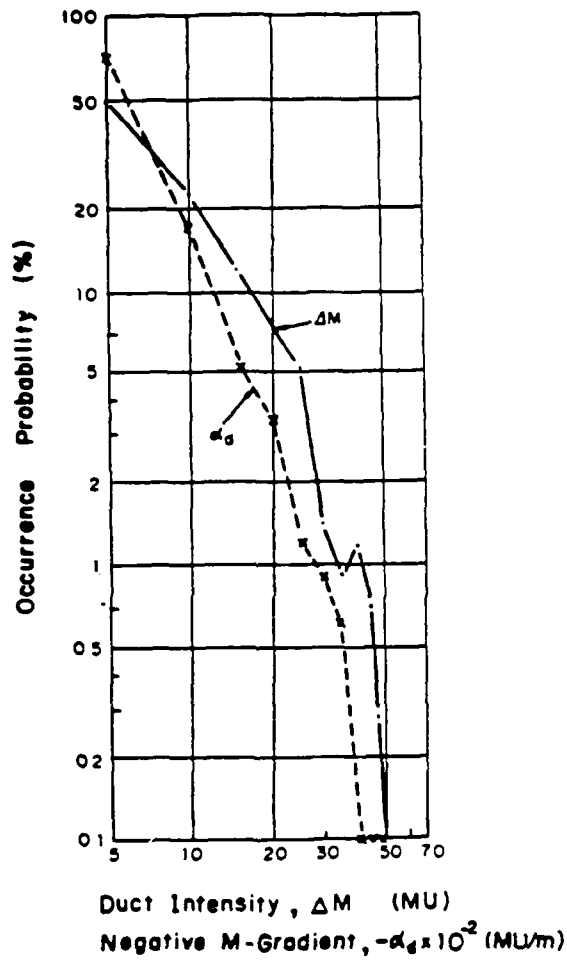


Figure 2-6 Distribution of Gradient
 (Sasaki and Akiyama, 1979)

The turbulent flow theory of Obukhov [1941] and Kolmogorov [1943] indicates that turbulence results from the breaking of eddies ('blobs') into progressively smaller and smaller eddies. Turbulence is characterized by a series of scale size parameters. The largest eddies are anisotropic, and larger than the outer scale L_0 of isotropic turbulence. This region of the wavenumber spectrum is called the buoyancy region, and little is known about the shape of the spectrum in this region. For troposcatter a power law of $\phi_n(\kappa) \sim \kappa^{-5}$ is recommended by NBS and CCIR. The size of the largest eddies contributing to the isotropic turbulence is the outer scale L_0 . The smallest eddy size is called the inner scale ℓ_0 . Turbulence of a scale size smaller than ℓ_0 is dissipated rapidly due to molecular viscosity and does not contribute to the refractive index fluctuations. For turbulence scale sizes in the range $\ell_0 < \ell < L_0$ (inertial sub-range), the Kolmogorov-Obukhov theory predicts a wavenumber spectrum of the form [Tatarskii, 1971]

$$\phi_n(\kappa) = 0.033 C_n^2 L_0^{+11/3} (1 + \kappa^2 L_0^2)^{-11/6} e^{-(\kappa \ell_0 / 2\pi)^2} \quad (2.11)$$

where C_n^2 is the structure constant of the isotropic turbulence. This is a modified von Karman spectrum. For anisotropic turbulence C_n^2 will be used to denote the vertical structure constant.

This description of the refractive index fluctuations assumes that the turbulent fluctuations are isotropic and in the inertial subrange. Refractive index fluctuations at larger scale sizes are highly anisotropic and cannot be modelled by Eq. (2.11). Refractive index fluctuations due to anisotropic turbulence may be modelled, locally, by a wavenumber spectrum of the form

$$\phi_n(K_x, K_y, K_z) = A [1 + (aK_x)^2 + (bK_y)^2 + (cK_z)^2]^{-m/2} \quad (2.12)$$

where a , b and c are the outer scales of the turbulence in the x , y and z planes, and m is called the wavenumber spectrum slope. In this region ($l > L_0$) the spectrum slope is not $11/3$ as predicted by the Kolomogorov-Obukhov theory. The spectrum slope is less than $11/3$ for horizontal wavenumbers and larger than $11/3$ for vertical wavenumbers (Crane, 1980b).

2.4.1 The Structure Constant C_n^2 For Isotropic Turbulence

The structure constant, C_n^2 , is a parameter which is proportional to the mean squared fluctuations of the refractive index and inversely proportional to the outer scale of the turbulence. It is defined by

$$E[(|n_1(\underline{r}) - n_1(\underline{r}')|^2)] \sim C_n^2 |\underline{r} - \underline{r}'|^{m-3}$$

where $1 + n_1(\underline{r})$ is the refractive index at the point \underline{r} . C_n^2 has units of (meters)^{-2/3} when the power law dependence of the wavenumber spectrum is $m=11/3$. Its significance stems from the fact that the scattering cross-section is proportional to C_n^2 and independent of the scale of the turbulence when in the inertial subrange. The structure constant is related to the variance σ_n^2 of the refractive index and the outer scale of turbulence L_0 by

$$C_n^2 = \sigma_n^2 \frac{\Gamma(\frac{5-m}{2})}{\Gamma(\frac{m-1}{2})} \frac{1}{(2L_0)^{m-3}}, \quad 3 < m < 5$$

where m is the spectrum slope parameter in (2.12), usually assumed to be $11/3$ for turbulent scatter. For that case we have (isotropic turbulence)

$$C_n^2(m = \frac{11}{3}) = 1.91 \sigma_n^2 / L_0^{2/3} .$$

Note that C_n^2 is only defined when the spectrum slope is in the interval (0,3). On the other hand, σ_n^2 is defined for all $m > 3$.

The parameter C_n^2 exhibits temporal (long-term), geographical (climate zone dependent) and height variations.

Long-term measurements made by Chadwick and Moran [1980] at fixed heights indicated that the hourly and monthly statistics of C_n^2 were well described by the lognormal distribution, i.e.,

$$p(y) = \frac{1}{\sqrt{2\pi} \sigma} \exp\left\{-\frac{(y - 10 \log \hat{C}_n^2)^2}{2\sigma^2}\right\} \quad (2-13)$$

where $y = 10 \log C_n^2$, and \hat{C}_n^2 is the median of C_n^2 and σ is the standard deviation in dB. The measurements of Chadwick and Moran [1980] indicated the standard deviation of $10 \log C_n^2$ was 6-dB for all time blocks in which the data was analyzed (hourly and monthly). The median, \hat{C}_n^2 , was a function of the hour of day, month, and height. When viewed as a function of time-of-day, the structure constant peaked at about midnight and midday with the lowest values occurring at sunrise and sunset. The ratio of the highest to lowest observed values in the course of a day was about 5. The monthly variations in \hat{C}_n^2 were greater than the diurnal variations with the greater values occurring in the summer time and the lower values in the winter. The ratio of the summer values to the winter values was around 10-20 and the April and September values were about half of the summer values.

The diurnal and yearly cycle variations in \hat{C}_n^2 measured by Chadwick and Moran in Colorado can be modelled as

$$\hat{C}_n^2 = \bar{C}_n^2 (1 + .66 \cos \frac{\pi T}{6}) (1 - .85 \cos \frac{\pi M}{6}) \quad (2.14)$$

where T is the time-of-day in hours, $1 < M < 12$ is the month (northern hemisphere) and \tilde{C}_n^2 varies with height and climate zone. The ratio of summer to winter values may also be climate dependent.

The height dependence of C_n^2 has been investigated by several authors. The simplest model is that of Fried (1967) for C_n^2 at optical frequencies,

$$C_{n,opt}^2 = C_{n0}^2 h^{-b} \exp(-h/h_0) \quad (2.15)$$

where $b = 1/3$, $h_0 = 3200\text{m}$, and $C_{n0}^2 = 4.2 \cdot 10^{-14} \text{m}^{-1/3}$. A more recent model is that of Hufnagel (1974)

$$C_{n,opt}^2 = 2.7 \cdot 10^{-16} \left[3\bar{u}^2 \left(\frac{h}{h_1} \right)^{10} e^{-h/h_2} + e^{-h/h_3} \right] \text{m}^{-2/3} \quad (2.16)$$

where

- \bar{u}^2 = mean square windspeed, typically $100-1000(\text{m/s})^2$,
- h_1 = 10 km,
- h_2 = 1 km,
- and h_3 = 1.5 km.

These optical models apply to radio frequencies only if the humidity is low. At microwave frequencies fluctuations in water vapor pressure (humidity) and their height dependence contribute significantly to the refractive index fluctuations, i.e., structure constant, at altitudes below 10 km. Sirkis [1971] has investigated the effects of water vapor pressure fluctuations and

their height dependence on the structure constant height profile assuming that temperature and water vapor pressure fluctuations are uncorrelated. Figure 2-7 shows the structure constant as a function of height for various values of the water vapor pressure at sea level. These curves show that at low altitudes 1-3 km, the structure constant for very humid conditions is 200 times greater than under very dry conditions. The rate at which the structure constant decreases with height increases as the surface water vapor pressure increases. These theoretical height profiles of the structure constant indicate that at microwave frequencies the strength of troposcatter signals will be less sensitive to rain attenuation as the occurrence of rain is accompanied by an increase in the humidity (water vapor pressure).

C_n^2 can be related to other atmospheric parameters, [Tatarskii, 1971; Ottersten, 1969], i.e.,

$$C_n^2 = 2.8 L_0^{4/3} M^2 \quad (2.17)$$

where L_0 is the outer scale of the turbulence and M is the mean vertical gradient of the refractive index. The formula shows that C_n^2 is large when the mean gradient is large and is associated with high wind shear. M can be calculated from [Van Zandt et al., 1978]:

$$M = -77.6 \cdot 10^{-6} \frac{P}{T} \frac{1}{\theta} \frac{\partial \theta}{\partial z} \left[1 + \frac{15,500q}{T} \left(1 - \frac{1}{2} \frac{\theta}{q} \frac{\partial q}{\partial z} / \frac{\partial \theta}{\partial z} \right) \right] \quad (2.18)$$

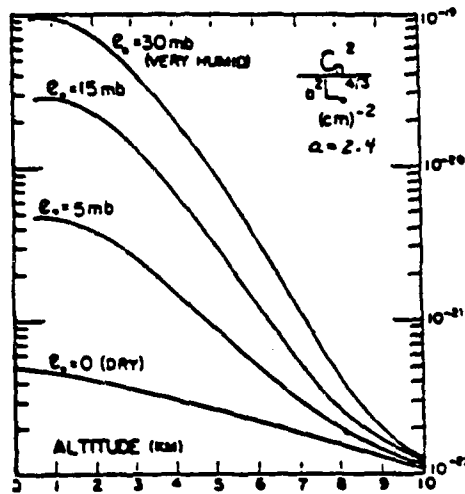


Figure 2-7 Structure Parameter as Function of Altitude with Sea-Level Water Vapor Pressure as Parameter. (From Sirkis, 1971)

where

- P = atmospheric pressure
- q = specific humidity $\sim 0.622 e/p$,
- e = water vapor pressure
- T = absolute temperature
- θ = potential temperature.

Van Zandt et al. [1978], suggest that this expression can be used to calculate C_n^2 averaged over a 1 km height and over several minutes, by using rawinsonde data with samples only every 100 m. They develop a layered model of C_n^2 that also takes into account the wind shear. Van Zandt et al. [1980], suggest an improved statistical model. The models have only been used above 4 km where humidity is less of a factor, but appear to give good results in that range.

Weinstock [1981] considers the turbulence to exist in relatively thin layers, which seems to agree with many observations of C_n^2 . He gives

$$C_n^2 = \frac{R_f}{1 - R_f} a^2 \frac{\alpha'}{\alpha''} \left(\frac{L_B}{2\pi C_1} \right)^{4/3} M^2 \quad (2.19)$$

where

L_B is the layer thickness,

R_f is the flux Richardson number

$R_f \sim 0.25$ (clear turbulence)

α'/α'' is the ratio of diffusivity of the refractive index and of heat. When significant turbulence exists we have

$$\alpha' / \alpha'' \sim 1 .$$

The constants a^2 and C_1 are given by

$$a^2 \sim 2.8 ,$$

and

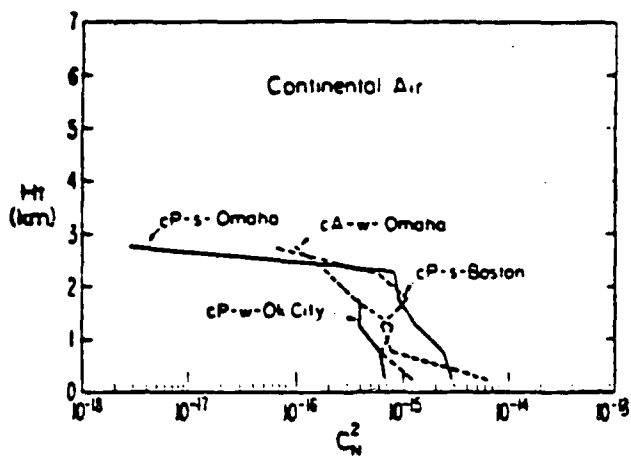
$$C_1 \sim 1.5 .$$

Hence

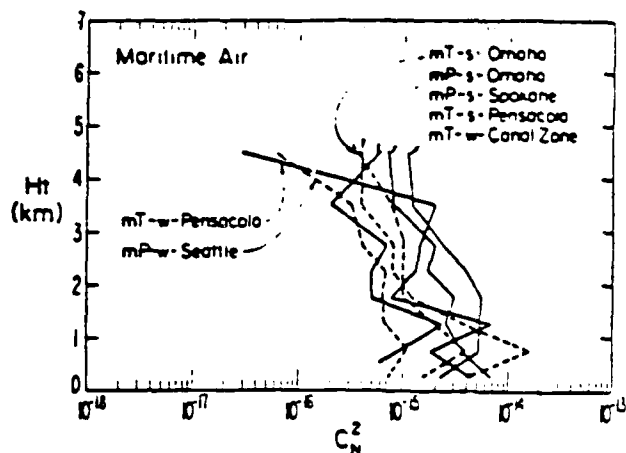
$$C_n^2 \sim 0.047 M^2 L_B^{4/3} . \quad (2.20)$$

Comparing this with (2.17) suggests that typically the layer thickness is 20 times the outer scale. This result applies to stable stratified turbulence only, which is more likely to occur above the tropopause than in the lower troposphere.

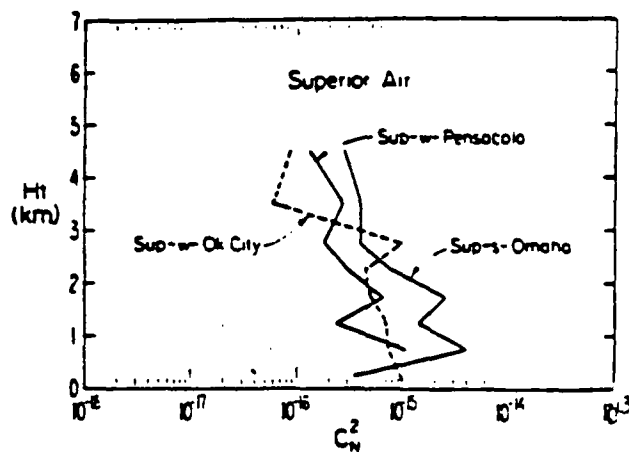
The climate zone dependence of the structure constant is correlated to humidity fluctuations. Gossard [1977] describes a technique for calculating the structure constant at microwave frequencies from measurements of temperature and water vapor pressure fluctuations and their correlation. Figure 2-8 shows height profiles calculated by Gossard [1977] for three types of air masses: continental (those originating over land), maritime (those originating over sea) and superior (masses formed at high levels in the atmosphere). These profiles show summer values about ten times greater than winter values. Median values for the year can be modeled as



(a)



(b)



(c)

Figure 2-8 Height Profiles of the Structure Constant (m^{-2/3})
(From Gossard, 1977)

$$\tilde{C}_n^2(h) = C_{n0}^2 e^{-h/h_0} \quad 0 < h < h_1 \quad (2.15a)$$

where C_{n0}^2 , and h_0 are climate zone dependent. For the three types of air masses in Gossard's measurements, they are given by

$$C_{n0}^2 = \begin{cases} 1.5 \times 10^{-15} \text{ m}^{-2/3}, & \text{Continental} \\ 5 \times 10^{-15} \text{ m}^{-2/3}, & \text{Maritime} \\ 1.5 \times 10^{-15} \text{ m}^{-2/3}, & \text{Superior} \end{cases} \quad (2.15b)$$

$$h_0 = \begin{cases} 2200 \text{ m}, & \text{Continental} \\ 2000 \text{ m}, & \text{Maritime,} \\ 2200 \text{ m}, & \text{Superior.} \end{cases} \quad (2.15c)$$

The vertical height dependence modeled by Eq. (2.15) assumes that the structure constant decreases monotonically with height while in practice this is not the case as indicated by the measured profiles of Figure 2-8. Smoothing of the structure constant height profile will not have a significant effect in the prediction of troposcatter signal strength. However, vertical stratification of the structure constant will have an effect on the long term variability of the delay spread as the largest delay spreads will occur when strong layers of turbulence occur in the upper part of the common volume. While there are no specific data available, the C_n^2 measurements to date suggest that turbulence layers have a thickness of 500-1000 m.

2.4.2 The Outer Scale of Turbulence

The outer scale L_0 usually depends on whether the turbulence is observed horizontally or vertically. The large scale turbulence can be extremely anisotropic. For troposcatter links the vertical scale is the most important. Fried (1967) suggest the simple model

$$L_0 \sim 2\sqrt{h}$$

where h is the height above sea level in meters. Crane (1980b) suggests a constant value of $2\pi L_0 \sim 70\text{m}$ in the lower troposphere. Van Zandt et al., (1978) used $L_0 \sim 10\text{ m}$ to fit their model to high altitude measurements. Other measurements have indicated L_0 in the range of 1-100 m. Crane (1981) suggests a typical value of $2\pi L_0 \sim 5\text{m}-20\text{m}$

2.4.3 The Inner Scale of Turbulence

Below the smallest scale of turbulence ℓ_0 the wavenumber spectrum falls off rapidly. For $m = 11/3$ the following modified Von Karman spectrum is often used:

$$\phi_n(k) = 0.033 C_n^2 k^{-11/3} \exp(-(k\ell_0/2\pi)^2) ,$$

ℓ_0 is on the order of a few millimeters. Fried (1967) uses $\ell_0 \sim 10^{-3} h^{1/3}$. In the lower troposphere $h \sim 10\text{ km}$ is a reasonable approximation.

2.5 ATMOSPHERIC ABSORPTION

At frequencies above 10 GHz oxygen and water vapor absorption as well as attenuation due to precipitation will be significant. The attenuation due to oxygen and water vapor absorption for a path of length, d , is given in dB by

$$A_G = \int_0^d [\gamma_0(r) + \gamma_w(r)] dr \quad (2.16)$$

where γ_0 is the specific attenuation of oxygen in dB/km, and γ_w is the specific attenuation of water vapor.

For line-of-sight or diffraction paths, the specific attenuation of oxygen and water vapor can be assumed to be constant along the entire path, so that Eq. (2.16) reduces to

$$A_G = [\gamma_0(0) + \frac{\rho}{7.5} \gamma_w(0)] d \quad (2.17)$$

where $\gamma_0(0)$ and $\gamma_w(0)$ are shown in Figure 2-9 as a function of frequency and ρ is the water vapor concentration in grams/m³. This also applies to troposcatter paths provided the height of the common volume is less than 2 km as absorption due to water vapor occurs mainly at heights of 2 km or less. Absorption due to oxygen occurs mainly at heights of 4 km or less.

The specific attenuation due to water vapor can be modeled as [Liebe, 1969]

$$\gamma_w(0) = 2.1 \times 10^{-5} f^2 + \frac{2.69 \times 10^{-3} f^2}{9 + (f - 22.235)^2} + \frac{2.69 \times 10^{-3} f^2}{9 + (f + 22.235)^2} \quad (2.18)$$

where f is the frequency in GHz. The second and third terms account for the absorption due to the 22 GHz absorption line while the first term is the so-called residual absorption.

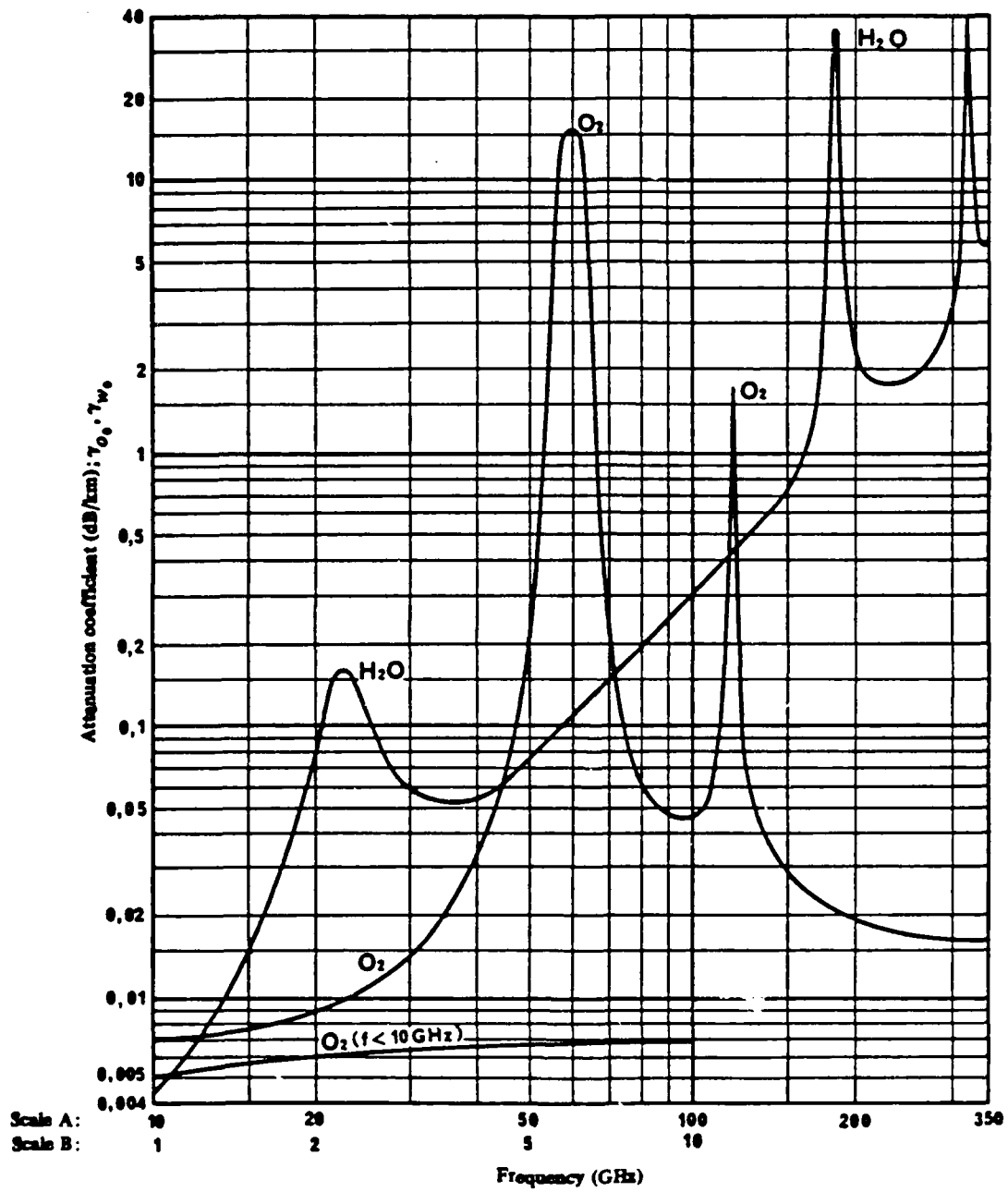


Figure 2-9 Atmospheric Attenuation Coefficient

At frequencies below 45 GHz, the attenuation due to oxygen is mostly due to the 60 GHz oxygen absorption line. It can be modelled as [VanVleck, 1947]

$$\gamma_0(f) = \frac{6.4 \times 10^{-3} f^2}{f^2 - .32} + \frac{1.9 \times 10^{-2} f^2}{5.07 + (f - 60)^2} + \frac{1.9 \times 10^{-2} f^2}{5.07 + (f + 60)^2} \quad (2.19)$$

The specific attenuations of Eqs. (2.18) and (2.19) and Figure 2-9 assume an atmospheric pressure of 1 atmosphere, temperature of 20°C and water vapor density of 7.5 g/m³. Since these parameters vary geographically and seasonally some variability in the atmospheric attenuation will occur.

2.6 RAIN ATTENUATION

Attenuation due to rain arises from the absorption of the energy by the water droplets and from the scattering of energy. For wavelengths which are long compared with the rain drop size, i.e., microwaves, the attenuation due to absorption will be greater than that due to scatter. At millimeter wavelengths, however, scatter will predominate.

The total attenuation due to rainfall over a path of length, d , is given in dB by

$$A_R = \int_0^d \gamma_R(r) dr \quad (2.20)$$

where $\gamma_R(r)$ is the specific attenuation of rain in dB/km.

The specific attenuation for a medium of sparsely distributed rain drops is given by [Ishimaru, 1978],

$$\gamma_R = 4.343 \int_0^{\infty} Q_t(D)N(D)dD \quad (2.21a)$$

where $Q_t(D)$ is the sum of the absorption and scattering cross sections (extinction cross section) of a rain drop of diameter D and $N(D)$ is the rain drop size distribution. The extinction cross section, $Q_t(D)$, of a rain drop depends on the frequency and closed form solutions of Eq. (2.21a) valid for all frequencies cannot be obtained. Propagation experiments in short radio paths show that the measured specific attenuation, when plotted as a function of rain rate, R , is of the form

$$\gamma_R = aR^b \quad (2.21b)$$

where R is the rain rate in mm/hr and a and b are constants which depend on frequency and temperature. Olsen, et al. [1978] have shown that (2.21b) can also be arrived at from Eq. (2.20) if the extinction cross-section $Q_t(D)$ at a given frequency is of the form

$$Q_t(D) = cD^n \quad (2.22)$$

where c and n are constants which depend on frequency and temperature, and the rain drop distribution is of the form

$$N(D) = \Lambda_1 D^p \exp\{-\Lambda_2 D^q\} \quad (2.23)$$

where Λ_1 and Λ_2 are of the form $\alpha_1 R^{\beta_1}$ and $\alpha_2 R^{-\beta_2}$, respectively. When $p=0$, $q=1$, and $\beta_1=0$, this distribution reduces to the exponential distributions used by Marshall and Palmer [1948] and Joss, et al. [1968].

Figure 2-10 plots the specific attenuation of rainfall as a function of frequency for various rain rates. The attenuation for all rain rates increases up to about 100 GHz. These curves correspond to the experimental rain drop size distribution of Laws and Parsons [1943], the terminal velocity of rain drops model of Gunn and Kinzer [1949] and an empirical model of the refractive index of water [Ray, 1972].

The specific attenuation gives the relationship between the rain rate at a point along the path and the attenuation which would be measured over a 1-km path if the rain rate were constant over the entire path. This is not true in practice. A number of methods for predicting the path attenuation given the point rain rate have been proposed in the literature. These methods fall into two categories:

1. Direct conversion methods, which use reduction coefficients to convert the point rain rate, R_p , to a path average rain rate \bar{R} from which the path attenuation and its distribution can be calculated [Battesti, et al., 1971; Lin, 1977; Crane, 1980].

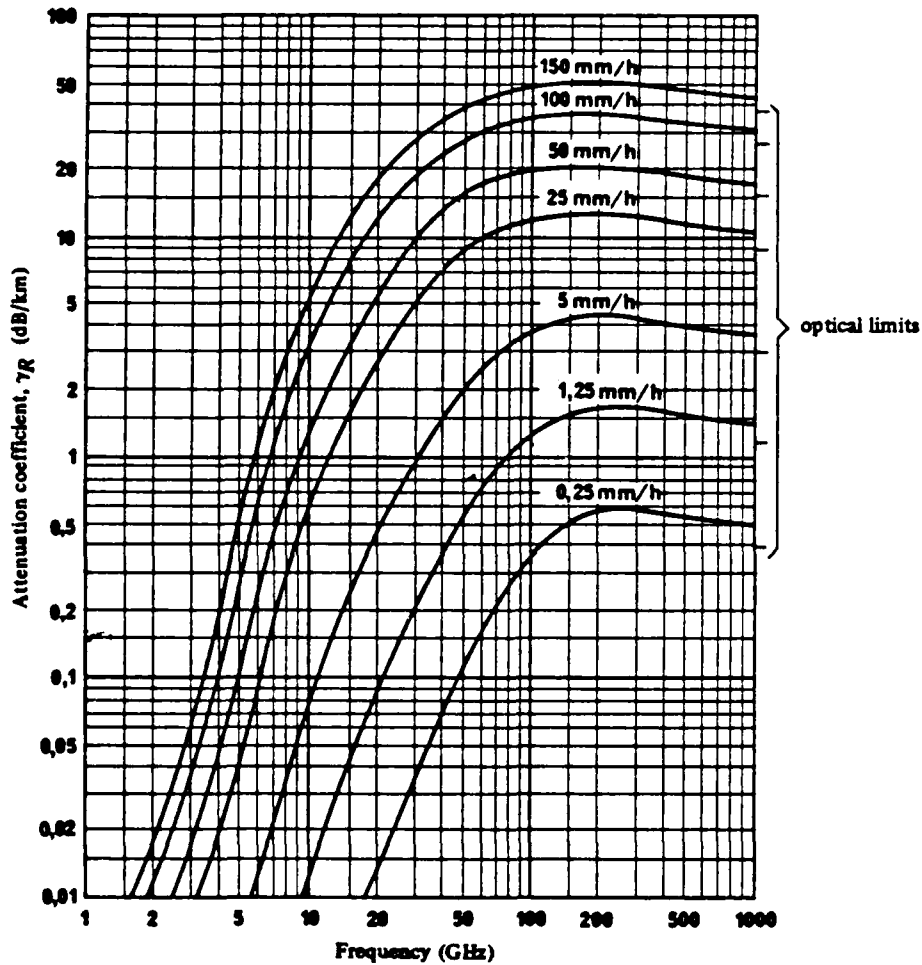


Figure 2-10 Rain Attenuation Coefficient

2. Parametric methods which employ an analytic approximation to the point rain rate distribution (e.g., Gamma distribution or lognormal distribution) and models of the spatial distribution of rain (e.g., constant over a cell of radius which depends on point rain rate) to derive a path average rain rate distribution from which the path attenuation distribution can be obtained [Misme, et al., 1975; Morita, et al., 1976].

SECTION 2
REFERENCES

- Battesti, J., L. Boithias, and P. Misme (1971), "Determination de l'affaiblissement des a la pluie pour les frequences superieures a 10 GHz", Ann des Telecommun., V. 26, pp. 439-444.
- Bean, B.R., and E.J. Dutton (1966), Radio meteorology, NBS Monograph No. 92, Supt. of Docs., US Govt. Printing Office, Washington, DC.
- Bean, B.R., B.A. Cahoon, C.A. Samson, and G.D. Thayer (1966), A world atlas of atmospheric radio refractivity, ESSA Monograph No. 1, Access No. AD648-805, NTIS, Springfield, VA.
- CCIR (1978), "Reference atmosphere for refraction", Recommendation 369-2, V. 5, XIVth Plenary Assembly, Kyoto, Japan, p. 68.
- Chadwick, R.B. and K.P. Moran (1980), "Long term measurements of C^2 in the boundary layer", Radio Science, V. 15, No. 2, pp. 355-361.
- Crane, R.K. (1980a), "Prediction of attenuation by rain", IEEE Trans. Commun., V. COMM-28, No. 9, pp. 1717-1733.
- Crane, R.K. (1980b), "A review of radar observations of turbulence in the lower stratosphere", Radio Science, V. 15, pp. 177-193.
- Fried, D.L., (1967) "Optical heterodyne detection of an atmospherically distorted wave front", Proc. IEEE V. 4, pp. 1179-1193.
- Gossard, E.E. (1977), "Refractive index variance and its geight distribution in different air masses", Radio Science, V. 12, No. 1, pp. 89-105.
- Gunn, K.L.S. and G.D. Kinzer (1949), "The terminal velocity of fall for water droplets in stagnant air", Journ. Meteorol., V. 6, pp. 243-248.
- Hall, M.P.M. (1979), Effects of the troposphere on radio communications, Peter Peregrinus LTD, New York.
- Hall, M.P.M. and C.M. Comer (1969), "Statistics of tropospheric radio refractive index soundings taken over a 3-year period in the UK", V. 116, pp. 685-690.

SECTION 2
REFERENCES (Continued)

- Hufnagel, R.E. (1974), "Variations of atmospheric turbulence" presented at Optical Society of America Topical meeting on optical propagation through turbulence.
- Ishimaru, A. (1978), Wave propagation and scattering in random media, Academic Press, New York.
- Joss, J., J.C. Thoms and A. Waldvogel (1968), "The variation of raindrops size distributions at Locarno", in Proc. Int. Conf. Cloud Physics, pp. 369-373.
- Kolmogorov, A.N. (1943), "Dissipation of energy in locally isotropic turbulence", Compte Rendus (Doklady) de l'Academic des Sciences al l'USSR, V. 32, No. 1, pp. 16-18.
- Laws, J.D. and D.A. Parsons (1943), "The relation of raindrops size to intensity", Trans. Amer. Geophys. Union, V. 24, pp. 452-460.
- Liebe, H.J. (1969), "Calculated tropospheric dispersion and absorption due to the 22 GHz water vapor line", IEEE Trans. Antennas and Prop., V. AP-17, pp. 621-627.
- Lin, S.H. (1977), "Nationwide long-term rain statistics and empirical calculation of 11 GHz microwave rain attenuation", Bell Syst. Tech. Journ., V. 56, pp. 1581-1604.
- Marshall, J.S. and W.M. Palmer (1948), "The distribution of raindrops with size", J. Meteorol. V. 5, pp. 165-166.
- Misme, P. and J. Fimbel (1975), "Determination theorique et experimentale de l'affaiblissement par la pluie sur un trajet radioelectrique", Ann. des Telecomm., V. 30, pp. 149-158.
- Morita, K. and I. Higuti (1976), "Prediction methods for rain attenuation distributions of micro and millimeter waves", Review Elec. Commun. Lab., V. 24, pp. 651-668.
- Obukhov, A.M. (1941), "On the distribution of energy in the spectrum of turbulent flow", Bull. Acad. Sci. USSR Geo and Geophys., V. 4, No. 5, pp. 453.
- Ottersten, H. (1969), "Atmospheric structure and radar backscattering in clear air", Radio Sci., Vol. 4, pp. 1179-1193.

SECTION 2
REFERENCES (Concluded)

- Olsen, R.L., D.V. Rogers, and D.B. Hodge (1978), "The aR^b relation in the calculation of rain attenuation", IEEE Trans. Antennas and Prop. V. AP-26, No. 2, pp. 318-328.
- Ray, P.S. (1972), "Broadband complex refractive indices of ice and water", Applied Optics, V. 11, pp. 1836-1844.
- Rice, P.L., A.G. Longley, K.A. Norton and A.P. Barsis (1967), "Transmission loss predictions for tropospheric communication circuits", NBS Tech. Note 101, US Dept of Commerce, Washington, DC.
- Samson, C.A. (1975), "Refractivity gradients in the northern hemisphere", ITS report OTR-75-59, Access No. Ad-A009-503, NTIS, Springfield, VA.
- Sasaki, O. and T. Akiyama (1979), "Multipath delay characteristics on line-of-sight microwave radio system", IEEE Trans. Commun., V. COM-27, No. 12, pp. 1876-1886.
- Schiavone, J.A. (1983), "Meteorological effects on diurnal and seasonal fading variations", in ICC-83 Conference Research, V. 2, pp. 641-644.
- Sirkis, M.D. (1971), "Contribution of water vapor to index of refraction structure parameter of microwave frequencies", IEEE Trans. Antennas & Prop., V. AD-19, pp. 572-575.
- Smith, E.K., and S. Weintraub (1953), "The constants in the equation for atmospheric refractive index at radio frequencies", Proc. IRE 41, 1035-1037.
- Tatarskii, V.I. (1971), The effects of the turbulent atmosphere on wave propagation, US Department of Commerce, NTIS, Springfield, VA.
- VanVleck, J.H. (1947), "The absorption of microwaves by oxygen", Phys. Rev. V. 71, pp. 425-433.

SECTION 3
TROPOSCATTER PROPAGATION

3.1 INTRODUCTION

This section describes the properties of troposcatter communication and the most recent advances in the understanding of the physical mechanisms that have led us to the development of a new propagation model. This discussion includes the relation to previous models, quantitative estimates for the important channel parameters, and the relations between troposcatter at frequencies above 1-3 GHz (dominated by locally isotropic turbulence) and at lower frequencies (dominated by anisotropic turbulence and layer reflection).

The troposcatter model has been developed over the last five years as a part of several contracts. The model is based on the philosophy that predictions must be directly related to the physical processes that govern the tropospheric scatter path. A well founded theoretical model is the only approach that allows extrapolation of observations to prediction of performance in cases where only limited data are available. We first developed this approach when faced with the task of predicting multipath characteristics and diversity correlations when the available empirical models only predicted path loss. The result is a model which relates path parameters (e.g., loss, multipath, diversity statistics) and modem performance to a few directly measurable atmospheric parameters. From the statistics of these parameters both short- and long-term statistics of the path parameters can be inferred. While this is not a trivial task, at least the methodology for solving the general problems is already defined, and should lead to significant new results in the future research to be performed.

The discussion of the model emphasizes

1. Frequencies above 1GHz
2. Low signal levels, i.e., abnormally strong signals due to ducting or rare layer occurrences are not explicitly considered.

3.2 THEORIES OF SCATTER PROPAGATION

A large number of theories have been advanced to explain the observed behavior of microwave signals received far beyond the horizon. Both theory and practice started developing around 1950, when Booker and Gordon [1950] explained the signals by scattering from turbulence. A number of different turbulence theories were proposed [Megaw, 1950; Villars and Weisskopf, 1954]. The theory that has received the widest acceptance today is the turbulence theory of Obukhov [1941] and Kolmogorov [1943], based on research first reported in 1941. This theory predicts that the path loss depends on a wavelength as $\lambda^{5/3}$ (isotropic antennas) and on the scattering angle as $\theta^{-11/3}$ (pencil beam antennas). The theory is based on single scattering from locally isotropic turbulence and has been validated experimentally. In the earlier days of troposcatter only very few local turbulence measurements were available, and many of these measurements showed apparent disagreements with the Kolmogorov-Obukhov theory. There were two reasons for this:

1. Many measurements were made at frequencies well below 1GHz where atmospheric layering and turbulence anisotropy can cause partial reflection of the electromagnetic waves.
2. Actual path data used assumed relatively wide antenna beams and did not properly take into account the large-scale inhomogeneity of the turbulence (layering) or the effect of the exact antenna pattern.

Theories of layer reflection [Friis, et al., 1957] and reflection from small local inhomogeneities (feuilletts) [DuCastel, 1966] were developed to account for the data measured at lower frequencies.

Based on these theories, but mostly on empirical results, a number of path loss prediction techniques have been developed, most notably the NBS method [Rice, et al., 1967] and the related CCIR method [CCIR, 1978]. These techniques which predict a scattering angle dependence of θ^{-5} are structured to calculate the path loss composed of several terms:

1. Basic transmission loss, the loss with ideal lossless isotropic antennas;
2. antenna gains G_T, G_R ;
3. line losses;
4. polarization losses;
5. aperture-to-medium coupling loss, the loss due to the fact that non isotropic antennas may not illuminate all of the turbulent atmosphere entering in the calculation of the basic transmission loss.

This structuring of the calculation assumed a model of the atmosphere at all elevations, since all of the atmosphere enters in the calculation of the basic transmission loss. The different models will therefore exhibit different aperture-to-medium coupling losses and different basic transmission losses, even if they all predict the same total path loss. It is therefore clear that one should be careful comparing different published expressions for the aperture-to-medium coupling loss.

The main deficiency of all the existing models is that they do not lend themselves to evaluation of

- delay spread
- receiver correlation distances
- fade rate
- angle diversity correlation
- microwave frequency dependence
- relation to standard atmospheric parameters.

The remainder of this section describes the theory required to allow prediction of the above parameters or relationships.

3.3 PATH GEOMETRY

A typical path is shown in Figure 3-1 defining some of the parameters involved. The parameters needed for characterizing the received waveform are

- Frequency f
- Transmitter Power P_T
- Distance d
- Antenna gains G_T and G_R
- Heights h_T , h_R of transmitter and receiver sites
- Heights h_{T0} , h_{R0} of antennas above ground
- Radio horizon elevation angles above horizontal (θ_T , θ_R) at transmitter and receiver. These angles can depend on the atmospheric conditions.
- Antenna boresight elevation angles above horizontal (θ_{T1} , θ_{R1}) at transmitter and receiver.

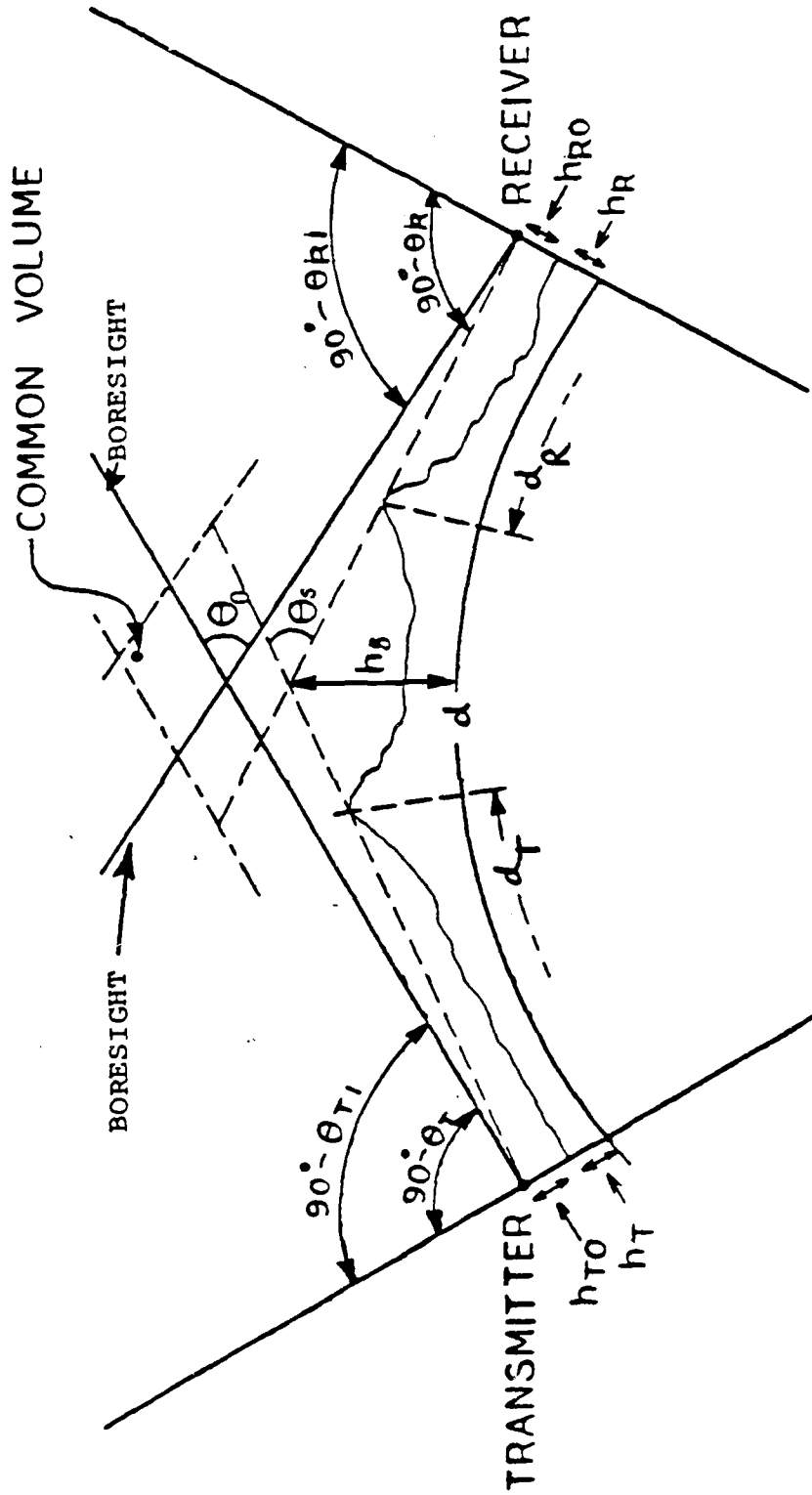


Figure 3-1 Path Geometry

- Note that $\theta_{T1} - \theta_T$ and $\theta_{R1} - \theta_R$ are then the elevation angles of the antennas above the horizon. The definition of "boresight" need not be the direction of maximum gain, but may be defined from geometrical considerations (e.g., the normal to a phased array).
- Azimuth pointing angles ϕ_T, ϕ_R if horizontal diversity is employed, or beam swinging experiments are performed.
- Gain patterns $g_T(\theta, \phi), g_R(\theta, \phi)$ of transmitting and receiving antennas. Determination of the gain patterns requires a number of additional parameters - size and type of antennas, height above ground, ground profile and reflectivity. The patterns should be referenced with respect to the boresight direction. Both amplitude and phase of the voltage gain patterns are required when the cross correlation between two (diversity) paths is to be calculated.
- Polarization of transmitter and receiver.
- Other system parameters such as bandwidth, power, and noise figure.
- Atmospheric parameters such as the effective earth radius factor K , the structure constant C_n^2 , the refractive index variance σ_n^2 , turbulence scale parameters L_0 and l_0 , wind velocity, humidity, etc.

3.4 CHARACTERIZATION OF THE TROPOSCATTER CHANNEL

The received signal is a sum of signals from a large number of scatterers in the common volume. The received waveform can

therefore be taken to be complex Gaussian. This means that the phase is uniformly distributed on $[0, 2\pi]$ and the amplitude is Rayleigh distributed,

$$p(A) = \frac{2A}{P_R} e^{-A^2/P_R}$$

where $P_R = E(A^2)$ is the average received power. In terms of the received complex waveform $r(t)$, we also have

$$E|r(t)|^2 = P_R.$$

This is easily generalized to the case of multiple received signals which occurs on diversity systems. Let $\underline{r}(t)$ be the received waveform. The covariance matrix at the receiver is then

$$\underline{P}_R = E\{\underline{r}(t)\underline{r}'(t)\}.$$

Let the transmitted waveform be $s(t)$. Ignoring transmitter and receiver filters, the received waveforms are

$$\underline{r}(t) = \int_0^{\infty} \underline{h}(\tau, t) s(t-\tau) d\tau$$

where the vector $\underline{h}(\tau, t)$ is the channel response at time t to an impulse at time $t-\tau$. For a nonchanging channel, this is independent of time t . The troposcatter channel is usually summed to be a complex Gaussian uncorrelated scatter channel. We show later that this is true as long as the relative bandwidth is small compared to the wavelength divided by the vertical scale L_0 and the scattering angle. In that case, we have

$$E[\underline{h}(\tau_1, t_1) \underline{h}^*(\tau_2, t_2)] = \underline{Q}(\tau_1, t_1, t_2) \delta(\tau_1 - \tau_2) .$$

The channel is said to be wide-sense stationary when \underline{Q} depends only on the time difference $t_1 - t_2$, $\underline{Q}(\tau; t_1 - t_2)$. When the channel variations are not considered, the delay power impulse response is defined by

$$\underline{Q}(\tau) \equiv \underline{Q}(\tau, 0) .$$

The covariance matrix \underline{P}_R of the received signal is

$$\underline{P}_R = P_T \int \underline{Q}(\tau) d\tau$$

where P_T is proportional to the transmitted power. For a single channel, the delay spread σ_τ is the width of this function. The frequency correlation function $B(f)$ is defined as the Fourier transform of $\underline{Q}(\tau)$. The coherence bandwidth, or Doppler spread, B_C , is the width of $B(f)$, so

$$B_C \sim 1/\sigma_\tau .$$

For a single channel, or a linear combination of several channels, we can also define the coherence time, T_C , and Doppler spread, B_d . The coherence time is the width of the temporal correlation function defined as

$$b(t_1-t_2) = \int Q(\tau, t_1-t_2) d\tau.$$

The Doppler spread B_d is the width of the Fourier transform of $b(t_1-t_2)$, so

$$B_d \sim \frac{1}{T_c}.$$

Another common characterization of the troposcatter channel is the scattering function:

$$S(\tau, f) = \int dt Q(\tau, t) e^{-j2\pi ft}.$$

The width of the scattering function in the τ direction is the multipath spread, while the f -dependence displays the Doppler spread. The convenience of using the scattering function is a result of the two basic assumptions: uncorrelated scattering, and wide-sense stationary fading.

3.5 SCATTERING FROM ISOTROPIC TURBULENCE WITH A SCALE SMALL COMPARED TO THE COMMON VOLUME

Detailed knowledge of the scattering mechanism and the characterization of turbulence is needed for reliable performance prediction involving not just path loss but multipath and diversity correlation as well. This section contains specific results for many of the important channel parameters.

3.5.1 Scattering Equation

In Appendix C we derive the following expression for the scattered field assuming the common volume is much larger than the size of the eddies,

$$P_R = P_T G_T G_R \frac{\pi k^2}{2} \int_V d^3 \underline{r} \frac{|g_T(\underline{r})|^2 |g_R(\underline{r})|^2}{R_T^2(\underline{r}) R_R^2(\underline{r})} \phi_n(k \underline{e}_s(\theta(\underline{r}))) \quad (3.1)$$

where

- \underline{e}_s is a nearly vertical vector and
- $|k \underline{e}_s| = 2k \sin[\theta(\underline{r})/2]$
- P_R, P_T are the received and transmitter power levels.
- G_T, G_R are the transmitter and receiver antenna gains.
- g_T, g_R are the voltage gains relative to bore-sight of the transmitter and receiver antennas, in the direction of the point \underline{r} of scattering volume.
- R_T, R_R are the distances from the point \underline{r} to the transmitter and receiver antennas.
- $k = 2\pi/\lambda = 2\pi f/c$ is the wavenumber.
- θ is the scattering angle, i.e., the angle between the lines from the transmitter and receiver terminals to the point \underline{r} .
- $\phi_n(\underline{k})$ is the wavenumber spectrum of the turbulence, or the three dimensional Fourier transform of the spatial correlation function of the refractive index fluctuations.

For convenience, we define the function $H(\underline{r})$ implicitly by (3.1) and (3.2):

$$P_R = \int_V d^3\underline{r} H(\underline{r}) . \quad (3.2)$$

The expression (3.1) was first defined in the context of troposcatter by Booker and Gordon [1950]. It relates the transmitted and received power levels in terms of parameters known from the link geometry, except for the spectrum ϕ_n . Although not indicated in (3.1), the spectrum ϕ_n can be a function of \underline{r} . This is discussed in Appendix C.

Equation (3.1) is valid under fairly general circumstances. All of the assumptions required in the derivation are discussed in Appendix C. The most important ones, however, are

1. the scattering volume must be large compared to the size of a correlation cell. This limits the antenna gain that is practical. The condition is

$$R_R \delta_R, R_T \delta_T \gg L_{0h}$$

where

$$\begin{aligned} \delta_T, \delta_R &= \text{beamwidth} \\ \text{and} \\ L_{0h} &= \text{horizontal outer scale of turbulence.} \end{aligned}$$

As long as this condition is satisfied anisotropy does not affect the functional form of the result.

2. The Fresnel zone condition

$$2L_0^3/\lambda < R_T^2, R_R^2 .$$

Both of these conditions put an upper limit on usable frequencies for troposcatter. The Fresnel zone condition above indicates the validity of the expression (3.1) for troposcatter at frequencies much higher than would be expected from Tatarskii's conditions.

ANTENNA COUPLING LOSS

If we increase the antenna gain at the receiver, the received signal does not necessarily increase in proportion to the antenna gain since the volume in the integral (3.1) gets smaller. It is convenient to separate the effects of increased antenna gain and decreased common volume. The loss due to the decrease in the common volume is called the aperture-to-medium coupling loss; denoted L_C . If the path loss with omnidirectional antennas is L_b (basic transmission loss) then the total path loss L_t is

$$L_t = L_b - G_T - G_R + L_C,$$

where G_T and G_R here denote antenna gains in dB.

The coupling loss is a mathematical convenience which is different for different models of the atmosphere and different again from what one would actually measure with two antennas one of which is omnidirectional. We will use the coupling loss extensively in the following, but the results should not be compared with other published estimates (NBS, CCIR, Yeh, Collins, etc.). Only the total path loss can be compared.

A heuristic explanation of aperture-to-medium coupling loss is simplified by assuming

1. Ideal beam shape (zero gain outside the beam, constant inside)
2. A volume of scatterers of finite extent.

Figure 3-2 illustrates the situation where the antenna beams are so large that the common volume illuminated by the antennas encompasses all the scatterers. With the idealized assumptions above it is convenient to define

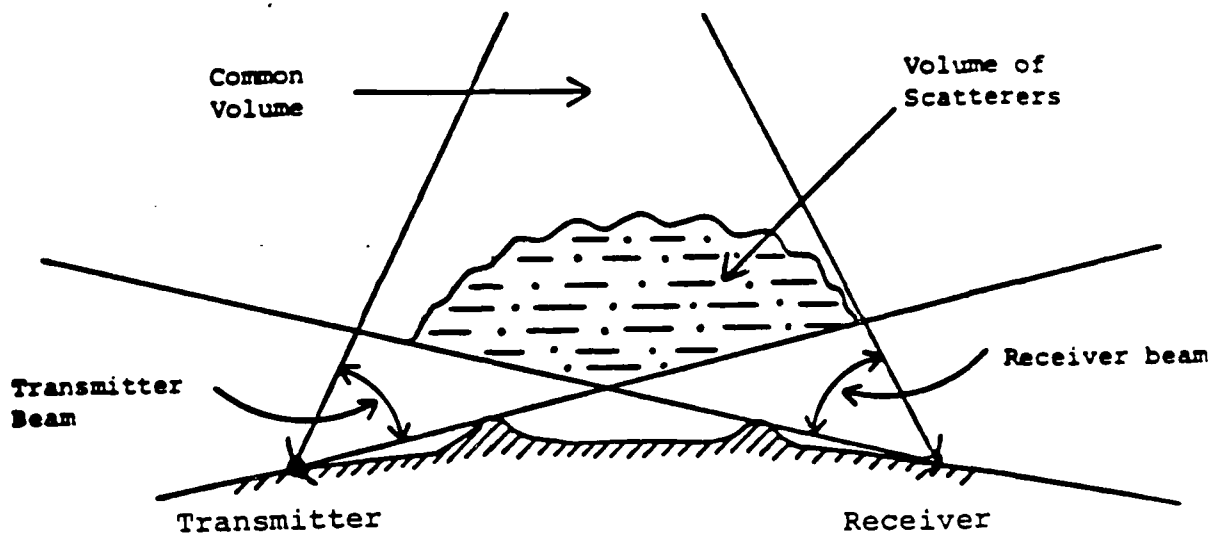


Figure 3-2 Link with No Coupling Loss: The common volume contains all scatterers.

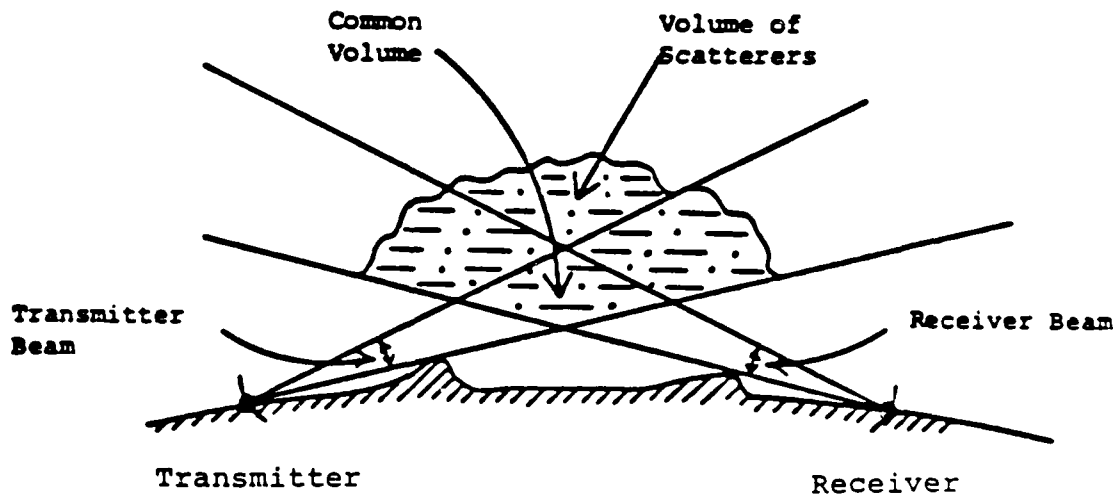


Figure 3-3 Link with Significant Coupling Loss: The common volume contains only a fraction of the scatterers.

<u>Common Volume:</u>	The volume in space which is illuminated by both the transmitter beam and the receiver beam
<u>Scattering Volume:</u>	The part of the common volume which contains scatterers.
<u>Volume of Scatterers:</u>	The total volume containing scatterers.

When the common volume is larger than the volume of scatterers then all scatterers contribute to the received field and there is no coupling loss. This is illustrated in Figure 3-2. When the beams are narrower (Figure 3-3) only a fraction of the scatterers are illuminated by both apertures and the received field does not include contributions from all scatterers. This lack of scattering contribution reduces the total realized antenna gain. This is the coupling loss, and will be evaluated in the following as a part of the path loss calculation. In Section 3.5.6 it will be seen that the coupling loss can also be considered due to the phase incoherence across a large aperture.

ANTENNA CORRELATION

For multiple receivers we have the correlation between the n'th and the m'th receiver as

$$(\underline{P}_R)_{nm} = \int_V d^3\underline{r} H_{nm}(\underline{r}) ,$$

where

$$H_{nm}(\underline{r}) = P_T G_T G_R \frac{\pi k^2}{2} \phi_n(k \underline{e}_s(\underline{r})) \frac{|g_T(\underline{r})|^2}{R_T^2(\underline{r}) R_R^2(\underline{r})} g_{R,n}(\underline{r}) g_{R,m}^*(\underline{r}) \times \exp(-jk|\underline{r}-\underline{r}_{R,n}| + jk|\underline{r}-\underline{r}_{R,m}|) , \quad (3.3)$$

where $g_{R,n}(\underline{r})$ is the normalized voltage gain pattern of the n 'th receiver and $\underline{r}_{R,n}$ is the location of the n 'th receiver. This assumes that all receivers are far from the common volume so the distance to the scatterers can be assumed to be the same except in the complex exponent. Assuming the coordinate system is centered at the receiving site and that $|\underline{r}| \ll |\underline{r}_{R,n}|$ we have

$$\frac{H_{nm}(\underline{r})}{\sqrt{H_{nn}(\underline{r})H_{mm}(\underline{r})}} = \frac{g_{R,n}(\underline{r})g_{R,m}^*(\underline{r})}{|g_{R,n}(\underline{r})g_{R,m}(\underline{r})|} e^{jk \frac{\underline{r} \cdot (\underline{r}_{R,n} - \underline{r}_{R,m})}{r}} . \quad (3.4)$$

3.5.2 Path Loss with Widebeam Antennas

We now describe briefly how the integral in (3.1) can be evaluated. The same steps are used later to evaluate correlations and delay spread. The integration is performed by integrating over the angles α and β shown in Figure 3-4 and the distance y from the great circle plane with both transmitter and receiver. α is the angle at the transmitter between lines to the projection of the scattering point onto the plane and to the receiver. β is the analogous angle at the receiver. The minimum values α_0 and β_0 are determined by the radio horizons. It is assumed that the scattering angle is small so that the straight line distance d_0 between the terminals is approximately equal to d . The scattering angle, or angular distance, is θ_s , as noted in Figure 3-4.

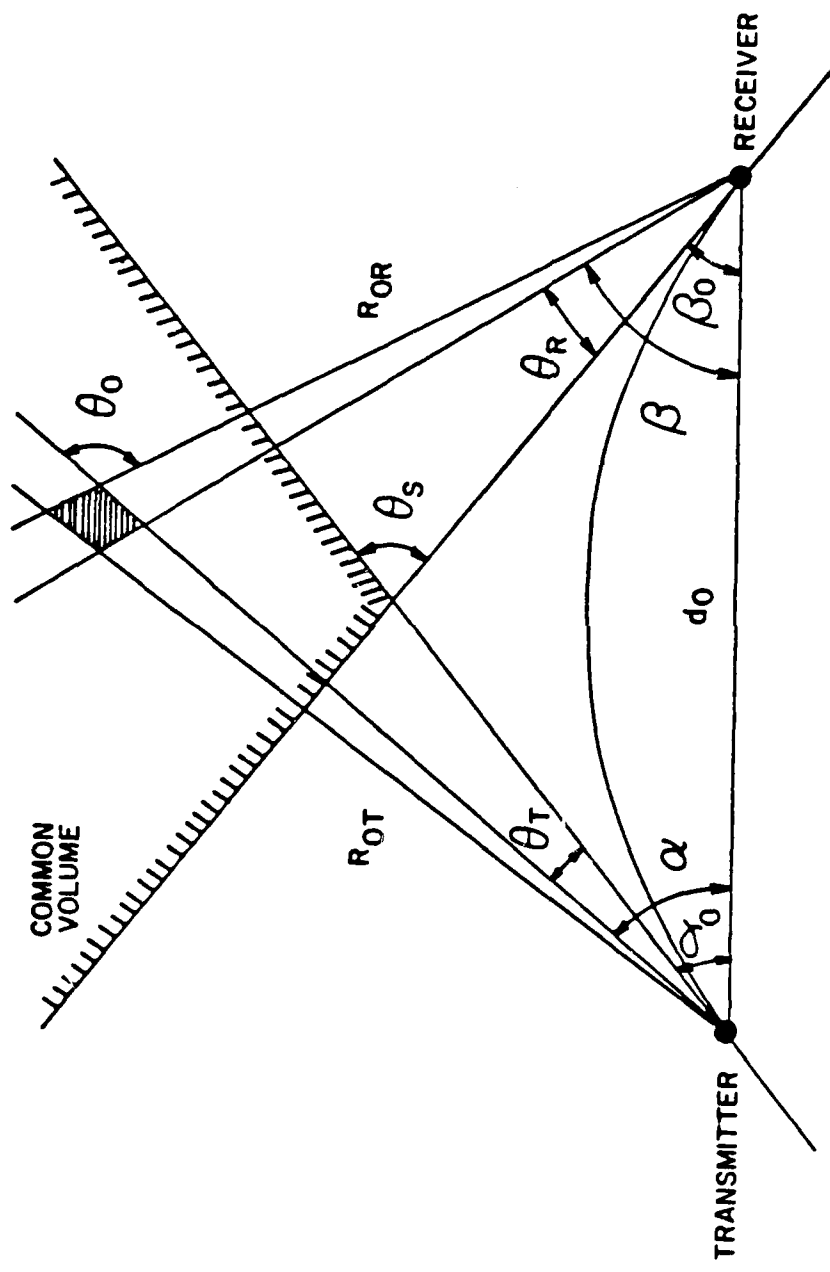


Figure 3-4 The Common Volume Integration

In the great circle plane ($y=0$) the scattering angle is

$$\theta_0 = \theta(\alpha, \beta, 0) = \alpha + \beta$$

when $y \neq 0$ the scattering angle is well approximated by [Parl and Monsen, 1980]

$$\left[2 \sin \frac{1}{2} \theta(\alpha, \beta, y)\right]^2 = \left[2 \sin \frac{1}{2} \theta(\alpha, \beta, 0)\right]^2 + \frac{y^2}{R_0^2} \quad (3.5a)$$

where R_0 depends on the distances to the scattering point,

$$R_0 = \frac{R_{0T}R_{0R}}{R_{0T} + R_{0R}} \sim \frac{\alpha\beta d}{(\alpha+\beta)^2} \quad (3.5b)$$

We have used the approximations

$$R_{0T} = d \sin\beta / \sin\theta_0 \sim \beta d / \theta_0$$

and

$$R_{0R} = d \sin\alpha / \sin\theta_0 \sim \alpha d / \theta_0$$

Equation (3.1) then becomes, assuming omnidirectional antennas ($g_T = g_R = 1$) and small angles,

$$P_R = Ck^{2-m} \int_{\alpha_0}^{\pi/2} d\alpha \int_{\beta_0}^{\pi/2} d\beta \int_{-\infty}^{\infty} dy \frac{R_{0T}R_{0R}}{R_{0T}R_{0R}} \frac{1}{\theta_0} \theta(\alpha, \beta, y)^{-m} \quad (3.6)$$

where

$$C = P_T G_T G_R \frac{\Gamma(m-1) \sin \frac{\pi}{2}(m-3)}{8\pi} C_n^2 \quad (3 < m < 5)$$

$$(\approx P_T G_T G_R \quad 0.0518 \quad C_n^2 \quad \text{for } m=11/3) \quad (3.7)$$

Integrating over y we get, replacing the upper limits by ∞

$$P_R = C k^{2-m} B\left(\frac{1}{2}, \frac{m-1}{2}\right) \int_{\alpha_0}^{\infty} d\alpha \int_{\beta_0}^{\infty} d\beta \frac{\theta_0^{-m}}{R_{0T} + R_{0R}} \quad (3.8)$$

where $B\left(\frac{1}{2}, \frac{m-1}{2}\right)$ is the beta function. For $m=11/3$, it equals 1.68. A good approximation for $3 < m < 5$ is $B\left(\frac{1}{2}, \frac{m-1}{2}\right) \sim 8/(m+1)$.

Replacing $R_{0T} + R_{0R}$ by d and using that $\theta_0 = \alpha + \beta$ we easily get the basic path loss

$$P_R = P_{R, \text{basic}} = \frac{CB\left(\frac{1}{2}, \frac{m-1}{2}\right)}{(m-1)(m-2)} (k\theta_S)^{2-m/d}, \quad (3.9a)$$

where $\theta_S = \alpha_0 + \beta_0$. This result applies to wide beams. For $m=11/3$, we get

$$P_R = P_T G_T G_R \quad 0.0196 \quad C_n^2 (k\theta_S)^{-5/3/d}. \quad (3.9b)$$

The result can be used also for $m > 5$, but the definition of C_n^2 no longer makes sense. Instead we can use the refractive index variance σ_n^2 and the outer scale L_0 directly to get

AD-A143 762

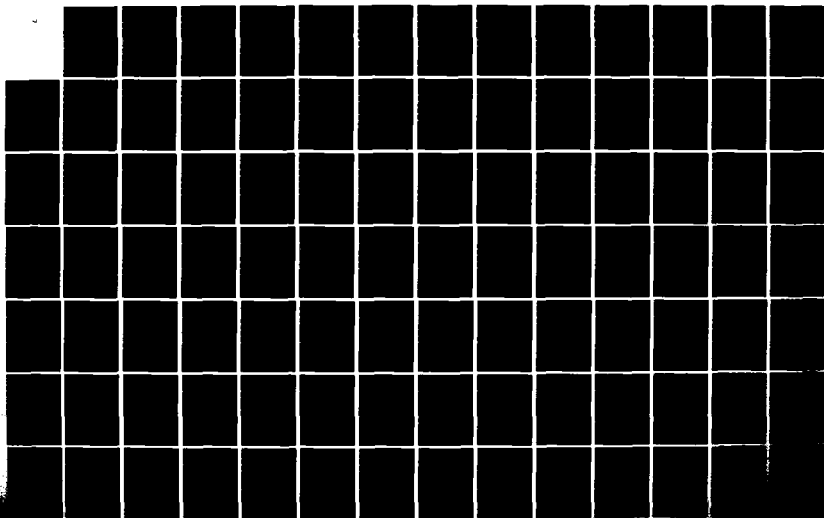
THEORETICAL ANALYSIS OF MICROWAVE PROPAGATION(U)
SIGNATRON INC LEXINGTON MA 5 PARL ET AL. APR 84
RADC-TR-84-74 F19628-88-C-8106

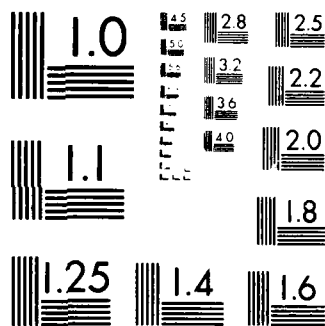
2/5

UNCLASSIFIED

F/G 28/14

NL





MICROCOPY RESOLUTION TEST CHART
NATIONAL BUREAU OF STANDARDS-1963-A

$$P_R = P_T G_T G_R \frac{m-3}{4(m-1)(m-2)} \sigma_n^2 L_0^{3-m} (k\theta_S)^{2-m}/d . \quad (3.10)$$

A spectrum slope $m < 3$ is not possible for large k .

3.5.3 Path Loss with Finite Beamwidth Antennas

First, let us assume a narrow horizontal beamwidth. Due to the weak scattering angle dependence on y (see Equation 3.5), this assumption is very often satisfied for practical antennas. Let L_H be the horizontal width of the common volume. If the transmitter and receiver antennas have the horizontal beamwidth b_{Th} and b_{Rh} , respectively, we have approximately

$$L_H \sim \frac{d}{\theta_0} \min(\beta b_{Th}, \alpha b_{Rh}) . \quad (3.11)$$

To simplify the results, assume equal beamwidths,

$$b_{Th} = b_{Rh} = b_h .$$

L_H can be approximated quite well by using the bounds

$$\frac{xy}{x+y} < \min(x,y) < \frac{2xy}{x+y} .$$

From (3.6) we then get, assuming broad beams in elevation,

$$\begin{aligned}
P_R &< Ck^{2-m} b_h \int_{\alpha_0}^{\infty} d\alpha \int_{\beta_0}^{\infty} d\beta \frac{\theta_0^{-m-1}}{R_{0T} R_{0R}} \frac{2\alpha\beta d}{\theta_0} \\
&= \frac{2C}{m(m-1)} \frac{b_h}{\theta_0} (k\theta_S)^{2-m/d} . \quad (3.12)
\end{aligned}$$

For a non symmetrical link we may use the following approximation

$$P_R \sim \frac{2C}{m(m-1)} \left(\frac{\beta_0}{b_{Rh}} + \frac{\alpha_0}{b_{Th}} \right)^{-1} (k\theta_S)^{2-m/d} . \quad (3.13)$$

Comparing this with (3.9a), the additional loss associated with the finite horizontal beamwidth is the horizontal coupling loss,

$$L_{Ch} \sim 10 \log \left(1 + \frac{mB \left(\frac{1}{2}, \frac{m-1}{2} \right)}{2(m-2)} \left[\frac{\beta_0}{b_{Rh}} + \frac{\alpha_0}{b_{Th}} \right] \right) . \quad (3.14a)$$

This has been found to be a good approximation in computer calculation with $b_{Rh} = b_{Th}$. For $m=11/3$ and $b_{Rh} = b_{Th}$ this becomes

$$L_{Ch} \sim 10 \log(1 + 1.85\theta_S/b_h) . \quad (3.14b)$$

Now suppose the beamwidth cannot be assumed to be infinite in elevation. Equation (3.12) then becomes

$$P_R = Ck^{2-m} \int_{\alpha_0}^{\alpha_0 + b_{Tv}} d\alpha \int_{\beta_0}^{\beta_0 + b_{Tv}} d\beta L_H \frac{(\alpha + \beta)^{1-m}}{d^2 \alpha \beta} . \quad (3.15)$$

Now, use the equality

$$\min(x,y) = \frac{2xy}{x+y} / \left(1 + \frac{|x-y|}{x+y}\right).$$

The denominator only varies by a factor of 2 (3 dB) and will be taken outside the integral in (3.15). For equal horizontal beamwidth we therefore use, at the point α, β

$$L_H \sim \frac{2d\alpha\beta b_h}{\theta_0^2} / \left(1 + \frac{|\alpha - \beta_0|}{\theta_S}\right). \quad (3.16)$$

Hence,

$$\begin{aligned} P_R &\sim Ck^{2-m} \frac{2b_h}{d(1+|\alpha_0 - \beta_0|/\theta_S)} \int_{\alpha_0}^{\alpha_0 + b_{TV}} d\alpha \int_{\beta_0}^{\beta_0 + b_{TV}} d\beta (\alpha + \beta)^{-1-m} \\ &= \frac{C}{(m-1)m} (k\theta_S)^{1-m}/d \frac{2b_h}{(1+|\alpha_0 - \beta_0|/\theta_S)} F_{m-1} \left(\frac{b_{TV}}{\theta_S}, \frac{b_{RV}}{\theta_S}\right) \end{aligned} \quad (3.17)$$

where

$$F_\nu(x,y) = 1 - (1+x)^{-\nu} - (1+y)^{-\nu} + (1+x+y)^\nu.$$

Comparing this with (3.9) shows that the coupling loss with relatively narrow horizontal beamwidths is

$$\begin{aligned}
L_{C1} \sim & -10 \log F_{m-1} \left(\frac{b_{Tv}}{\theta_S}, \frac{b_{Rv}}{\theta_S} \right) \\
& + 10 \log \left(1 + \frac{|\alpha_0 - \beta_0|}{\theta_S} \right) \\
& - 10 \log \left(\frac{2 b_H (m-2)}{\theta_B \left(\frac{1}{2}, \frac{m-1}{2} \right)_m} \right) .
\end{aligned}$$

Combining this with (3.14) yields an expression good for most links with equal horizontal beamwidths,

$$\begin{aligned}
L_C = & -10 \log F_{m-1} \left(\frac{b_{Tv}}{\theta_S}, \frac{b_{Rv}}{\theta_S} \right) && \text{(vertical loss)} \\
& + 10 \log \left(1 + \frac{|\alpha_0 - \beta_0|}{\theta_S} \right) && \text{(asymmetry loss)} \\
& + 10 \log \left(1 + \frac{mB \left(\frac{1}{2}, \frac{m-1}{2} \right)}{2(m-2)} \frac{\theta_S}{b_h} \right) && \text{(horizontal loss)}. \quad (3.18)
\end{aligned}$$

This equation, in conjunction with (3.9) is useful for hand calculations of the path loss. It has been verified in numerous numerical integrations. The total loss is

$$P_{R,\text{total}} = P_{R,\text{basic}} - L_C \quad (3.19)$$

where $P_{R,\text{basic}}$ is the basic path loss given by Eq. (3.9) and L_C is the aperture-to-medium coupling loss given by Eq. (3.18).

3.5.4 Horizontal Correlation at the Receiver

Now assume the receiving antenna is omnidirectional but that the transmitting antenna is arbitrary. We wish to develop approximate expressions for the horizontal correlation distance at the receiving site. This is useful for space diversity applications and for explaining the coupling loss in terms of phase decorrelation across a large receiving aperture.

Let z be the horizontal separation of two small antennas at the receiver. From (3.4) and (3.6) we have the correlation

$$\begin{aligned} \overline{r_1} &= Ck^{2-m} \int_{\alpha_0} d\alpha \int_{\beta_0} d\beta \int dy \frac{R_{0T} R_{0R}}{R_T R_R} \frac{1}{\theta_0} \theta^{-m} e^{jkyz/R_{0R}} \\ &= \rho_H(z) \cdot P_R \end{aligned} \quad (3.20)$$

In the case of wide beams the derivation proceeds as in Section 3.5.2. The details can be found in Monssen and Parl [1980]. We get

$$P_R \int_{-\infty}^{\infty} \rho_H(z) dz = P_R \frac{\lambda}{\theta_S} \frac{m-2}{m-1} \frac{\beta_{m-1}(\alpha_0/\theta_S)}{B(\frac{1}{2}, \frac{m-1}{2})} \quad (3.21)$$

where

$$\beta_n(x) \equiv n \sum_{k=0}^{\infty} \frac{x^k}{n+k}, \quad 0 < x < 1.$$

The horizontal correlation distance is defined by

$$\begin{aligned} R_H &= \int \rho_H(z) dz / P_R \\ &= \frac{\lambda}{\theta_S} \frac{m-2}{m-1} \frac{\beta_{m-1}(\alpha_0/\theta_S)}{B(\frac{1}{2}, \frac{m-1}{2})} \end{aligned} \quad (3.22)$$

For a symmetrical link we have $\alpha_0 = \frac{1}{2} \theta_S$. Substituting $m=11/3$ we get

$$R_H \left(m = \frac{11}{3} \right) \sim 0.6 \frac{\lambda}{\theta_S} \quad (\text{wide beamwidth}) \quad (3.23)$$

Now assume the transmitter beam is sufficiently narrow so that θ does not depend on y . The y dimensions are $R_{0T} b_{Th}$, so

$$P_R \rho_H(z) = C k^{2-m} \int_{\alpha_0} d\alpha \int_{\beta_0} d\beta \frac{\theta_0^{-1-m}}{R_{0T} R_{0R}} \frac{\sin(kz b_{th} R_{0T} / (2R_{0R}))}{kz / (2R_{0R})}$$

When integrating over z this reduces to (3.21) when the transmitter and receiver have sufficiently wide elevation beamwidths and where P_R equal $\rho_H(0)$ is given by (3.13). Therefore, the horizontal correlation distance is increased by the horizontal coupling loss, leading to

$$R_H = \frac{\lambda}{\theta_S} \frac{\alpha_0}{b_{Th}} \frac{m \beta_{m-1} (\alpha_0 / \theta_S)}{2(m-1)} \quad (3.24)$$

for the case of a narrow horizontal beam. R_H is only slightly affected by the vertical beamwidth.

A direct expression for the correlation coefficient is sometimes desirable. It can be shown that

$$\rho_h(z) = (m-2) \theta_S^{m-2} \int_0^{\infty} dx (\theta_S + x)^{1-m} \frac{m-1}{2} \left(\frac{2\pi z}{\lambda} (\beta_0 + x) \right)$$

where

$$f_{\nu}(x) = \frac{2}{\Gamma(\nu)} \left(\frac{x}{2}\right)^{\nu} K_{\nu}(x) .$$

$f_{\nu}(x)$ can be approximated by

$$f_{4/3}(x) \sim \frac{1+3x}{1+3x+1.5x^2} , \quad x < 0.75$$

$$1.114 \left(1 + \frac{0.764}{x+0.063}\right) e^{-x} x^{5/6} , \quad x > 0.75 .$$

The integral above must be evaluated numerically in general. The asymptotic form is

$$\rho_h(z) \sim \frac{(m-2)}{\Gamma\left(\frac{m-1}{2}\right)} \sqrt{\pi} 2^{-\frac{m}{2}} \theta_S^{-1}(kz\beta_0)^{\frac{m}{2}-2} e^{-kz\beta_0} , \quad z \text{ large}$$

or

$$\rho_h(z) \sim 1.9 \theta_S^{-1}(kz\beta_0)^{-1/6} e^{-kz\beta_0} . \quad (3.27)$$

This expression can be used to find the required space diversity separation.

3.5.5 Vertical Correlation at the Receiver

For vertically displaced receivers, the correlation distance is defined as

$$R_V = \frac{\int \rho_V(z) dz}{\max \rho_V(z)} .$$

It can be shown in the same way as before that for a widebeam transmitter

$$R_v = (m-2) \frac{\lambda}{\theta_s} . \quad (3.25)$$

For a narrow beam transmitter, we find

$$R_v = (m-1) \frac{\lambda}{\theta_s} , \quad (3.26)$$

almost the same as in (3.25).

3.5.6 A Second Look at Aperture-To-Medium Coupling Loss

The coupling loss is often explained in terms of the decorrelation of the phase front over a large aperture. We now show that this is equivalent to considering it in terms of the common volume restricting the number of scatterers.

Let $E(y,z)$ be the received field. The output of an aperture A in the y - z plane is (assuming perfect polarization match)

$$r = \frac{1}{A} \int \int_A dy dz E(y,z) . \quad (3.28)$$

The received power is then

$$P = E|r|^2 = \frac{P_R}{A^2} \int \int_A dy_1 dz_1 \int \int_A dy_2 dz_2 \rho(y_1-y_2, z_1-z_2)$$

where $\rho(y,z)$ is the correlation function and P_R is the received power. The coupling loss is

$$L_C^{-1} = \frac{1}{A^2} \iint dy_1 dz_1 \iint dy_2 dz_2 \rho(y_1 - y_2, z_1 - z_2) .$$

For a large square aperture of dimensions $a_h \times a_v$, this is approximately

$$L_C^{-1} \sim \frac{R_h}{a_h} \cdot \frac{R_v}{a_v} \quad (3.29)$$

where R_h is the horizontal correlation distance and R_v is the vertical correlation distance. It is therefore possible to evaluate the coupling loss from the correlation distances derived in Sections 3.5.4 and 3.5.5. The results may deviate slightly from the results for L_C in Sections 3.5.2 and 3.5.3, but only due to differences in approximations. That the equivalence is exact can be seen directly from (3.26). The received field $E(y,z)$ is of the form given in Appendix C, Equation (C-10)

$$E(y,z) = \frac{1}{2\pi} \int_V dV n_1 \frac{e^{-jkR_R}}{R_R} E_0$$

where E_0 is the incident field in the common volume, n_1 is the random refractive index fluctuation (turbulent scatterer) and R_R is the distance from the integration point to the observation point (y,z) . Inserting this in (3.28) and interchanging the order of integration yields

$$r = \int_V dV \frac{n_1 g_R}{R_R} E_0$$

where g_R is the antenna pattern. This is the form used in the preceding sections, so the two viewpoints are equivalent.

3.5.7 Delay Spread

If the integral in (3.1) is performed only over the part of the common volume where the delay is in the range $[\tau, \tau + d\tau]$ we would get $Q(\tau)d\tau$, where $Q(\tau)$ is the power impulse response. In general an accurate representation of $Q(\tau)$ requires a numerical integration. However, we will apply some rather crude approximations to get an approximate analytical form. It is important to note that the commonly defined rms delay spread,

$$\frac{1}{P_R} \int (\tau - \bar{\tau})^2 Q(\tau) d\tau$$

does not lead to a convergent integral with omnidirectional antennas due to the slow fall off of the tail of $Q(\tau)$. To see this note that the delay relative to the baseline is approximately

$$\tau = \frac{d}{2c} \alpha\beta \tag{3.30}$$

using in (3.6) or (3.8) it is seen that the fall off is too slow. Instead we find an approximation to $Q(\tau)$ directly. Assume that $\tau - \tau_0$ is small, where τ_0 is the minimum delay

$$\tau_0 = \frac{d}{2c} \alpha_0 \beta_0 . \quad (3.31)$$

Next we make the approximation that τ is independent of y in (3.6). This is a good assumption for narrowbeam antennas but can lead to some error for wide beam antennas. We will correct for this error later on.

For the case of wide beam antennas we set

$$\beta = \frac{2c\tau}{ad}$$

and

$$d\beta = \frac{2c}{ad} d\tau$$

in (3.8), and get

$$Q(\tau)d\tau = Ck^{2-m} B\left(\frac{1}{2}, \frac{m-1}{2}\right) \int_{\alpha_0}^{A/\beta_0} d\alpha \frac{2c}{ad^2} (\alpha + A/\alpha)^{-m} d\tau \quad (3.32)$$

where

$$A = 2c\tau/d .$$

When A is small we can replace $\alpha + A/\alpha$ by its geometric mean value,

$$\bar{\alpha} = \left(\frac{A\alpha_0}{\beta_0}\right)^{1/2} ,$$

yielding

$$Q(\tau) \sim \frac{2Ck^{2-m} B(\frac{1}{2}, \frac{m-1}{2}) c}{d^2} \log\left(\frac{2c\tau}{\alpha_0 \beta_0 d}\right) \left(\frac{2c\tau}{d}\right)^{-m/2} \left[\sqrt{\frac{\alpha_0}{\beta_0}} + \sqrt{\frac{\beta_0}{\alpha_0}}\right]^{-m}$$

From (3.9) we get

$$Q(\tau)/P_R = \frac{2(m-1)(m-2)c}{d \theta_S^2} \log\left(\frac{\tau}{\tau_0}\right) \left(\frac{\tau}{\tau_0}\right)^{-m/2}, \quad \tau > \tau_0, \quad (3.33)$$

where

$$\tau_0 = \alpha_0 \beta_0 d / (2c)$$

For a symmetric link $\tau_0 = \theta_S^2 d / (8c)$, and thus

$$Q(\tau)/P_R = \frac{(m-1)(m-2)}{4\tau_0} \log\frac{\tau}{\tau_0} \left(\frac{\tau}{\tau_0}\right)^{-m/2}, \quad \tau > \tau_0$$

Even though the approximations are not likely to be good for large τ , it is of interest to integrate (3.33). Define $q(\tau) \equiv Q(\tau)/P_R$. We get, after some simple algebra,

$$\int q(\tau) d\tau = \frac{m-1}{m-2} \left(\frac{s^{1/2} + s^{-1/2}}{2} \right)^{-2}$$

where $s = \frac{\alpha_0}{\beta_0}$ is the asymmetry parameter. For a symmetric link $s = 1$ and the error in the integral of $Q(\tau)$ is only $(1 + 1/(m-2))$, or 2 dB.

The delay spread can be defined by

$$\sigma_{\tau, sq} = \frac{\int Q(\tau) d\tau}{\max Q(\tau)} .$$

The maximum of $Q(\tau)$ is achieved for

$$\tau = \tau_m = \frac{\alpha_0 \beta_0 d}{2c} e^{2/m} = \tau_0 e^{2/m} . \quad (3.34)$$

For $m = 11/3$ $\tau_m = 1.73 \tau_0$.

The delay spread for wide beams is then, from (3.33)

$$\sigma_{\tau, sq} = \frac{d}{c} \theta^2 \frac{me}{4(m-1)(m-2)} \quad (3.35)$$

for $m = 11/3$ $\sigma_{\tau, sq} = 0.56 d \theta^2 / c$.

Now include the additional delay from off-axis scatterers. We have

$$\tau = \frac{\alpha \beta d}{2c} + \frac{y^2}{2R_0 c} ,$$

where R_0 is given by (3.5b).

The y component contributes significantly to the delay when the horizontal beamwidth satisfies

$$b_h > \theta_s / (1 + |\alpha_0 - \beta_0| / \theta_s) .$$

From (3.6) we have, using $R_T \sim R_{0T}$ and $R_R \sim R_{0R}$,

$$Q(\tau)d\tau = C k^{2-m} \int \frac{d\alpha d\beta dy}{dv_1(\tau)} \frac{1}{R_{0T} R_{0R} (\alpha + \beta)} \left[(\alpha + \beta)^2 + \frac{y^2}{R_0^2} \right]^{-\frac{m}{2}}$$

where $dv_1(\tau)$ is given by

$$\frac{\alpha\beta d}{2c} + \frac{y^2}{2R_0 c} \in \left[\tau - \frac{d\tau}{2}, \tau + \frac{d\tau}{2} \right]; \quad \alpha > \alpha_0, \quad \beta > \beta_0 .$$

We next substitute

$$y = x \sqrt{2R_0 c \tau}$$

and note that

$$(1-x^2)\tau = \alpha\beta d / (2c) > \tau_0$$

where τ_0 is given by (3.31). Interchanging the order of integration yields (defining $x_1 = \sqrt{1 - \tau_0 / \tau}$)

$$Q(\tau)d\tau = C k^{2-m} \int_0^{x_1} dx \int \frac{d\alpha d\beta}{dv_2(\tau)} (\alpha + \beta)^{-m} (1-x^2)^{m/2 - 1/2} / d$$

where

$$dv_2(\tau) = \{ \alpha, \beta \mid \alpha > \alpha_0, \beta > \beta_0, \frac{2\beta d}{2c} \varepsilon [(1-x^2)\tau - d\tau/2, (1-x^2)\tau + d\tau/2] \}.$$

Eliminating β this becomes,

$$Q(\tau) = \frac{2ck^{2-m}}{d} \int_0^{x_1} dx \int_{\alpha_0}^{P(x)/\beta_0} d\alpha \frac{(1-x^2)2c}{\alpha d} (\alpha + P(x)/\alpha)^{-m} (1-x^2)^{(m-1)/2}$$

where $P(x) \equiv 2c\tau(1-x^2)/d$.

The following approximation is good for small τ :

$$\alpha + P(x)/\alpha \sim \text{const.} \sim \left[\frac{\alpha_0}{\beta_0} P(x) \right]^{1/2} + \left[\frac{\beta_0}{\alpha_0} P(x) \right]^{1/2}.$$

With this approximation we get

$$\begin{aligned} Q(\tau) &= \frac{4Ck^{2-m}}{d} \frac{c}{d} \int_0^{x_1} dx \int_{\alpha_0}^{P(x)/\beta_0} \frac{1}{\alpha} dx \sqrt{1-x^2} \left(\frac{\tau}{\tau_0} \right)^{-m/2} \\ &= \frac{4Ck^{2-m}}{d} \frac{c}{d} \left(\frac{\tau}{\tau_0} \right)^{-m/2} \theta_s^{-m} \int_0^{\sqrt{1-\tau_0/\tau}} dx \sqrt{1-x^2} \log \left[\frac{\tau}{\tau_0} (1-x^2) \right]. \end{aligned}$$

For small $\tau (t = \tau_0)$, this becomes

$$Q(\tau) = \frac{4Ck^{2-m}}{d} \frac{c}{d} \theta_s^{-m} \left(\frac{\tau}{\tau_0} \right)^{-m/2} \sqrt{1-\tau_0/\tau} \log \frac{\tau}{\tau_0} \quad (3.36a)$$

or

$$Q(\tau)/P_R = \frac{4(m-1)(m-2)}{B\left(\frac{1}{2}, \frac{m-1}{2}\right)} \frac{c}{d\theta_s^2} \sqrt{1-\tau_0/\tau} (\tau/\tau_0)^{-m/2} \log(\tau/\tau_0). \quad (3.36b)$$

Comparing this with (3.33) we see that the correction factor

$$\frac{2}{B\left(\frac{1}{2}, \frac{m-1}{2}\right)} \sqrt{1-\tau_0/\tau}$$

is due to the off-axis contributions to the delay.

For $m=11/3$ the maximum of $Q(\tau)$ in (3.36) is achieved for

$$\tau = 1.47 \tau_0$$

and is

$$\max_{\tau} Q(\tau)/P_R = 0.56 \frac{c}{d\theta_s^2}$$

so that the delay spread is

$$\sigma_{sq} = 1.78 \theta_s^2 d/c .$$

This is three times larger than (3.35), showing that off-axis scatter can contribute significantly to the power impulse response. Note that we have assumed P_R given by (3.9) so the inaccuracy of the tail of (3.36) does not significantly affect this result.

Figure 3-5 shows the theoretical profiles (3.33) and (3.36) together with the results of numerical integration. The oscillations in the tails of the numerical curves are due to delay quan-

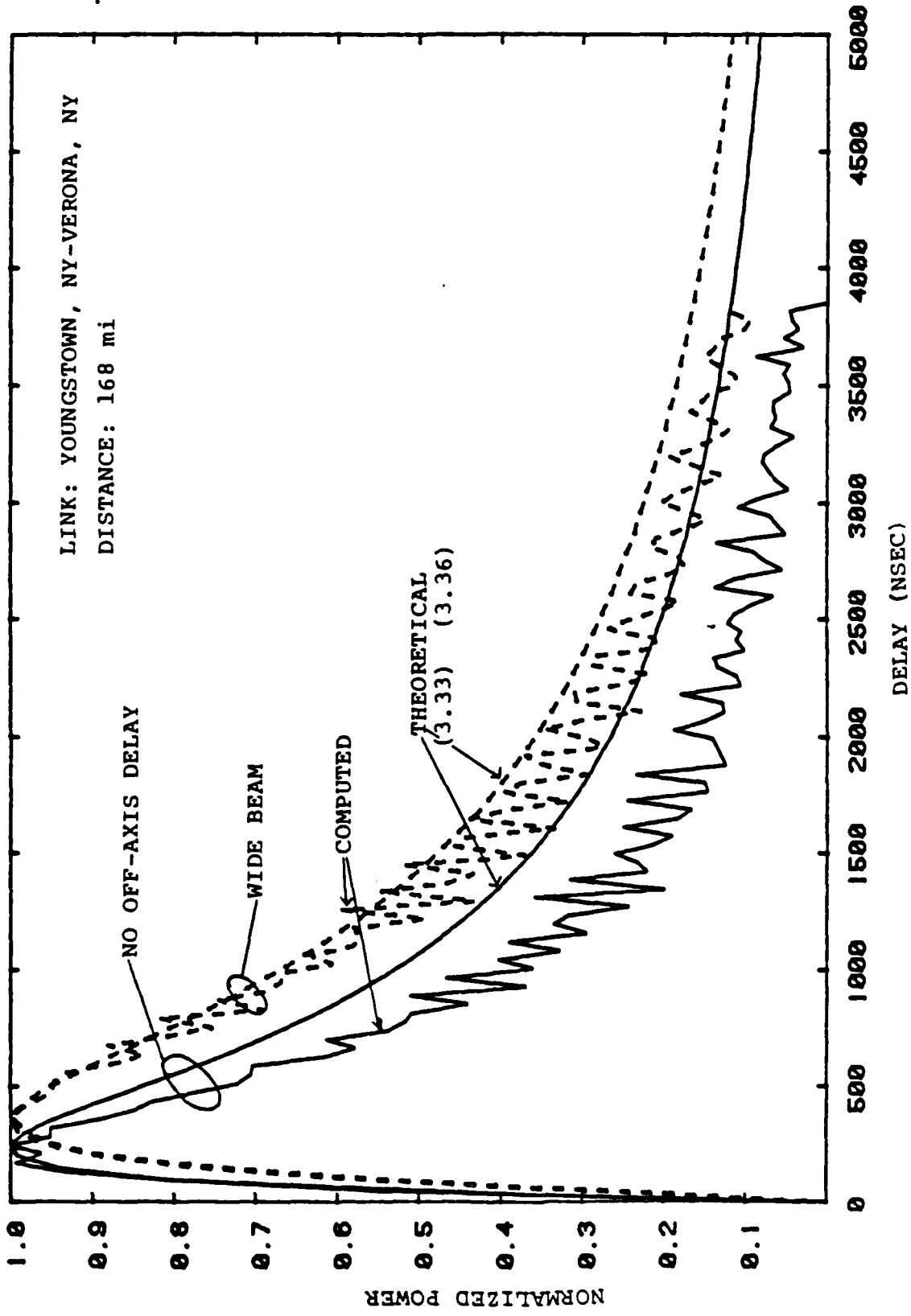


Figure 3-5 Theoretical and Numerically Integrated Power Impulse Response Function

tization errors in the computer program. It is seen that the approximations are good at least to the maximum of $Q(\tau)$, which is sufficient to generate the accuracy of the delay spread approximations. The approximations to $Q(\tau)$ are too large for large τ , but the discrepancy is almost insignificant.

The integral of (3.36) is

$$\int Q(\tau) d\tau = \frac{4Ck^{2-m}}{d} \frac{c\tau_0}{d} \theta_s^{-m} B\left(\frac{3}{2}, \frac{m}{2} - 1\right) \left[\psi\left(\frac{m+1}{2}\right) - \psi\left(\frac{m}{2} - 1\right) \right]$$

where $B(x,y)$ is the Beta function and ψ is the digamma function.

For $m=11/3$ this becomes using P_R from (3.9)

$$\int Q(\tau)/P_R \sim 6.57 \alpha_0 \beta_0 / \theta_s^2 .$$

This is 2 dB too large for a symmetric link, less for asymmetric links. The error is due to the fact that the tail of $Q(\tau)$ in (3.36) is too large.

Next, consider ideal narrow beams with directivity pattern

$$g(\alpha, \gamma) = \begin{cases} 1 & \text{for } |\alpha| < \Omega_v/2 \\ & \text{and } |\gamma| < \Omega_h/2 \\ 0 & \text{otherwise} \end{cases}$$

where α is the vertical angle and γ is the azimuth angle. The horizontal (γ) integration is limited by

$$y < \Omega_h \min(R_{OT}, R_{OR})$$

$$= \frac{\Omega_h d}{\alpha + \beta} \min(\alpha, \beta)$$

$$\sim c_{12} \Omega_h d \frac{\alpha \beta}{(\alpha + \beta)^2}$$

where c_{12} is a constant in the range $1 < c_{12} < 2$. For small delays, $c_{12} = (1 + |\alpha_0 - \beta_0| / \theta_s)$. Using the same transformation as before

$$y = x \sqrt{2R_0 c \tau}$$

we must have

$$x^2 < (c_{12} \Omega_h / \theta_s)^2 (1 - x^2),$$

or

$$x^2 < 1 / (1 + (\theta_s / (c_{12} \Omega_h))^2) .$$

Defining

$$x_2^2 = \min(1 - \tau_0 / \tau, [1 + (\theta_s / (c_{12} \Omega_h))^2]^{-1})$$

we get

$$Q(\tau) = \frac{4Ck^{2-m}c}{d^2} \int_0^{x_2} dx \int_{\alpha_a}^{\alpha_b} d\alpha (1-x^2)^{(m-1)/2} (\alpha + P(x)/\alpha)^{-m}/\alpha$$

where

$$\alpha_a = \max\left\{\alpha_0, (1-x^2) \frac{\alpha_0 \beta_0}{\beta_1} \frac{\tau}{\tau_0}, r_1\right\}$$

$$\alpha_b = \min\left\{\alpha_1, (1-x^2) \alpha_0 \frac{\tau}{\tau_0}, r_2\right\}$$

$$\alpha_1 = \alpha_0 + \Omega_v$$

$$\beta_1 = \beta_0 + \Omega_v$$

and r_1, r_2 are the real positive roots of

$$\alpha + \alpha^{-1} \frac{2c\tau}{d} (1-x^2) = \Omega_h c_{12} \sqrt{x^{-2}-1}.$$

The contribution of the limits r_1 and r_2 will be ignored in what follows. For narrow beams x_2 is small and we again set $x=0$ in the integral and get $\alpha = [\alpha_a \alpha_b]^{1/2} \sim \theta_s \sqrt{\tau/\tau_0}$. The last approximation is good for nearly symmetrical links and for small τ . Hence,

$$Q(\tau) \sim \frac{4c_1^{2-m}}{d} \frac{c}{d} \theta_s^{-m} \left(\frac{\tau}{\tau_0}\right)^{-\frac{m}{2}} \log \frac{\alpha_b}{\alpha_a} x_2(\tau), \quad \tau < \tau_0 \alpha_1 \beta_1 / \alpha_0 \beta_0.$$

(3.37)

The following approximation is sometimes useful:

$$\alpha_b / \alpha_a \sim \frac{\tau/\tau_0}{[1 + \beta_0 \tau / (\beta_1 \tau_0)][1 + \alpha_0 \tau / (\alpha_1 \tau_0)]}.$$

Eq. (3.37) is shown in Figure 3-6 together with the power impulse response using the computer program TRODIF. The agreement is reasonably good in spite of the somewhat crude approximations.

The tails of the power impulse response $Q(\tau)$ will usually differ from (3.33), (3.36), or (3.37) due to the decay in the C_n^2 profile, or due to finite antenna beamwidth. It is necessary to take these factors into account to calculate the 2σ delay spread.

The height above the baseline is

$$h = d \frac{\alpha\beta}{\alpha + \beta} .$$

When we are looking at a constant delay,

$$\alpha\beta = \frac{2c\tau}{d} ,$$

then h is also nearly constant. $\alpha + \beta$ varies in the range $2\left(\frac{\tau}{\tau_0}\right)^{1/2} (\alpha_0\beta_0)^{1/2} < \alpha + \beta < \beta_0 + \alpha_0\left(\frac{\tau}{\tau_0}\right)$, where we have assumed $\alpha_0 > \beta_0$. For most links we can assume $\tau \ll 2\tau_0$ in which case the ratio of the upper limit and the lower limit is only 1.06, so the scattering angle changes only by 6%. Replacing $\alpha + \beta$ by its geometric mean we get

$$h \sim \sqrt{2cd\tau / (s^{1/2} + s^{-1/2})} . \quad (3.38)$$

Hence height is proportional to the square root delay.

YOUNGSTOWN, NY -- VERONA, NY

$d = 168 \text{ mi}$

$\alpha_0 = 1.76^\circ$

$\beta_0 = 1.34^\circ$

Antenna
Diameter

— CALCULATED
- - - ANALYTICAL APPROX.

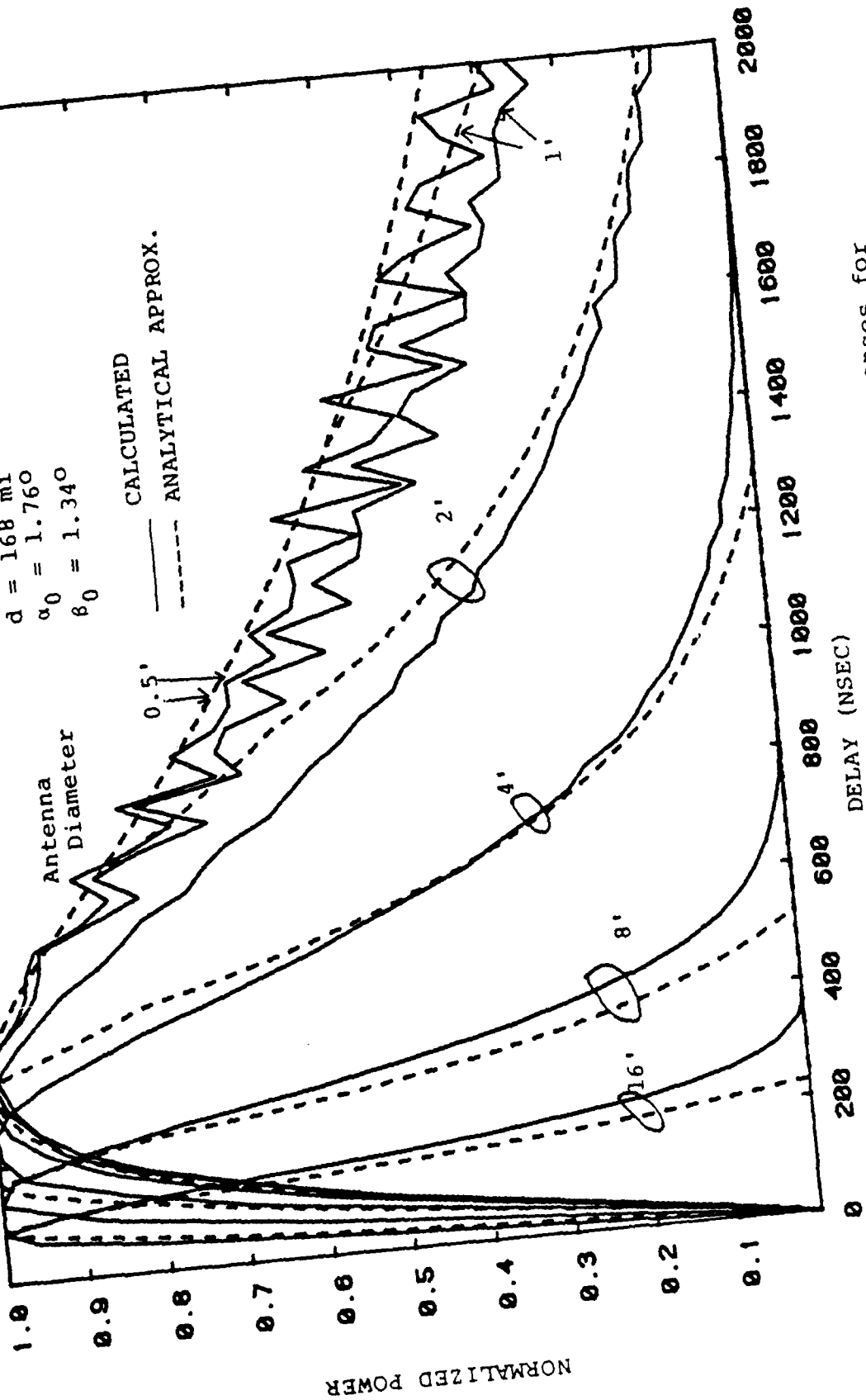


Figure 3-6 Theoretical and Computed Power Impulse Responses for Different Aperture Dimensions

Now assume a C_n^2 profile of the form

$$C_n^2 = C_n^2(h_0) e^{-(h-h_0)/h_1} \quad (3.39)$$

where h_0 is the bottom of the common volume. $Q(\tau)$ in (3.33) is then modified to

$$Q(\tau) = A \log\left(\frac{\tau}{\tau_0}\right) \left(\frac{\tau}{\tau_0}\right)^{-\frac{m}{2} - \frac{\alpha_0 \beta_0 d}{h_1 \theta_0} (\sqrt{\tau/\tau_0} - 1)} e^{-\frac{\alpha_0 \beta_0 d}{h_1 \theta_0} (\sqrt{\tau/\tau_0} - 1)}$$

define $B = \alpha_0 \beta_0 d / (h_1 \theta_0)$. Then the moments of Q can now be found from

$$\begin{aligned} \int_{\tau_0}^{\infty} \tau^n Q(\tau) d\tau &= \tau_0^{n+1} \int_1^{\infty} dt t^n Q(\tau_0 t) = A e^{-B \tau_0^n} \int_1^{\infty} t^{n - \frac{m}{2}} e^{-B\sqrt{t}} \log t dt \\ &= A e^{-B \tau_0^n} \frac{\partial}{\partial \alpha} \bigg|_{\nu = n - \frac{m}{2}} \left[\int_1^{\infty} t^{\nu} e^{-B\sqrt{t}} dt \right] \\ &= 2A e^{-B \tau_0^n} \frac{\partial}{\partial \nu} \left[\frac{\Gamma(2+2\nu, B)}{B^{2\nu+2}} \right]_{\nu = n - \frac{m}{2}} \end{aligned}$$

The same approach is used to modify the wide beam result (3.36). When the vertical antenna patterns limit the width of the common volume the power impulse response $Q(\tau)$ falls off rapidly for $\tau > \tau_1$, where

$$\tau_1 = \frac{\alpha_1 \beta_1 d}{2c} .$$

In this case, (3.37) should be used together with (3.39).

3.5.8 Doppler Spread

The Doppler spread, i.e., the inverse of the coherence time, is another important parameter, particularly for a realistic evaluation of adaptive troposcatter techniques. In order for the adaptive loops to operate, the channel coherence time must be longer than the time constants of the loops. In other words, the channel must be essentially time invariant long enough to allow a reliable measurement of the channel.

The Doppler spread is found from the refractive index spectrum using Taylor's hypothesis of frozen turbulence. The received spectrum is then

$$S_R(f) = \int_V d^3 \underline{r} H(\underline{r}) S_T(f - (\underline{e}_T - \underline{e}_R) \cdot \underline{u} / \lambda) \quad (3.40)$$

where

$\underline{e}_T, \underline{e}_R$ = direction vectors of the incident and scattered fields

- $S_T(f)$ = spectrum of the transmitted waveform, normalized to unit power,
 \underline{u} = wind velocity vector,
 $H(\underline{r})$ = integrand in (3.1), see (3.2).

the l 'th moment μ_l of the Doppler spectrum is then found from

$$\mu_l = \int_V d^3 \underline{r} H(\underline{r}) ((\underline{e}_T - \underline{e}_R) \cdot \underline{u}/\lambda)^l \quad (3.41)$$

The rms Doppler spread is defined from

$$\sigma_{\text{Doppler}}^2 = (\mu_0 \mu_2 - \mu_1^2) / \mu_0^2 \quad (3.42)$$

In the special case where the wind is perpendicular to the path (worst case) we find

$$(\underline{e}_T - \underline{e}_R) \cdot \frac{\underline{u}}{\lambda} = \frac{u}{\lambda} \frac{(\alpha + \beta)^2}{\alpha\beta} \frac{y}{d} \quad (3.43)$$

where $u = |\underline{u}|$ is the wind velocity perpendicular to the path. From (3.40) and (3.6) the Doppler spectrum is

$$B(\delta f) = Ck^{2-m} \int_{\alpha_0} d\alpha \int_{\beta_0} d\beta \frac{R_{0T} R_{0R}}{R_T^2 R_R^2} \frac{\alpha\beta}{\theta_0^3} \frac{\lambda d}{u} \theta^{-m}(\alpha, \beta, y(\delta f)) \quad (3.43a)$$

where

$$y(\delta f) = \frac{\alpha\beta}{\theta_0^2} \frac{\lambda d}{u} \delta f \quad .$$

Instead of evaluating the moments we calculate the Doppler spread by the definition

$$B_{c,sq} = \int B(\delta f) / B(0) \quad .$$

$B(0)$ is

$$\begin{aligned} B(0) &= Ck^{2-m} \frac{\lambda}{ud} \int d\alpha d\beta \theta_0^{-1-m} \\ &= \frac{Ck^{2-m}}{m(m-1)} \frac{\lambda}{ud} \theta_s^{1-m} \quad . \end{aligned} \quad (3.44)$$

From (3.9a) we then have

Doppler spread for wide beams:

$$\begin{aligned} B_{c,sq} &\equiv \int B(\nu) d\nu / B(0) \\ &= \frac{mB\left(\frac{1}{2}, \frac{m-1}{2}\right)}{m-2} \frac{\theta_s u}{\lambda} \quad . \end{aligned} \quad (3.45a)$$

For $m = 11/3$ this reduces to

$$B_{c,sq} = 3.70 \theta_s u / \lambda . \quad (3.45b)$$

For a beam with narrow azimuth beam width $B(0)$ is unchanged. Hence the Doppler spread is reduced by the aperture-to-medium coupling loss. Using (3.14b) we get

$$B_{c,sq} = \frac{3.70 \theta_s u / \lambda}{1 + 1.85 \theta_s / b_h} \sim 2 \frac{ub_h}{\lambda} . \quad (3.46)$$

The results are also easily generalized to the case of arbitrary vertical beamwidth, again assuming an ideal square beam. This approximation is not as good for the Doppler spread calculation since the antenna sidelobes may contribute to the spectrum. However it is still useful and we get

$$B(0) = \frac{Ck^{2-m}}{m(m-1)} \frac{\lambda \theta_s^{1-m}}{ud} F_{m-1} \left(\frac{b_{Tv}}{\theta_s}, \frac{b_{Rv}}{\theta_s} \right)$$

and thus from (3.17)

$$B_{c,sq} = \frac{2ub_h}{\lambda} / (1 + |\alpha_0 - \beta_0| / \theta_s) . \quad (3.47)$$

Using the same approximation as in (3.18) we find the general result

Doppler spread for arbitrary beamwidth ($b_{Th} = b_{Rh} = b_h$):

$$B_{c,sq} = \frac{A_d \theta_s u / \lambda}{(1 + A_d \theta_s / 2b_h)(1 + |\alpha_0 - \beta_0| / \theta_s)} \quad (3.48)$$

where

$$A_d = \frac{mB\left(\frac{1}{2}, \frac{m-1}{2}\right)}{m-2} \quad (= 3.7 \text{ for } m = 11/3) .$$

These results assume isotropic scattering. The Doppler spectrum narrows considerably with nonisotropic turbulence [Birkemeier et al., 1969]. This is due to the small amount of off-axis scattering with near specular reflections. It is shown in Section 3.6 that A_d in (3.48) should be reduced by the anisotropy factor, the ratio of horizontal and vertical scales.

3.5.9 Validity of the Uncorrelated Scatterer Assumption

The validity of the uncorrelated scatterer model presumes that resolvable delay cells are small compared to the correlation distance of the turbulence. Consider a link with slant range d and the angles α, β as defined in Figure 3-7. It can be shown [Monsen et al., 1981] that the relative delay is

$$\tau = (R_{OT} + R_{OR} - d)/c = 2 \frac{d}{c} \frac{\sin \frac{\alpha}{2} \sin \frac{\beta}{2}}{\cos \frac{\alpha + \beta}{2}} .$$

Differentiating this expression yields

$$\frac{\Delta \tau}{\Delta \alpha} = \frac{d \sin \beta}{2c \cos^2\left(\frac{\alpha + \beta}{2}\right)} .$$

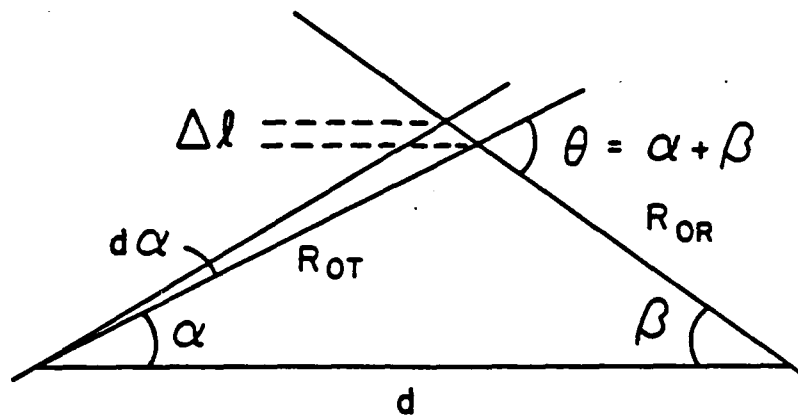


Figure 3-7 Geometry for Determination of the Uncorrelated Scatter Condition

The change in height, Δl , with a change in the angle α by $\Delta\alpha$ is given by

$$\frac{\Delta l}{\Delta\alpha} = d \left[\frac{\sin \beta}{\sin(\alpha+\beta)} \right]^2 .$$

Hence if $\Delta l = L_0$, the vertical correlation distance of the turbulence we get

$$\Delta\tau = \frac{L_0}{2c} \frac{\sin^2(\alpha+\beta)}{\sin \beta \cos(\frac{\alpha+\beta}{2})} \sim \frac{L_0}{2c} \frac{\theta_0^2}{\beta} .$$

The condition for uncorrelated scatter is

$$\Delta\tau \ll 1/W$$

where W is the bandwidth. Assume $\theta_0 \sim \theta_s$. Since $\theta/2\beta$ is on the order of one we get the condition

$$\frac{W}{f} \frac{L_0}{\lambda} \theta_s \ll 1 . \quad (3.49)$$

This condition is almost always satisfied. As an example take $L_0 = 70$ m and $\theta_s = 12$ mrad (corresponding to a 100 km link). Then the condition is

$$W \ll 350 \text{ MHz} .$$

3.6 SCATTERING FROM ANISOTROPIC TURBULENCE

3.6.1 Small Scale Turbulence

The results of Section 3.5 are modified in certain ways when the turbulence is anisotropic. The assumption here is that the outer scale of the turbulence is small compared to the common volume. For simplicity assume that the two horizontal scales are identical. Then the modified Kolmogorov spectrum is of the form

$$\phi_n(k_v, k_h) = C_0 [1 + k_h^2 L_{0h}^2 + k_v^2 L_{0v}^2]^{-m/2} \quad (3.50)$$

$$C_0 = \sigma_n^2 L_{0h}^2 L_{0v} \Gamma\left(\frac{m}{2}\right) / (\pi^{3/2} \Gamma\left(\frac{m-3}{2}\right)),$$

where k_h and k_v are the horizontal and vertical wave numbers and L_{0h} and L_{0v} are the corresponding outer scales. For $m=11/3$, we have

$$\phi_n(k_v, k_h) = 0.033 C_{nv}^2 \left(\frac{L_{0h}}{L_{0v}}\right)^2 \left[k_v^2 + \frac{1+k_h^2 L_{0h}^2}{L_{0v}^2} \right]^{-m/2},$$

where C_{nv}^2 is the vertical structure constant. The covariance function is

$$\phi_n(r, z) = \phi_{iso} \left(\sqrt{\left(\frac{r}{L_{0h}}\right)^2 + \left(\frac{z}{L_{0v}}\right)^2} \right)$$

where ϕ_{iso} is the covariance function for isotropic turbulence with unit correlation scale,

$$\phi_{iso}(\phi) = \frac{\sigma_n^2 (5-m)/2}{\Gamma(\frac{m-3}{2})} \phi^{(m-3)/2} K_{\frac{m-3}{2}}(\phi) .$$

The received power is determined from (3.1), where, to the first order approximation,

$$k_{e_s} = k(0, y \theta_0^2 / (\alpha \beta d), \theta_0) . \quad (3.51)$$

The coordinate system is the same as in Figure 3-4. The longitudinal component is ignored, but the off-axis component is included. The dominant component is the vertical component θ_0 . Hence we find (3.6) is modified

$$P_R = C_a k^{2-m} \int_{\alpha_0} d\alpha \int_{\beta_0} d\beta \int dy \frac{R_{0T} R_{0R}}{R_T^2 R_R^2} \frac{1}{\theta_0} [\theta_0^2 + A^2 y^2 / R_0^2]^{-m/2} \quad (3.52)$$

where R_0 was defined in (3.5) and A is the anisotropy

$$A = L_{0h} / L_{0v} . \quad (3.53)$$

Data indicate that A can be much larger than one. The propagation constant for the anisotropic medium is

$$C_a = \frac{1}{2} P_T G_T G_R \pi C_0 L_{0v}^{-m} \quad (3.54)$$

This is the generalization of (3.7). For $m=11/3$ it becomes $C_a = 0.0518 C_{nv}^2 A^2 P_T G_T G_R$. Integrating (3.52) over y , α , and β we get the equivalent of (3.9)

$$P_R = R_{R,basic} = \frac{C_a B(\frac{1}{2}, \frac{m-1}{2})}{A(m-1)(m-2)} (k\theta_s)^{2-m/d} \quad (3.55)$$

$$[= 0.0196 C_{nv}^2 A(k\theta_s)^{-5/3/d} \text{ for } m=11/3]$$

This is proportional to (3.9). Note that for a given measured C_{nv}^2 this is increased by a factor A over what is predicted from the isotropic case. The main differences from Section 3.5 will be the effects of off-axis scattering. This means that the horizontal coupling loss is affected. The equivalent of (3.12) yields the received power with a narrow beam (in azimuth)

$$P_R = \frac{2C_a}{m(m-1)} \frac{b_h}{\theta_s} (k\theta_s)^{2-m/d} \quad (3.56)$$

and the horizontal coupling loss is approximately

$$L_{ch} \sim 10 \log\left(1 + \frac{mB(\frac{1}{2}, \frac{m-1}{2})}{2(m-2)} \frac{\theta_s}{Ab_h}\right) \quad (3.57)$$

We conclude that: For narrow beams the horizontal coupling loss is reduced by the anisotropy factor.

The other coupling loss terms in (3.18) are not affected.

Next consider the horizontal correlation distance. Following (3.20) and (3.21) we have

$$P_R \int \rho_H(z) dz = C_a k^{2-m} \frac{\lambda \theta_s^{1-m} / d}{(m-1)^2} \beta_{m-1} \left(\frac{\alpha_0}{\theta_s} \right), \quad (3.58)$$

so the horizontal correlation distance is

$$R_H = A \frac{\lambda}{\theta_s} \frac{m-2}{m-1} \frac{\beta_{m-1}(\alpha_0/\theta_s)}{B\left(\frac{1}{2}, \frac{m-1}{2}\right)}. \quad (3.59)$$

Hence, the horizontal correlation distance is increased by the anisotropy factor when compared with (3.22).

The vertical correlation and the power impulse response depend primarily on the vertical scale, and are unaffected by the anisotropy.

The Doppler spread, however, relies almost exclusively on off-axis scatter and is clearly dependent on A. Assume a wind perpendicular to the path.

It is easily seen that the spectrum is simply scaled by A,

$$B(v; A) = B(v/A; 1) \quad (3.60)$$

where $B(v; 1)$ is given by the isotropic result (3.43a). The Doppler spread, as defined in (3.45) is

$$B_{c,sq} = \frac{mB\left(\frac{1}{2}, \frac{m-1}{2}\right)}{m-2} \frac{\theta_s u}{A\lambda} \quad (3.61)$$

For sufficiently narrow beams this is reduced by the coupling loss and equals (3.46), independent of A. The general expression is that of (3.48) with A_d replaced by

$$A_d = \frac{mB\left(\frac{1}{2}, \frac{m-1}{2}\right)}{(m-2)A} \quad (3.62)$$

3.6.2 Large Scale, Highly Anisotropic Turbulence

When the pancake-shaped eddies are so large that they are not completely contained within the common volume, then all the parameters, including path loss, have a different form. Such large anisotropic turbulence has effects similar to layer reflection. Layer reflection will be considered in the next section.

In Appendix C, Equation (C-29) we found the following general expression for P_R ,

$$P_R = \frac{P_R G_T G_R k^2}{16\pi^2} \int_V d^3 \underline{r} \frac{|g_T(\underline{r})|^2 |g_R(\underline{r})|^2}{|R_T(\underline{r})|^2 |R_R(\underline{r})|^2} I(\underline{r}) \quad (3.63)$$

where $I(r)$ is proportional to the scattering cross section, and is given by

$$I(\underline{r}) = \int_V d^3 \underline{r}_1 \frac{\phi_n(\underline{r}_1)}{v_1(\underline{r})} e^{jk\underline{r}_1 \cdot \underline{e}_s}$$

The volume V_1 consists of points $\{\underline{r}' - \underline{r}'' | \underline{r}' \text{ and } \underline{r}'' \text{ and in } V \text{ and } \underline{r}' + \underline{r}'' = 2\underline{r}\}$. Until now we have assumed I equals $(2\pi)^3 \phi_n(k\underline{e}_s)$. Now suppose the beamwidth is narrow so that the anisotropic eddies in the x (along the path) and y (perpendicular to the path direction) may be larger than the size of V . We assume, however, that the vertical scale (z direction) is small. We consider two limiting cases

A. Large Scale Perpendicular to the Path.

This is likely to happen with azimuthally narrow beams in the presence of highly anisotropic turbulence. Then

$$I(\underline{r}) \sim L_H \iint dx dz \phi_n(x, 0, z) e^{jk\underline{r}_1 \cdot \underline{e}_s}$$

where L_H is the average width of the common volume in the y direction. In terms of the spectrum this equals

$$I(\underline{r}) \sim (2\pi)^2 L_H \int_{-\infty}^{\infty} dk_y \phi_n(k_{sx}, k_y, k_{sz})$$

Using (3.50) with $k_h^2 = k_x^2 + k_y^2$ we find

$$I(\underline{r}) \sim \frac{(2\pi)^2 L_H B\left(\frac{1}{2}, \frac{m-1}{2}\right)}{2L_{0h}} C_0 \left[1 + (k_{sx} L_{0h})^2 + (k_{sz} L_{0v})^2 \right]^{\frac{1-m}{2}}$$

Using (3.51) we get

$$I(\underline{r}) \sim \frac{2\pi^2 L_H B\left(\frac{1}{2}, \frac{m-1}{2}\right) C_0}{2L_{0h}} [1 + (k_{\theta_0} L_{0v})^2]^{\frac{1-m}{2}} \quad (3.64)$$

For $m = 11/3$ the effective spectrum slope is now $8/3$. This means that the frequency dependence is only $f^{2/3}$ with a spectrum slope of $m = 11/3$. If $m = 6$ the frequency dependence of the NBS technique is obtained.

B. Both Horizontal Scales Large.

In this case the above results are modified to (L_{H1} and L_{H2} are the horizontal dimensions of the common volume):

$$\begin{aligned} I(\underline{r}) &\sim 2\pi L_{H1} L_{H2} \int_{-\infty}^{\infty} dk_x \int_{-\infty}^{\infty} dk_y \phi_{\pi}(k_x, k_y, k_{e_{sx}}) \\ &= (2\pi)^2 L_{H1} L_{H2} C_0 \int_0^{\infty} dk_h k_h [1 + k_h^2 L_{0h}^2 + (k_{e_{sx}} L_{0v})^2]^{-m/2} \\ &= \frac{(2\pi)^2 L_{H1} L_{H2}}{(m-2) L_{0h}^2} C_0 [1 + (k_{\theta_0} L_{0v})^2]^{1-m/2} \quad (3.65) \end{aligned}$$

In this case the effective spectrum slope is only $5/3$. A value of $m = 7$ is required to model the NBS spectrum slope of 5.

Note that in both cases when the scale is large in the direction perpendicular to the path there is no off-axis contri-

butions to the fields. The effect is very similar to that of layer reflection. There will be no horizontal coupling loss, and the horizontal correlation distance approaches infinity.

Since the common volume is much larger in the x direction than in the y direction, condition A is more likely to happen. The main conclusion is that anisotropy will tend to decrease the apparent spectrum slope.

3.6.3 Common Volume Dimensions

It is helpful to have an idea of the common volume dimensions in order to interpret the anisotropy effects. Assume equal beamwidth at both ends of the link,

$$\text{beamwidth} = \Omega .$$

Then,

$$\text{Height difference of common volume} = d \frac{\Omega(\alpha_0^2 + \beta_0^2 + \Omega \theta_s)}{\theta_s} \quad (3.66)$$

$$\text{Length of common volume} = d \frac{\Omega}{\theta_s + \Omega} \quad (3.67)$$

$$\text{Width of common volume} = \frac{d\Omega}{\theta_s} \min(\alpha_0, \beta_0) . \quad (3.68)$$

For the special case of narrow beams on a symmetric link ($\alpha_0 = \beta_0$),

$$\text{Height} : \frac{1}{2} \Omega d$$

$$\text{Width} : \frac{1}{2} \Omega d$$

$$\text{Length} : \Omega d / \theta .$$

For small θ the common volume is much longer in the x-direction than in the other two directions.

3.7 LAYER REFLECTION

At frequencies below approximately 1GHz, over-the-horizon communication is thought to rely primarily on layer reflection. It is difficult to establish a unified theory of layer reflection due to the many different layer structures that can cause reflection. This is evidenced by the wealth of theories developed to explain the statistical behavior of early troposcatter experiments. We will discuss briefly the effect of well developed layers in this section in order to compare layer reflection with troposcatter. The layers will be assumed large, so that they can be assumed to be of infinite extent.

Consider a layer with a linear gradient, so that the refractive index as a function of height is

$$n(h) = \begin{cases} n(0) - 39 \cdot 10^{-9} h & \text{below the layer } (h < 0) \\ n(0) - (39 \cdot 10^{-9} + n_1)h & \text{in the layer } (0 < h < \ell) \\ n(\ell) - 39 \cdot 10^{-9} (h-\ell) & \text{above the layer } (\ell < h) \end{cases}$$

where h is the height above the layer boundary in meters, ℓ is the layer thickness and n_1 is the gradient relative to the normal gradient of -39 N/km. This is the type of profile used by Friis et al [1957]. The reflection coefficient is

$$\rho^2 = \left| \frac{2 n_1 \ell}{\theta^2} \frac{\sin(\pi \ell \theta / \lambda)}{\pi \ell \theta / \lambda} \right|^2 \quad (3.69a)$$

where θ is the grazing angle (half the scatter angle). In most practical cases at high frequencies we will have $\pi l \theta / \lambda \gg 1$, so that the mean power reflection coefficient is

$$\rho^2 \sim \frac{2}{\pi^2} \frac{\lambda^2}{\theta^6} n_1^2 \quad (3.69b)$$

Note that this is independent of layer thickness. The reason is that the reflection is primarily due to the discontinuity of the gradient at the layer boundary. The effect of the layer thickness is primarily to modulate ρ^2 by a number between 0 and 2. The fact that the discontinuity is the primary cause of the reflection coefficient makes the above layer model questionable at wavelengths of 10 cm or less. A layer model which does not exhibit discontinuities is given by

$$n^2(h) = \left(1 - A_\ell \frac{e^{mh}}{1 + e^{mh}}\right) (n_0 - 39 \cdot 10^{-9} h)^2$$

After the usual effective earth radius transformation we get

$$n^2(h) \sim 1 - A_\ell \frac{e^{mh}}{1 + e^{mh}}$$

and the reflection coefficient [Brekhovskikh, 1960]

$$\rho^2 = \left[\frac{\sinh \left[\frac{\pi S}{2} (\sin \theta - \sqrt{\sin^2 \theta - A_\ell}) \right]}{\sinh \left[\frac{\pi S}{2} (\sin \theta + \sqrt{\sin^2 \theta - A_\ell}) \right]} \right]^2 \quad (3.70)$$

Here A_ℓ represents the total change in n^2 across the layer, and

$$S = \frac{4\pi}{\lambda m}$$

is a measure of the layer thickness relative to the wavelength. In contrast to (3.69) the reflection coefficient falls off exponentially with layer thickness.

Let us compare layer reflection and scattering assuming relatively broad beams. The effect of narrowing the beams would be to

1. reduce the scattered signal due to aperture-to-medium coupling loss,
2. reduce the median reflected signal due to the lower likelihood of a layer in the common volume.

The relative strength of reflection and scattering with narrower beams is therefore more complicated to evaluate. For broad beams the layer reflection loss is

$$L_\ell^{-1} = \frac{P_R}{P_T G_T G_R} = \rho^2 \left(\frac{\lambda}{4\pi D} \right)^2 \quad (3.71)$$

where D is the path length. The scattering loss is (see Section 4.7)

$$L_t = \frac{P_R}{P_T G_T G_R} = 0.0196 C_n^2 (2\pi\theta/\lambda)^{-5/3} / D \quad (3.72)$$

where C_n^2 is the structure constant. If the first layer model is assumed; then

$$\rho^2 \sim \lambda^2 / \theta^6$$

so that the frequency, scattering angle, and distance dependence is

$$L_l^{-1} \sim f^{-4} \theta^{-6} D^{-2}$$

and

$$L_t^{-1} \sim f^{-5/3} \theta^{-5/3} D^{-1} .$$

From Equation (3.70) note that perfect reflection occurs for $\sin \theta < \sqrt{A_l}$. We saw in Section 2 that multiple internal reflections (refractive multipath) can occur in that case. Clearly troposcatter will dominate for

1. high frequencies
 2. large scattering angles
- and
3. large distances.

The distance dependence is even more dramatic if the scattering angle is approximated by

$$\theta \sim D/R_e ,$$

where R_e is the effective earth radius.

With the smooth exponential transition we have

$$\rho^2 \sim e^{-\frac{4\pi^2}{\lambda m} \sqrt{\theta^2 - A_\ell}}$$

assuming the effective layer thickness is large compared to the wavelength. This shows exponential falloff with both frequency and scattering angle.

From (3.69b), (3.71) and (3.72) we can find the value of C_n^2/n_1^2 required for equal values of the reflection and scatter losses:

$$\text{required } \frac{C_n^2}{n_1^2} = 1.4 \lambda^{7/3} \theta^{-13/3}/D .$$

This is shown as a function of frequency and distance in Table 3-1.

If the gradient is -300 N/km Table 4-2 shows that tropo-scatter is dominant if C_n^2 is $2.5 \cdot 10^{-13}$ at 4GHz. Such values of C_n^2 are not uncommon, especially in connection with a steep gradient layer as assumed in this example. It is interesting to note that C_n^2 will tend to be large when n_1^2 is large. In fact, C_n^2 is proportional to the square of the gradient of the potential refractive index M [Tatarskii, 1971, Ottersten, 1969]:

$$C_n^2 = 2.8 L_0^{4/3} M^2 .$$

If we use (2.20) and assume $M^2 \approx n_1^2$ then we see from Table 3-1 that scatter dominates at 1 GHz and above for turbulent layers of 10 m thickness or more.

Table 3-1

RATIO OF STRUCTURE CONSTANT AND THE
SQUARED REFRACTIVE INDEX GRADIENT

C_n^2/n_1^2 Required for Equal Layer Reflection and Scatter			
Frequency	1 GHz	4 GHz	16 GHz
Distance			
40 km	67.3	2.7	.10
60 km	103	4.1	.16
80 km	95	3.8	.15
100 km	71	2.8	.11

Note: 75 m obstacles a quarter of the path distance away are assumed at each end to represent a typical tactical environment. This accounts for the non-monotonic dependence on distance.

For the idealized constant gradient layer it appears that reflection is significant at 1GHz or below. However, if we consider the exponential reflection model with smooth transitions the reflection coefficient is so small that reflection can be ignored even at 1GHz. For instance, with a layer thickness of 100 m and a gradient of 1000 N/km the reflection coefficient is so low that a reflection is 106 dB below the troposcatter signal for a 100 km path with the same geometry as in Table 3-1.

Layer reflection is associated with large changes in the gradient over an interval less than the wavelength. This will be a relatively infrequent event above 1-3 GHz. It is therefore reasonable to base performance prediction on a pure troposcatter model which will exhibit all of the critical parameters including low level signal statistics, large multipath spread, and the fade rates associated with wind motion.

3.8 RAIN EFFECTS

3.8.1 Pathloss Above C-Band

At higher frequencies rain can cause complete outages. For troposcatter the scattering crosssection of the atmospheric turbulence is larger when the atmosphere is humid and this fact helps to reduce the path loss. In addition, rain in the common volume will cause additional scattering, as discussed in Section 3.8.2.

Figure 3-8 illustrates how the RSL increases with increasing humidity (water vapor pressure) and that rain attenuation in light rain (5 mm/hr) still yields a stronger signal at 15 GHz than one would have on a dry day. The dashed curve for rain is pessimistic because it assumes that scattering from turbulence predominates in the common volume. The results of Section 3.8.2 indicate that the scatter from rain drops is greater than that from turbulence at frequencies above 5 GHz.

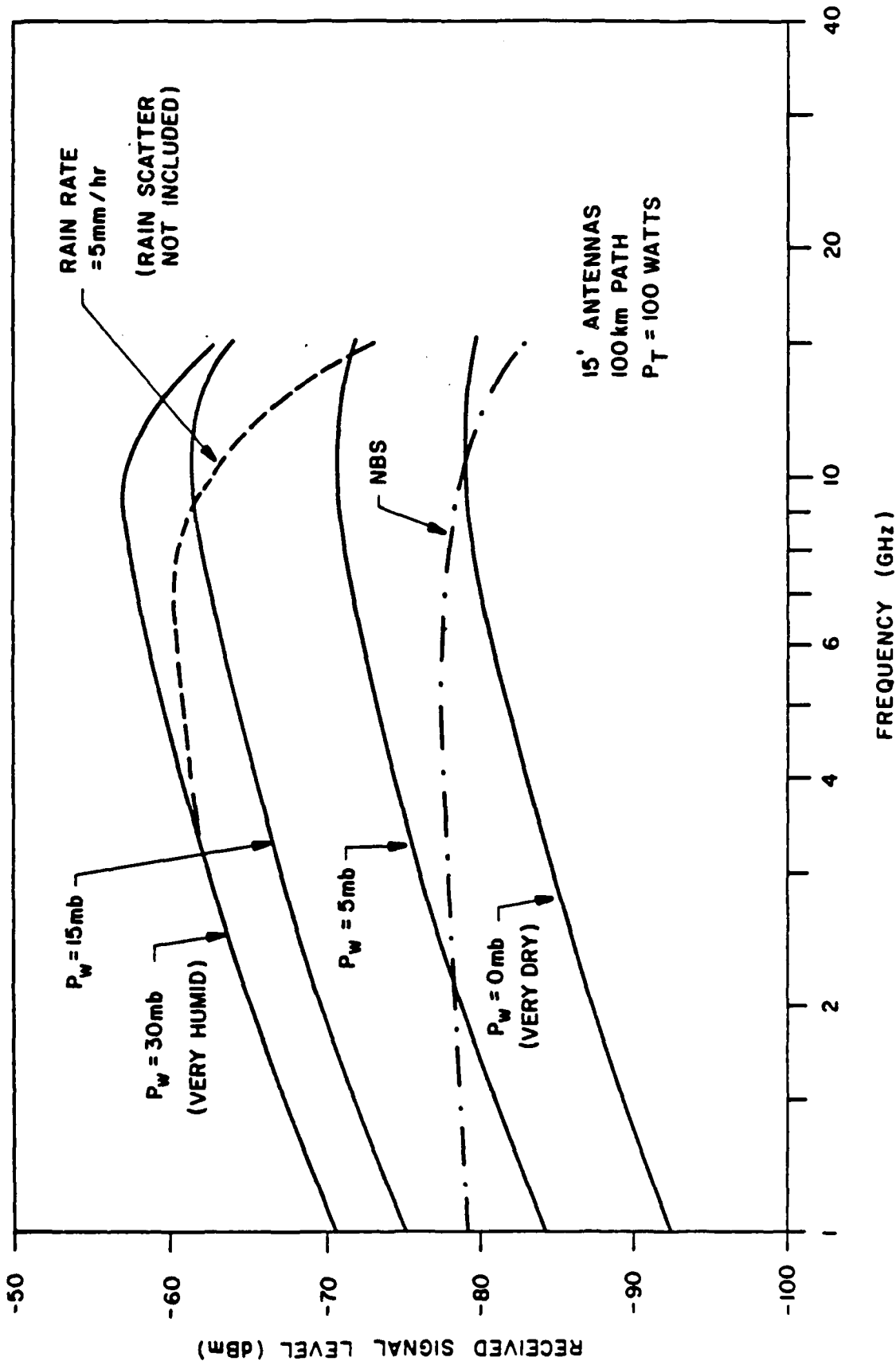


Figure 3-8 RSL vs. Frequency with Rain

Figure 3-9 shows the distance dependence with rain at 5 GHz and 15 GHz. The rain attenuation model is described in Section 2.

3.8.2 Rain Scatter

Assuming single (Rayleigh) scattering, the scattering crosssection per unit volume is

$$(A_s)_{\text{rain}} = \frac{\pi^5}{\lambda^4} \left| \frac{\epsilon-1}{\epsilon+2} \right|^2 \int_0^{\infty} (2a)^6 n(a) da$$

where $n(a)$ is the number of drops of radius $[a, a+da]$ per unit volume, and ϵ is the dielectric constant. At microwave frequencies at normal temperatures we can take $|(\epsilon-1)/(\epsilon+2)|$ to be unity. Next assume a Marshall-Palmer drop size distribution,

$$n(a) = N_0 e^{-\Lambda a}$$

where

$$N_0 = 1.6 \cdot 10^7 \text{ m}^{-4} ,$$

$$\Lambda = 8.2 \cdot 10^3 R^{-0.21} \text{ m}^{-1}$$

and where R is the rain rate in mm/hour.

Then

$$(A_s)_{\text{rain}} \sim 10^{-11} \left(\frac{f}{1 \text{ GHz}} \right)^4 R^{1.47} .$$

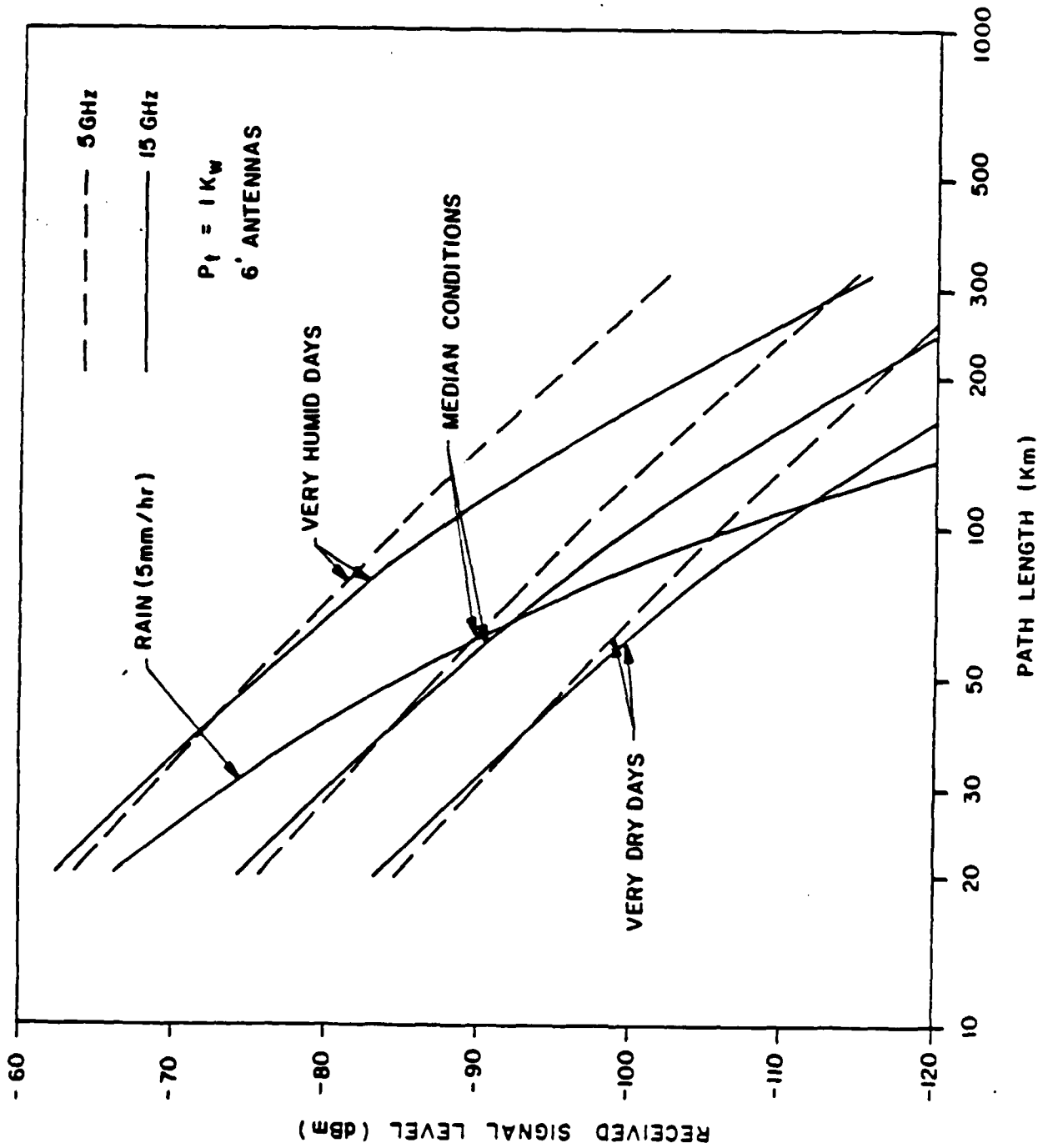


Figure 3-9 Troposcatter signal RSL, at 5 and 15 GHz as a function of path length for typical (median) and extreme conditions.

The scattered power is

$$P_R = \frac{P_T G_T G_R \lambda^2 A_r}{(4\pi)^3} \int_V d^3 \underline{r} \frac{A_s(\underline{r}) g_T(\underline{r}) g_R(\underline{r})}{R_T^2(\underline{r}) R_R^2(\underline{r})}$$

where A_r is the rain attenuation outside the common volume V .

For troposcatter from turbulence we have seen that the scattering cross section per unit volume is given by

$$\begin{aligned} (A_s)_{\text{turb}} &\sim 8\pi^2 k^4 \phi_n(k\theta_s) \\ &\sim 7.18 C_n^2 \left(\frac{f}{1 \text{ GHz}}\right)^{1/3} \theta_s^{-11/3} . \end{aligned}$$

Rain scatter increases sharply with frequency, but does not have the scattering angle dependence of troposcatter. As a numerical example take $C_n^2 = 10^{-15} \text{ m}^{-2/3}$, $f = 5 \text{ GHz}$, and $\theta_s = 2^\circ$. Then

$$(A_s)_{\text{turb}} \sim 2.7 \cdot 10^{-9} \text{ m}^{-1}$$

and

$$(A_s)_{\text{rain}} \sim 6.25 \cdot 10^{-9} R^{1.47} \text{ m}^{-1} .$$

Rain scatter dominates turbulent scatter for $R > 0.6 \text{ mm/hour}$ which is very light rain. For smaller angles rain will be less important. At higher frequencies rain attenuation must be included, but both scattering modes are equally affected.

For wideband links, the key effect of rain could be an increased delay spread when rain occurs high in the common volume.

3.9 A PROPOSED 2-COMPONENT MODEL

The Kolmogorov turbulence scatter model applies at high frequencies. At lower frequencies no reliable physical model exists. The observed effects can be explained by isotropic turbulence with a spectrum slope of 5, anisotropic turbulence with a spectrum slope of 6, or by layer reflection. Both anisotropic turbulence and layer reflection do not involve off-axis scatter and therefore predict a large spatial correlation. For simplicity we assume isotropic scattering here, the effects of anisotropy can be evaluated by scaling by the anisotropy factor A as described in Section 3.6.

To match solutions at high and low frequencies assume a wavenumber spectrum of the form

$$\phi_n(\kappa) = \phi_{n1}(\kappa) + \phi_{n2}(\kappa)$$

where ϕ_{n1} is the Kolmogorov turbulence scattering model and ϕ_{n2} is the, possibly anisotropic, low frequency model matching the NBS measurement. Both terms have long term variations which are likely to be independent.

The NBS model has a spectrum slope $m=5$. Since C_n^2 is not defined in this case the refractive index variance is used instead. From (3.10),

$$P_R = P_T G_T G_R \frac{\sigma_{nL0}^{2-2}}{24} (k \theta_s)^{-3/d} .$$

This matches the NBS model when $\sigma_n^2 L_0^{-2}$ depends on the height h_c of the bottom of the common volume ($h_c \sim \theta d/8$) if

$$\sigma_n^2 L_0^{-2} = \begin{cases} 5.8 \cdot 10^{-15} \text{ m}^{-2} \exp\{-h_c/1635\text{m}\} & 0 < h_c < 1250\text{m} \\ 2.47 \cdot 10^{-14} \text{ m}^{-2} \left[\frac{h_c}{125\text{m}}\right]^{-3/4} \exp\{-h_c/2560\} & 1250\text{m} < h_c < 6250\text{m} \end{cases} .$$

The approximation $h_c \sim \theta d/8$ is based on an approximation requiring a nearly symmetrical link.

The coupling loss can be calculated from (3.18). However, this expression does not include the effects of the height dependence of $\sigma_n^2 L_0^{-2}$. This effect can be accounted for, however, by using the delay spread evaluated in Section 3.5.7. The NBS coupling loss can also be used.

An important topic for future work would be the further development of this model, particularly as it is simplified on the basis of the analytical expression for $Q(\tau)$.

For a numerical comparison assume $m = 11/3$ in ϕ_{n1} and that C_n^2 is given by the continental air mass profile in (2.15),

$$C_n^2 = 1.5 \cdot 10^{-15} \exp(h_c/2200) .$$

Figure 3-10 shows the two components for a 200 km link. The NBS method is good up to about 10 GHz. Figure 3-11 shows the losses for a 500 km link. Here the NBS method is good up to 2 GHz. Figure 3-12 shows the effect of different values of C_n^2 for $d = 200$ km.

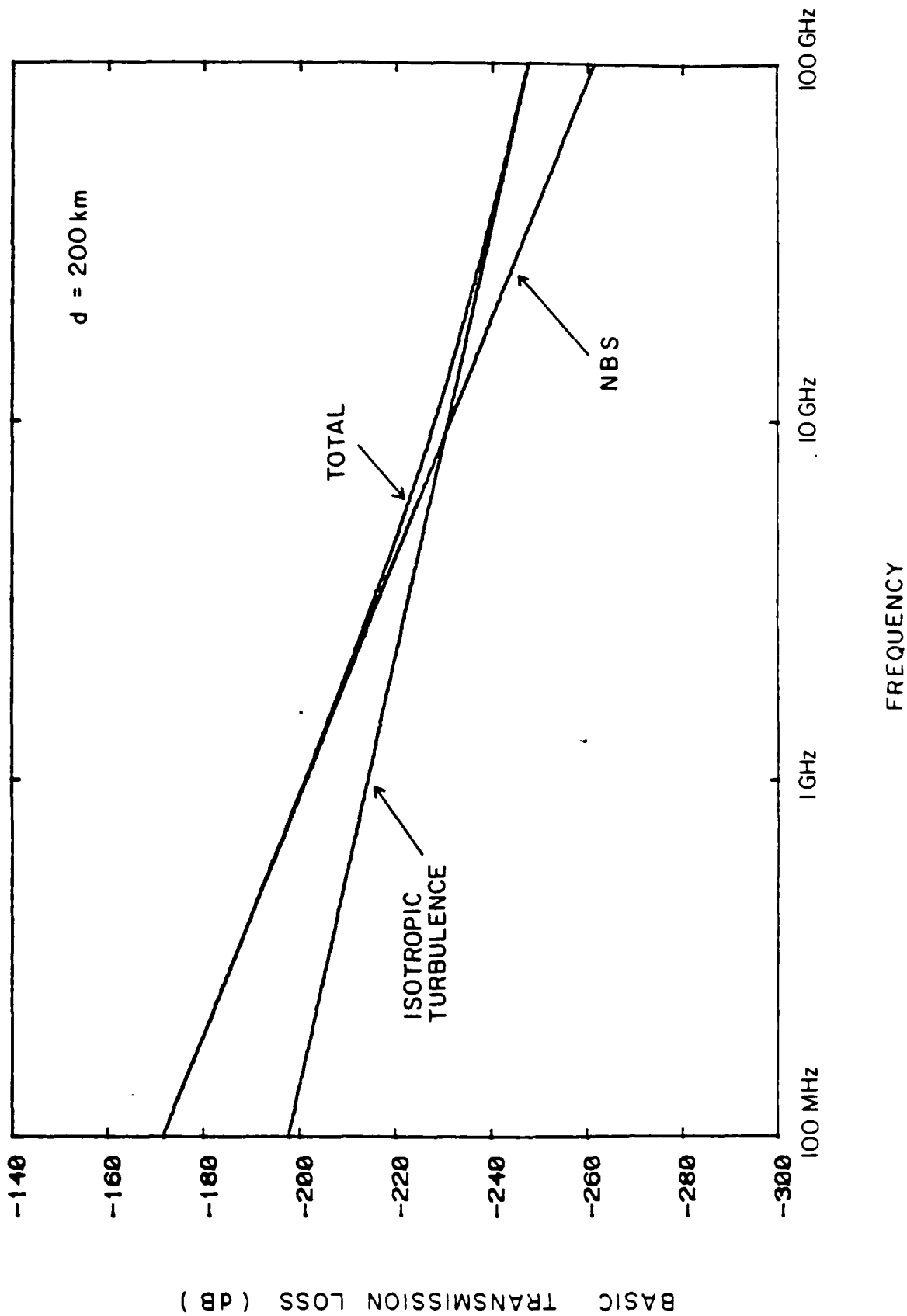


Figure 3-10 Transmission loss of 2 component model for $d=200$ km

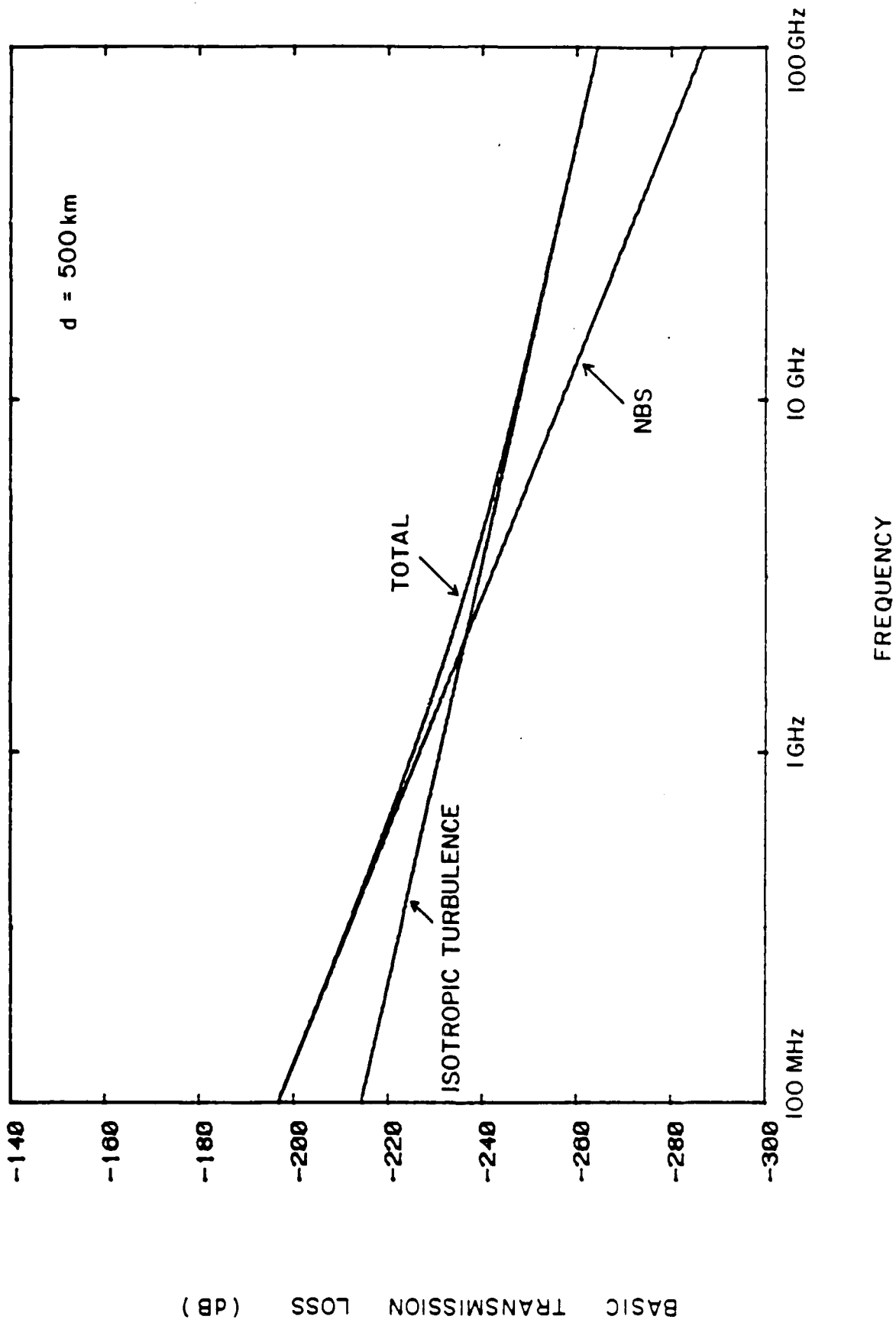


Figure 3-11 Transmission loss of 2 component model for d=500km

BASIC TRANSMISSION LOSS (DB)

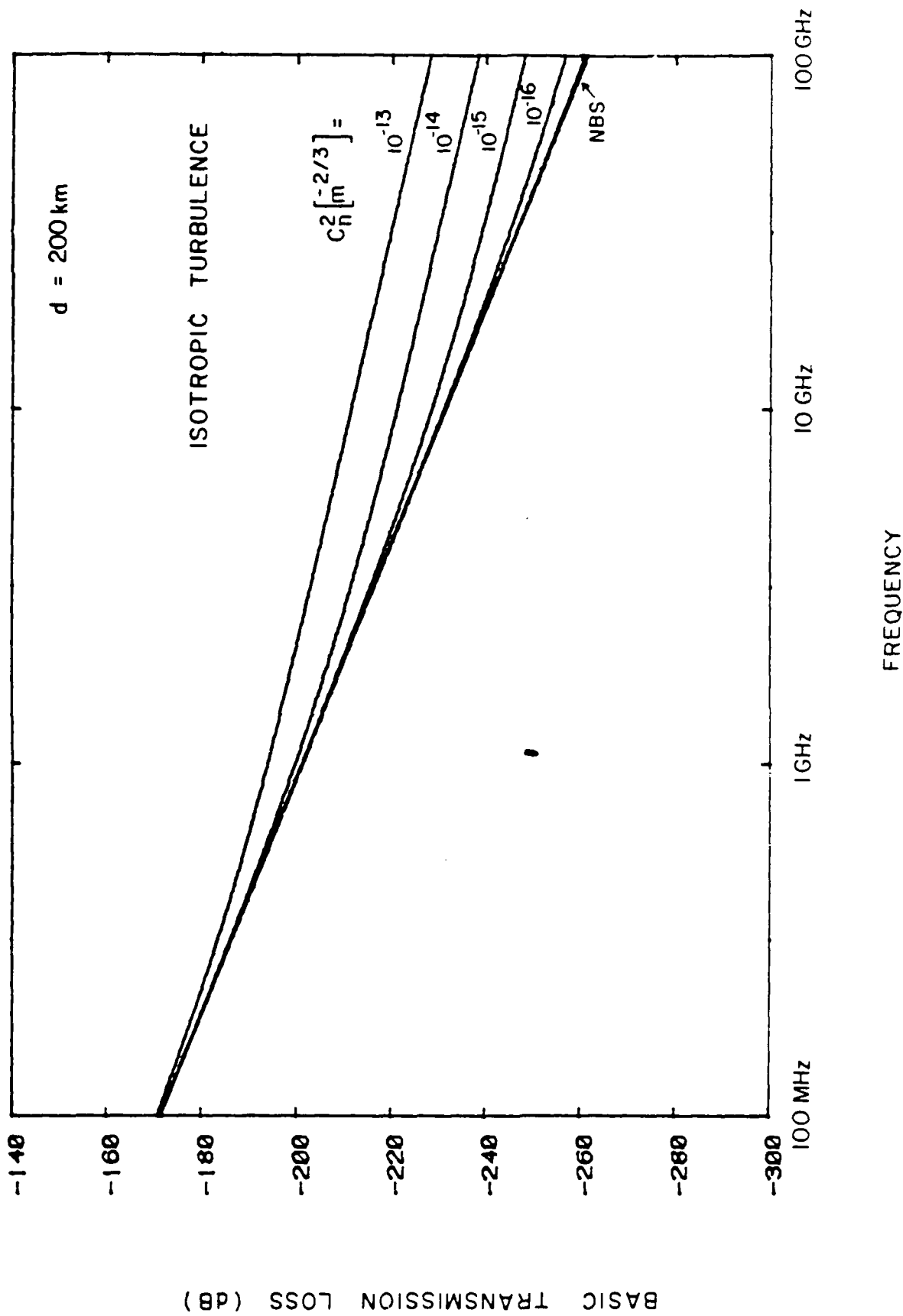


Figure 3-12 Total transmission loss for $d=200\text{km}$ and various C_N^2 values

While the turbulence scatter model is expected to be accurate at high frequencies it is not clear exactly what the cut-off frequency is, or that the NBS model can be used unmodified as different values of C_n^2 are used.

SECTION 3
REFERENCES

- Birkemeier, W.P., P.F. Duvoisin, A.B. Fontaine, and D.W. Thomson (1969), "Indirect atmospheric measurements utilizing RAKE tropospheric scatter techniques - Part II: radio meteorological interpretation of RAKE channel-sounding observations", Proc. IEEE, Vol. 57, No. 4, pp. 552-559
- Boithias, L., and Battesti, J. (1967) "Nouvelles experimentations sur la baisse de gain d'antenne dans les liaisons trans-horizon", Annales des Telecommunications.
- Booker, H.G., and Gordon, W.E. (1950), "A theory of radio scattering in the troposphere", Proc. IRE, Vol. 38, pp 401-402.
- Bean, B.R., Cahoon, B.A., Samson, C.A., and Thayer, G.D. (1966), A world atlas of atmospheric radio refractivity, ESSA Monograph 1, U.S. Government Printing Office, Washington, DC.
- Brekhovskikh, L.M. (1960), Waves in layered media, Academic Press.
- CCIR (1978) "Recommendations and reports of the CCIR, 1978, Vol. 5: propagation in non-ionized media" Report 238-3.
- Cianos, N. and Waterman, A.T., Jr. (1973) "Angle and doppler measurements of the quasi-coherent and incoherent components of microwave transhorizon signals" IEEE Trans. Ant. Prop. Vol. AP-29, No. 5, pp 746-750.
- duCastel, F. (1966) Tropospheric Radiowave Propagation Beyond the Horizon, Pergamon Press.
- Eklund, F., and Wickerts, S. (1968), "Wavelength dependence of microwave propagation far beyond the radio horizon", Radio Science, Vol. 3, No. 11, pp 1066-1074.
- Friis, H.T., Crawford, A.B., and Hogg, D.C. (1957), "A reflection theory for propagation beyond the horizon", Bell System Tech. J., Vol. 36, p. 627.
- Gossard, E.E. (1977), "Refractive index variance and its height distribution in different air masses", Radio Science, Vol. 12, No. 1, pp 89-105.

SECTION 3
REFERENCES (Continued)

- Ikegami, F., Akyama, T., Aoyagi, S. and Yoshida, H., (1968), "Variation of radio refraction in the lower atmosphere", IEEE Trans., Vol. AP-16,3.
- Kolmogorov, A.N. (1943), "Dissipation of energy in locally isotropic turbulence", Compte Rendus (Doklady) l'Academie des Sciences de l'USSR, Vol. 32, No. 1, pp 16-18.
- Kropfli, R.A., Katz, I., Konrad, T.G., and Dobson, E.B., (1968), "Simultaneous radar reflectivity measurements and refractive index spectra in the clear atmosphere", Radio Science, Vol. 3, pp 991-994.
- Megaw, E.C.S., (1950), "Scattering of electromagnetic waves by atmospheric turbulence", Nature, Vol. 166, pp 1100-1104.
- Monsen, P., and Parl, S.A., (1978), "Adaptive antenna control 2nd interim report" for U.S. Army EMOM, Report No. ECOM-76-8085-2, October 1977.
- Monsen, P., and Parl, S.A., (1980) Final report, adaptive antenna control (AAC) program, CSA-76-8085-6, for U.S. Army, Ft. Monmouth, NJ, March 1980.
- Obukhov, A.M., (1941), "On the distribution of energy in the spectrum of turbulent flow, Bull. Acad. Sci. USSR Geo. and Geophys. Ser. 4-5, 453. See also Comptes Rendus (Doklady) l'Academie des Sciences de l'USSR Vol. 32, No. 1, (1941).
- Ottersten, H. (1969) "Mean vertical gradient of potential refractive index in turbulent mixing and radar detection of CAT", Radio Science Vol. 4, pp. 1247-1249.
- Parl, S.A., (1979), "New formulas for tropospheric scatter path-loss", Radio Science, Vol. 14, No. 1, pp 49-57.
- Rice, P.L., Longley, A.G., Norton, K.A., and Barsis, A.P., (1965, Rev. 1967), "Transmission loss predictions for tropospheric communications circuits", N.B.S. Tech. Note 101.
- Sherwood, A. and Suyemoto, L., (1976), "Multipath measurements over troposcatter paths", MTP-170, the Mitre Corp.
- Sirkis, M.D. (1971), "Contribution of water vapor to index of refraction structure parameter at microwave frequencies", IEEE Trans. Ant. Prop. AP-19, pp 572-575, July 1971.

SECTION 3
REFERENCES (Concluded)

Tatarskii, V.I., The effects of the turbulent atmosphere on wave propagation, U.S. Department of Commerce, NTIS, Springfield, VA.

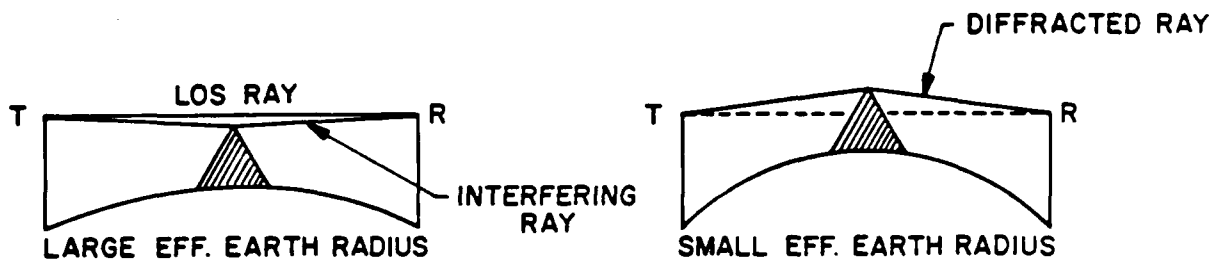
Villars, F., and Weisskopf, V.F. (1955), "On the scattering of radio waves by turbulent fluctuations of the atmosphere", Proc. IRE, Vol. 43, No. 10, pp 1232-1239.

SECTION 4 DIFFRACTION

Diffraction over terrain obstacles is a frequent mode of propagation on some over-the-horizon microwave links. In this section we describe some analytical and computational techniques useful in predicting the propagation parameters, path loss and delay.

4.1 BACKGROUND

Communication systems relying on diffraction propagation are rare. Usually a diffraction mode of propagation occurs when the link parameters are not as expected in the link design. The diffracted signal will then often be considered as interference with the desired signal. Assume the frequency is high enough so that ray theory is meaningful. Figure 4-1 shows how an obstacle can interfere with a line-of-sight path. Under normal conditions the ray scattered from the obstacle will be sufficiently attenuated that the interference with the direct ray is minimal. When the obstacle is within the first Fresnel zone of the direct ray the interference can be significant. When there is a direct ray as in Figure 4-1a the receiver is said to be in the lit zone. In this zone the diffracted ray is also a reflected ray. When the direct ray is blocked, as in Figure 4-1b the receiver is said to be in the shadow zone, in this case we talk about a diffracted ray. Keller [1962] has developed a complete Geometrical Theory of Diffraction (GTD) for diffracted rays which will be applied later in this section. Note from Figure 4-1a that the diffracted (reflected) ray will have a different delay than the direct ray, causing multipath that may degrade wideband communications. This delay dispersion effect can be much more serious on troposcatter links, as shown in Figure 4-2. Two separate horizon obstacles



(a) LIT ZONE : THE RAY REFLECTED FROM THE OBSTACLE MAY ADD DESTRUCTIVELY TO THE DIRECT RAY

(b) SHADOW ZONE : THE DIRECT RAY IS BLOCKED BY THE OBSTACLE, THE RECEIVED SIGNAL CAN BE EXPLAINED BY THE DIFFRACTED RAY SHOWN

Figure 4-1 Diffraction on an LOS Link

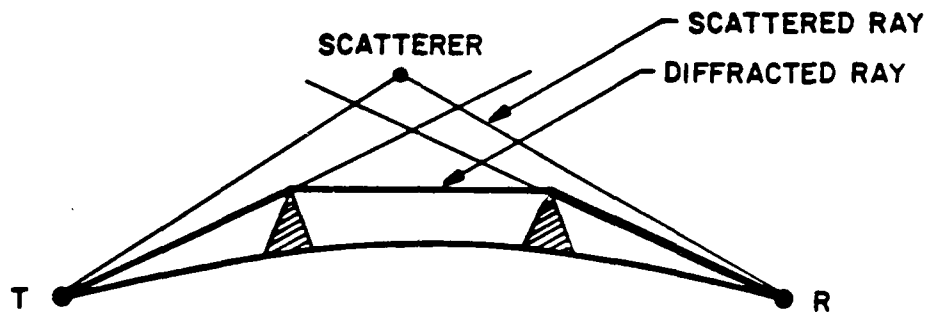


Figure 4-2 Mixed Troposcatter/Diffraction Mode

are common on troposcatter links. When the double diffracted ray is strong enough it can combine with the troposcatter signal to produce a large delay spread on the received signal. This effect has been found to degrade the new digital tactical troposcatter system AN/TRC-170 in tests on some links.

The above mentioned diffraction effects are strong reasons to investigate techniques for predicting the diffraction path loss and delay. In addition many over-the-horizon links depend solely on diffraction. In fact, the received signal level can sometimes be improved by introducing a knife-edge obstacle. The reason is simply that the reflection interference (Figure 4-1a) may produce a deep fade and hence a weaker signal than a diffracted ray in Figure 4-1b. Predicting diffraction effects is difficult, however, since the results are extremely sensitive to the assumed link parameters. Past experience with standard prediction techniques have proved them to be quite unreliable. This section will describe both the existing techniques as well as some new technique that may prove more successful when powerful digital computers are used to gather the necessary data as well as calculate more precisely than before the diffraction path loss.

Historically, the study of diffraction of radio waves by terrain features has been approached from two different points of view. One is diffraction by isolated obstacles such as mountain ridges or hills and the other is diffraction over the bulge of the earth. Transmission loss prediction methods based on diffraction theory for isolated obstacles have been used for radio paths where both the transmitter and receiver have a common radio horizon. On the other hand, prediction methods based on the theory of diffraction over the bulge of the earth (ground wave propagation) have been used for radio paths where transmitter and receiver do not have a common radio horizon [e.g., Rice, et al., 1967; CCIR, 1978]. These prediction methods are most useful at VHF (30-300 MHz) where obstacle and terrain irregularity are

relatively small compared to the radio wavelength. However as the applications have progressed from VHF to microwave frequencies, these approaches have become increasingly unreliable.

There are several reasons for the unreliability of the different methods:

1. Diffraction loss calculations based on diffraction theory for propagation over the bulge of the earth are only accurate when the surface of the earth is smooth and devoid of any prominent obstructions (the ocean surface is the best example). This technique is impractical with highly irregular surfaces.
2. Prediction based on multiple knife-edge diffraction theories is ideal for highly irregular terrain such as mountains. They fail when the edges are rounded or when the terrain is flat. When diffraction is over more than one edge many techniques fail in the transition region between the lit zone and the shadow zone.
3. Modification to rounded edges can be used with some of the techniques when the edges can be approximated by circular cylinders. Keller's Geometrical Theory of Diffraction can be extended to multiple rounded edges but the technique fails in the transition region between the lit zone and the shadow zone.
4. Edge irregularity can significantly affect the diffraction loss [Hacking, 1970; Haakinson, 1980; Reudink and Wazowitz, 1973]. It can cause multipath and fading which may be difficult to model. Theory and experiments show that edge roughness make a rounded edge behave more like a knife edge. [Bachynski, 1963; Hacking, 1970]

Two different techniques have been investigated to treat the problem of diffraction by multiple edges. These two techniques are discussed in detail in this section. We start off by discussing in Section 4.2 the application of Huyghens' principle to knife edge diffraction. This leads to the introduction of a direct numerical technique for the treatment of the multiple knife-edge diffraction problem. This technique is shown to reduce to the classical results of Millington et al. [1962] for double knife-edge diffraction. Then the technique is compared with the recent results of Vogler [1982] for multiple knife-edge diffraction. The technique is then extended to include ground reflections and is applied to diffraction by rounded and square edges. Comparisons are made with the theoretical results of Wait and Conda [1959] and the experimental results of Hacking [1970].

The direct application of Huyghens' principle can be quite time consuming even with a powerful computer. A number of simpler techniques have been used in the past to treat the multiple knife-edge diffraction problem, the most popular being the Epstein-Peterson technique and the Deygout method. These techniques are described in some detail in Section 4.3. Then a new uniform GTD (ray) technique for treating the problem of diffraction by multiple knife edges is described in Section 4.4, as well as its extension to rounded edges.

We conclude the section with discussions of the effects of the edge profile perpendicular to the path, spatial and long-term temporal variations in diffraction paths.

4.2 APPLICATION OF HUYGHENS' PRINCIPLE

4.2.1 Single Knife Edge

Huyghens' principle is illustrated in Figure 4-3. The field at R is composed of the field radiated from secondary sources in the plane of the knife edge. This representation can be made precise as we shall see. When the diffraction angle θ is large only the secondary sources near the top of the edge contribute, and the field at R can be computed as if there is only a single diffracted ray through the point P. This is the basis of GTD which is asymptotically valid (high frequencies) as long as the receiver (R) is in the shadow zone. When R is in the transition region GTD fails because the higher secondary sources can not be ignored.

In applying Huyghens' principle it is assumed that the field above the edge depends only on the field incident from the transmitting source (T) (Kirchhoff's assumption). In other words, the edge must not distort the incident field significantly and for any obstacles on the far side of the edge, reflections back to the plane of the edge are ignored.

Let $u_1(\underline{r})$ be the field incident on the knife edge plane. Let $R(\underline{r})$ be the distance from a secondary source location to the receiver. The field at the receiving point \underline{r}_p can then be found from Helmholtz's integral,

$$u(\underline{r}_p) = \int_S \left[v(\underline{r}) \frac{\partial u_1(\underline{r})}{\partial n} - u_1(\underline{r}) \frac{\partial v(\underline{r})}{\partial n} \right] ds \quad (4.1)$$

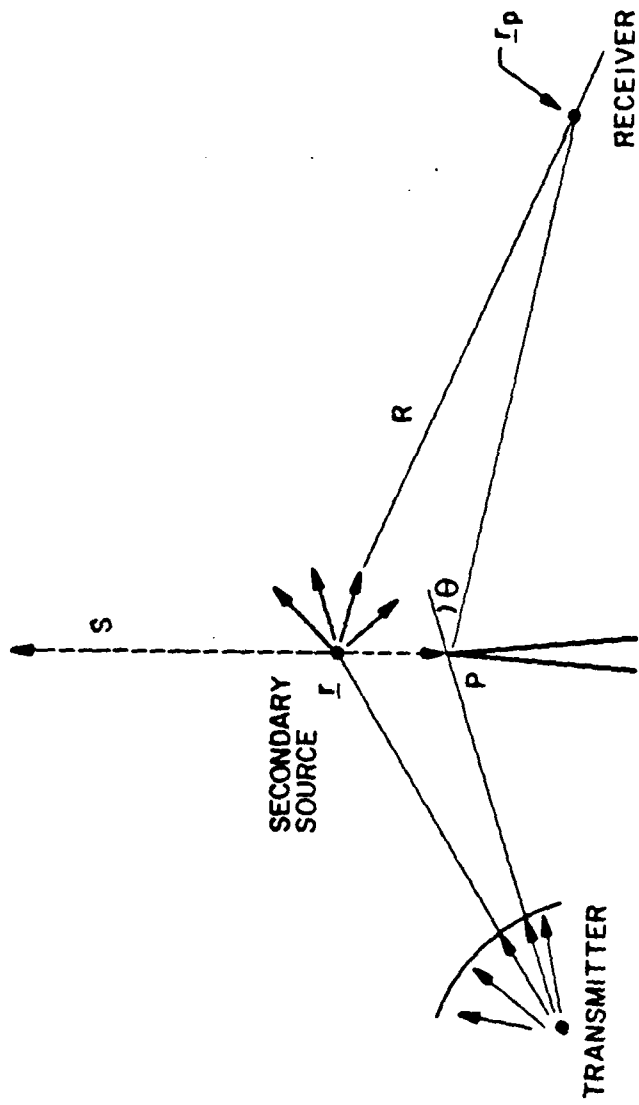


Figure 4-3 Huyghen's Principle for Knife-Edge Diffraction

where the integral is over the (half plane) surface S above the edge and $v(\underline{r})$ is given by

$$v(\underline{r}) = \frac{e^{-jkR(\underline{r})}}{4\pi R(\underline{r})} \quad (4.2)$$

$u(\underline{r}_p)$ then satisfies the wave equation on the receiver side of the plane, $\nabla^2 u + k^2 u = 0$ with the boundary condition $u = u_1$ on S and $u = 0$ on the edge. Equation (4.1) requires knowledge of both the value $u_1(\underline{r})$ of the incident field on S and the derivative of u_1 along the normal to the surface. This actually over specifies the solution to the wave equation. To see this in general requires introduction of the Green's function, and this will be done in Section 4.2.5 when ground reflections are taken into account. For the plane surface considered here the Helmholtz formula (4.1) can be reduced to the Rayleigh formula

$$u(\underline{r}_p) = 2 \int_S u_1(\underline{r}) \frac{\partial v}{\partial x} dS$$

where the X-coordinate is perpendicular to the plane S. In terms of the Y and Z coordinates in the plane we have

$$u(\underline{r}_p) = -2 \int_{-\infty}^{\infty} dy \int_{h_1}^{\infty} dz u_1(x, y, z) \frac{\partial}{\partial x_p} v(x_p - x, y_p - y, z_p - z) \quad (4.3)$$

where h_1 is the height of the edge and

$$v(x, y, z) = \frac{e^{-jk \sqrt{x^2 + y^2 + z^2}}}{4\pi \sqrt{x^2 + y^2 + z^2}} \quad (4.4)$$

$v(x_p - x, y_p - y, z_p - z)$ is the field at \underline{r}_p due to a monopole at the location of the secondary source \underline{r} . Assume now that the incident field is cylindrical, i.e., independent of y . Integrating (4.3) over y yields

$$u(x_p, z_p) = \frac{j}{2} \int_{h_1}^{\infty} u_1(x, z) \frac{\partial}{\partial x_p} H_0^{(1)}(k \sqrt{(x_p - x)^2 + (z_p - z)^2}) dz \quad (4.5)$$

At high frequencies the Bessel function in (4.5) can be replaced by its asymptotic expression, yielding

$$\begin{aligned} u(x_p, z_p) &= \frac{e^{-j\pi/4} (x_p - x)}{\sqrt{\lambda}} \int_{h_1}^{\infty} u_1(x, z) \frac{e^{-jk \sqrt{(x_p - x)^2 + (z_p - z)^2}}}{[(x_p - x)^2 + (z_p - z)^2]^{3/4}} \\ &= \left[\frac{j}{\lambda(x_p - x)} \right]^{1/2} e^{-jk(x_p - x)} \int_{h_1}^{\infty} u_1(x, z) \frac{e^{-jk(x_p - x)\psi^2 / (1 + \sqrt{1 + \psi^2})}}{[1 + \psi^2]^{2 \cdot 3/4}} dz \\ &= \int_{h_1}^{\infty} u_1(x, z) v_1(x_p - x, z_p - z) dz \quad (4.6) \end{aligned}$$

where

$$\psi = \psi(z) = \frac{z_p - z}{x_p - x}$$

and $v_1(x_p - x, z_p - z)$ represents the field at (x_p, z_p) due to a cylindrical source at (x, z) . v_1 is sometimes called the propagator. For most propagation links ψ is much less than one and then we have the approximation

$$u(x_p, z_p) = \left[\frac{j}{\lambda(x_p - x)} \right]^{1/2} e^{-jk(x_p - x)} \int_{h_1}^{\infty} u_1(x, z) e^{-jk(x_p - x)\psi^2/2} dz \quad (4.7)$$

In essentially this form the Huyghens' principle was applied to the case of two knife edges by Millington et al [1962].

For the single knife edge consider the case where the incident field is a cylindrical field from a source at (x_s, z_s) ,

$$\begin{aligned} u_1(x, z) &= \left[\frac{-j\pi}{2} \right]^{1/2} H_0^{(1)} \left(k \sqrt{(x-x_s)^2 + (z-z_s)^2} \right) \\ &= \frac{e^{-jk\sqrt{(x-x_s)^2 + (z-z_s)^2}}}{\sqrt{k} [(x-x_s)^2 + (z-z_s)^2]^{1/4}} \end{aligned}$$

Assuming again that the angles are small ($z-z_s \ll x-x_s$) we have

$$u_1(x, z) \sim e^{-jk(x-x_s)} e^{-jk \frac{(z-z_s)^2}{2(x-x_s)}} / \sqrt{k(x-x_s)} .$$

Hence

$$u(x_p, z_p) = \frac{e^{j\pi/4}}{\sqrt{2\pi}} \frac{e^{-jk(x_p-x_s)}}{\sqrt{(x-x_s)(x_p-x)}} \int_{h_1}^{\infty} dz \exp\left[-jk\left(\frac{(z-z_s)^2}{2(x-x_s)} + \frac{(z_p-z)^2}{2(x_p-x)}\right)\right]$$

and the attenuation due to the edge is found to be

$$\frac{u(x_p, z_p)}{u_1(x_p, z_p)} = F(\theta) \sqrt{\frac{k(x-x_s)(x_p-x)}{2(x_p-x_s)}} \quad (4.8)$$

where

$$F(x) = \frac{e^{j\pi/4}}{\sqrt{\pi}} \int_x^{\infty} e^{-jt^2} dt$$

is the Fresnel integral and θ is the diffraction angle,

$$\theta = (z-z_s)/(x-x_s) + (z-z_p)/(x_p-x).$$

This is the usual single knife edge solution. Deep in the lit zone $F(x) \sim 1$ as would be expected since the obstacle can then be ignored. At the transition we have $F(0)=1/2$ corresponding to a 6 dB attenuation independent of range. In the deep shadow region we get

$$u(x_p, z_p) \sim \frac{e^{-jk\left(x-x_s + \frac{(h_1-z_s)^2}{2(x-x_s)}\right)}}{\sqrt{k(x-x_s)}} \cdot \frac{e^{-jk\left(x_p-x + \frac{(z_p-h_1)^2}{2(x_p-x)}\right)}}{\sqrt{k(x_p-x)}} \cdot D(\theta)$$

(4-9)

where the first term is the cylindrical field from the source to the first edge and the second term is the field at the receiving point (x_p, z_p) due to a cylindrical source at the edge. The factor $D(\theta)$ is Keller's diffraction coefficient. Geometrical optics can be extended in this case by including the diffracting ray and the diffraction coefficient. The coefficient $D(\theta)$ is given by

$$D(\theta) = \frac{e^{-j\pi/4}}{\theta\sqrt{2\pi}}$$

(4.10)

The Geometrical Theory of Diffraction uses (4.9) iteratively on successive edges. This technique is successful only when in the deep shadow zone of all the edges. Near the transition region it breaks down since $D(\theta) \rightarrow \infty$ as $\theta \rightarrow 0$. A number of uniform asymptotic techniques for single edge diffraction [Ahluwalia et al., 1968; Kouyoumjian and Pathak, 1974] have been developed that avoid this difficulty. A generalization of the Uniform Geometrical Theory of Diffraction (UGTD) of Kouyoumjian and Pathak [1974] for the treatment of multiple edge diffraction is discussed in Section 4.4.

4.2.2 Iterative Computational Technique for Multiple Edges

The numerical evaluation of (4.6) and (4.7) requires a truncation of the infinite integral and a Riemann sum approximation to the resulting finite limit integral.

A truncation of the integral is equivalent to approximating the edge by a slit as shown in Figure 4-4. If an artificial obstacle in the form of an upside down knife edge is introduced, the lobes caused by a reflection from the artificial obstacle can distort the waveform at the receiver. It is therefore practical to use a window function to eliminate most of the reflection from the upper obstacle. Another way of looking at this is to perform a weighted average of knife edges located at various heights above the actual obstacle. Assume a window function, $w(z; h_{1a}, h_{1b})$ which satisfies

$$w(z) = \begin{cases} 1 & \text{for } z < h_{1a} < h_{1b} \\ 0 & \text{for } z > h_{1b} \end{cases} .$$

ARTIFICIAL OBSTACLE TO LIMIT
RANGE OF INTEGRATION

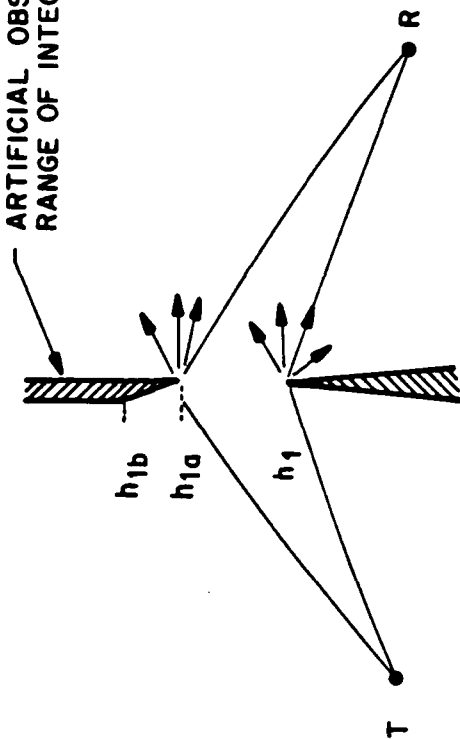


Figure 4-4 Finite Opening Approximation

For the numerical examples in this section, a raised cosine window is assumed. With the window function we have the approximation to (4.6),

$$u(x_p, z_p) \sim \int_{h_1}^{h_{1b}} w(z; h_{1a}; h_{1b}) u_1(x, z) v_1(x_p - x, z_p - z) dz . \quad (4.11)$$

where h_{1b} is usually large enough when it is several Fresnel zones removed from h_1 (or from the LOS ray if in the lit zone). The convolution in (4.11) is best implemented with an FFT, but care must be taken when approximating (4.11) by a finite sum. Let us assume that the step size δ is small enough so that the incident field $u_1(z)$ does not vary much between adjacent samples $z = n\delta$ and $z = (n+1)\delta$. Assume also that the magnitude of v_1 in (4.6) is slowly varying (which it is) but that the phase may have a linear dependence on z between samples. In other words approximate $v_1(x_p - x, z_p - z)$ in the vicinity of $z = z_n \triangleq h_1 + n\delta$ by

$$v_1(x_p - x, z_p - z_n - z') \sim v_1(x_p - x, z_p - z_n) \exp\left(\frac{-jk\psi_n}{1 + \sqrt{1 + \psi_n^2}} 2z'\right)$$

where

$$\psi_n = (z_p - z_n) / (x_p - x) .$$

Hence

$$u(x_p, z_p) \sim \sum_{n=0}^{N-1} w(z_n; h_{1a}, h_{1b}) u_1(x, z_n) v_1(x_p - x, z_p - z_n) \delta \frac{\sin U_n}{U_n} \quad (4.12)$$

where

$$\delta = (h_{1b} - h_1) / (N-1)$$

and

$$U_n = \frac{k \psi_n \delta}{1 + \sqrt{1 + \psi_n^2}} \sim k \psi_n \delta / 2$$

It is convenient to define

$$v_2(x_p - x, z_p - z_n) = v_1(x_p - x, z_p - z_n) \sin U_n(z_p - z_n) / U_n(z_p - z_n)$$

The numerical approximation (4.12), although looking rather formidable, is relatively easy to evaluate with an FFT. It is simply a discrete convolution of w , u_1 and v_2 . Let U and V be two $2N$ dimensional complex vectors and fill U_{n1} $n = 0, \dots, N-1$ with the N weighted samples of the incident field u_1 and fill the rest of U with zeros,

$$U_n = \begin{cases} w(z_n; h_{1a}, h_{1b}) u_1(x, z_n) & n = 0, 1, \dots, N-1 \\ 0 & n = N, \dots, 2N-1 \end{cases}$$

Next fill the V vector with the samples from the v_2 function,

$$V_n = \begin{cases} v_2(x_p - x, h_2 - h_1 + n\delta) & , \quad \text{for } n = 0, 1, \dots, N-1 \\ v_2(x_p - x, h_2 - h_1 + (n-2N)\delta) & , \quad \text{for } n = N, N+1, \dots, 2N-1 \end{cases}$$

where h_2 is the height of the next edge at $x = x_p$.

Then

$$u(x_p, h_2 + m\delta) = \text{INV.FFT}\{\text{FFT}\{U\} \text{FFT}\{V\}\} . \quad (4.13)$$

With a $2N$ -point FFT the field at n points above the observation point (x_p, h_2) can then be calculated from the field at the N points above the edge at (x, h_1) . This can be used iteratively to compute the field over several knife edges. This technique is similar to that of Vogler (1982). Vogler uses a more efficient complex integration path that reduces to repeated integrals of the error function. The advantage of the technique described here is that the integration is over real physical rays, simplifying the interpretation of the results and the extension to non-knife edges.

With N edges an $N-1$ fold integration is required. If infinitely many edges are introduced the integration reduces to a Feynman path integral. This point of view can be quite illuminating. Consider a number of edges and assume that they are all significant, i.e., that each edge is in the shadow of the previous edge or at least is close to the transition region. Figure 4-5 shows an example with 4 edges where the shortest path over the edges is drawn. We can now consider rays with a slightly longer path length, say $\lambda/2$. This yields the rays within the first Fresnel tube around the shortest path. It is intuitively clear that the integral over all paths connecting transmitter and receiver can be approximated by including only the first N Fresnel tubes, or rays within $N\lambda/2$ of the shortest rays. When many edges are involved, this gives us a good way to pick the upper limit h_{1b} in the truncated integration at each edge: simply use the upper limit of the N 'th Fresnel tube.

4.2.3 Numerical Comparison with the Results of Vogler [1982]

As a check on the accuracy of the technique consider some cases also evaluated by Vogler [1982]. The first case (Figure 2 in Vogler's paper) is a 30 km link with three knife edges. The first is 10 km from the transmitter and 100 meters high. The second is 15 km from the transmitter and varies in height. The third edge is 20 km from the transmitter and 100 meters high. The frequency is 100 MHz. The results of the iterative technique are shown in Figure 4-6. It shows the diffraction loss which is defined as the total loss relative to normal line-of-sight. It is found using up to the 20th Fresnel tube with a varied cosine window on the 10th to 20th tube, using the truncation windowing technique described in the previous section. The results agree with Vogler's. Note that maximum signal strength is achieved for $h_2 = 270$ m, where the middle obstacle is so high that it has direct line-of-sight to both transmitter and receiver. This is

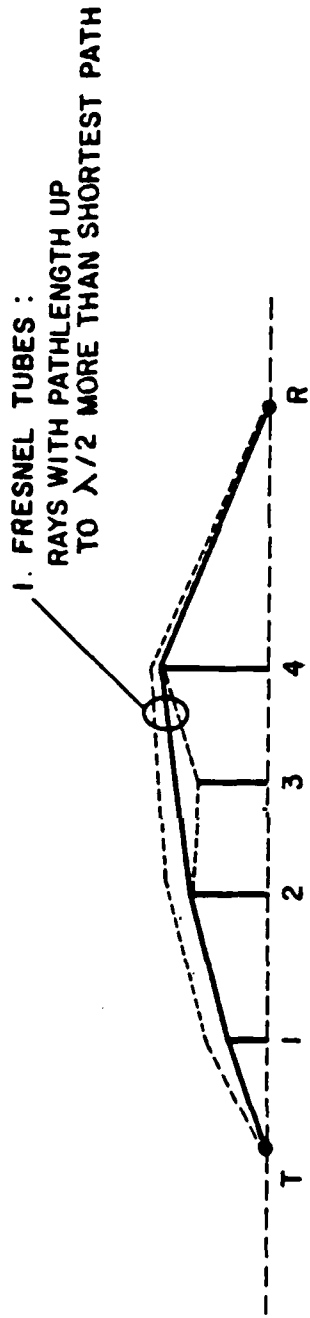


Figure 4-5 Multiple Edge Path Integration

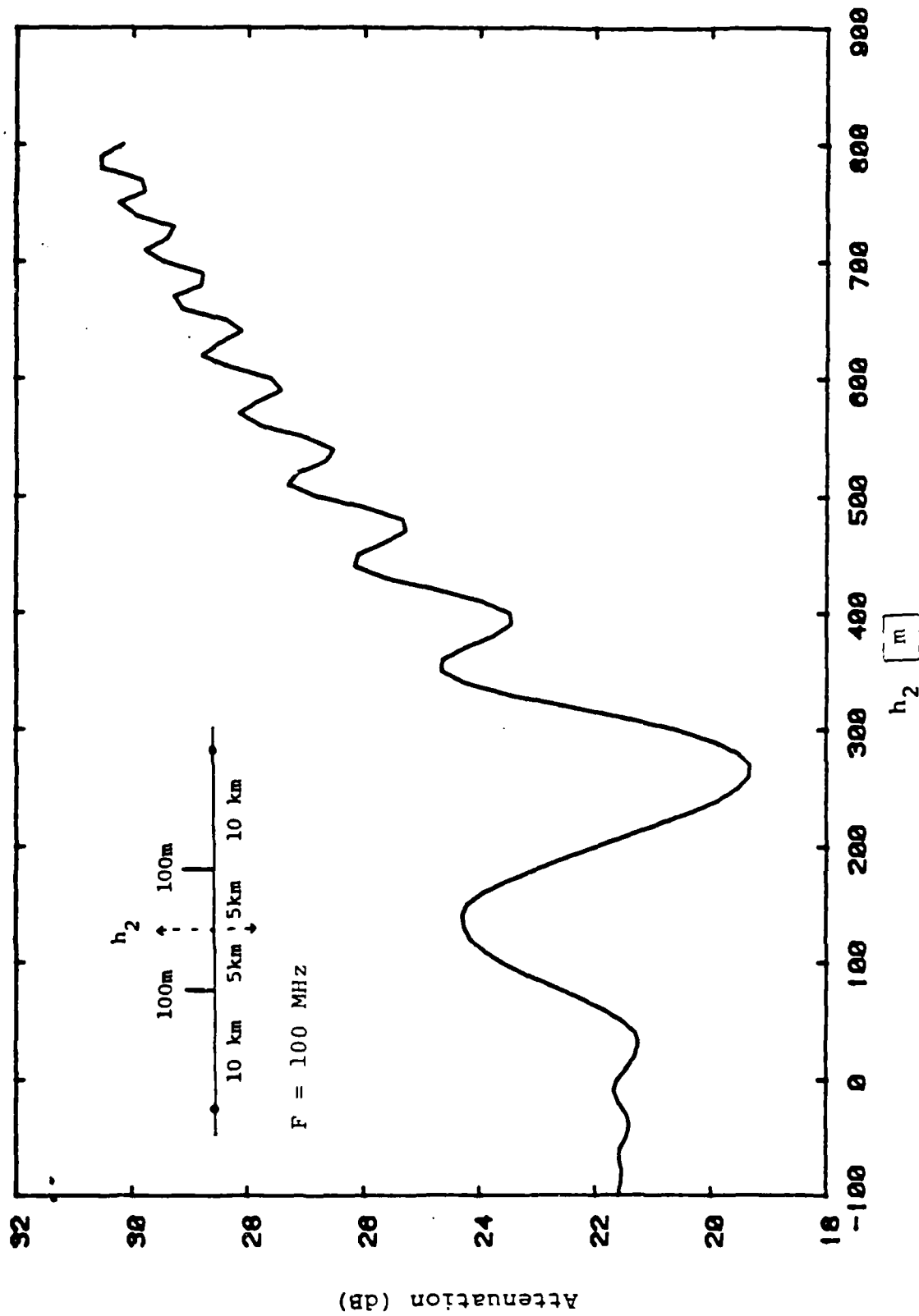


Figure 4-6 Attenuation vs. height of middle knife edge in Vogler's 3-knife edge example.

an example of the situation mentioned in the introduction, that introducing an obstacle can actually improve performance. When h_2 is high the result approaches that of a single knife edge, while for small h_2 only the attenuation of the two fixed obstacles is observed.

Figure 4-7 reproduces the results of Figure 3 in Vogler (1982) using the technique in 4.2.2. This is for a 50 km link at 500 MHz with N obstacles with distances

$$d_n = \frac{n}{N} 42 \text{ km} , \quad n = 1, 2, \dots, N$$

and heights

$$h_n = \frac{n}{N} 420 \text{ m} , \quad n = 1, 2, \dots, N$$

The diffraction loss is shown as a function of the height of the receiver.

These results validate the iterative technique described in Section 4.2.2. In Section 4.2.5 it will be shown how the technique can be extended to include ground reflections and approximate rounded edges.

4.2.4 The Double-Knife Edge Case, and Other Special Cases

It may be instructive to summarize the results for two edges, and also describe special cases where an analytical solution is possible.

Consider the 2-edge geometry in Figure 4-8. By repeated use of (4.7) we get

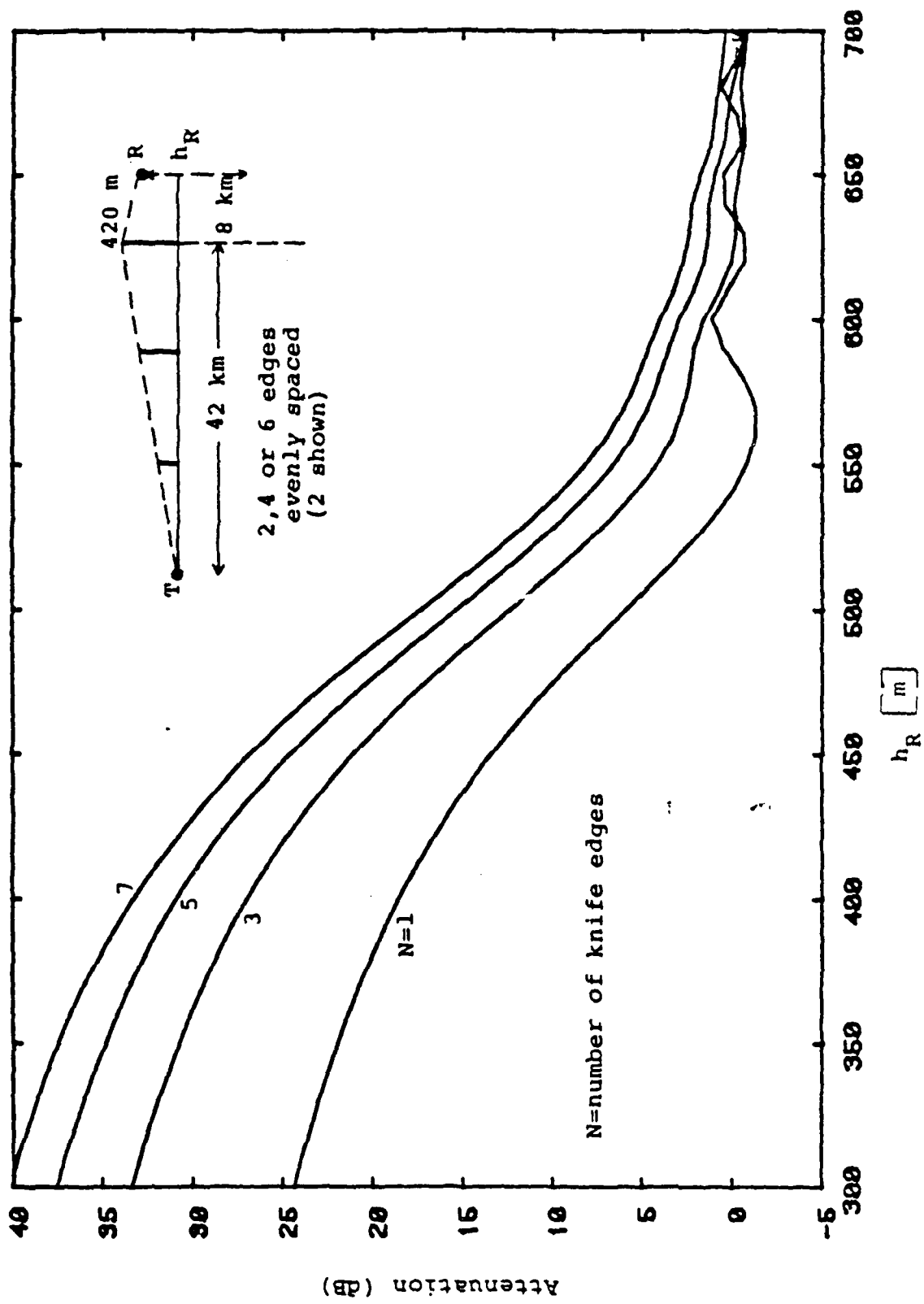


Figure 4-7 Attenuation versus receiver heights h_R for a 50 km path and various numbers of knife edges on a line through the transmitter.

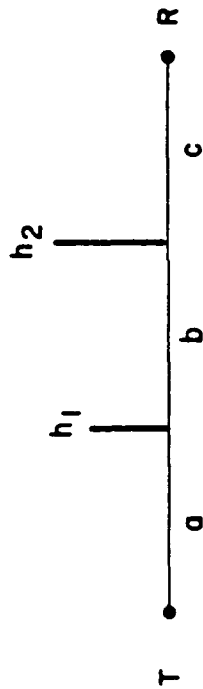


Figure 4-8 2-Knife Edge Geometry

$$U(a+b+c, 0) = \frac{j\sqrt{k}}{2\pi} \frac{e^{-jk(a+b+c)}}{\sqrt{abc}} \int_{h_1}^{\infty} dz_1 \int_{h_2}^{\infty} dz_2 \exp\left[-\frac{jk}{2} z^2\right]$$

which is the expression used by Millington et al. it is possible to get an asymptotic expression geometry, a much simpler uniformly valid exp possible. The diffraction loss relative to LOS is

$$A = \frac{jk}{2\pi} \sqrt{\frac{a+b+c}{abc}} I,$$

where I is the integral above. Following Milling this can be written as

$$A = \frac{jk}{\pi} \int_{r_0}^{\infty} dr r (\phi_2(r) + \phi_1(r)) e^{-jkr^2}$$

where r_0 is the distance detour, the length of the path over the edges relative to the straight line between transmitter and receiver.

$$r_0 = \sqrt{\frac{h_1^2}{2a} + \frac{(h_1 - h_2)^2}{2b} + \frac{h_2^2}{2c}},$$

$$\phi_1(r) = \psi_1 - \text{Arccsin}\left[\frac{r_0}{r} \sin \psi_1\right]$$

$$\phi_2(r) = \psi_2 - \text{Arccsin}\left[\frac{r_0}{r} \sin \psi_2\right]$$

and

$$\sin \psi_1 = \frac{h_2}{r_0} \left[\frac{a+b+c}{2c(a+b)} \right]^{1/2} ,$$

$$\sin \psi_2 = \frac{h_1}{r_0} \left[\frac{a+b+c}{2a(c+b)} \right]^{1/2} .$$

The integral can be evaluated numerically in terms of the function

$$G(r_0, \alpha) \equiv \int_{r_0}^{\infty} t \left[\alpha - \text{Arcsin} \left(\frac{r_0}{t} \sin \alpha \right) \right] e^{-jkt^2} dt, \quad (4.14)$$

yielding the diffraction attenuation

$$A = \frac{jk}{\pi} \{ G(r_0, \psi_2) + G(r_0, \psi_1) \} . \quad (4.15)$$

A few special cases can be evaluated directly:

(i) $h_1=h_2=0$ (T-R line just grazing both edges)

then

$$r_0 \sim 0$$

and

$$\begin{aligned} A &= \frac{1}{2\pi}(\psi_1 + \psi_2) \\ &= \frac{1}{2\pi} \left[\pi - \text{Arctan} \left[\frac{b(a+b+c)}{ac} \right]^{1/2} \right], \end{aligned} \quad (4.16)$$

a result first found by Millington et al [1962]. Simply squaring the single edge result would indicate a 12 dB loss independent of a, b , and c . It is seen that the actual loss is between 6 dB (b small) and 12 dB ($b \gg a, b \gg c$).

(ii) $ac = b(a+b+c)$

and

$$h_1 = h_2 \frac{a}{a+b} > 0 \quad (\text{edges lined up with transmitter}).$$

In this case we have $\psi_1 = \frac{\pi}{2}$, $\psi_2 = \pi$ so that

$$A = F(0)F(\sqrt{k} r_0) + \frac{1}{2} F^2(\sqrt{k/2} r_0)$$

when $F(x)$ is the Fresnel integral in (4.8)

(iii) $b \gg a, c$ (Edges far apart)

so
$$\psi_1 + \psi_2 = \pi/2 .$$

Then

$$A = F(\sqrt{k} J_{012})F(\sqrt{k} J_{123})$$

where J_{012} is the distance detour over edge 1, going from 0 to 2,

$$J_{012}^2 = \sqrt{a^2 h_1^2} + \sqrt{b^2 (h_2 - h_1)^2} - \sqrt{(a+b)^2 + h_2^2}$$

and similarly

$$J_{123}^2 = \sqrt{c^2 + h_2^2} + \sqrt{b^2 + (h_2 - h_1)^2} - \sqrt{(c+b)^2 + h_1^2} .$$

This is simply the repeated application of the single edge result in (4.8). The GTD solution is therefore valid in this case.

(iv) Asymptotic solution ($r_0\sqrt{k}$ large) .

Even for large values of the detour parameter r_0 we have
[Millington et al., 1962]

$$G(r_0, \alpha) \sim -\tan(\alpha) e^{-jkr_0^2} / (2kr_0)^2 .$$

Then

$$\begin{aligned} A &= \frac{-j}{4\pi k} \frac{e^{-jkr_0^2}}{r_0^2} (\tan \psi_1 + \tan \psi_2) \\ &= \frac{-j}{4\pi k} e^{-jkr_0^2} \frac{\sin(\psi_1 + \psi_2)}{(r_0 \cos \psi_1)(r_0 \cos \psi_2)} . \end{aligned}$$

If θ_{012} is the diffraction angle at the first edge,
and θ_{123} is the diffraction angle at the second edge, then

$$r_0 \cos \psi_1 = \theta_{012} \left[\frac{ab}{2(a+b)} \right]^{1/2}$$

and

$$r_0 \cos \psi_2 = \theta_{123} \left[\frac{cb}{2(c+b)} \right]^{1/2} .$$

since

$$\sin(\psi_1 + \psi_2) = \left[\frac{b(a+b+c)}{(a+b)(c+b)} \right]^{1/2},$$

we get

$$A \sim e^{-jkr_0^2} \sqrt{\frac{k(a+b+c)}{(ka)(kb)(kc)}} D(\theta_{012}) D(\theta_{123}) \quad (4.17)$$

where the diffraction coefficients are given by (4.10). This expresses the loss of cylindrical propagation to the first edge, followed by cylindrical propagation from the first to the second edge and finally from the second edge to the receiver, relative to a free space ray directly from transmitter to receiver. This result is the basis of the GTD solution discussed in Section 4.2.

(v) For a triple knife edge link Vogler (1982) has found the following exact result for the case of $h_1=h_2=h_3=0$ (LOS ray grazing all edges):

$$\begin{aligned}
A(3) &= (1/4\pi) \left[\frac{\pi}{2} + \tan^{-1} a_1 + \tan^{-1} \left(\frac{t}{(A^2 - t^2)^{1/2}} \right) \right]_{t_0}^1 \\
&= (1/4\pi) \left[\frac{\pi}{2} + \tan^{-1} a_1 + \tan^{-1} a_2 \right. \\
&\quad \left. + \tan^{-1} \left(\frac{a_1 a_2}{(1 + a_1^2 + a_2^2)^{1/2}} \right) \right] \\
&= (1/4\pi) \left[\frac{\pi}{2} + \tan^{-1} (\alpha_1 / C_3) + \tan^{-1} (\alpha_2 / C_3) \right. \\
&\quad \left. + \tan^{-1} (\alpha_1 \alpha_2 / C_3) \right] .
\end{aligned}$$

In this expression we have

$$a_i = \alpha_i / C_3, \quad i = 1, 2 .$$

$$\alpha_1^2 = \frac{r_{01} r_{23}}{r_{02} r_{13}}$$

$$\alpha_2^2 = \frac{r_{12} r_{34}}{r_{13} r_{24}}$$

$$C_3^2 = \frac{r_{12} r_{23} r_{04}}{r_{02} r_{13} r_{24}}$$

and r_{nm} is the distance between edge no. n and edge no. m , where 0 indicates the transmitter and 4 indicates the receiver.

4.2.5 Extension of the Computational Technique to Include Ground Reflections

The repeated use of the Huyghen's Principle in Section 4.2.2 assumes there are no foreground reflections. Such reflections play a key role in the diffraction over rounded obstacles. The basic assumption we need to make is again that there is no backscattering. We need to introduce the Green's function $G(\underline{r}_s, \underline{r}_p)$. Referring to Figure 4-9 we place a source at the point Q and a receiver at the point P_1 , on opposite sides of the interface S and above the obstacle surface B. $G(\underline{r}_s, \underline{r}_p)$ is the field at \underline{r}_p due to a monopole at \underline{r}_s , subject to the boundary conditions on B. The Green's function satisfies

Reciprocity: $G(\underline{r}_s, \underline{r}_p) = G(\underline{r}_p, \underline{r}_s)$

Wave equations: $\nabla_p^2 G(\underline{r}_s, \underline{r}_p) + k^2 G(\underline{r}_s, \underline{r}_p) = -\delta(\underline{r}_p - \underline{r}_s)$

Boundary conditions: $\alpha(\underline{r}_p)G(\underline{r}_s, \underline{r}_p) + \beta(\underline{r}_p)\frac{\partial}{\partial n(\underline{r}_p)}G(\underline{r}_s, \underline{r}_p) = 0; \underline{r}_p \text{ on } B$

where n is the normal to the boundary.

Let $u(\underline{r})$ be the field at \underline{r} . For simplicity a scalar field is assumed, this could be the vertically polarized component of the field, for instance.

From the wave equation for G and u we get by integrating over the volume V enclosed by S and the boundary B,

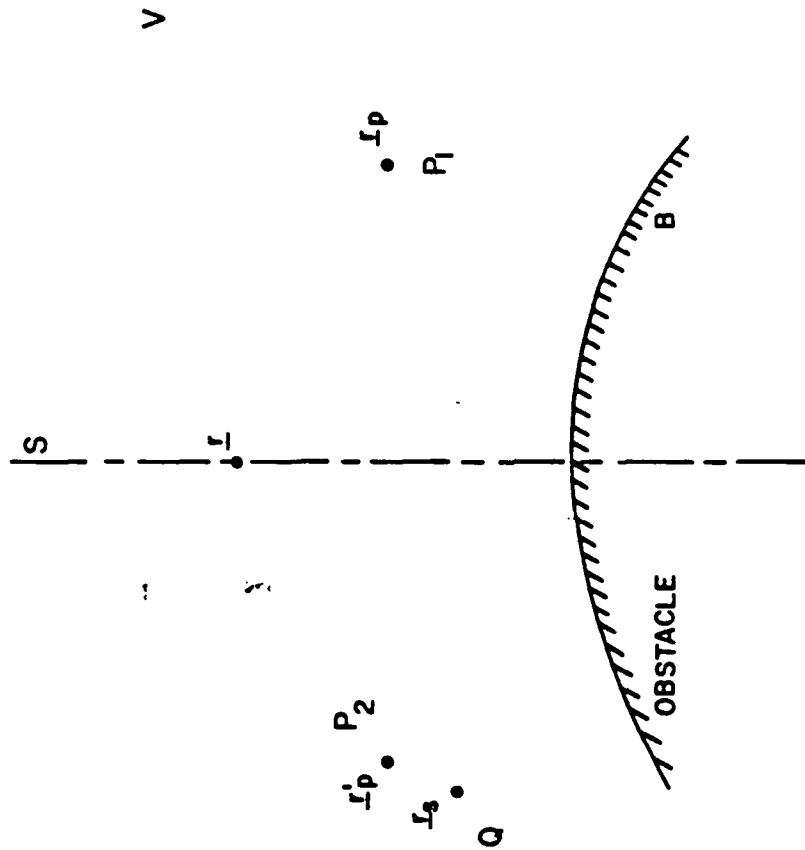


Figure 4-9 Fields over a Curved Obstacle

$$\int_V u(\underline{r}) \nabla_S^2 G(\underline{r}, \underline{r}_p) - G(\underline{r}, \underline{r}_p) \nabla^2 u(\underline{r}) d\underline{r} \quad (4.18)$$

$$= - \int_V u(\underline{r}) \delta(\underline{r} - \underline{r}_p) d\underline{r}_S$$

$$= -u(\underline{r}_p) \quad .$$

From Green's Formula, (4.18) reduces to a surface integral over S and B,

$$u(\underline{r}_p) = - \int_{S+B} u(\underline{r}) \frac{\partial G(\underline{r}, \underline{r}_p)}{\partial n(\underline{r})} - G(\underline{r}, \underline{r}_p) \frac{\partial u(\underline{r})}{\partial n(\underline{r})} d\underline{r} \quad .$$

On B both $u(\underline{r})$ and $G(\underline{r}, \underline{r}_p)$ satisfy a homogeneous boundary condition of the form

$$\alpha(\underline{r})u(\underline{r}) + \beta(\underline{r})\frac{\partial u(\underline{r})}{\partial n(\underline{r})} = 0 \quad .$$

The integral over B is therefore zero, and we get

$$u(\underline{r}_p) = - \int_S u(\underline{r}) \frac{\partial G(\underline{r}, \underline{r}_p)}{\partial n(\underline{r})} - G(\underline{r}, \underline{r}_p) \frac{\partial u(\underline{r})}{\partial n(\underline{r})} d\underline{r} \quad (4.19)$$

This expresses the field at \underline{r}_p in terms of the field on the interface S. It assumes there are no sources in the volume V and that the observation point \underline{r}_p is inferior to V. It is similar to

(4.3) except that both u and $\partial u/\partial n$ must be known on S . However, we assume that the part of the obstacle on the source side of S does not affect the field at P_1 when the field on S is known. In other words, backscatter is ignored. Assume S is a plane surface. The obstacle can then be assumed to be symmetric with respect to S .

For a symmetric obstacle, calculate the field at P_2 where P_2 and P_1 are symmetric points relative to the plane S . Since both Q and P_2 are outside the volume V we have

$$0 = \int_S u(\underline{r}) \frac{\partial G(\underline{r}, \underline{r}'_p)}{\partial n(\underline{r})} - G(\underline{r}, \underline{r}'_p) \frac{\partial u(\underline{r})}{\partial n(\underline{r})} d\underline{r} \quad (4.20)$$

By symmetry we have that

$$G(\underline{r}, \underline{r}'_p) = G(\underline{r}, \underline{r}_p)$$

and

$$\frac{\partial G(\underline{r}, \underline{r}'_p)}{\partial n(\underline{r})} = - \frac{\partial G(\underline{r}, \underline{r}_p)}{\partial n(\underline{r})} \quad .$$

Inserting this in (4.20) and subtracting the result from (4.19) yields

$$u(\underline{r}_p) = -2 \int_S u(\underline{r}) \frac{\partial}{\partial n(\underline{r})} G(\underline{r}, \underline{r}_p) \partial \underline{r} \quad (4.21)$$

This is the generalization of (4.3). Without the ground reflection the Green's function is simply

$$G(\underline{r}, \underline{r}_p) = v(\underline{r})$$

where $v(\underline{r})$ is given by (4.2).

When the surface B is plane the Green's function is

$$G(\underline{r}, \underline{r}_p) = v(\underline{r}) + \rho(\theta)v(\underline{r}')$$

where r' is the point \underline{r} reflected in the surface B, and $\rho(\theta)$ is the reflection coefficient. This is illustrated in Figure 4-10. Let ϕ be the slope of the ground,

$$\tan\phi = (h_2 - h_1) / (x_p - x) .$$

The grazing angle at the point of reflection is θ , where

$$\tan(\theta + \phi) = \frac{(z_p - h_1) + (z - h_1)\cos 2\phi}{(x_p - x) - (z - h_1)\sin 2\phi} .$$

Eq. (4.6) is then generalized to

$$u(x_p, z_p) = \int_{h_1}^{\infty} u(x, z) [v_1(x_p - x, z_p - z) + \rho(\theta)v_1(x_p - x', z_p - z')] dz \quad (4.22)$$

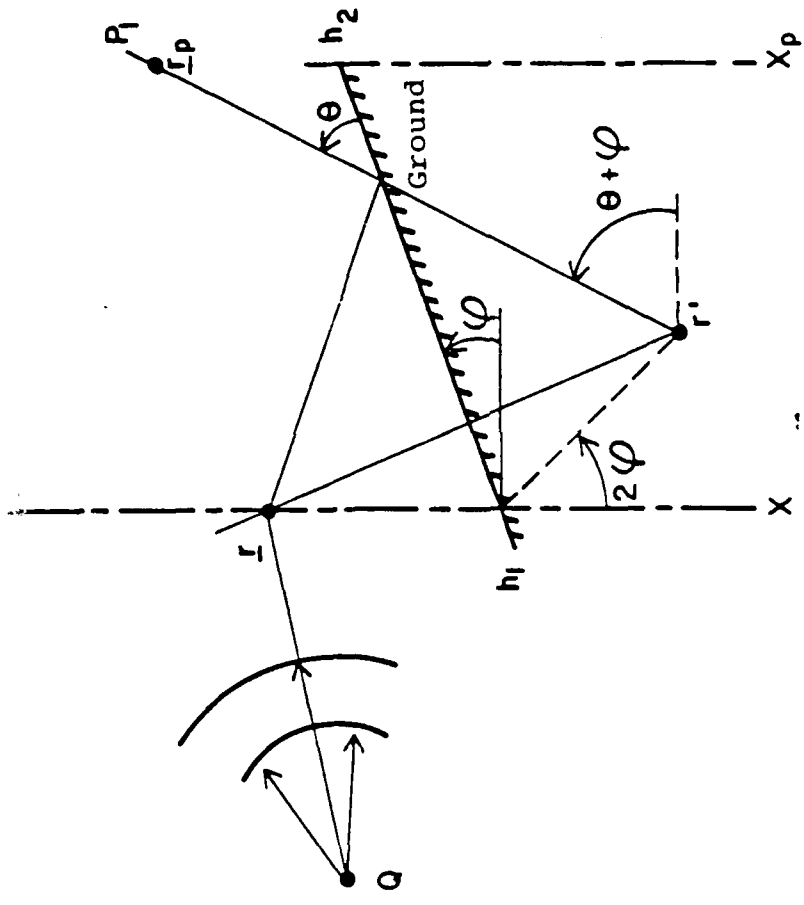


Figure 4-10 Ground Reflection Geometry

where

$$\begin{aligned}x' &= x+(z-h_1)\sin 2\theta \\z' &= h_1-(z-h_1)\cos 2\theta.\end{aligned}$$

Eq. (4.12) is similarly generalized, but the integral in (4.22) is no longer a convolution so the FFT solution is not directly applicable. However, in practice only points with a small grazing angle θ will contribute. It is therefore possible to do the integration in (4.22) on a point by point basis.

The reflection coefficient $\rho(\theta)$ can be found from most text books on electromagnetic propagation. For a smooth earth we have for vertical polarization [Beckmann and Spizzichino, 1963]

$$\rho_V(\theta) = \frac{Y^2 \sin \theta - \sqrt{Y^2 - \cos^2 \theta}}{Y^2 \sin \theta + \sqrt{Y^2 - \cos^2 \theta}} \quad (4.23)$$

and for horizontal polarization

$$\rho_H(\theta) = \frac{\sin \theta - \sqrt{Y^2 - \cos^2 \theta}}{\sin \theta + \sqrt{Y^2 - \cos^2 \theta}} \quad (4.24)$$

where Y is the normalized ground admittance

$$Y^2 = \frac{\epsilon}{\epsilon_0} - i 60 \lambda \sigma, \quad (4.25)$$

ϵ = dielectric constant of the ground,

σ = conductivity of the ground.

AD-A143 762

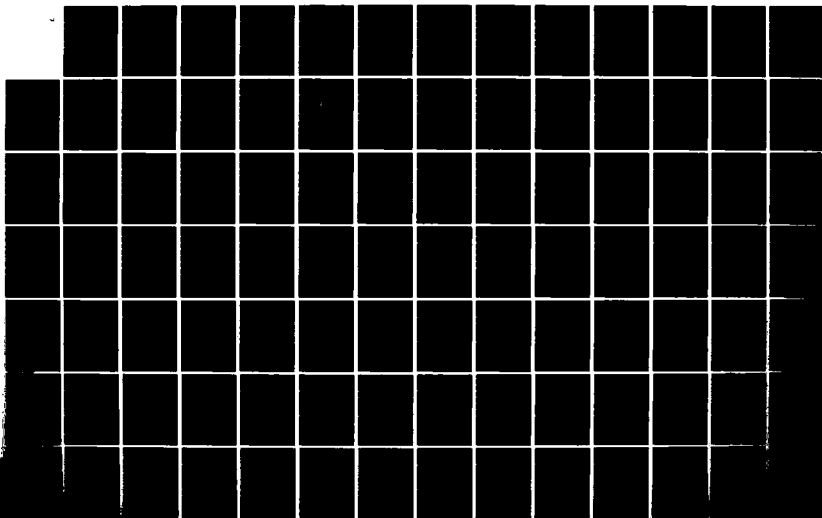
THEORETICAL ANALYSIS OF MICROWAVE PROPAGATION(U)
SIGNATRON INC LEXINGTON MA S PARL ET AL. APR 84
RADC-TR-84-74 F19628-88-C-0106

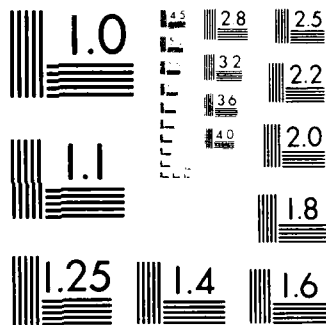
3/5

UNCLASSIFIED

F/G 28/14

NL





MICROCOPY RESOLUTION TEST CHART
NATIONAL BUREAU OF STANDARDS-1963-A

Typical values are $\epsilon/\epsilon_0=10$ and $\sigma=10^{-3}$ mho/m for ground, and $\epsilon/\epsilon_0=80$ and $\sigma=10^{-3}$ mho/m for the sea. At microwave frequencies it is usually reasonable to ignore the conductivity. Figure 4-11 shows the horizontal and vertical reflection coefficients at various wavelengths.

When the surface is rough the power in the specular reflection is reduced in favor of a diffusely scattered component. The specular reflection coefficient due to surface roughness can be modeled as [Beckmann and Spizzichino, 1963]

$$\rho_s^2 = \exp\left[-\left(\frac{4\pi\sigma_h\sin\theta}{\lambda}\right)^2\right] \quad (4.26)$$

where

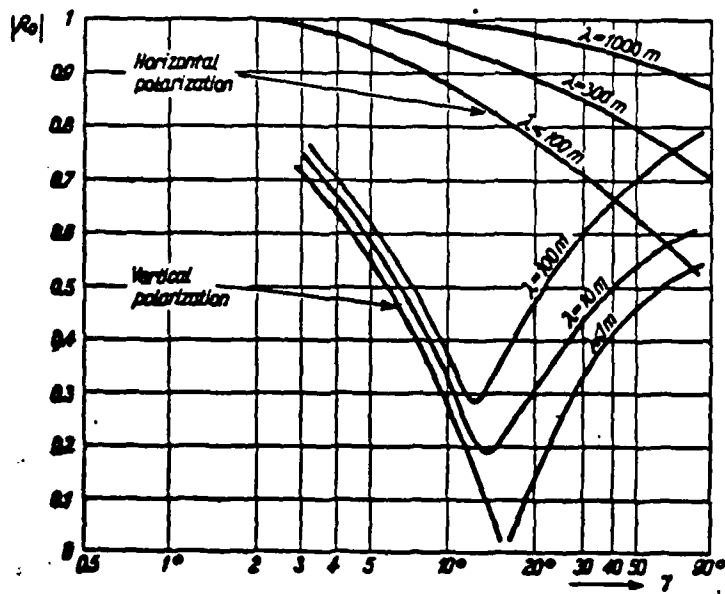
σ_h = rms standard deviation of the surface height.

The total reflection coefficient is

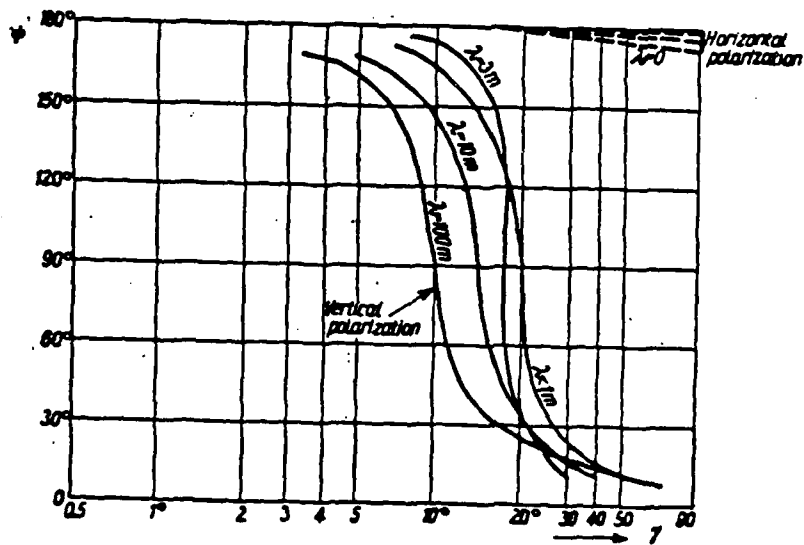
$$\rho(\theta) = \rho_{H,V}(\theta)\rho_s(\theta) .$$

4.2.6 Diffraction Over a Flat-Top

By incorporating the ground reflection we can determine the diffraction loss over a square topped edge (Figure 4-12). The example in Figure 4-12 was chosen to match the experimental results by Hacking [1970]. In that paper scale models of the obstacles were used to measure directly the diffraction loss.



(a) Magnitude



(b) Phase

Figure 4-11 Reflection coefficient of a perfectly plane earth with $\epsilon/\epsilon_0 = 10, \sigma = 10^{-3}$ mho/m [Beckmann and Spizzichino, 1963]

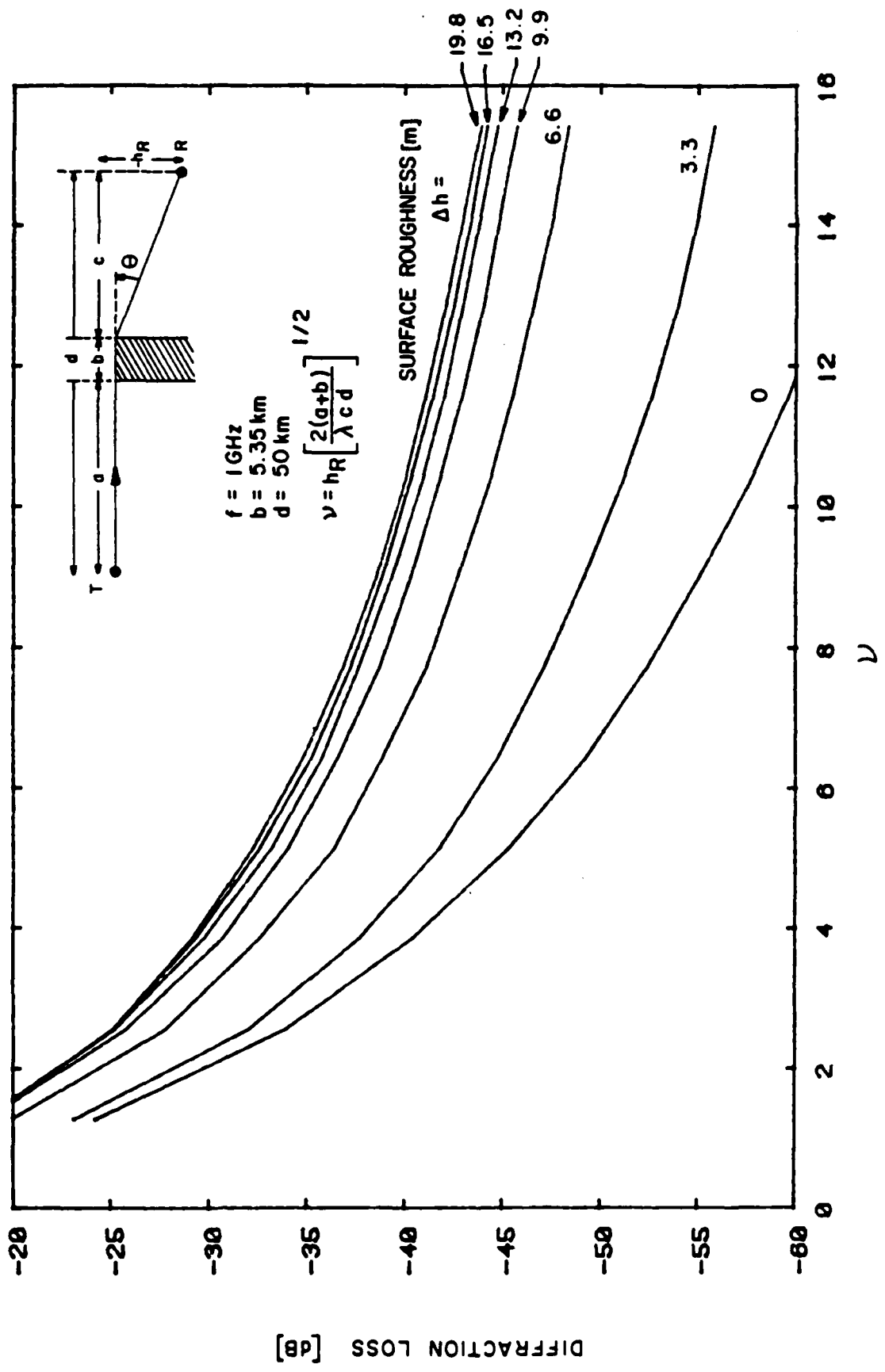


Figure 4-12 Diffraction over Square-Topped Edge

Figure 4-12 shows the diffraction loss, relative to the unobstructed field, as a function of the Fresnel parameter v . For a smooth edge ($\Delta h = 0m$) the results match the theoretical predictions in Figure 18 in Hacking's paper, but predict a larger loss than measured (6 dB more for $v = 7$). This can be attributed to the difficulties of producing a perfectly smooth surface, and other measurement difficulties at high diffraction losses. The measurements agree with the theory in Figure 4-12 for small v ($v < 5$). Hacking also presented a set of measurements for the diffraction loss due to a rough edge, with $\Delta h = 3.3m$ at 1 GHz. The prediction of the diffraction loss in Figure 4-12 shows about 5 dB more loss than measured at $v = 10$, but the measurements would match the prediction if the latter were performed for $\Delta h \sim 5m$. This shows that surface roughness is extremely important for the prediction of microwave diffraction losses, and also that the smooth edge model often used in prediction techniques such as NBS or CCIR are very inaccurate at microwave frequencies.

4.2.7 The Computational Technique with Straight Line Approximations to Rounded Edges

Diffraction over rounded edges is frequently studied in the literature. At microwave frequencies a completely smooth and rounded profile is unlikely to occur, but it is a good verification of the computational technique to consider the diffraction loss due to a rounded edge.

A rounded obstacle can be approximated by a series of inner or outer chords. Due to the excessive computer time required we have been unable to get a consistently good approximation to a rounded edge this way. However, it is interesting to note that a properly scaled flat-top obstacle will have approximately the same loss as a rounded obstacle. Figure 4-13 illustrates a rounded edge and the flat topped square edge approximation. Figure 4-14 shows the diffraction loss as a function of the parameter

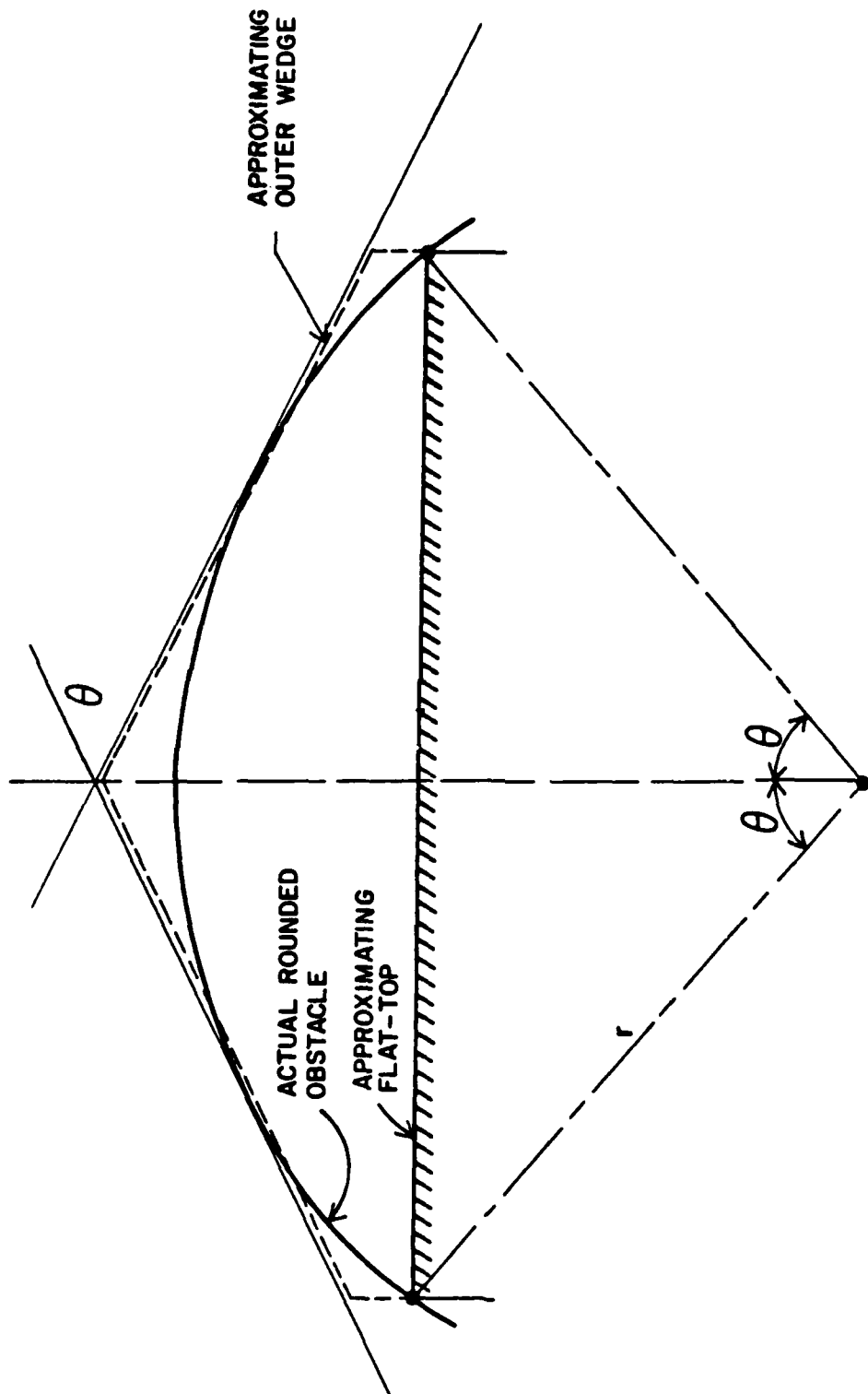


Figure 4-13 Flat-top and Wedge Approximations to a Rounded Edge

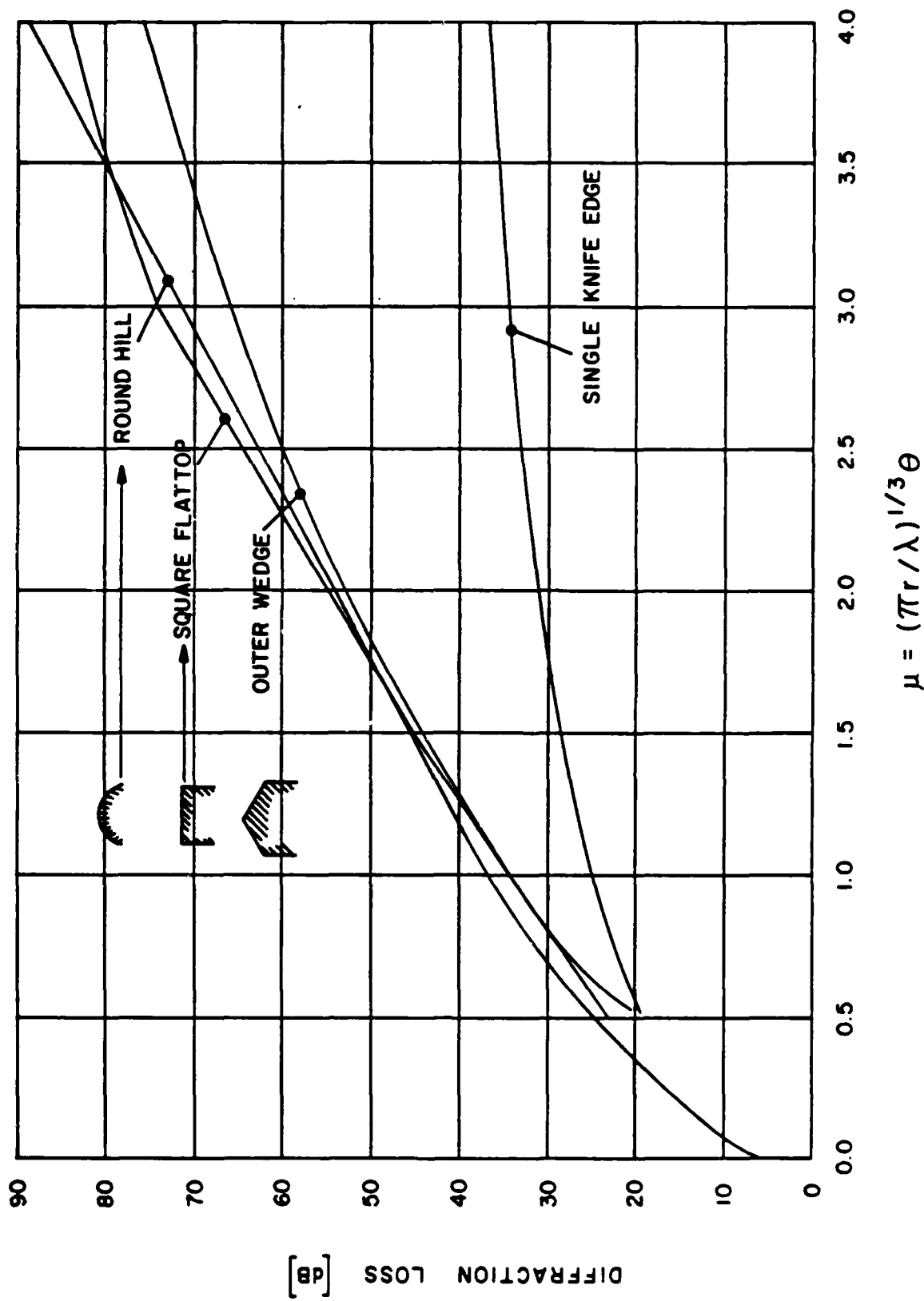


Figure 4-14 Diffraction Loss over Various Perfectly Reflecting Obstacles Approximating a Rounded Obstacle

$$\mu = \theta \left(\frac{\pi R}{\lambda} \right)^{1/3}$$

where θ is the diffraction angle and R is the radius of curvature of the rounded obstacle in Figure 4-13. The flat-top loss is within a few dB of the rounded hill. It should be noted however, that this result may not apply to diffraction over multiple rounded edges due to the drastically different shapes.

It is surprising that the flat-top, although completely contained within the rounded obstacles, sometimes has a larger loss than the rounded obstacles. Perhaps even more surprising is the result that a wedge outside the rounded edge (also shown in Figure 4-13) has a smaller loss, as seen in Figure 4-14.

This effect, that enlarging the obstacle can reduce the loss, is an extension of the similar result for the knife-edge seen in Figure 4-6. To see this, we repeat the case in Figure 4-6 but with the edges joined by plane surfaces. The result is shown in Figure 4-15.

Several results are noted from this figure.

1. At high diffraction angles the loss of a perfectly reflecting edge is approximately 6 dB higher than if a knife-edge is assumed.
2. A moderate amount of surface roughness will bring the loss at high diffraction angles down to that of a knife-edge.
3. At more shallow angles the surface roughness plays a more important role.

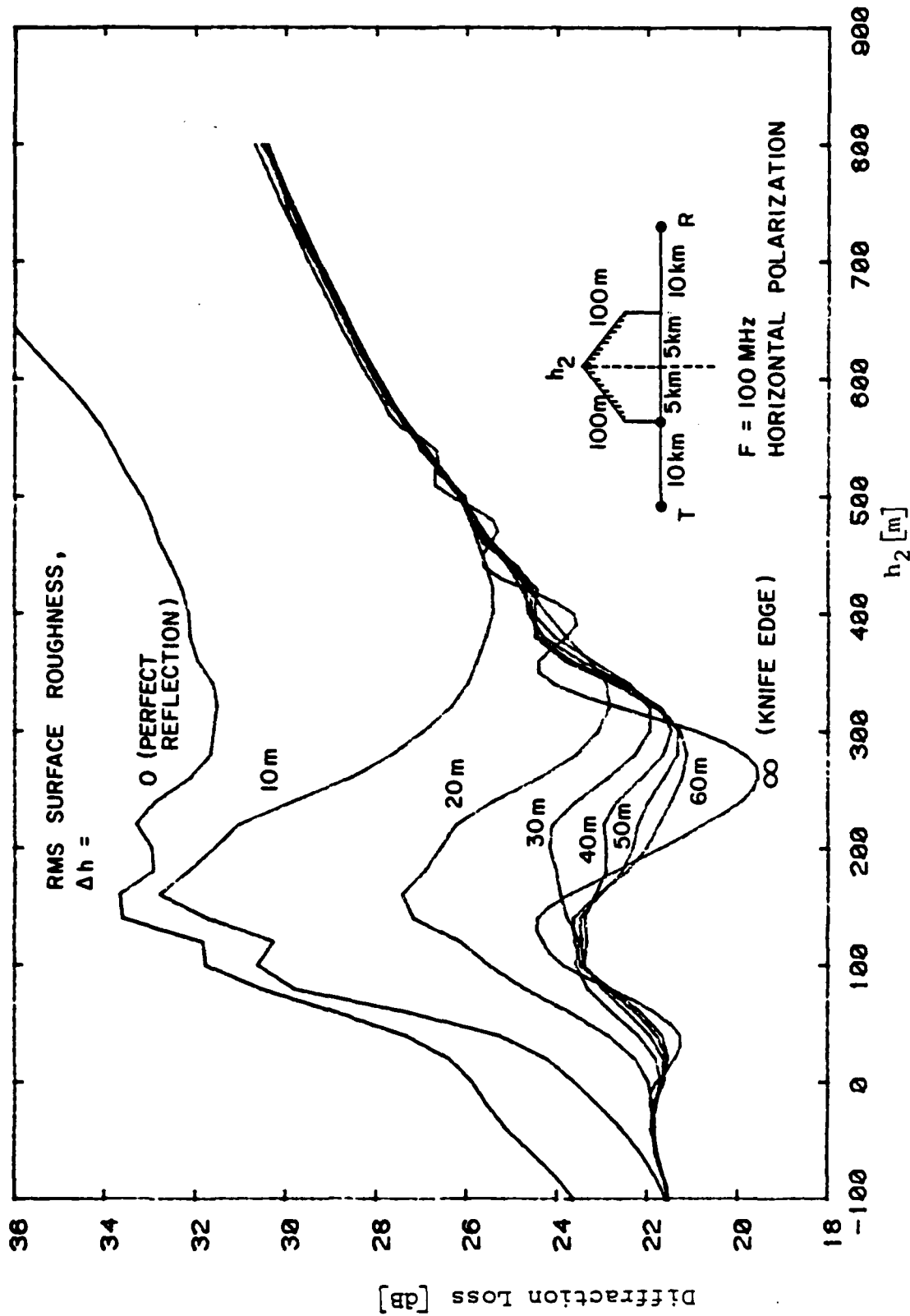


Figure 4-15 Effect of ground reflections on diffraction

4.3 AD-HOC TECHNIQUES FOR CALCULATION OF MULTIPLE EDGE DIFFRACTION

The extension of the Fresnel-Kirchhoff Theory (Huyghens' Principle) to treat the problem of diffraction by two or more edges results in multiple integrals which are difficult to handle analytically. Due to the complexity of the Fresnel-Kirchhoff theory for multiple knife-edges many simple geometric methods have been proposed such as those of Bullington [1947], Epstein and Peterson [1953], the Japanese Atlas [1957] and Deygout [1966].

4.3.1 Bullington Method

The Bullington method consists of replacing the multiple edges by a single virtual edge whose height (above source/receiver line) is determined by the horizon lines from each terminal. This method has been shown to be inaccurate under most conditions [Millington, et al., 1962] and is not discussed further.

4.3.2 Epstein Peterson Method

In the Epstein-Peterson method, the diffraction loss is calculated as the product (sum in dB) of losses obtained from each diffraction edge. The loss for an edge is obtained assuming the path is from the previous edge (or transmitter for the first edge) to the subsequent edge (or receiver for the last edge). This is also the method recommended by NBS Technical Note 101 [Rice, et al., 1967] and hence merits discussion.

Consider the geometry of Figure 4-16 where multiple diffraction occurs with three ridges. The source (transmitter) is situated at T_0 and the receiver at R with P_1 , P_2 , and P_3 representing the intervening edges, and the interseparations being d_1 , d_2 , d_3 and d_4 as shown. The angles of diffraction at each edge are θ_1 , θ_2 , and θ_3 , respectively.

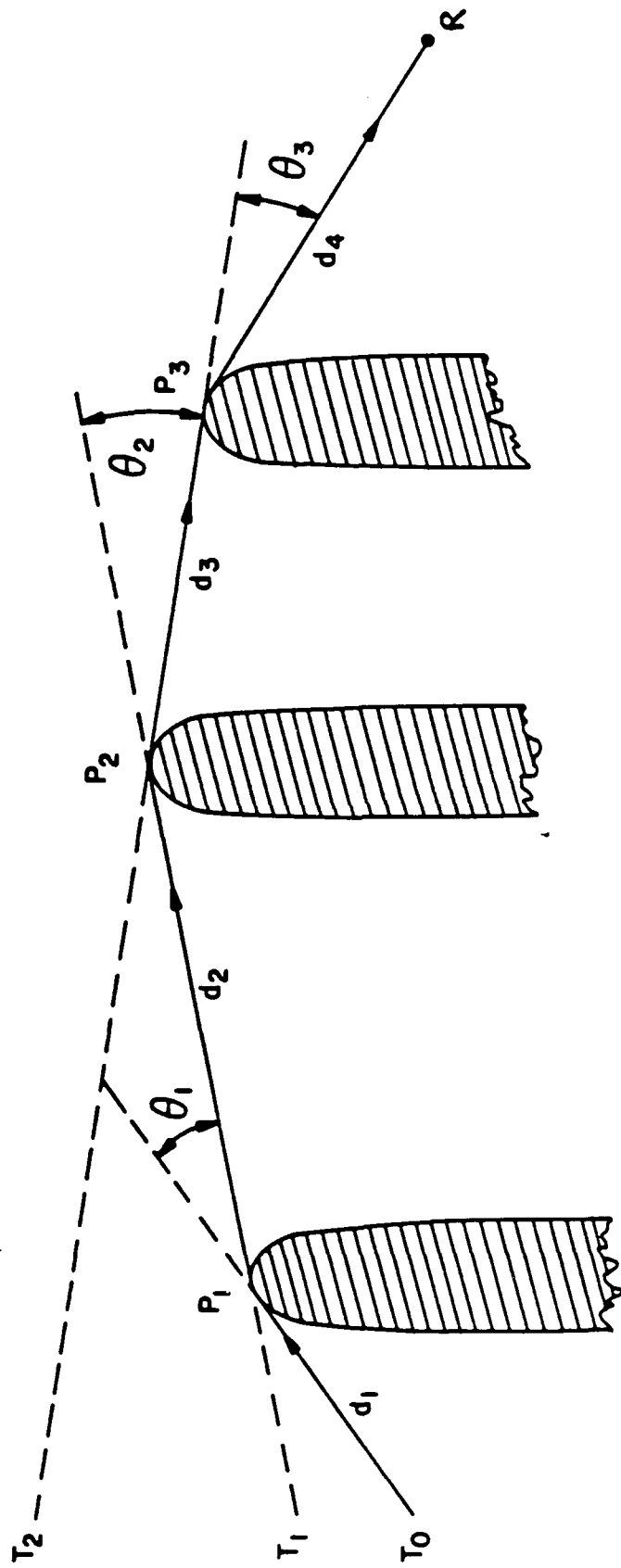


Figure 4-16 Multiple Diffraction: Construction

The relative field strength at P_2 , which is in the shadow cast by P_1 , is first calculated. When the obstacle at P_1 is a knife-edge, the relative field at P_2 will be $F_0(v_1)$ where v_1 is the Fresnel parameter for the path $T_0P_1P_2$ and $F_0(v_1)$ is given by (4.26). The relative field at P_3 is obtained by multiplying $F_0(v_1)$ by the relative field which would be obtained at P_3 if the source were located at P_1 ; this second factor is denoted $F_0(v_2)$ where v_2 is the Fresnel parameter for the path $P_1P_2P_3$. Finally, the relative field at R is obtained by multiplying the relative field at P_3 by a third factor $F_0(v_3)$ calculated by assuming the source is located at P_2 ; thus v_3 is the Fresnel parameter for the path P_2P_3R , and the field strength at R is given by

$$E(R) = E_0(R)F_0(v_1)F_0(v_2)F_0(v_3) \quad (4.27)$$

where $E_0(R)$ is the free-space field at R , $F_0(v)$ is the Fresnel integral defined as

$$F_0(v) = \frac{e^{j\pi/4}}{\sqrt{2}} \int_v^{\infty} e^{-j\frac{\pi}{2}t^2} dt \quad (4.28)$$

and the Fresnel parameters v_1 , v_2 , and v_3 are defined as

$$v_1 = \theta_1 \sqrt{\frac{2d_1d_2}{\lambda(d_2+d_3)}}$$

$$v_2 = \theta_2 \sqrt{\frac{2d_2d_3}{\lambda(d_2+d_3)}}$$

and

$$v_3 = \theta_3 \sqrt{\frac{2d_3 d_4}{\lambda(d_3 + d_4)}} .$$

Note that in their notation, the Fresnel parameter is positive when the terminals and edges are in the shadow zone and negative when they are in the lit zone.

This method has also been analyzed by Millington, et al. [1962] for the case of two edges and has been found to underestimate the diffraction loss when the loss due to both edges are large, and to overestimate the diffraction loss when both edges lie on or near the line-of-sight.

The Epstein-Peterson method breaks down completely when one or more of the diffraction angles is negative as it does not account explicitly for the appropriate number of rays. Consider for example the geometry of Figure 4-17 where there are three ray paths between transmitter and receiver. Since the diffraction angles at the second and third edges are negative, the Fresnel parameters v_2 and v_3 are also negative. Furthermore, making use of the fact that $F_0(v) = 1 - F_0(-v)$, it can be seen that mechanical application of the Epstein-Peterson method to this geometry yields a received field strength given by

$$E(R) = E_0(R)F_0(v_1)F_0(v_2)[1 - F_0(-v_3)]$$

which gives the field strength due to two rays: one double scattered ray and one triple scattered ray. The geometry of Figure 4-17 shows three rays, one of which has undergone single scattering.

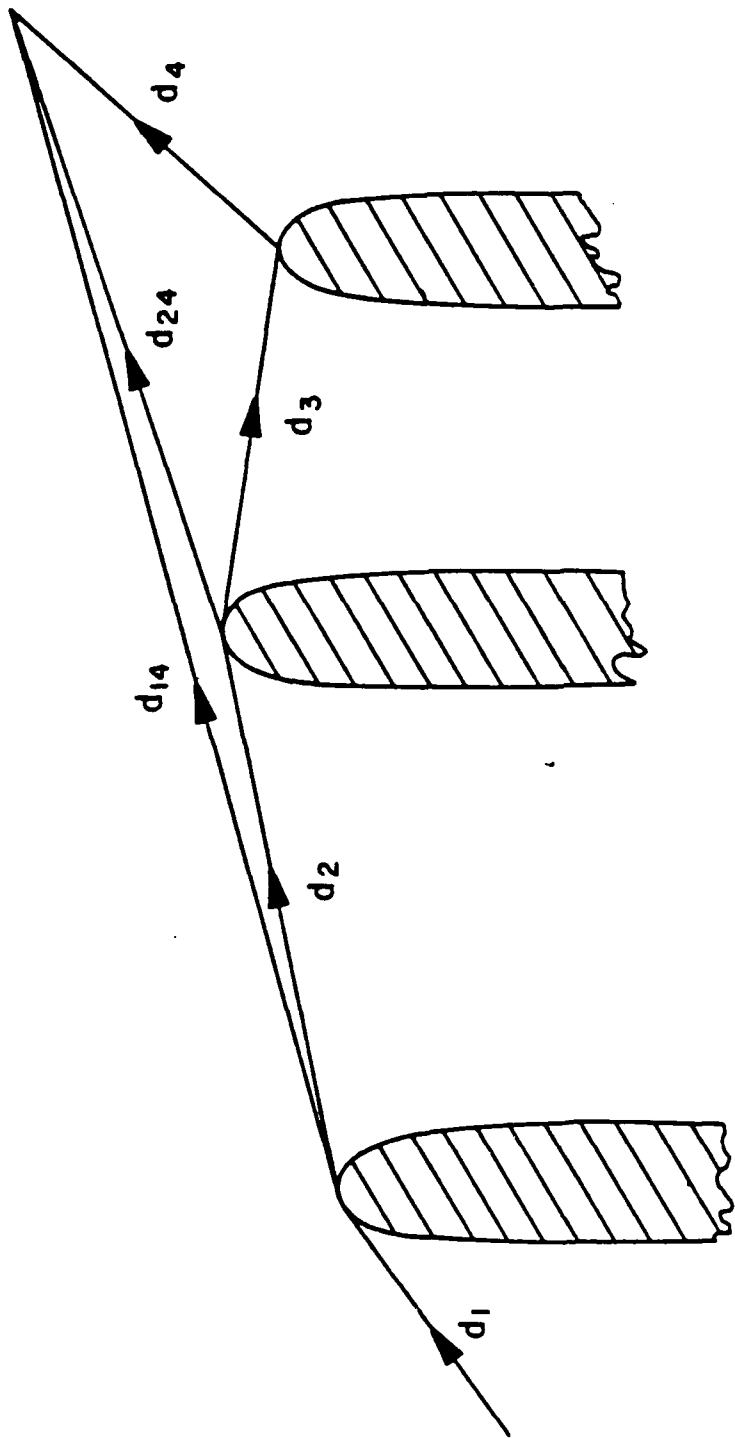


Figure 4-17 Multiple Edge Diffraction Geometry with Multiple Rays

In order to arrive at the correct result each ray must be accounted for explicitly. A uniform GTD technique which does just this is discussed in Section 4.4.

4.3.3 Japanese Atlas Method

The Japanese Atlas method [1957] is similar to the Epstein-Peterson method with the difference that the distance on one side of the diffracting edge is measured from the terminal rather than the adjacent edge. If we refer to the geometry of Figure 4-16 where multiple diffraction occurs over three ridges, the diffraction path between the source at T_0 and the receiver at R is $T_0P_1P_2P_3R$. The field strength E_d , relative to the free-space field, E_0 , at R is again calculated from Equation (4.27) but the Fresnel parameters are redefined as

$$v_1 = \theta_1 \sqrt{\frac{2d_1d_2}{\lambda(d_1+d_2)}}$$

$$v_2 = \theta_2 \sqrt{\frac{2d_3(d_1+d_2)}{\lambda(d_1+d_2+d_3)}}$$

$$v_3 = \theta_3 \sqrt{\frac{2d_4(d_1+d_2+d_3)}{\lambda(d_1+d_2+d_3+d_4)}} .$$

This method yields the correct result when the diffraction angles are large and is reciprocal even though the losses due to each obstacle differ depending on which obstacle is taken as the transmitter. The total diffraction loss is the same, though. When one or more of the diffraction angles is negative, mechanical application of the Japanese Atlas method suffers from the same deficiencies as the Epstein-Peterson method, i.e., it does not account for the proper number of rays.

4.3.4 Deygout Method

The Deygout method [Deygout, 1966] is an ad hoc technique which consists of obtaining a loss for each diffraction edge in turn as if the remaining edges were absent. The largest of these losses is used to divide the path in two and the process repeated in the two halves as if the edge were a terminal. This process is repeated until each of the diffracting edges has been used. The resulting loss factor is the product of the factors corresponding to the larger loss in each of the steps. When there are only two edges, the Deygout method is the same as the Japanese Atlas Method. However, when there are three or more edges, the two methods will give different answers in general. For the geometry of Figure 4-16, the Deygout method gives the received field strength also by Eq. (4.27). However, the Fresnel parameters v_1 , v_2 and v_3 are defined in terms of the obstacle heights, h_1 , h_2 and h_3 (where $h_2 > h_1, h_3$) as

$$v_1 = h_1 \sqrt{\frac{(d_1 + d_2)}{\lambda d_1 d_2}}$$

$$v_2 = h_2 \sqrt{\frac{(d_1 + d_2 + d_3 + d_4)}{\lambda (d_1 + d_2)(d_2 + d_3)}}$$

$$v_3 = h_3 \sqrt{\frac{2(d_3 + d_4)}{\lambda d_3 d_4}} .$$

The Deygout method also yields the correct result for large obstacle heights (diffraction angles). When one or more of the diffraction angles is negative, mechanical application of the Deygout method by defining the obstacles heights to be negative

can also yield the wrong result as the number of rays included in the calculation will not always necessarily reflect the actual geometry.

4.4 UNIFORM GEOMETRICAL THEORY OF DIFFRACTION (UGTD)

The Geometrical Theory of Diffraction [Keller, 1962] (GTD) is an extension of Fermat's principle of stationary phase paths (ray theory) to include paths around obstacles (e.g., diffraction, scattering, etc.). Since the GTD is an extension of ray theory, it is very intuitive and lends itself to the treatment of more complicated problems (such as multiple edge diffraction) where the exact boundary-value problem cannot be solved in closed form. Unlike Sommerfeld's solution, Keller's GTD solution is not valid at every point behind the obstacle. The region where the GTD solution is not valid is called the transition region. Outside the transition region, the GTD solution reduces asymptotically to the Sommerfeld solution as the frequency approaches infinity. More recently, new solutions which combine the simple construction of the GTD solution with the more accurate representation of the diffracted field have been developed. The technique developed by Kouyoumjian and Pathak [1974] for diffraction by a single edge is referred to as the Uniform Geometrical Theory of Diffraction (UGTD) and has the property that it is valid everywhere including the transition region. Another technique called the Uniform Asymptotic Theory (UAT) has been developed by Ahluwalia, et al. [1968]. The two techniques yield similar results [Boersma and Rahmat-Samii, 1980], but the UGTD approach appears to be simpler to apply to propagation problems. The UGTD solution also suits itself to the treatment of more complex problems, e.g., rounded edge diffraction and multiple edge diffraction. Therefore, it will be instructive to summarize the approach for the case of a single knife-edge. The extension to more complicated geometries will be discussed in subsequent sections.

Consider the geometry of Figure 4-18. Let us assume that a spherical wave is incident on the edge. Then if the observation point P_s is in the shadow region ($\theta > 0$, top of Figure 4-18), the total field at the observation point can be expressed in terms of the field incident on the edge as follows.

Let $E(0)$ be the edge diffracted field right at the edge. Then the field at the observation point P_s is given to first order of magnitude by the geometrical optics stationary phase solution, i.e.,

$$E(P_s) = E(0) \sqrt{\frac{\rho_1 \rho_2}{(\rho_1 + d_2)(\rho_2 + d_2)}} e^{-jkd_2}. \quad (4.29)$$

where

- $E(P)$ = diffracted field at point P
- ρ_1, ρ_2 = distance from the diffraction point to the caustics of the diffracted ray
- d_2 = distance from the diffraction point to the observation point.

The radical in (4.29) is the ray bundle expansion law of geometrical optics. The distances, ρ_1 and ρ_2 are the principal radii of curvature of the wavefront at the reference point (i.e., the edge) $d_2 = 0$. In Figure 4-19, ρ_1 and ρ_2 are shown in relationship to the rays and wavefronts. The intersection of the rays at the lines 1-2 and 3-4 of the astigmatic tube of rays is called a caustic. Equation (4.29) is a valid high-frequency approximation on either side of the caustic; the field at a caustic must be found from separate considerations. In the case of the diffracted ray, the reference point 0 is a caustic of the diffracted field in elevation, i.e., $\rho_2 = 0$, while the source is a caustic in azimuth, i.e., $\rho_1 = d_1$. On the other hand, the diffracted field must be independent of the reference point;

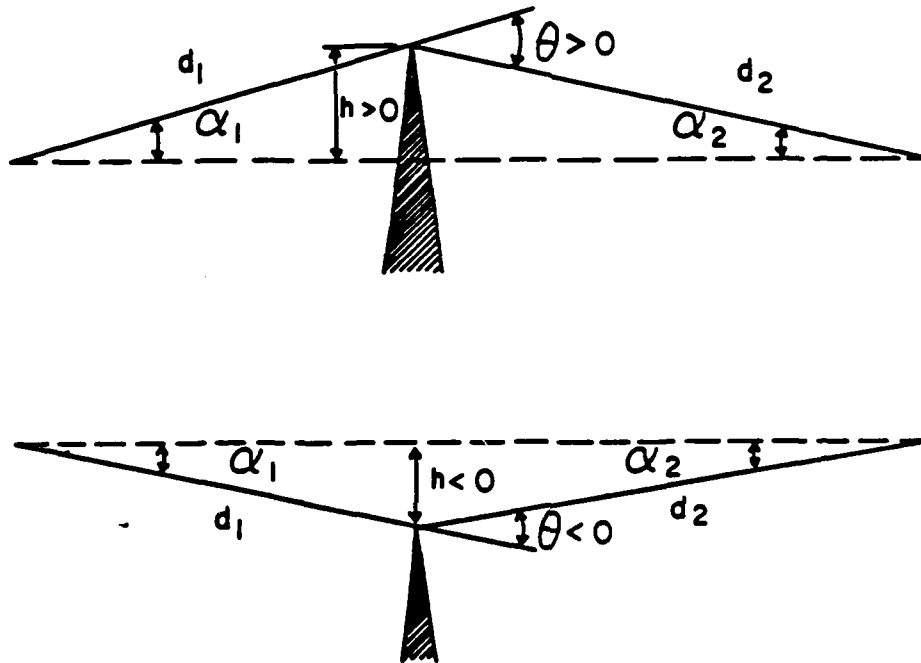


Figure 4-18 Knife-edge Diffraction Geometry

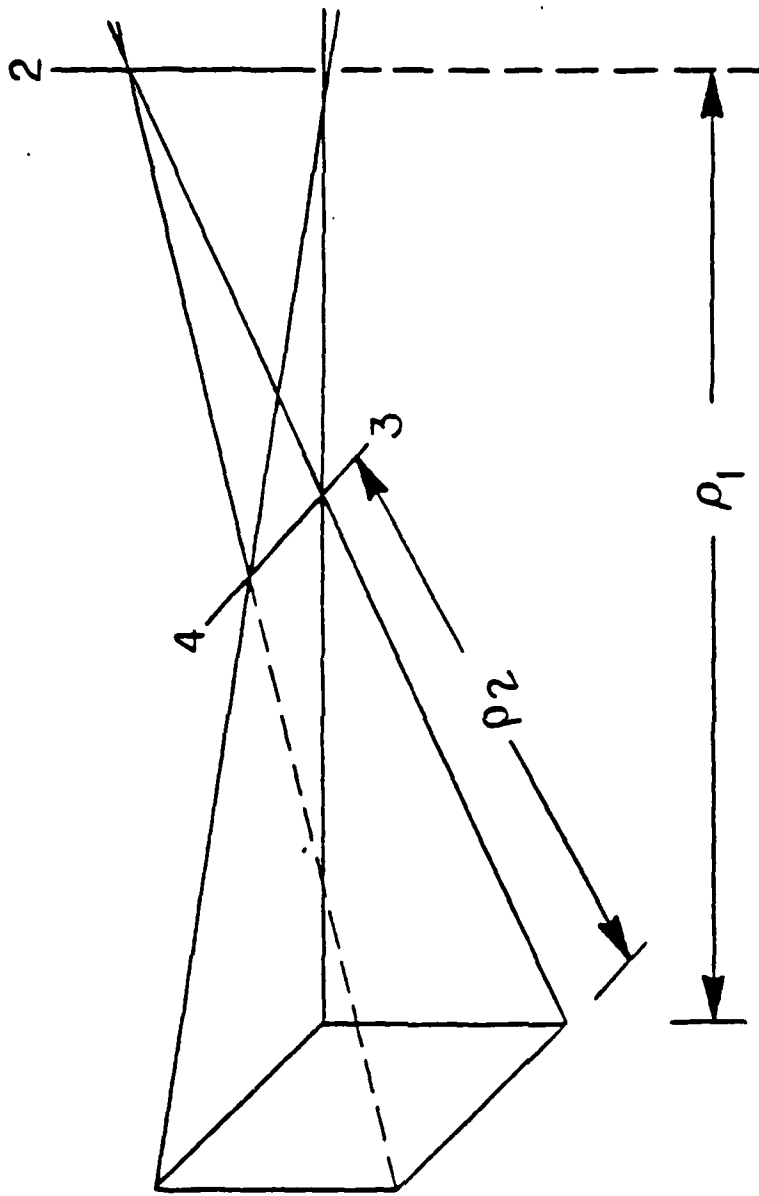


Figure 4-19 Caustics of an Astigmatic Tube of Rays

hence in the limit as $\rho_2 \rightarrow 0$, $E(0) \sqrt{\rho_2}$ exists. Since the diffracted field is proportional to the field incident on the edge,

$$\lim_{\rho_2 \rightarrow 0} E(0) \sqrt{\rho_2} = E_i(0) \hat{D}_0 \quad (4.30)$$

where \hat{D}_0 is referred to as the diffraction coefficient. It depends upon the angles of incidence and diffraction, the boundary conditions on the surfaces meeting at the edge, the angle between the surfaces, etc. From (4.30) we see that the diffraction coefficient \hat{D}_0 has the dimensions of (length)^{1/2} so we can define a dimensionless diffraction coefficient \hat{D} as

$$\hat{D} = \sqrt{k} \hat{D}_0 \quad (4.31)$$

where $k = 2\pi/\lambda$ is the wavenumber. Thus, using (4.30) and (4.31) in (4.29) we find that the edge diffracted field is given by

$$E(P_S) = E_i(0) \frac{\hat{D}}{\sqrt{k d_2}} \sqrt{\frac{d_1}{d_1 + d_2}} e^{-j k d_2} \quad (4.32)$$

which shows that the diffracted field behaves as a cylindrical wave close to the edge ($d_2 \ll d_1$) and as a spherical wave sufficiently far from the edge ($d_2 \gg d_1$).

The ratio of received power to transmitted power (transmission loss) can be obtained by noting that the received power is directly proportional to the received field intensity, i.e.,

$$P_R = \frac{\lambda^2}{4\pi} G_R |E(P_S)|^2 / 120\pi \quad (4.33a)$$

where G_R is the receiving antenna gain, $G_R \lambda^2 / 4\pi$ is the receiving aperture area and 120π is the free space impedance. The received field intensity is proportional to the field intensity incident on the edge as seen from Equation (4.32). The incident field intensity is directly proportional to the transmitted power P_T and transmitting antenna gain G_T and is given by

$$E_i(0) = \frac{\sqrt{30P_T G_T}}{d_1} \quad (4.33b)$$

Therefore, the transmission loss is

$$\frac{P_R}{P_T} = G_T G_R \left(\frac{\lambda}{4\pi d_1}\right)^2 \left(\frac{|\hat{D}|^2}{kd_2}\right) \left(\frac{d_1}{d_1+d_2}\right) \quad (4.34)$$

The first factor is due to the spherical spreading loss between the transmitter and the edge, the second factor is the edge diffraction loss assuming cylindrical wave spreading after diffraction, and the third factor is the correction factor to account for azimuthal spreading of the wave between the edge and the receiver (observation point).

Often it is convenient to express the transmission loss as the product of two factors, one representing the free-space loss, i.e., spherical spreading loss between transmitter and receiver in the absence of an obstacle, and another representing the diffraction loss, i.e., loss due to the obstacle.

The free-space transmission loss between two terminals separated by a distance d is defined as

$$L_F = G_T G_R \left(\frac{\lambda}{4\pi d} \right)^2 . \quad (4.35)$$

The diffraction loss can be found from (4.34) and (4.35) and is given by

$$L_D = \frac{|\hat{D}|^2}{k d_2} \frac{d^2}{(d_1 + d_2) d_1} \quad (4.36)$$

that is, it is equal to the edge diffraction loss assuming cylindrical spreading divided by the azimuthal spreading correction factor.

Although diffraction effects are normally discussed in terms of the diffraction loss defined above, we can see by comparing (4.34) and (4.36) that the form of the transmission loss is more intuitive and lends itself to interpretation more easily than the form of the diffraction loss. In either case, the edge diffraction effects are completely defined by the edge diffraction coefficient \hat{D} . To determine \hat{D} we must solve a canonical problem. This is a simpler problem which has the same local geometry and other local properties. In the case of a knife-edge, the canonical problem is that of diffraction by a semi-infinite, perfectly conducting screen. Before we proceed to discuss the form of the diffraction coefficient, however, a discussion of the implications when the observation point (receive location) is in the lit zone is necessary, that is the case when both terminals are above the obstacle.

When the observation point P_L is in the lit region ($0 < \theta$, bottom of Figure 4-18) the total field is given by the direct and reflected rays of geometrical optics. Thus,

$$E(P_L) = E_i(P_L) + E_i(0)R \sqrt{\frac{\rho_1 \rho_2}{(\rho_1 + d_2)(\rho_2 + d_2)}} e^{-jkd_2} \quad (4.37)$$

where $E_i(P)$ is the incident field at location P , R is the dimensionless reflection coefficient of the surface, a factor analogous to the diffraction coefficient of Equation (4.37), while ρ_1 and ρ_2 are the principal radii of curvature of the reflected wave, i.e., they are distances from the reflection point to the caustics of the reflected wave. In general, the principal radii of curvature of the reflected ray differ from those of the incident ray. The relationship between the radii of curvature of the incident and reflected waves at the reference point, in this case at the edge, has been derived by Deschamps [1972] for the general case of a curved reflecting surface. In the special case of a knife-edge, the edge is at one of the caustics of the reflected wave, i.e., $\rho_1 = d_1$. If we were to use these values in (4.37), it would appear that the contribution of the reflected wave to the total field at the observation point would be identically zero. However, the reflection coefficient R also depends on the extent of the reflecting surface. When the surface is flat, perfectly conducting and of infinite extent, the reflection coefficient is +1 if the polarization of the incident wave is parallel to the plane of incidence (vertical polarization) and -1 if the polarization is perpendicular to the plane of incidence (horizontal polarization). In the case of a knife-edge of infinitely small width, the reflection coefficient can be expressed in terms of an edge diffraction coefficient as

$$\lim_{\rho_2 \rightarrow 0} R\sqrt{\rho_2} = \hat{D}_0 = \hat{D}/\sqrt{k}$$

where \hat{R} is the reflection coefficient of a flat, infinite surface of similar conductivity as the knife-edge, and \hat{D} is the edge diffraction coefficient which accounts for the effects of finite extent and shape of the reflecting surface.

The total field at the observation point in the lit region is then of the form

$$\begin{aligned} E(P_L) &= \frac{\sqrt{30P_t G_t}}{d} e^{-jkd} + E_i(0) \frac{\hat{D}}{\sqrt{kd_2}} \sqrt{\frac{d_1}{d_1+d_2}} e^{-jkd_2} \\ &= \sqrt{30P_t G_t} \left[\frac{e^{-jkd}}{d} + \frac{1}{d_1} \frac{\hat{D}}{\sqrt{kd_2}} \sqrt{\frac{d_1}{d_1+d_2}} e^{-jk(d_1+d_2)} \right]. \quad (4.38) \end{aligned}$$

The first term in (4.38) is the direct ray contribution to the received field and the second term is the scattered (or partially reflected) ray.

In order for the field to be continuous across the shadow boundary ($\theta=0$), the edge diffraction coefficient \hat{D} must be such that (4.32) and (4.38) are identical when $\theta=0$. In the next two sections, we discuss the form of the edge diffraction coefficient which satisfies this condition for the case of a semi-infinite plate (knife-edge) and a semi-infinite cylinder (rounded edge).

4.4.1 Diffraction Coefficient for a Knife-Edge

Starting from a spectral representation* of the field diffracted by a semi-infinite half-plane (knife-edge) due to an incident cylindrical wave, Boersma and Rahmat-Sahmii [1980] have shown that the field diffracted by a knife-edge is given by

$$E_r = E_i(d) \cdot [1 - H(\phi - \Omega)] + E_i(d_1) \frac{\hat{D}}{\sqrt{kd_2}} \sqrt{\frac{d_1}{d_1 + d_2}} e^{-jkd_2} \quad (4.38)$$

where

$$E_i(x) = \sqrt{30P_t G_t} \frac{e^{-jkx}}{x} \quad (4.39)$$

$$\hat{D} = - \frac{e^{-j\pi/4}}{2\sqrt{2\pi}} \left[\frac{F_{kp}[k(d_1 + d_2 - d)]}{\sin \frac{1}{2}(\Omega - \phi)} - R \frac{F_{kp}[k(d_1 + d_2 - d_r)]}{\sin \frac{1}{2}(\Omega + \phi)} \right] \quad (4.40)$$

$$F_{kp}(x) = 2\sqrt{\pi x} e^{jx + j\pi/4} F(\sqrt{x}) \quad (4.41)$$

$$F(\tau) = \frac{e^{j\pi/4}}{\sqrt{\pi}} \int_{\tau}^{\infty} e^{-jt^2} dt \quad (4.42)$$

$$H(x) = \begin{cases} 1 & , \quad x > 0 \\ 0 & , \quad x < 0 \end{cases} .$$

* NOTE: This spectral (integral) representation is similar to Equation (4.3) in Section 4.2, except that polar coordinates are used and angles are allowed to be complex.

The angles ϕ and Ω are shown in Figure 4-20 and represent the radiation angle of the scattered (or diffracted) ray measured from the vertical, and Ω is the scattering angle measured from the plane above the edge. The difference $\phi - \Omega = \theta$ is the commonly defined diffraction angle. The distance d is the distance between the source (transmitter) and observation point (receiver) r , d_1 is the distance between the source and the edge, d_2 is the distance between the edge and the observation point and d_r is the distance between the 'image' of the source (see Figure 4-20) and the observation point. The first term in (4.38) is the free space field which contributes to the total field only when $\phi < \Omega$ (i.e., with lit zone). The second term is the field scattered by the edge and consists of two contributions, the first of which is that due to the field incident on the edge directly from the source and the second is the contribution from the 'image' (reflection from half plane). This last term contributes negligibly to the total field in knife-edge diffraction and will not be considered further. It is often included when a knife-edge is viewed as a limiting case of a wedge. In the case of the wedge the reflections from the sides of the wedge contribute significantly to the total field.

The function $F_{kp}(x)$ is the function defined by Kouyoumjian and Pathak [1974] and has the property that it approaches unity for large arguments and zero for small arguments. Its argument in Equation (4.40), i.e., $k(d_1+d_2-d)$, is the detour parameter which approaches zero when $\phi = \Omega$, i.e., at the shadow boundary. To demonstrate that this edge diffraction coefficient yields a solution which is continuous across the shadow boundary, and which reduces to Keller's classical solution for large diffraction angles, we make use of the fact that

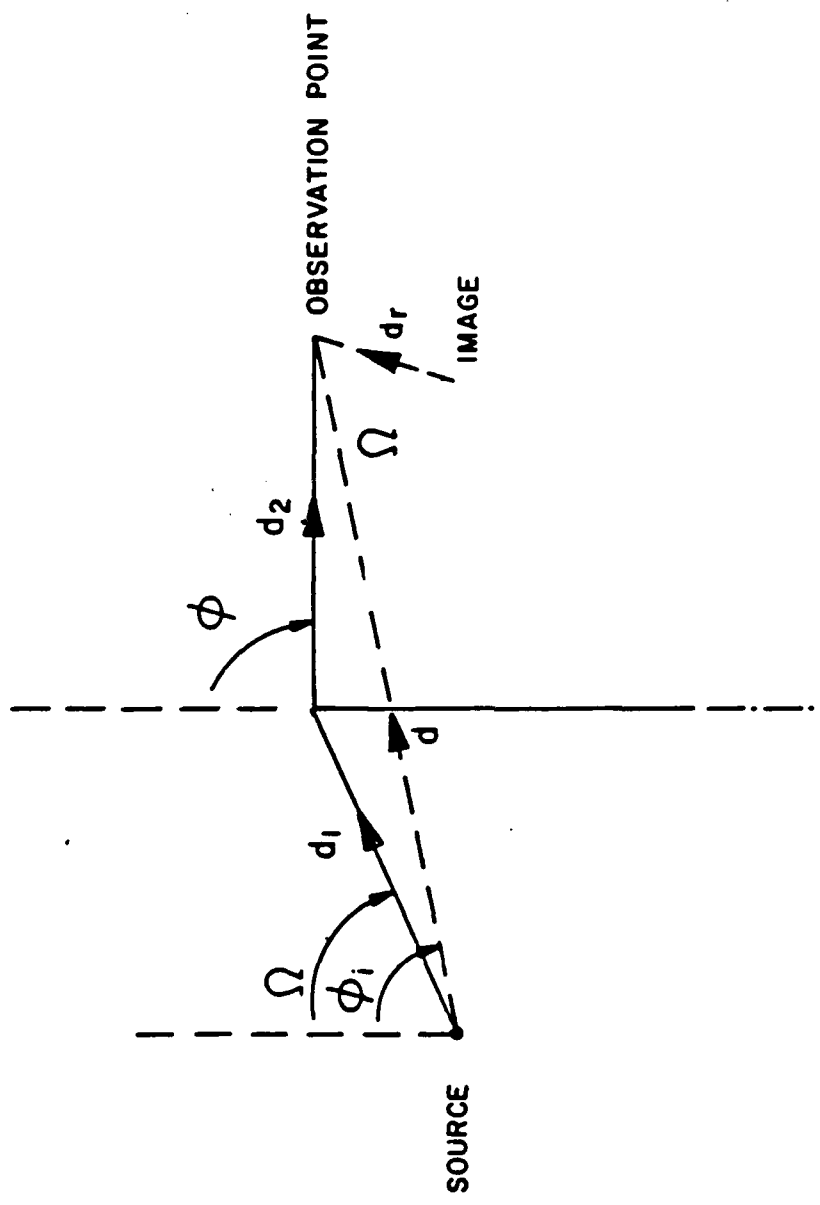


Figure 4-20 Geometry for Knife-Edge Diffraction

$$k(d_1+d_2-d) = \frac{4kd_1d_2}{d_1+d_2+d} \sin^2 \frac{1}{2} (\Omega-\phi) \quad (4.44)$$

The edge diffraction coefficient can now be rewritten as

$$\hat{D} = - \operatorname{sgn}(\Omega-\phi) \sqrt{\frac{2kd_1d_2}{d_1+d_2+d}} F_0(v) e^{jk(d_1+d_2-d)} \quad (4.45)$$

where we have dropped the contribution from the 'image', $F_0(v) = F(\sqrt{\pi/2} v)$ is the Fresnel integral defined earlier in Equation (4.28), and v is the Fresnel parameter defined as

$$v = \sqrt{\frac{2k(d_1+d_2-d)}{\pi}} = \sqrt{\frac{16d_1d_2 \sin^2 \frac{1}{2} (\Omega-\phi)}{\lambda(d_1+d_2+d)}} \quad (4.46)$$

Note that in the UGTD formulation, the Fresnel parameter is positive in the shadow ($\phi > \Omega$) and lit zones ($\phi < \Omega$). However the edge diffraction coefficient is positive in the shadow zone and negative in the lit zone.

On the shadow boundary ($\Omega = \phi$), $F_0(v) = 1/2$ so that the total field is given by

$$\lim_{\Omega \rightarrow \phi} E_r = \begin{cases} \frac{1}{2} E_i(d) & , \text{ if } \phi > \Omega \\ E_i(d) - \frac{1}{2} E_i(d) & , \text{ if } \phi < \Omega \end{cases} \quad (4.47)$$

which shows that the field is continuous across the shadow boundary.

In the shadow and lit zones far away from the shadow boundary, where the scattering angle $\theta = \phi - \Omega$ is large, the argument of the Fresnel integral, v , is large and

$$\lim_{v \rightarrow \infty} F_0(v) = \frac{e^{-j\pi/4} e^{-j\pi/2v^2}}{\sqrt{2} \pi v}$$

so that the edge diffraction coefficient is asymptotically given by

$$\hat{D} = - \frac{e^{-j\pi/4}}{2\sqrt{2}\pi \sin \frac{1}{2}(\Omega - \phi)} \quad (4.48)$$

This asymptotic form of the edge diffraction coefficient is identical to Keller's [1962] and shows that for sufficiently large diffraction angles, the edge diffraction coefficient depends only on the diffraction angle.

The diffraction loss when the observation point is in the shadow zone can be found by substituting the edge diffraction coefficient defined in (4.44) into Equation (4.36) and is given by

$$L_D = \frac{|\hat{D}|^2}{kd_2} = |F_0(v)| \quad (4.49)$$

where use has been made of the approximation $d = d_1 + d_2$. This is the classical result for the diffraction loss due to a single knife-edge.

4.4.2 Diffraction Coefficient for a Rounded Edge

The problem of diffraction by an obstacle whose cross section along the great circle plane has an arbitrary shape is extremely difficult and has not been completely solved to date. However, various asymptotic solutions for the diffraction of electromagnetic radio waves by obstacles whose cross section is smooth and convex have been given in the literature. The simplest and most convenient result for practical applications is the GTD (geometrical theory of diffraction) solution of the problem of scattering of waves by a perfectly conducting smooth convex cylinder [Keller, 1956]. In the GTD solution, the total field in the region exterior to the cylinder is associated with the usual incident and reflected rays of geometrical optics, (lit region) or with the surface diffracted rays (which are not the same as the edge diffracted range) introduced by Keller (shadow region). The geometric optical rays do not penetrate the convex obstacle; hence they do not contribute to the total field within the shadow region cast by the obstacle. Therefore in the shadow region, the field is entirely associated with the surface diffracted rays which are excited by the incident ray that grazes the convex surface as shown in Figure 4-21. The incident ray at grazing launches a set of surface rays which propagate along a geodesic path on the convex surface, thereby carrying energy into the shadow region. The field associated with these surface rays decays exponentially due to a continuous shedding or diffraction of rays from the surface along the forward tangents to the geodesic surface rays as shown in Figure 4-21. The GTD solution is valid in the lit (region I) and deep shadow (region III) zones of Figure 4-21 (large diffraction angle), but fails in the transition (region II) zone adjacent to the shadow boundary (small diffraction angles). The angular extent of this transition region is of the order of $(\lambda/\pi R_{01})^{1/3}$ where λ is the wavelength of the incident wave and R_{01} is the radius of curvature of the

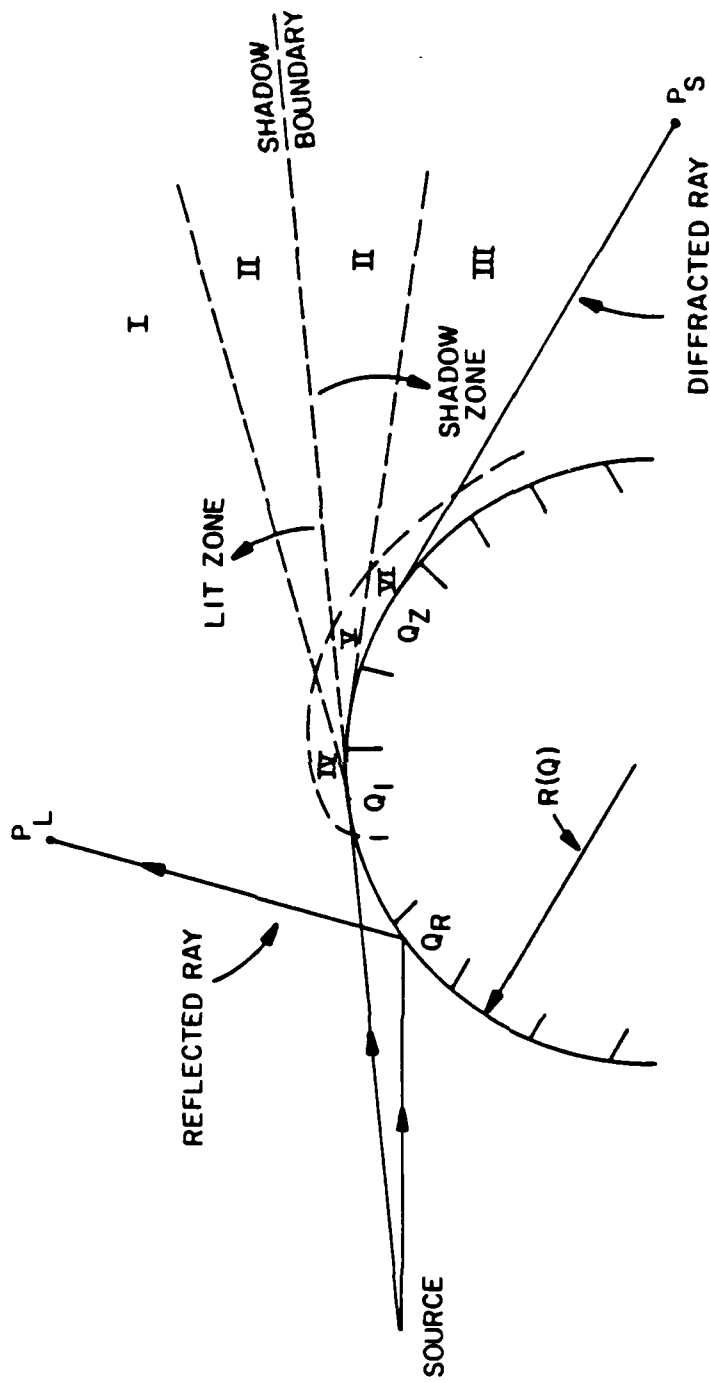


Figure 4-21 Rays and regions associated with the diffraction and scattering by a convex surface.

surface at the point of grazing incidence (Q_1). The GTD solution also fails in the region near the surface. This region is called the surface boundary layer and is denoted by subregions IV, V, and VI in Figure 4-21. Region IV is in the lit zone and is in the neighborhood of Q_1 which is a caustic (i.e., point where the GTD solution yields an infinite value for the field) of the reflected ray for grazing incidence. Regions V and VI are in the shadow-zone and close to the surface which is a caustic of the surface diffracted rays.

The problem of estimating the field within the transition region (small diffraction angle) and the surface boundary layer has received much attention especially in connection with the theory of radio wave propagation around the earth. Fock was the first to develop a general asymptotic theory for the diffraction of radio waves by large convex surfaces [Fock, 1946]. The solution was expressed in terms of a canonical integral. Subsequently, Fock treated the problem of Fresnel diffraction by a sphere [Fock, 1951] in which he approximated the canonical integral asymptotically within the transition region between the lit and shadow zones; as a result he was able to obtain a simpler solution in terms of tabulated functions. Fock's [1951] result is valid for heights of the source and observation points above the sphere which are small compared with the radius of the sphere. Wait and Conda [1959] were able to relax this condition so that the source and observation points could now be far from the diffracting surface. Their results are in terms of functions similar to those in the work of Fock, but they are obtained from an asymptotic analysis of the canonical problem of the diffraction of a plane wave by a circular cylinder. The results of Fock [1951] and Wait and Conda [1959], although in terms of tabulated functions, are still somewhat complicated for propagation path loss predictions. Dougherty and Maloney [1964] reduced the theoretical solution of Wait and Conda [1959] for horizontal polari-

zation and highly conducting rounded obstacles to simple arithmetic formulas for the magnitude and phase of the diffracted field. Their formulas were arrived at by fitting fourth order polynomials to the asymptotic solutions of Wait and Conda [1959]. These formulas can also be used for vertical polarization when the obstacle is poorly conducting, as the diffraction loss is nearly independent of the polarization in that case.

When the diffraction angle is large (shadow and lit regions), the results in the work of Fock [1951], and Wait and Conda [1959] do not reduce uniformly to the usual GTD ray solution in the regions exterior to the transition region. Recently, Pathak, et al., [1980] have used UGTD methods to obtain an asymptotic solution for the diffracted field in the transition region (small diffraction angle) which reduces uniformly to the usual GTD solution exterior to the transition region (large diffraction angle). The diffracting obstacle is assumed to be perfectly conducting with a convex cylindrical shape while the incident polarization is either horizontal or vertical. This solution eliminates the need for separate representations inside and outside the transition regions. It is expressed in terms of tabulated universal functions which are similar to those occurring in the work of Fock [1951] and Wait and Conda [1959]; hence it is amenable to numerical computation. James [1980] has also used a method similar to UGTD to obtain asymptotic solutions for the general case of a cylinder of arbitrary conductivity. This solution also reduces to Wait and Conda's solution within the transition region and to the usual GTD ray solution outside the transition region.

In this section, we recast the UGTD solutions of Pathak, et al., [1980] and James [1980] into a form which makes them simpler to compare with the well known solution of Wait and Conda [1959], show that it is continuous across the shadow boundary and that it reduces to Keller's GTD solution [1956] in the regions exterior to the shadow boundary.

The total field diffracted by a rounded edge can be written as

$$E_r = E_i(d) \cdot [1-H(\theta)] + E_i(d_i) \frac{\hat{D}}{\sqrt{kd_2}} \sqrt{\frac{d_1+\tau}{d_1+\tau+d_2}} e^{-jkd_2} \quad (4.49)$$

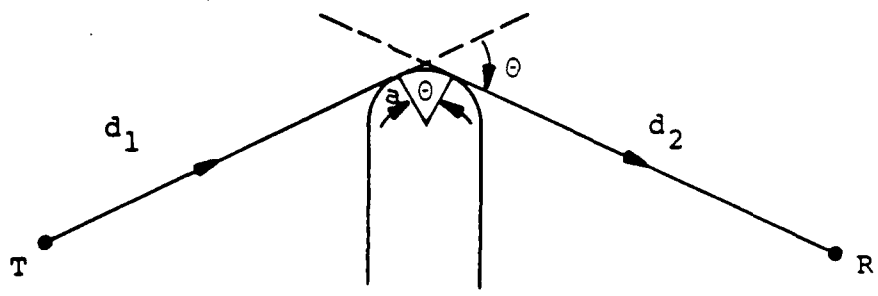
where $E_i(x)$ is the free-space field at a distance x (Eq. (4.39)), \hat{D} is the rounded edge diffraction coefficient, and d_1 , d_2 and τ are the distances shown in Figure 4-22. Note that when the observation point is in the shadow zone, $\tau=a\theta$ is the distance that the diffracted ray propagates along the round surface. When the observation point is in the lit zone, $\tau=0$.

The edge diffraction coefficient for a rounded (cylindrical) edge with radius of curvature a and of arbitrary conductivity can be shown to be given by [James, 1980; Pathak, et al., 1980]

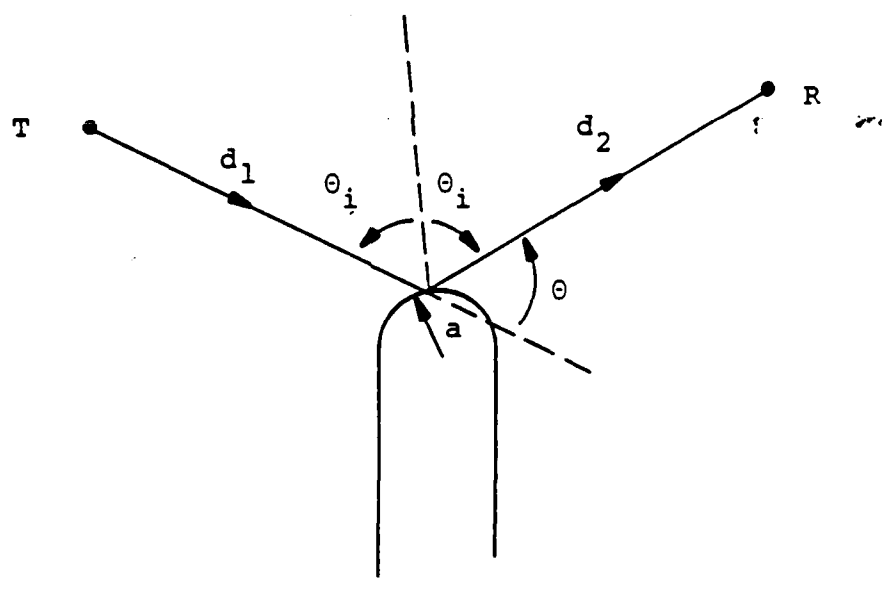
$$\hat{D} = g(\theta) \left\{ \frac{e^{-j\pi/4}}{2\sqrt{2\pi} \sin \frac{\theta}{2}} [F_{kp}(\xi) - 1] - \sqrt{2M} \hat{P}(x, q) \right\} \quad (4.50)$$

where $F_{kp}(\xi)$ is the function defined earlier in Eq. (4.41), θ is the diffraction angle (positive in the shadow zone and negative in the lit zone), and

$$g(\theta) = \begin{cases} \sqrt{\frac{d_1}{d_1+\tau}} e^{-jk\tau} & , \text{shadow zone } (\theta > 0) \\ \sqrt{\frac{2d_1d_2}{a(d_1+d_2)\cos\theta_i + 2d_1d_2}} e^{-jx^3/12} & , \text{lit zone } (\theta < 0) \end{cases} \quad (4.51)$$



(a)



(b)

Figure 4-22 Shadow zone (a) and lit zone (b) geometries for the diffraction by a rounded edge.

$$\xi = 2 \sin^2 \frac{\theta}{2} \frac{kd_1 d_2}{d_1 + d_2} \quad (4.52)$$

$$x = 2M \sin^2 \frac{\theta}{2} = \begin{cases} M\theta & , \text{ shadow zone } (\theta > 0) \\ -2M \cos \theta_i & , \text{ lit zone } (\theta < 0) \end{cases} \quad (4.53)$$

$$M = \left(\frac{ka}{2}\right)^{1/3} \quad (4.54)$$

$$q = -jMz \quad (4.55)$$

$$z = \begin{cases} (\epsilon_r - j60\sigma\lambda)^{-1/2} & , \text{ vertical polarization} \\ (\epsilon_r - j60\sigma\lambda)^{1/2} & , \text{ horizontal polarization} \end{cases} \quad (4.56)$$

$$\hat{P}(x, q) = \frac{e^{-j\pi/4}}{\sqrt{\pi}} \int_0^{\infty} e^{-jxt} \frac{v'(t) - qv(t)}{w_1'(t) - qw_1(t)} dt \quad (4.57)$$

$$+ \frac{e^{j\pi/12}}{\sqrt{\pi}} \int_0^{\infty} e^{jxt(1+j\sqrt{3})/2} \frac{v'(t) - qe^{-j2\pi/3}v(t)}{w_2'(t) - qe^{-j2\pi/3}w_2(t)} dt .$$

The functions $w_1(t)$, $w_2(t)$, $v(t)$ and their derivatives w_1' , w_2' , and v' are Fock type Airy functions defined as [Wait and Conda, 1959]

$$w_1(t) = \frac{1}{\sqrt{\pi}} \int_{-\infty}^{\infty} e^{j2\pi/3} \exp(st-s^3/3) ds = u(t)-jv(t) \quad (4.58)$$

$$w_2(t) = \frac{1}{\sqrt{\pi}} \int_{-\infty}^{\infty} e^{-j2\pi/3} \exp(st-s^3/3) ds = u(t)+jv(t) .$$

These functions have been tabulated by Fock [1964] and are related to the Miller type Airy functions, $Ai(t)$ and $Bi(t)$, by

$$u(t) = \sqrt{\pi} Bi(t)$$

$$v(t) = \sqrt{\pi} Ai(t)$$

The first term in the rounded edge diffraction coefficient in Eq. (4.50) is identical to the knife-edge diffraction coefficient defined in Eq. (4.40) (except for the image contribution). The other two terms account for the curvature and extent of the edge along the direction of propagation.

Defining a set of parameters

$$v = |2\sin\theta| \sqrt{\frac{2d_1 d_2}{\lambda(d_1+d_2)}} \quad (4.59)$$

and

$$\rho = \sqrt{\frac{2}{\pi}} \frac{|x|}{v} = \sqrt{\frac{\lambda(d_1+d_2)}{\pi d_1 d_2}} M \quad (4.60)$$

the rounded edge diffraction coefficient can also be written as

$$\hat{D} = g(\theta) \sqrt{\frac{kd_1 d_2}{d_1 + d_2}} \left\{ \text{sgn}(\theta) F_0(v) e^{j\frac{\pi}{2}v^2} - \rho G(x, q) \right\} \quad (4.61)$$

where

$$G(x, q) = \frac{e^{-j\pi/4}}{2\sqrt{\pi x}} + \hat{P}(x, q) \quad (4.62)$$

The diffraction loss when the observation point is in the shadow zone is then given by

$$L_D = \frac{|\hat{D}|^2}{kd_2} \frac{d^2}{d_1(d_1 + \tau + d_2)} = \left| \text{sgn}(\theta) F_0(v) e^{j\frac{\pi}{2}v^2} - \rho G(x, q) \right|^2 \quad (4.63)$$

where use has been made of the approximation $d = d_1 + \tau + d_2$. This expression for the diffraction loss due to a rounded edge is identical to that obtained by Wait and Conda [1959].

4.4.2.1 Transition Region and Shadow Boundary Solutions

On the shadow boundary ($\theta=0$, $\theta_1=\pi/2$), we have that $v=0$, $x=0$, $\tau=0$, and $F_0(0)=1/2$ so that the total field is given by

$$\lim_{\theta \rightarrow 0} E_r = \begin{cases} E_i(d) \left[\frac{1}{2} - \rho G(0, q) \right] & , \text{ if } \theta < 0 \\ E_i(d) + E_i(d) \left[-\frac{1}{2} - \rho G(0, q) \right] & , \text{ if } \theta > 0 \end{cases} \quad (4.64)$$

which shows that the field is continuous across the shadow boundary.

The function $G(x, q)$ has been solved numerically for $q=0$ (perfectly conducting obstacle and vertical polarization) and $q=\infty$

(perfectly conducting obstacle and vertical polarization) and $q=\infty$ (perfectly conducting obstacle and horizontal polarization) by Wait and Conda [1959] for values of $-3 < x < 2$. The real and imaginary parts of $G(x,0)$ and $G(x,\infty)$ are shown in Figure 4-23. The diffraction loss due to a perfectly conducting rounded edge is shown in Figure 4-24 as a function of the Fresnel parameter, v , for values of the normalized curvature of the edge $0 < \rho < 0.5$. These curves show that when the incident field is vertically polarized, the field in the shadow zone ($\theta > 0$) increases as the edge curvature increases ($\rho > 0$). However, if the incident field is horizontally polarized the field in the shadow zone decreases (greater diffraction loss) as the edge curvature increases.

Finite obstacle conductivity results in values of q other than 0 or ∞ . The range of values of q that might be encountered in practice depends on the polarization, radius of curvature, and the electrical constants of the diffracting obstacles. The dielectric constant and conductivity of the obstacle jointly influence the field strength behind the obstacles in accordance with the following expression for the complex dielectric constant relative to vacuum:

$$\epsilon = \epsilon_r - j 18 \sigma / f_{\text{GHz}} = \epsilon_r - j 60 \sigma \lambda$$

where σ is in mho/m, f_{GHz} is the frequency in GHz, and λ is the wavelength in meters. At frequencies above 100 MHz both the dielectric constant ϵ_r and conductivity σ of different types of soil and terrain vary with frequency so that account must be taken of these variations. The dependence of the electrical constants on frequency is shown in Figure 4-25 for various types of terrain. The ratio of $60 \sigma \lambda$ to ϵ_r for frequencies between 1GHz

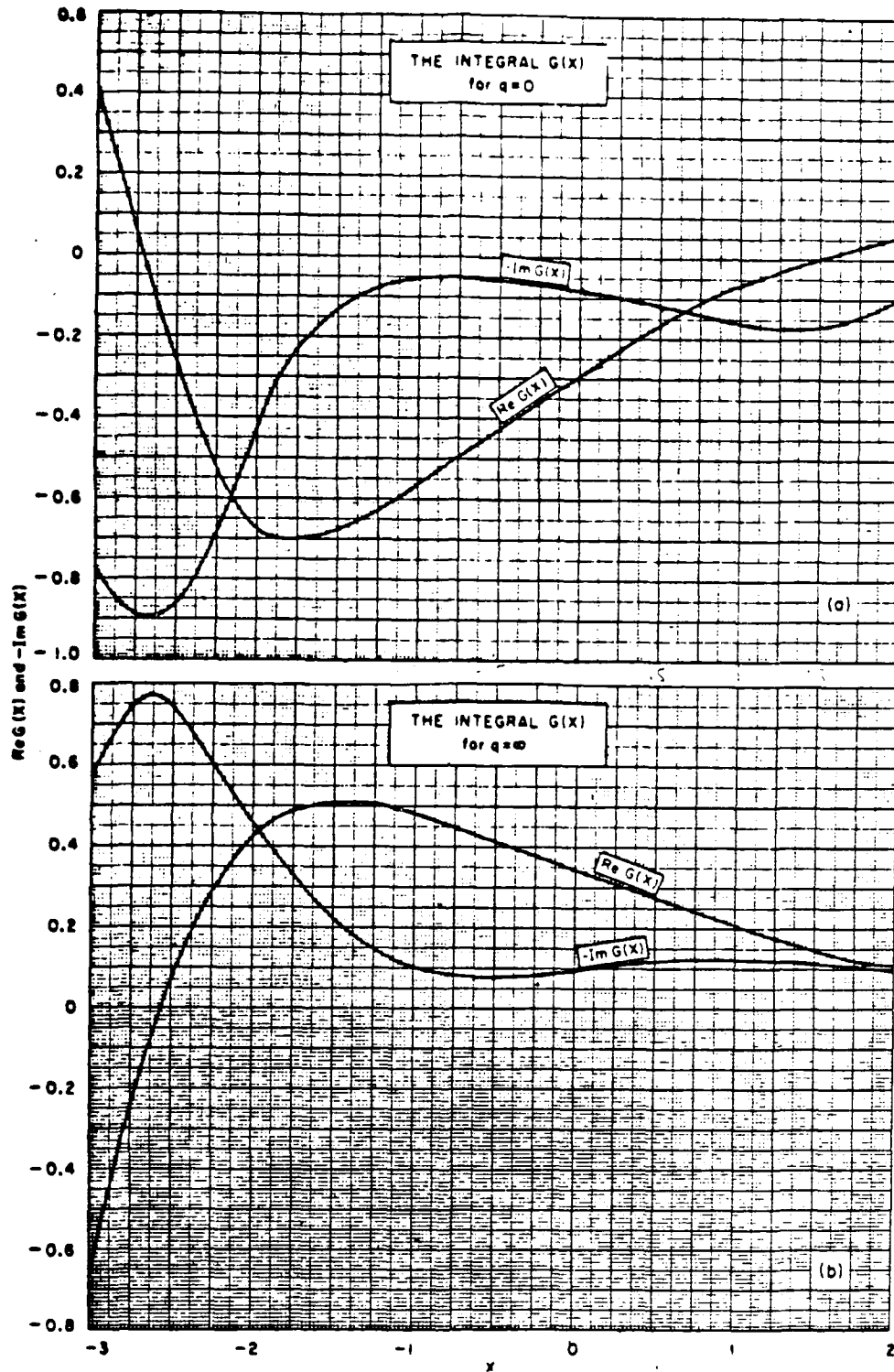


Figure 4-23 (a) Real and imaginary parts of the integral $G(x)$ as a function of x for $q=0$. (b) Real and imaginary parts of the integral $G(x)$ as a function of x for $q=\infty$. [Wait and Conda, 1959]

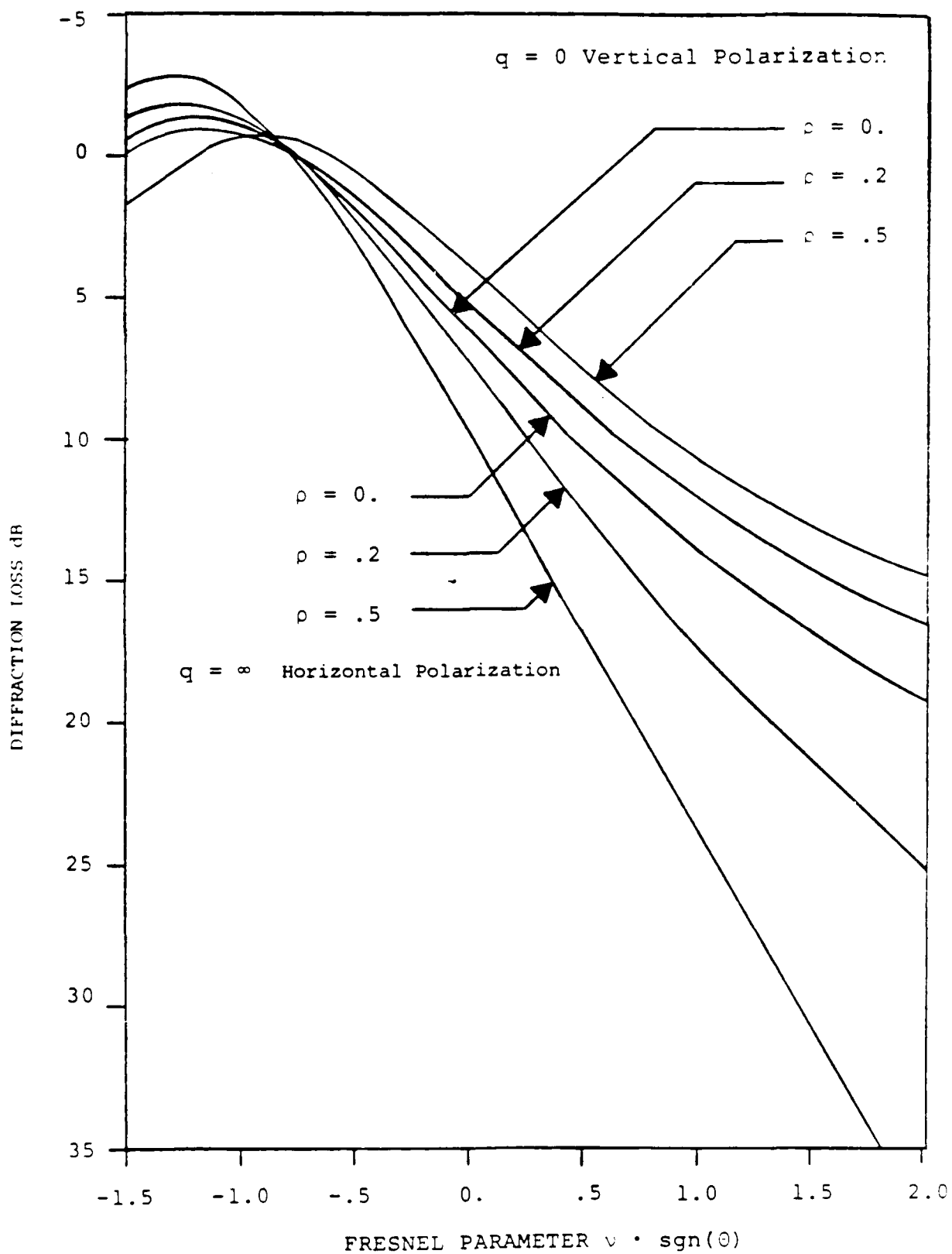


Figure 4-24 Diffraction Loss Due to a Perfectly Conducting Rounded Obstacle

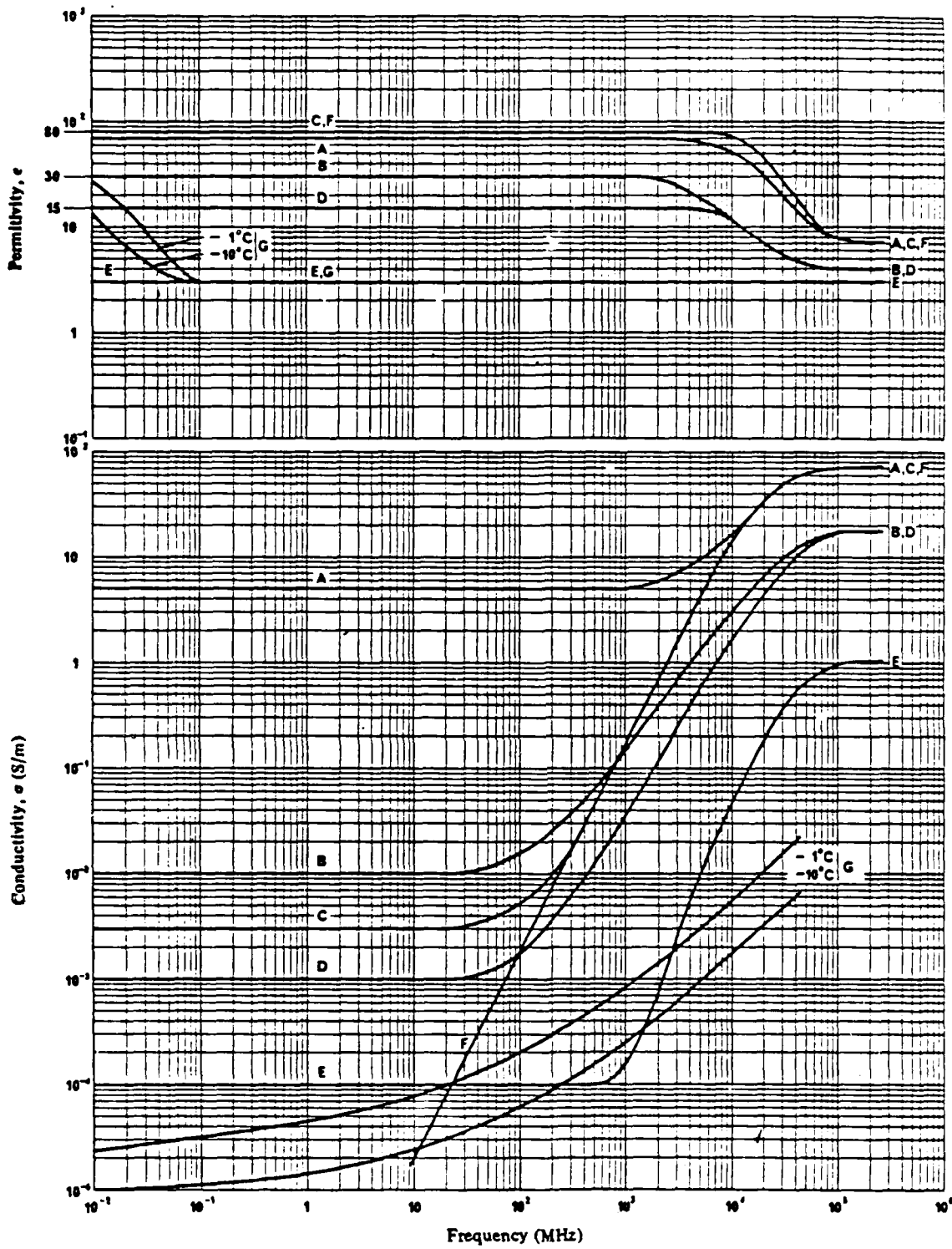


Figure 4-25 — Permittivity, ϵ , and conductivity, σ , as a function of frequency (CCIR, 1978)

- A: Sea water (average salinity), 20°C
- B: Wet ground
- C: Fresh water, 20°C
- D: Medium dry ground
- E: Very dry ground
- F: Pure water, 20°C
- G: Ice (Fresh water)

and 30 GHz for rocky (very dry ground), and sparsely vegetated (medium dry ground) obstacles is given below in Table 4-1.

Table 4-1
Ratio $60 \sigma\lambda/\epsilon_r$ vs. Frequency

Frequency	Very Dry Ground	Medium Dry Ground
1 GHz	9×10^{-4}	4.2×10^{-2}
3 GHz	5×10^{-3}	$1. \times 10^{-1}$
10 GHz	2.7×10^{-2}	2.5×10^{-1}
30 GHz	7.6×10^{-2}	7.5×10^{-1}

The ratios of Table 4-1 indicate that at the frequencies of interest the diffracting obstacles are mostly dielectric rather than conducting so that the parameter q is approximately given by

$$q = -j \left(\frac{\pi a}{\lambda} \right)^{1/3} / \sqrt{\epsilon_r} \quad , \text{ vertical polarization}$$

$$q = -j \left(\frac{\pi a}{\lambda} \right)^{1/3} \sqrt{\epsilon_r} \quad , \text{ horizontal polarization .}$$

Hence, for equal obstacle characteristics the magnitude of q for vertical polarization is smaller than that for horizontal polarization (since $\epsilon_r > 1$).

Wait and Conda [1959] have evaluated the rounded edge correction factor $\hat{G}(x, q)$ for various values of q between 0 and ∞ . Their results show that when the magnitude of q is greater

than 2.25 there is no noticeable difference between the factor $\hat{G}(x,q)$ corresponding to the actual value of q and that for $q=\infty$. This implies that when the radius of curvature of the diffracting obstacle a is such that

$$M = \left(\frac{\pi a}{\lambda}\right)^{1/3} > 8.7 \quad (4.65)$$

we can use the curves of Figure 4-24 for $q=\infty$ to estimate the diffraction loss for vertically polarized incident fields as well as for horizontally polarized. The above restriction (4.65) applies only to vertical polarization. When the incident field is horizontally polarized, the radius of curvature of the obstacle need only be greater than the wavelength in order for the curves for $q=\infty$ to apply.

At the other extreme, when the magnitude of q is less than 0.1, the curves for $q=0$ apply to both vertical and horizontal polarization. However when $|q| < 0.1$, the radius of curvature is much smaller than the wavelength so that the obstacle is for all practical purposes a knife-edge ($\rho=0$). This implies that the field strength behind a knife-edge is not only independent of the polarization but also of the electrical constants of the edge.

4.4.2.2 Shadow and Lit Region Solutions

The function $G(x,q)$ converges poorly for values of $x > 2$ (shadow region) and $x < -3$ (lit region).

In the shadow region, we have that $v \gg 1$, $\xi \gg 1$ and $x > 2$ so that the following asymptotic solutions apply

$$F_0(v) \sim \frac{e^{-j\pi/4}}{\sqrt{2}\pi v} e^{-j\frac{\pi}{2}v^2}$$

$$F_{kp}(x) \sim 1$$

$$\hat{P}(x, q) = -\frac{e^{-j\pi/12}}{2\sqrt{\pi}} \sum_{n=1}^{\infty} \beta_n \exp(\alpha_n x e^{-j5\pi/6}) \quad (4.66)$$

where the α_n are roots of the equation

$$A_i'(-\alpha_n) + qe^{-j\pi/3} A_i(-\alpha_n) = 0 \quad (4.67)$$

and

$$\beta_n = \frac{1}{[\alpha_n A_i^2(-\alpha_n) + A_i'^2(-\alpha_n)]} \quad (4.68)$$

The edge diffraction coefficient in the shadow zone ($x > 2$) reduces to

$$\hat{D} = \frac{e^{-j\pi/12}}{\sqrt{2}\pi} M \sqrt{\frac{d_1}{d_1 + \tau}} \sum_{n=1}^{\infty} \beta_n \exp\{\alpha_n x e^{-j5\pi/6} - jk\tau\} \quad (4.69)$$

which is identical to that obtained by Keller [1956] for the cases $q=0$ and $q=\infty$.

In the lit region we have that $v \gg 1$, $\xi \ll 1$ and $x < -3$ so that the following asymptotic solutions apply [James, 1980]

$$F_{kp}(x) \sim 1$$

$$\hat{P}(x, q) = - \frac{jx-2q}{jx+2q} \frac{-x}{4} e^{jx^3/12} \quad (4.70)$$

The total field in the lit region reduces to

$$E_r = E_i(d) + E_i(d_1)R(q, \theta_i) \sqrt{\frac{ad_1^2 \cos \theta_i}{[a(d_1+d_2) \cos \theta_i + 2d_1 d_2](d_1+d_2)}} e^{-jkd_2} \quad (4.71)$$

where $R(q, \theta_i)$ is the Fresnel reflection coefficient

$$R(q, \theta_i) = \frac{jx-2q}{jx+2q} = \frac{\cos \theta_i - Z}{\cos \theta_i + Z} \quad (4.72)$$

and Z is the normalized surface impedance defined in Equation (4.56). Note that when the surface is perfectly conducting $R=1$ for vertical polarization ($q=0$) and $R=-1$ for horizontal polarization ($q=\infty$) in which case (4.71) reduces to the geometrical optics field solutions for a perfectly conducting cylindrical surface [Pathak, et al., 1980].

4.4.2.3 Polynomial Approximations

The use of Equation (4.63) to calculate the diffraction loss due to a rounded edge is cumbersome and requires numerical evaluation of Equation (4.62) for a given edge curvature a , diffraction angle θ , and wavelength λ . The calculation of the diffraction loss can be simplified considerably by using suitable polynomial approximations. The diffraction loss for observation points in the shadow zone can be expressed in dB as

$$A(v, \rho) = -20 \log | F_0(v) e^{-j\frac{\pi}{2}v^2} - \rho G_1(x) | \quad (4.73)$$

where $G_1(x) = G(x, \infty)$ and $x = \sqrt{\pi/2} v\rho$. Equation (4.73) can also be expressed in the form

$$A(v, \rho) = A(v, 0) + A(0, \rho) + U(v\rho) \quad (4.74)$$

by defining

$$A(v, 0) = -20 \log | F_0(v) |$$

$$A(0, \rho) = -20 \log | 1/2 - \rho G_1(0) |$$

$$U(v\rho) = A(v, \rho) - A(v, 0) - A(0, \rho) .$$

The first term in (4.74) is the well known knife-edge diffraction loss which is well approximated by

$$A(v, 0) = -10 \log \left[\frac{1}{2} \{f^2(v) + g^2(v)\} \right], \theta > 0 \quad (4.75)$$

where [Abramowitz and Stegun, 1964]

$$f(v) = \frac{1 + .926v}{2 + 1.792v + 3.104v^2}$$

$$g(v) = \frac{1}{2 + 4.142v + 3.492v^2 + 6.67v^3}$$

The second term in (4.74) is a correction term for the additional loss at grazing incidence ($\theta=0$, $v=0$) due to the curvature of the edge. A polynomial approximation to this factor has been obtained by Dougherty and Wilkerson [1967] and is of the form

$$A(0, \rho) = 6.02 + 7.192\rho - 2.018 \rho^2 + 3.63 \rho^3 - 0.754 \rho^4 \text{ dB.} \quad (4.76)$$

This polynomial approximation is somewhat different from that used in NBS Tech. Note 101 [Rice, et al., 1967]. They use an approximation based on the earlier results of Dougherty and Maloney [1964] which contained an error in the derivation of the diffraction factor $G_1(x)$ at grazing incidence ($x=0$). The corrected version is given in a subsequent paper by Dougherty and Wilkerson [1967].

For points within the shadow region ($\theta > 0$), an additional term $U(v\rho)$ must be added to account for propagation losses along the surface between horizons. A polynomial approximation to this factor is given by Dougherty and Wilkerson [1967] and is of the form:

For $v\rho < 2$

$$U(v\rho) = -6.02 - 6.7v\rho + (43.6 + 23.5 v\rho) \log_{10}(1+v\rho) \text{ dB.} \quad (4.77a)$$

For $v\rho > 2$

$$U(v\rho) = -14.13 + 22 v\rho - 20 \log v\rho \text{ dB.} \quad (4.77b)$$

This polynomial approximation is also different from that used in NBS Tech. Note 101 [Rice, et al., 1967] for the same reasons given above.

4.5 MULTIPLE EDGE DIFFRACTION

The Uniform Geometrical Theory of Diffraction (UGTD) can be extended to treat the problem of multiple-edge diffraction provided some care is taken in defining the detour (Fresnel) parameter for each edge to ensure continuity of the diffracted field across shadow boundaries. The form of the total diffracted field depends on the number of ray paths between transmitter and receiver. If each edge is in the shadow zone of the previous edge and the receiver is in the shadow zone of the last edge, then there is a single ray path between transmitter and receiver as shown in Figure 4-26a. If that is not the case, then there may be as many as 2^n ray paths, depending on the obstacle and terminal heights (see Figures 4-26b and c), where n is the number of edges. The field due to each of these rays must be accounted for explicitly.

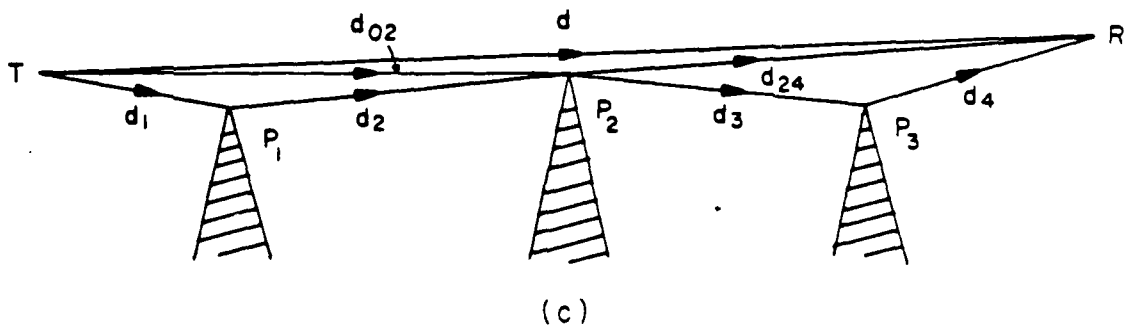
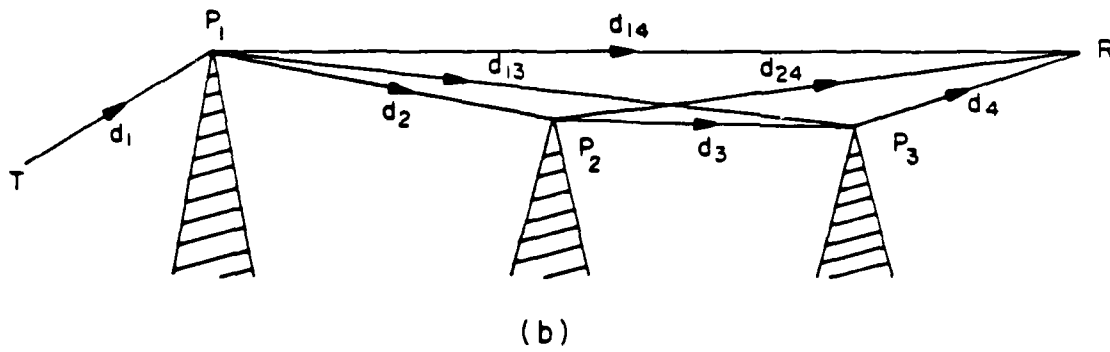
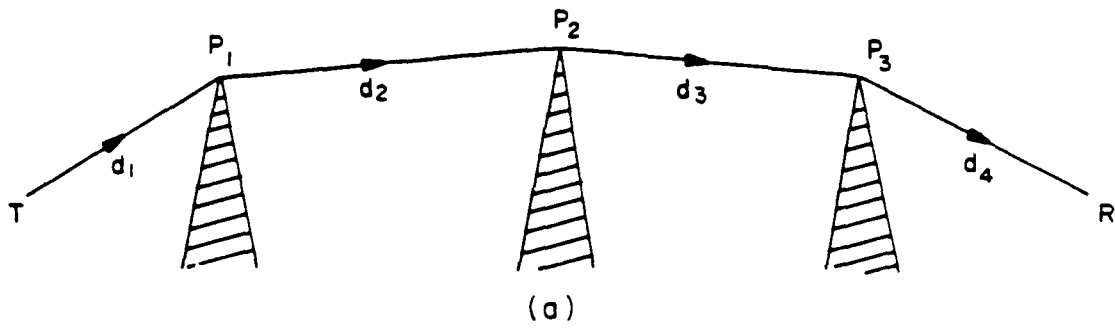


Figure 4-26 Multiple edge diffraction geometries

4.5.1 Field in the Shadow Zone

Let us first consider the geometry of Figure 4-26a. The received field at R may be expressed in terms of the field incident on the last edge at P_3 , $E(P_3)$, as

$$E(R) = E(P_3) \frac{\hat{D}_{234}}{\sqrt{kd_4}} \sqrt{\frac{d_1+d_2+d_3}{d_1+d_2+d_3+d_4}} e^{-jkd_4} \quad (4.78)$$

where \hat{D}_{234} is the edge diffraction coefficient for the third edge taking the second edge as the source and the receiver as the observation point, and $E(P_3)$ is the field incident on the third edge. The factor $\sqrt{kd_4}$ accounts for the cylindrical spreading between the edge and the receiver and the factor inside the other radical accounts for the azimuthal spreading between the edge and the receiver.

The field incident on the third edge, $E(P_3)$, can similarly be expressed in terms of the field incident on the second edge, $E(P_2)$, as

$$E(P_3) = E(P_2) \frac{\hat{D}_{124}}{\sqrt{kd_3}} \sqrt{\frac{d_1+d_2}{d_1+d_2+d_3}} e^{-jkd_3} \quad (4.79)$$

where \hat{D}_{124} is the edge diffraction coefficient for the second edge taking the first edge as the source and the receiver as the observation point, and $E(P_2)$ is the field incident on the second edge. The other factors account for cylindrical spreading between the second and third edges in the azimuthal and elevation planes.

By following the same procedure to calculate the field incident on P_2 and recalling that the field incident in the first

edge is inversely proportional to d_1 , it can be shown that the ratio of the received power at R to the transmitted power (transmission loss) is given by

$$\frac{P_R}{P_T} = G_T G_R \left(\frac{\lambda}{4\pi d_1} \right)^2 \frac{|\hat{D}_{014}|^2}{kd_2} \frac{|\hat{D}_{124}|^2}{kd_3} \frac{|\hat{D}_{234}|^2}{kd_4} \left(\frac{d_1}{d_1+d_2+d_3+d_4} \right) \quad (4.80)$$

where \hat{D}_{014} , \hat{D}_{124} and \hat{D}_{234} are the edge diffraction coefficients for the first, second and third edges, respectively, taking the previous edge (or the transmitter in the case of the first edge) as the source and the receiver as the observation point. The factor proportional to d_1^{-2} represents the spherical spreading loss between the transmitter and the first edge, while the factors proportional to d_2^{-1} , d_3^{-1} and d_4^{-1} represent the cylindrical spreading loss (in the elevation plane) between edges, and last factor in brackets is the azimuthal cylindrical spreading loss between the first edge and the receiver.

We will now show that the diffraction loss for the case in which each edge is in the shadow zone of the previous edge, and the receiver is in the shadow zone of the last edge (all diffraction angles are positive) is equal to the product (i.e., sum in dB) of the diffraction losses due to each edge.

The edge diffraction coefficients are of the form of Eq. (4.44) if the edges are knife-edges and Eq. (4.61) if they are rounded edges. In either case, the edge diffraction for the n^{th} edge is given by

$$\hat{D}_{mn4} = \sqrt{\frac{kd_{mn}d_{n4}}{d_{mn}+d_{n4}}} f(\phi_{np}-\phi_{mn}, \nu_{mn}, \rho_{mn}), \quad \begin{matrix} n=1,2,3 \\ m=n-1 \\ p=n+1 \end{matrix} \quad (4.81)$$

where d_{mn} is the distance from the previous edge (or transmitter if $n=1$) to the n^{th} edge, d_{n4} is the distance from the n^{th} edge to the receiver (see Figure 4-27) and $f(\theta_n, v_{mn}, \rho_{mn})$ is the diffraction loss due to the n^{th} edge which is a function of the diffraction (or scattering) angle $\theta_n = \phi_{np} - \phi_{mn}$ (see Figure 4-27), the Fresnel parameter v_{mn} , and normalized edge curvature parameter ρ_{mn} . In fact $f(\theta, v, \rho)$ is given by the quantity in brackets in Eq. (4.63), which reduces to the modified Fresnel integral when the edge is a knife-edge (zero curvature). The Fresnel parameter and normalized edge curvature parameters are defined as

$$v_{mn} = \left| 2 \sin \frac{\phi_{np} - \phi_{mn}}{2} \right| \sqrt{\frac{2d_{mn}d_{n4}}{\lambda(d_{mn} + d_{n4})}} \quad (4.82)$$

$$\rho_{mn} = \left(\frac{kR_n}{2} \right)^{1/3} \sqrt{\frac{\lambda(d_{mn} + d_{n4})}{\pi d_{mn}d_{n4}}} \quad (4.83)$$

where the distances are shown in Figure 4-27 and R_n is the curvature of the n^{th} edge.

Substituting (4.81) into Eq. (4.80) yields the following expression for the received power:

$$\frac{P_R}{P_T} = G_T G_R \left(\frac{\lambda}{4\pi d_{04}} \right)^2 \left| f(\theta_1, v_{01}, \rho_{01}) f(\theta_2, v_{12}, \rho_{12}) f(\theta_3, v_{23}, \rho_{23}) \right|^2 \quad (4.84)$$

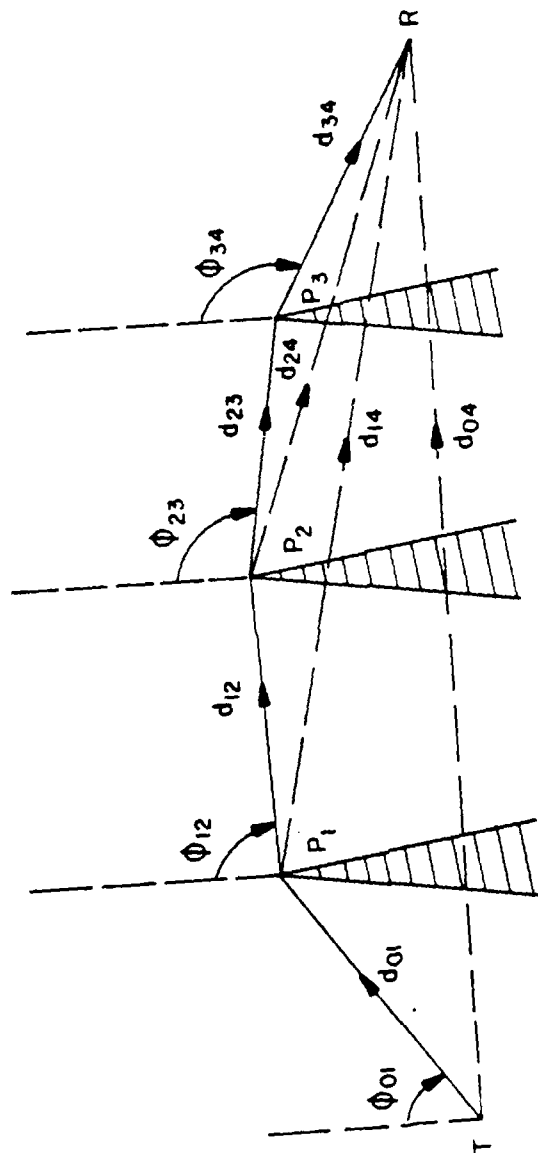


Figure 4-27 Distances and scattering angles for triple-edge diffraction (shadow zone)

where use has been made of the approximations

$$d_{04} = d_{01} + d_{12} + d_{23} + d_{34}$$

$$d_{14} = d_{12} + d_{23} + d_{34}$$

$$d_{24} = d_{23} + d_{34}.$$

Equation (4.84) is recognized as the product of the free-space propagation loss and the diffraction losses. The diffraction loss due to each obstacle is not reciprocal because the receiver location is used as the observation point in the calculation of the losses (i.e., the attenuation function $f(\theta, \nu, \rho)$) and therefore it depends on which of the terminals is designated as the receiver. The total diffraction loss (product of the attenuation functions) is, however, reciprocal. Reciprocity can be proved rigorously for large diffraction angles as the edge diffraction coefficients (Eqs. (4.47) or (4.69) depend on the diffraction angle and edge radius of curvature only and Eq. (4.77) is reciprocal. For small diffraction angles, reciprocity can only be proved by evaluating the attenuation functions numerically. If the Fresnel (detour) parameters had been chosen so as to make the diffraction loss due to each obstacle reciprocal, then the expression for the total received field, Eq. (4.84), would contain additional spreading factors and the field would not be continuous across shadow boundaries [Parl and Malaga, 1980].

4.5.2 Field in the Lit Zone

When the receiver is in the lit zone of one or more edges (except the last one) or the source, i.e., there is a line-of-sight path between them, then there are multiple ray paths between the source, each edge and the observation point. The

number of rays depends on the actual geometry. For example the geometry of Figure 4-26b shows four rays, one of which has undergone single scattering (from 1st edge), two of which have undergone double scattering (from 1st and 2nd edges, and 1st and 3rd edges), and one which has undergone triple scattering. The geometry of Figure 4-26c shows five rays: one is a line-of-sight ray, one has undergone single scattering from the second edge, another has undergone double scattering from the second and third edges, a fourth ray has undergone double scattering from the first and second edges and the fifth has undergone triple scattering.

The total received field for arbitrary obstacle heights relative to the transmitter and receiver heights can be expressed as a sum of the contributions from each individual ray as*

$$\begin{aligned}
 E_R = & E_{123} + H(\phi_{23} - \phi_{34})E_{12} + H(\phi_{12} - \phi_{23})E_{13} + H(\phi_{01} - \phi_{12})E_{23} \\
 & + H(\phi_{12} - \phi_{24})H(\phi_{13} - \phi_{34})E_1 + H(\phi_{23} - \phi_{34})H(\phi_{01} - \phi_{12})E_2 \\
 & + H(\phi_{01} - \phi_{13})H(\phi_{02} - \phi_{23})E_3 + H(\phi_{01} - \phi_{14})H(\phi_{02} - \phi_{24})H(\phi_{03} - \phi_{34})E_i .
 \end{aligned}
 \tag{4.85}$$

where E_i is the field due to the direct (or LOS) ray, E_1 , E_2 and E_3 are the field contributions due to rays which have undergone single scattering from the first, second, and third edges, respectively, E_{12} is the field contribution from the ray which

* NOTE: The electric field is a vector quantity and therefore the sum of Eq. (4.85) should be interpreted as a vector sum.

has undergone double scattering from the first and second edges, E_{13} is the field contribution from the ray which has undergone double scattering from the first and third edges, E_{23} is the field due to the ray scattered by the second and third edges and E_{123} is the field due to the triple scattered ray. The function $H(x)$ is the Heaviside step function which is unity when its argument is greater than zero and zero otherwise. Thus, the number of rays which contribute to the total received field depends on the values of the angles ϕ_{ij} , $i=0,1,2,3$, and $j>i$ defined in Figure 4-28, which in turn vary according to the geometry. Note that Eq. (4.85) also applies to the case in which all edges are in the shadow zone of the previous edges and the observation point is in the shadow zone of the last edge.

The field due to the direct or LOS ray is given by

$$E_i = \frac{\sqrt{30 P_T}}{d_{04}} e^{-jkd_{04}} \quad (4.86)$$

The field due to the single scattered rays is given by

$$E_n = \frac{\sqrt{30 P_T}}{d_{0n}} \frac{\hat{D}_{0n4}}{\sqrt{kd_{n4}}} \sqrt{\frac{d_{0n}}{d_{0n}+d_{n4}}} e^{-jk(d_{0n}+d_{n4})}, \quad n=1,2,3 \quad (4.87)$$

where the \hat{D}_{0n4} are the edge diffraction coefficients and the distances d_{0n} and d_{n4} are shown in Figure 4-28.

The field due to the double scattered rays is given by

$$E_{mn} = \frac{\sqrt{30 P_T}}{d_{0m}} \frac{\hat{D}_{0m4}}{\sqrt{kd_{mn}}} \frac{\hat{D}_{mn4}}{\sqrt{kd_{n4}}} \sqrt{\frac{d_{0m}}{d_{0m}+d_{mn}+d_{n4}}} e^{-jk(d_{0m}+d_{mn}+d_{n4})} \quad (4.88)$$

where $m=1,2$, $n=2,3$ and $m \neq n$.

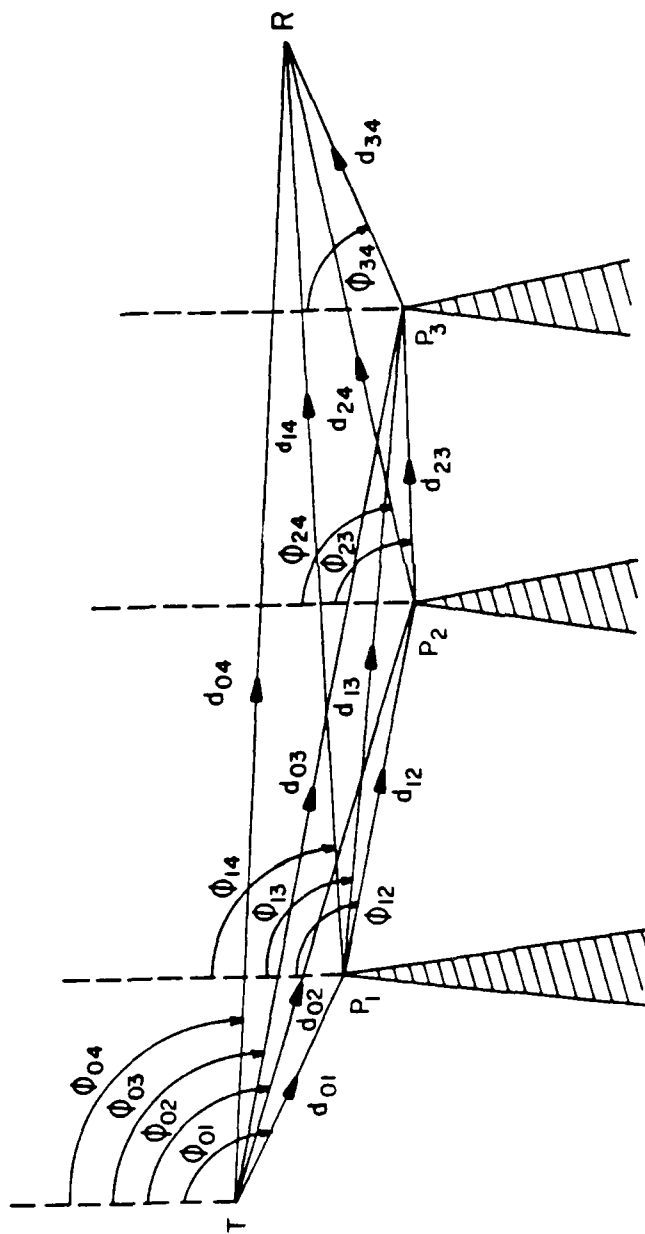


Figure 4-28 Distances and scattering angles for triple-edge diffraction (lit zone)

The field due to the triple scattered ray is given by

$$E_{123} = \frac{\sqrt{30 P_T} \hat{D}_{014}}{d_{01}} \frac{\hat{D}_{124}}{\sqrt{kd_{12}}} \frac{\hat{D}_{234}}{\sqrt{kd_{23}}} \frac{\hat{D}_{234}}{\sqrt{kd_{34}}} \cdot \sqrt{\frac{d_{01}}{d_{01}+d_{12}+d_{23}+d_{34}}} e^{-jk(d_{01}+d_{12}+d_{23}+d_{34})} \quad (4.89)$$

The edge diffraction coefficients \hat{D}_{mn4} , with $m=0,1,2$, and $n=1,2,3$, $n>m$ are as defined earlier in Eqs. (4.81), (4.82) and (4.83) but without the restrictions $m=n-1$ and $p=m+1$. The parameter p should be chosen so that the scattering angle $\phi_{np}-\phi_{mn}$ corresponds to that shown in Figure 4-28 for the appropriate ray and the edge where the ray is scattered. The choice of edge diffraction coefficients of Eq. (4.81) results in continuity of the electric field across shadow boundaries as the height of the observation point varies while the heights of the source and the edges remain fixed. The extension of Eqs. (4.85) through (4.89) to the case of more than 3 edges is straightforward. It merely requires that the appropriate number of rays be accounted for a particular geometry.

4.5.3 Comparison with Other Methods

The diffraction loss due to three knife-edges is plotted in Figures 4-29, 4-30 and 4-31, respectively, as a function of the receiver height for various combinations of obstacle heights as shown in each figure. The transmitter is assumed to be at ground level, the frequency is 1 GHz and the obstacles are spaced as shown in each figure. Two curves are shown in each plot. One represents the diffraction loss calculated using the UGTD ray technique (dashed line), and the other (solid line) is the diffraction loss calculated using the technique described in Section 4.2, i.e., the repeated application of Huyghens' principle. Good

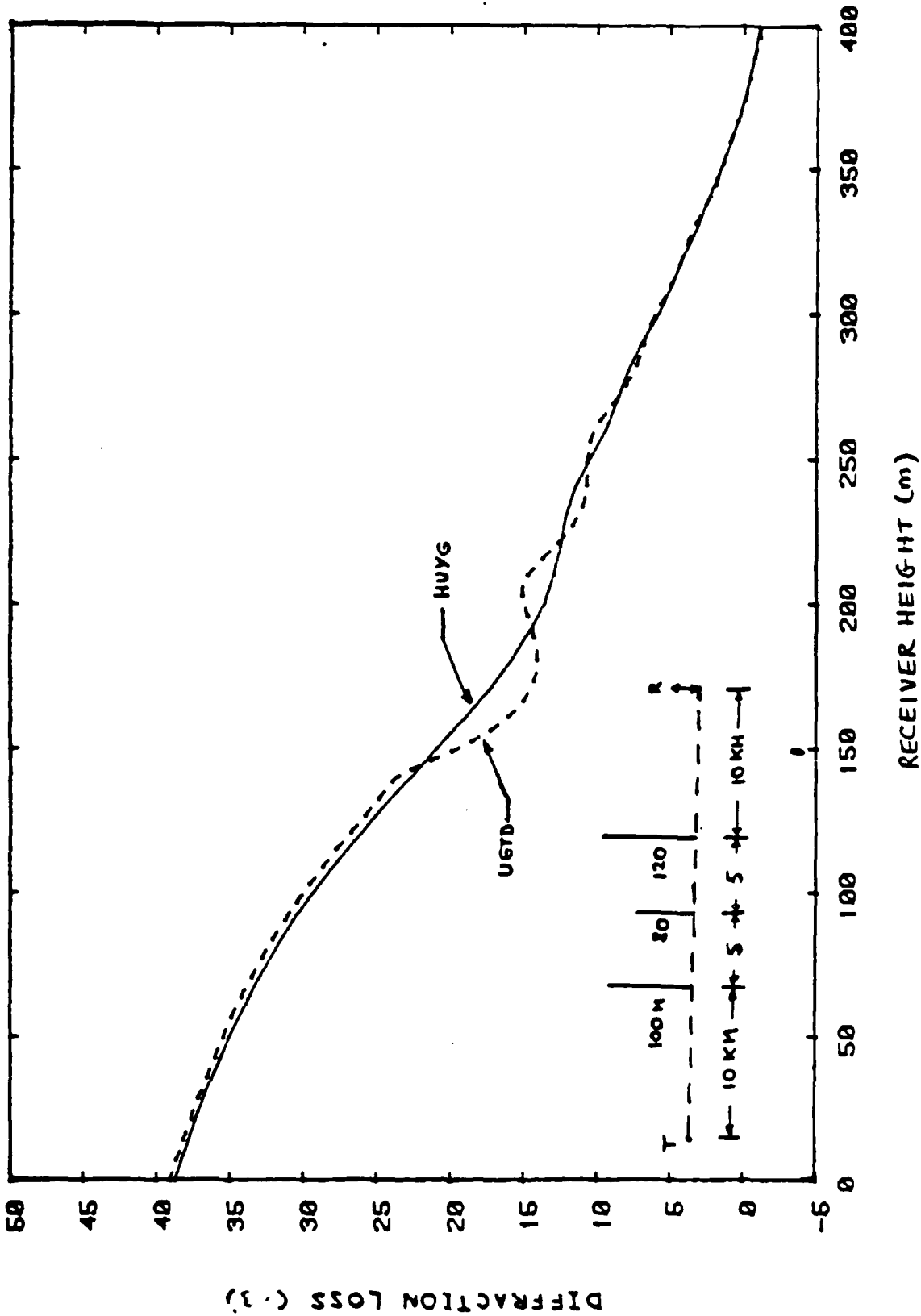


Figure 4-29 Comparison between UGTD ray method and integral solution (Huyghens' principle) for triple knife-edge geometry shown (Frequency = 1 GHz).

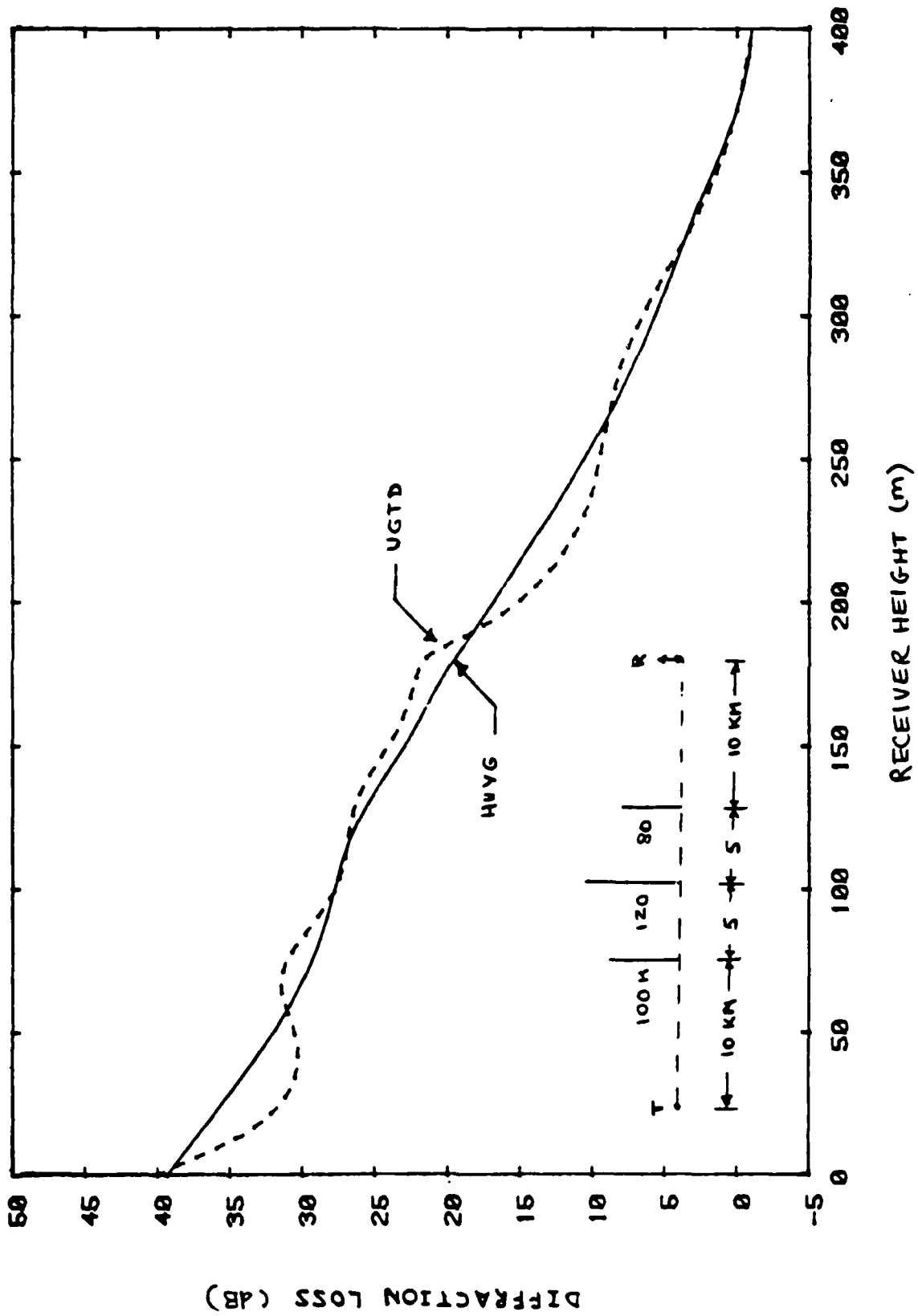


Figure 4-30 Comparison between UGTD ray method and integral solution (Huyghens' principle) for triple knife-edge geometry shown (Frequency = 1 GHz).

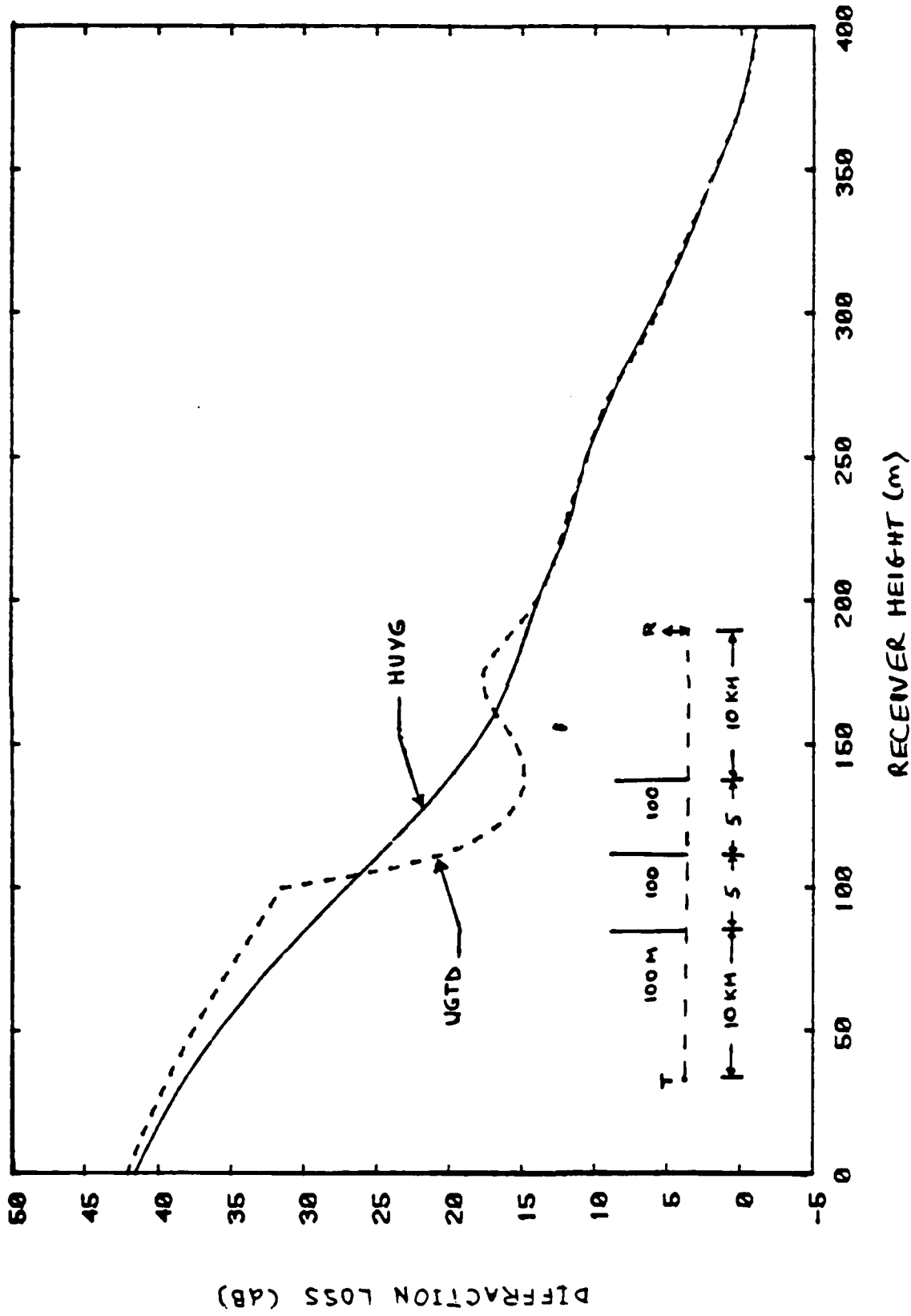


Figure 4-31 Comparison between UGTD ray method and integral solution (Huyghens' principle) for triple knife-edge geometry shown (Frequency = 1 GHz).

agreement is seen to occur for nearly all receiver heights, especially for the geometries of Figure 4-29 and 4-30. In the case where all knife-edges have equal heights (Figure 4-31) good agreement occurs for all receiver heights, except for heights around 100 meters. At those heights, the third edge is in the transition region of the second edge and the receiver is in the transition region of the third edge. The UGTD ray technique for multiple edge diffraction described in Section 4.5.2 is not accurate when the geometry results in overlapping transition regions.

Another example of the inaccuracy of the ray technique in multiple edge geometries with overlapping transition regions is shown in Figure 4-32. The diffraction loss calculated by the UGTD ray technique and the method of Section 4.2 for triple knife-edge diffraction is plotted in this figure as a function of the height of the second knife-edge while holding the heights of the first and third edges at 100 meters, and the transmitter and receiver fixed at zero. The frequency chosen for this example is 100 MHz to facilitate comparison with Vogler's [1982] results for this same geometry. Good agreement is seen when the height of the second obstacle is much less or greater than that of the other edges. However, when the height of the second edge crosses the shadow boundary of the first edge ($h_2=150$ meters), the diffraction loss calculated by the UGTD ray method is discontinuous. The reason for the discontinuity is that when the second edge is on the shadow boundary of the first edge, the field incident on the second edge is not a ray field. The total received field and the diffraction loss for this case can only be determined by the technique described in Section 4.2 or by Vogler's solution [1982] which is equivalent to that of Section 4.2 (i.e., solid line in Figure 4-32).

For geometries when the edges are not in transition regions of preceding edges, the UGTD ray solution is a good approximation

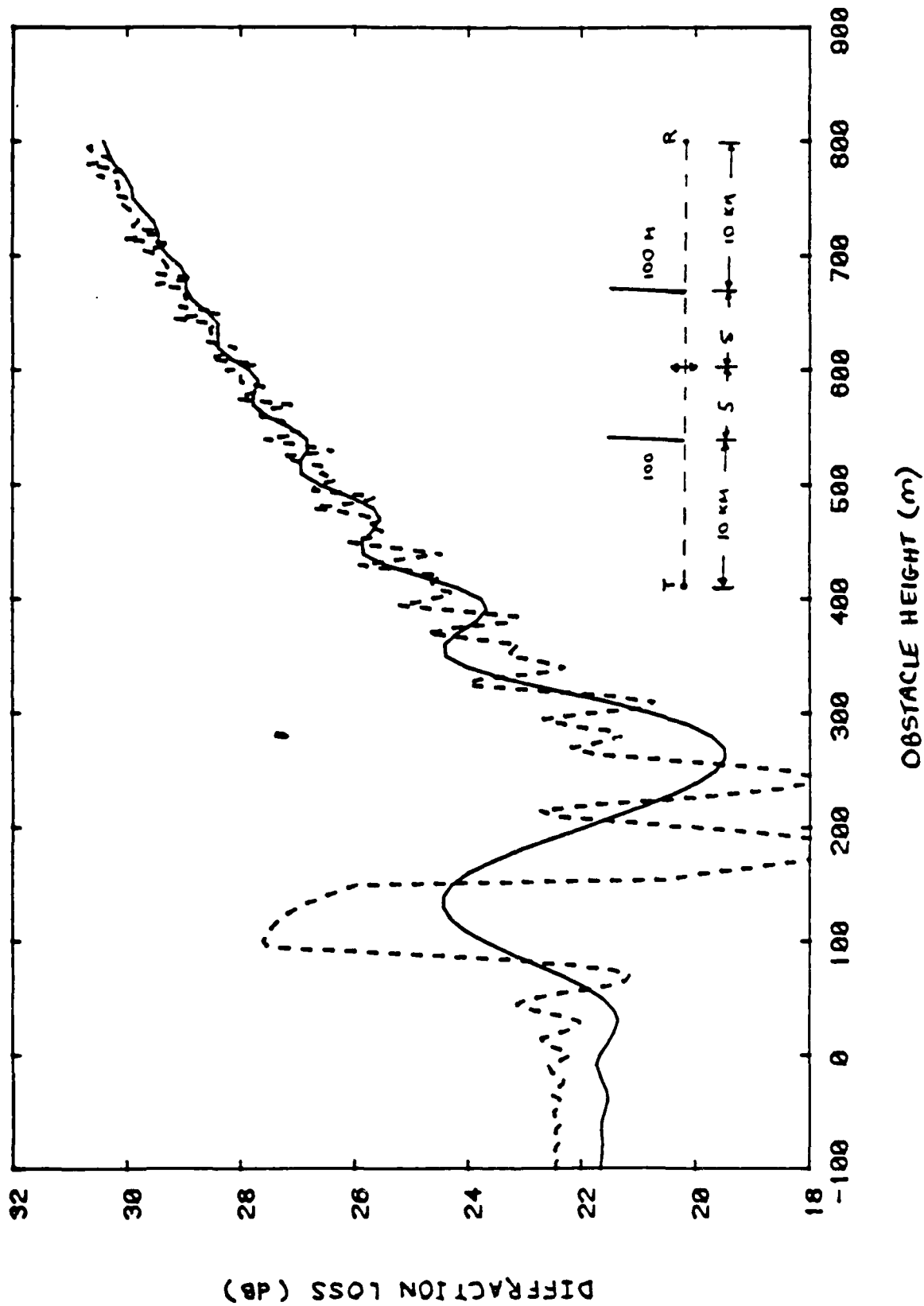


Figure 4-32 Comparison between UGTD ray method and integral solution (Huyghens, principle) for various triple knife-edge geometries (Frequency = 100 MHz).

to the exact solution and is computationally more efficient. Figures 4-33, 4-34 and 4-35 compare the UGTD ray solution with the Epstein-Peterson (E-P), Japanese-Atlas (J-A) method and Deygout (DEYG) method for calculating multiple edge diffraction losses for the geometries shown in each figure. The path is assumed to be a triple knife-edge diffraction path and the diffraction loss calculated using each technique is plotted as a function of the receiver height. For geometries and receiver heights where there is only one ray path (shadow zone), there is close agreement between all four solutions. However, in the region where there are multiple ray paths, the Epstein-Peterson and Japanese-Atlas solutions overestimate the loss by a large amount because they do not account for the appropriate number of rays and more importantly, do not use the correct diffraction angle for the more significant rays. The Deygout solution is in closer agreement in the multiple ray region because it does use the correct diffraction angle for the more significant rays but it is still not as accurate as the UGTD ray solution because it does not always account for the proper number of rays.

4.6 EDGE PROFILE EFFECTS

In earlier sections we discussed the theory of multiple diffraction by semi-infinite edges and its extension to account for the curvature of the obstacles along the propagation path. The profile of the obstacles in the plane transverse to the direction of propagation was assumed to be flat and of infinite extent. In this section we will discuss the effects of irregularity in the transverse profile of the obstacle. This is an important consideration because obstacle profile irregularity can be significant relative to the wavelength at microwave frequencies and may account for discrepancies between predicted and observed diffraction field patterns. Profile irregularity may be due to actual terrain variations or to the presence of houses,

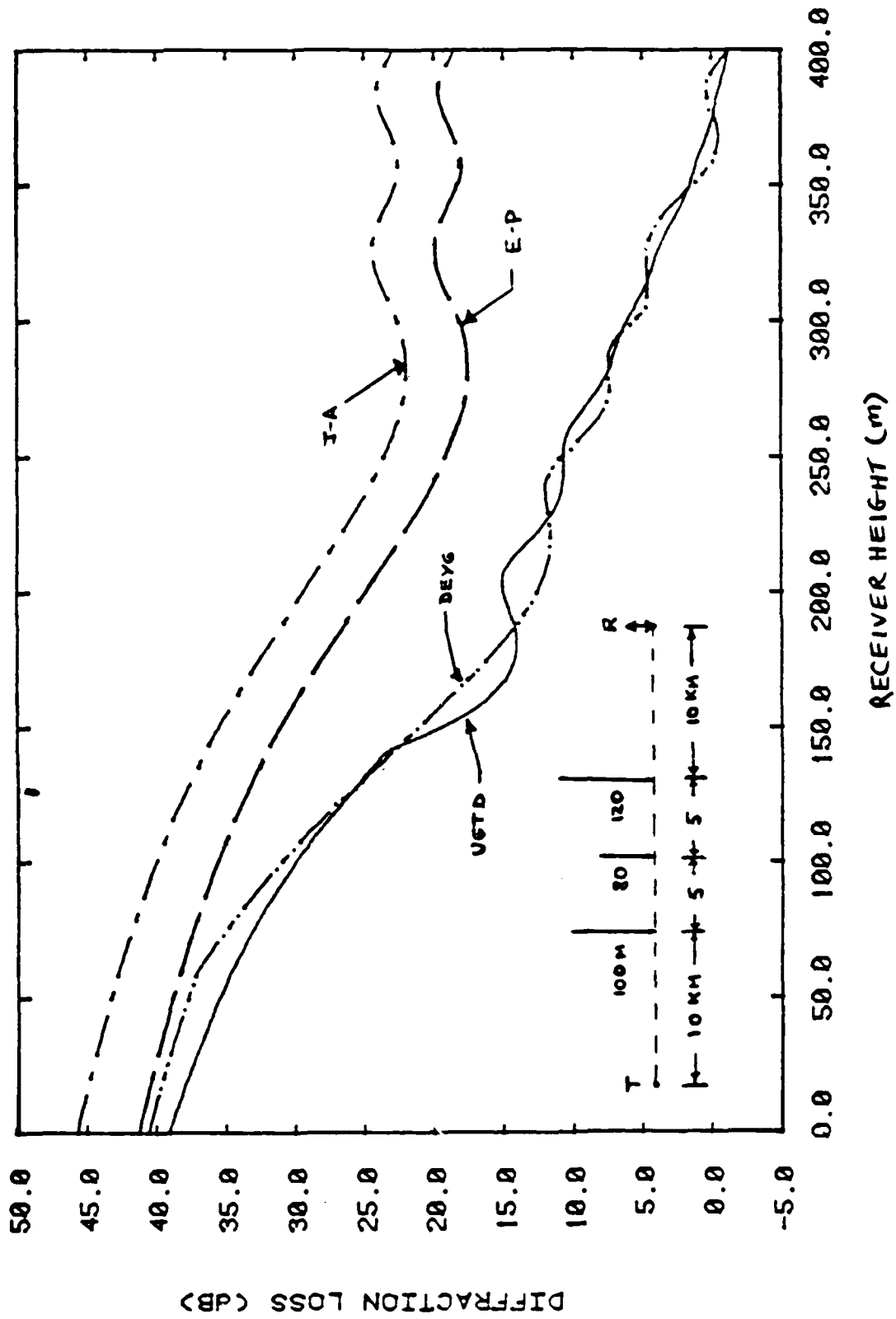


Figure 4-33 Comparison between UGTD, Epstein-Peterson, Japanese-Atlas and Deygout methods for triple knife-edge geometry shown (Frequency = 1 GHz).

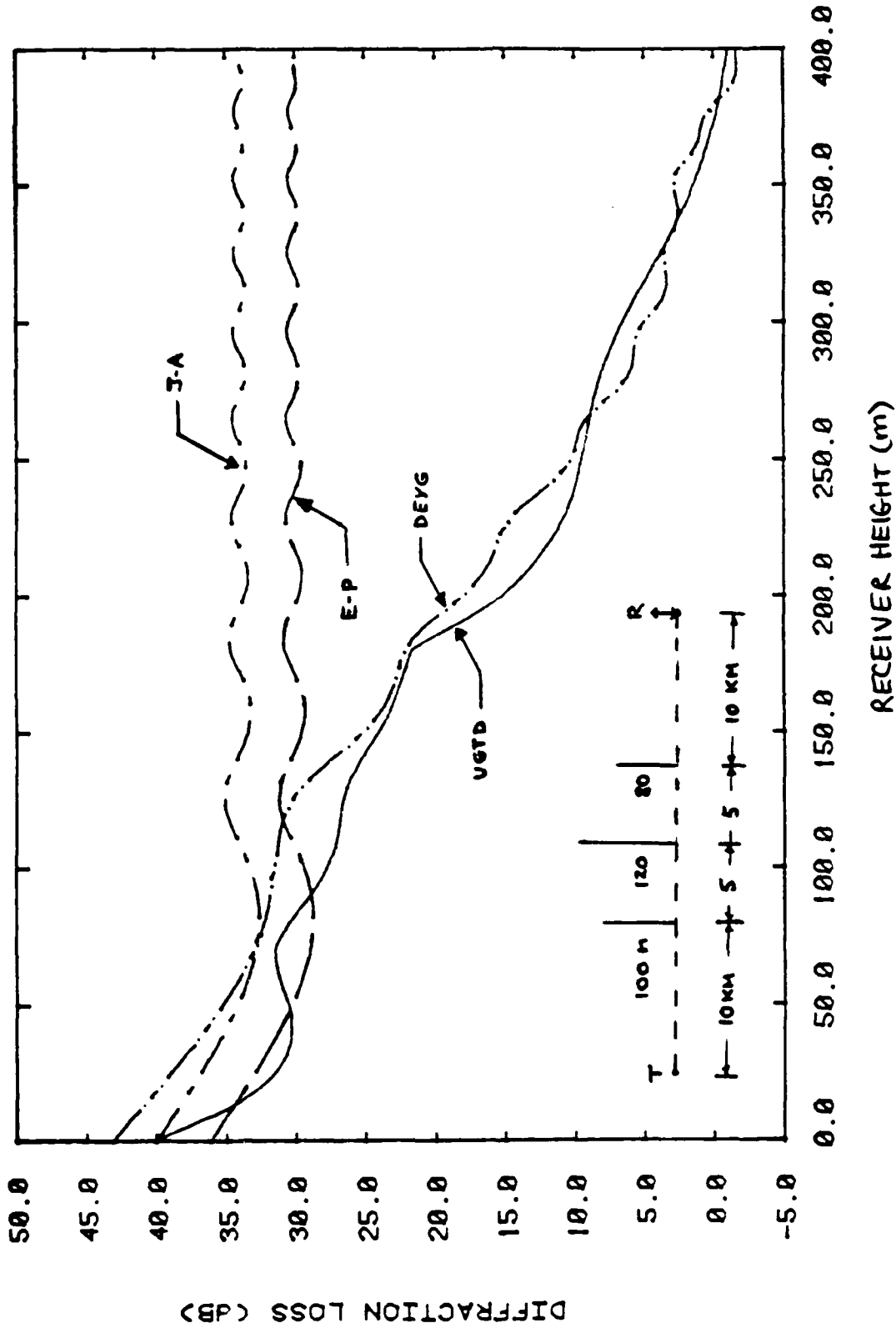


Figure 4-34 Comparison between UGTD, Epstein-Peterson, Japanese-Atlas and Deygout methods for triple knife-edge geometry shown (Frequency = 1 GHz).

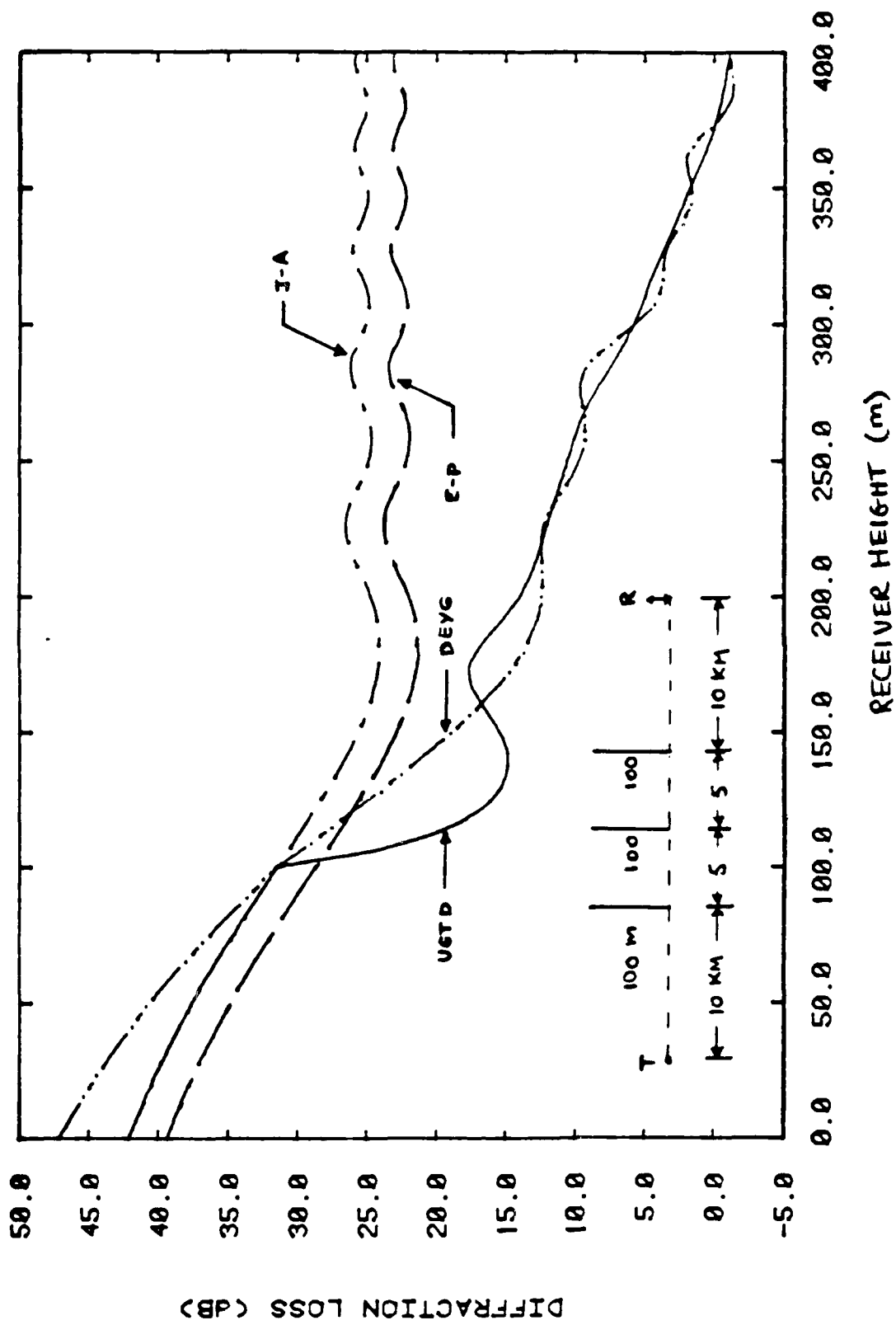


Figure 4-35 Comparison between UGTD, Epstein-Peterson, Japanese-Atlas and Deygout methods for triple knife-edge geometry shown (Frequency = 1 GHz).

isolated trees, outcroppings, etc., on the crest of otherwise flat or smooth hills.

The diffraction pattern of an obstacle with a slowly varying convex profile (transverse to the propagation path) has been shown to be similar to that for a semi-infinite knife-edge [Dougherty, 1969] except for a correction factor which accounts for the departure of the profile from a straight edge. When the profile is not slowly varying but rather irregular there may be more than one diffraction path which contributes to the total field behind the diffraction obstacle [Dougherty, 1970b]. To illustrate this effect consider the diffraction by a knife-edge with a triangular profile also referred to as a bilinear screen. An obstacle with such a profile can have more than one point of stationary phase. The total diffracted field is then the superposition of the contributions from each point of stationary phase.

Formally, the location of a point of stationary phase is given by the point on the diffracting edge at which the phase function of a wave incident on the edge is a minimum. For a knife-edge of semi-infinite extent in the plane perpendicular to the path, this point is where the straight lines directed from the source at T and the observation point at R towards the edge form supplementary angles with a unit tangent along the straight edge. That is the source T, receiver R and diffraction point O are all points on a common plane.

In the case of a bilinear screen, and obstacles with irregular profiles in general, we can visualize the existence of multiple stationary phase points by using an alternate view of the point of stationary phase. The source and observation points T and R are the foci of a family of confocal surfaces. Each surface is a surface of revolution about the line TR generated by the locus of points O for which the path-length difference $TOR - TR$

is constant. For a spherical wave source, these surfaces are Fresnel ellipsoids for which the phase due to the path difference $\phi=2\pi(\text{TOR}-\text{TR})/\lambda$ is given by $\phi=n\pi=\pi v^2/2$. The n is the order of the Fresnel ellipsoid and the TR line is the zero'th ($n=0$) order ellipsoid. The points of stationary phase on a screen are points at which the screen is tangent to a Fresnel ellipsoid as illustrated by points A, B, and C on the bilinear screen in Figure 4-36.

The total field diffracted by the bilinear screen for observation points in the shadow zone is then given by

$$E(R) = \sum_{n=1}^3 E_i(O_n) \frac{\hat{D}_n(\theta_n)}{\sqrt{kd_{2n}}} \sqrt{\frac{d_{1n}}{d_{1n}+d_{2n}}} e^{-jkd_{2n}} \quad (4.90)$$

where $E_i(O_n)$ is the field incident on the n th point of stationary phase at $O_n = A, B, \text{ or } C$, $\hat{D}_n(\theta_n)$ is the diffraction coefficient for the n th point of stationary phase where the diffraction angle is θ_n , and d_{1n} and d_{2n} are the distances from the transmitter and receiver to the point of stationary phase, respectively. The diffraction coefficient for the n th point of stationary phase is given by

$$\hat{D}_n(\theta_n) = |\theta_n| \sqrt{\frac{kd_{1n}d_{2n}}{(d_{1n}+d_{2n})}} F_0(v_n) T_n[K(y_n, v_n)+K(z_n, v_n)] e^{j\pi v_n^2/2} \quad (4.91)$$

where v_n is the Fresnel parameter defined earlier in Eq. (4.45), $F_0(v_n)$ is the knife-edge Fresnel integral defined in (4.28), T_n is a correction factor for the departure of the edge profile from a straight edge. When the point of stationary phase is on a straight-edge portion (e.g., points A and B in Figure 4-36) of the bilinear screen, this factor is given by [Dougherty, 1970b]

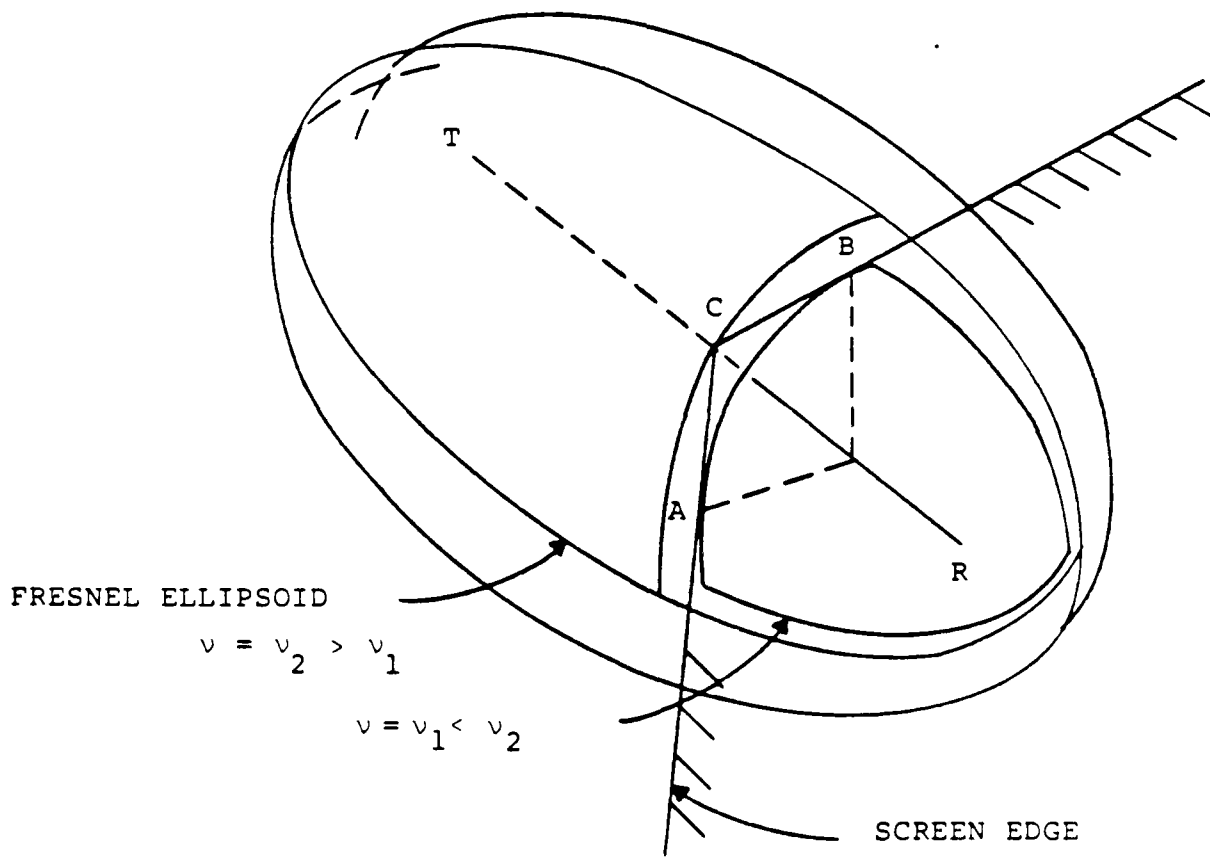


Figure 4-36 Illustration of Multiple Diffraction Points on a Bilinear Screen

$$T_n = \begin{cases} 1 & \text{if } \phi > 180^\circ, \theta_n > 0 \text{ or } \phi < 180^\circ, \theta_n < 0 \\ 2 - \frac{\phi}{180^\circ} & \text{if } \phi > 180^\circ, \theta_n < 0 \text{ or } \phi < 180^\circ, \theta_n > 0 \end{cases} \quad (4-92)$$

where ϕ is the complement of the angle (in degrees) included by the edges of the bilinear screen. For a semi-infinite straight edge, $\phi=180^\circ$, while $\phi>180^\circ$ for a triangular knife-edge. If the point of stationary phase is at the apex (e.g., point C in Figure 4-33), the profile correction factor is given by

$$T_n = 2 - \phi/180^\circ .$$

The factors $K(y_n, \nu_n)$ and $K(z_n, \nu_n)$ are correction factors for the finite separation distance between adjacent points of stationary phase on the edge [Dougherty, 1970, a]. The parameters y_n and z_n are measures of path length difference and are defined as

$$\frac{\pi}{2} y_n^2 = 2\pi(Tl_{y_n}R - TO_nR)/\lambda \quad (4-93a)$$

$$\frac{\pi}{2} z_n^2 = 2\pi(Tl_{z_n}R - TO_nR)/\lambda \quad (4-93b)$$

where O_n is the n th point of stationary phase on the screen edge, while l_{y_n} and l_{z_n} are points on the screen edge which separate the n th point of stationary phase from the others. For example if O_n is point A on the bilinear screen of Figure 4-33, then l_{y_n} is the point on the screen which separates A from C; in this case it coincides with C. Similarly l_{z_n} is the point on the screen which separates A from any other points of stationary phase on the side (opposite side to C) of A; since there are none, l_{z_n} is at an infinite distance from A. The correction factor is formally given by [Dougherty, 1970a]

$$K(u, v) = F_1(v) \frac{e^{j\pi/4}}{\sqrt{2}} \int_0^u e^{-j\pi t^2/2} dt \quad (4-94)$$

where

$$F_1(v) = \frac{\int_v^\infty e^{-j\pi t^2/2} dt}{\int_v^\infty e^{-j\pi t^2/2} dt} .$$

The magnitude and phase of the factor $K(u, v)$ are shown in Figure 4-37 as a function of u for various values of v . It is seen that for a given value of v , $K(0, v) = 0$ and $K(\infty, v) = .5$. Thus, when the separation distance between points of stationary phase approaches infinity, the sum $K(y_n, v_n) + K(z_n, v_n)$ approaches unity as expected.

The total received power is proportional to the square of the magnitude of the total diffracted field, when the observation point is in the shadow zone of the bilinear screen, the total received power is given by

$$P_R = P_T G_T G_R \sum_n \sum_m \frac{(\lambda/4\pi)^2}{d_{1n} d_{1m}} \frac{\hat{D}_n \hat{D}_m^*}{k \sqrt{d_{2n} d_{2m}}} \sqrt{\frac{d_{1n} d_{1m}}{(d_{1n} + d_{2n})(d_{1m} + d_{2m})}} e^{-j(\phi_n - \phi_m)} \quad (4.95)$$

where $\phi_n = k(d_{1n} + d_{2n})$. This expression is of the form

$$P_R = P_T G_T G_R \sum_n \sum_m A_n A_m e^{-j(\psi_n - \psi_m)} \quad (4.96)$$

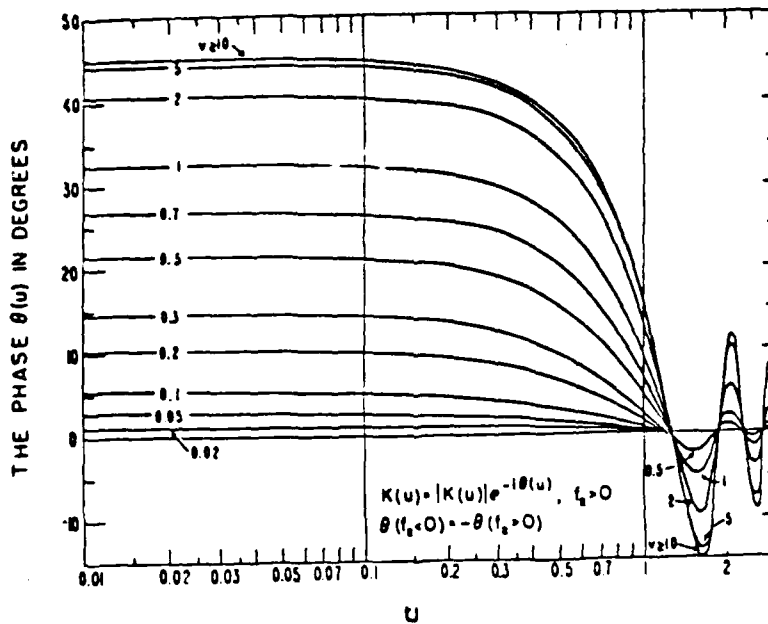
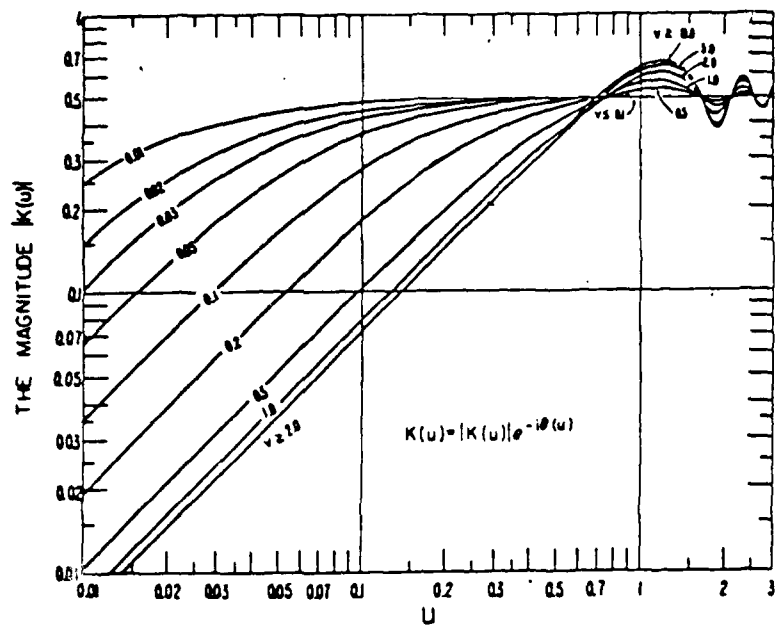


Figure 4-37 Magnitude and Phase of the Correction Factor $K(u,v)$ (from Dougherty, 1970a)

which is the expression for the magnitude squared of the sum of complex phasors. If the phasors add in phase (i.e., $\psi_n = \psi_m$), then the total received power will be greater than the contribution from a single point of stationary phase. On the other hand, if the phasors add out of phase ($\psi_n - \psi_m = \pi$), the total received power will be much lower. This type of behavior is often referred to as multipath or interference fading and is not to be confused with the interference pattern associated with multiple rays when the observation point is in the lit zone of the diffracting obstacle. The multipath associated with a single obstacle with irregular profile (in the plane perpendicular to the great circle plane) has different angles of arrival in the azimuth direction. If the transmitter and receiver locations are fixed, then there will be a set of frequencies for which the phase differences $\psi_n - \psi_m \sim \pi$. Therefore multipath fading is also referred to as frequency selective fading.

Multipath fading on diffraction paths is not limited to obstacles with profiles resembling bilinear screens. In fact when the profile of a diffracting edge is irregular, either due to terrain variations and/or the presence of trees, houses, etc., on the crest of a hill (modelled as a knife edge), then the number of ray paths (points of stationary phase) between transmitter and receiver may be more than one with high probability. The contributions from the various ray paths may add constructively or destructively as seen from the diffraction loss measurements at 9.6 GHz and 28.8 GHz made over a smooth hill cluttered with trees [Haakinson, et al., 1980] and shown in Figure 4-38. These measurements show clearly how the contributions from various ray paths add constructively or destructively as the receiving antenna height is lowered (increasing v) behind the crest of the hill. If we were to superimpose the theoretical diffraction loss for a semi-infinite knife-edge on the curves of Figure 4-38, it would be seen that the diffraction pattern of a cluttered edge exhibits on the average characteristics similar to those of a semi-infinite screen with random variations about the mean.

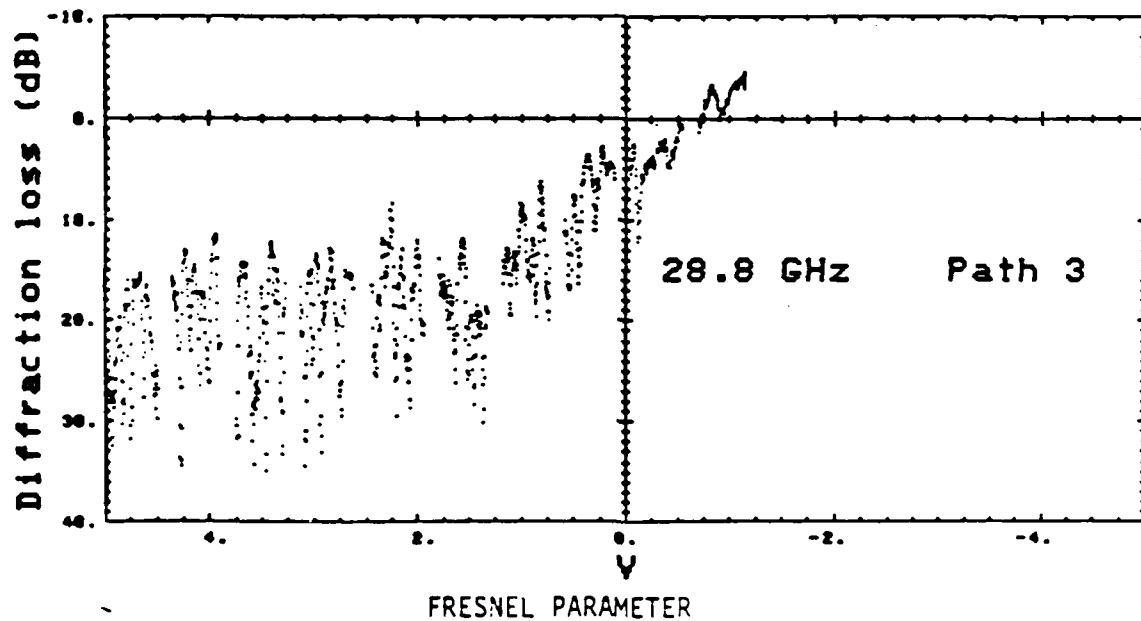
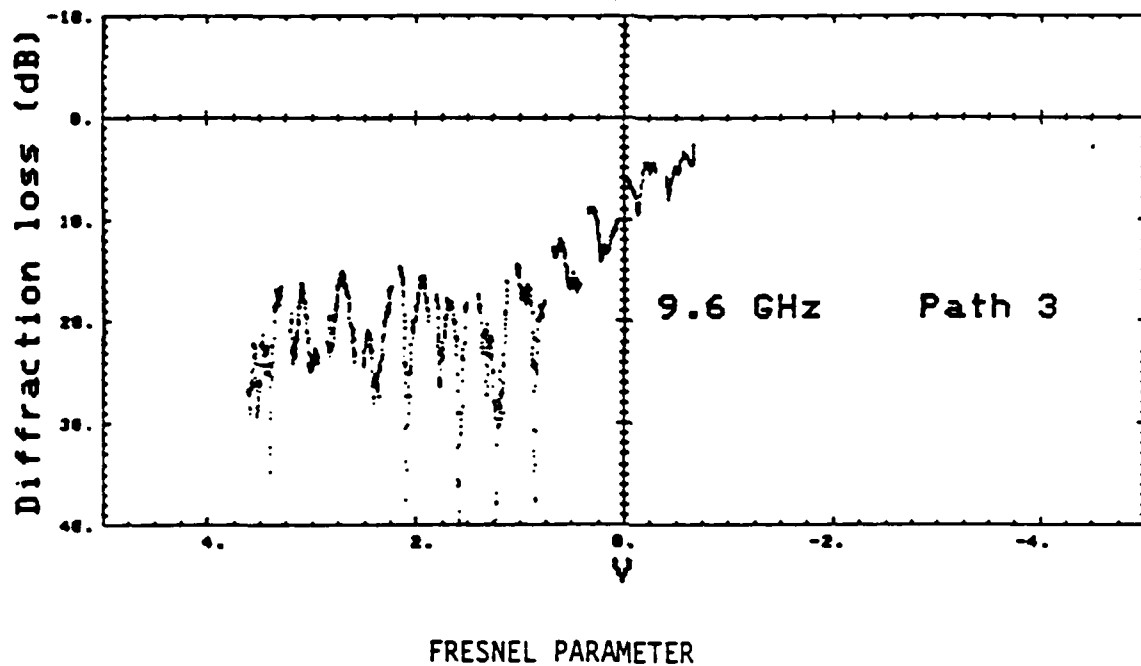


Figure 4-38. Diffraction Loss Measured on a Cluttered Path with Multiple Diffraction Paths (from Haakinson, et al., 1980)

If we rewrite (4.96) as

$$P_R = P_T G_T G_R \left[\sum_{n=1}^N A_n^2 + 2 \sum_{n=1}^N \sum_{m=n+1}^N A_n A_m \cos \psi_{nm} \right] \quad (4-97)$$

it can be seen that the first sum term in this expression is the mean diffracted field while the random variations about the mean are due to the double sum term.

In practice obstacle profiles, while resembling bilinear screens, will not have perfectly straight or smooth edges (irregular profile) so that predicting the exact location and number of points of stationary phase will not be possible nor accurate. This is particularly the case when propagation is over built-up areas where the diffracting obstacles are buildings and/or trees [Reudink and Wazowicz, 1973]. The presence of azimuthal multipath results in a spatial interference pattern as in Figure 4-38. The spatial separation between nulls and peaks is of the order of a half-wavelength. Within a small area, the field amplitude is proportional to the sum of the contributions from each point stationary phase, i.e.,

$$E_r = \sum_{n=1}^N A_n e^{-j\psi_n} \quad (4-98)$$

Because of the difficulty in isolating the points of stationary phase, we can assume that E_n is a random variable. If the contributions of the individual points of stationary phase are of the same order of magnitude, we can assume that the A_n are equal to A and that the relative phases ψ_n are independent and uniformly distributed. Then, if N is sufficiently large, the magnitude of the random variable E_n , call it r , is Rayleigh distributed, that is the probability density function of r is given by

$$P_r(R) = \frac{2R}{\alpha} e^{-R^2/\alpha} \quad (4.99)$$

where $\alpha = E(r^2)$ is the average (normalized) received power.

The mean-squared value of r is directly proportional to the number of points of stationary phase which contribute to the total diffracted field and in fact is given by

$$\alpha = NE(A_n^2) = NA^2, \quad (4.100)$$

where A^2 is the received power due to an obstacle with a single point of stationary phase. If the number of diffracting obstacles is small and can be identified from topographical maps, then the average (mean) diffraction loss can be determined by the methods described in earlier sections. When the number of diffracting obstacles is uncertain and each obstacle is irregular with multiple diffracting edges, the process of identifying the number of multipath components becomes cumbersome (e.g., built-up areas). Empirical path loss prediction methods based on measurements at various frequencies have been used to handle such situations [Okumura, et al., 1968; Malaga, 1981].

4.7 TEMPORAL VARIABILITY IN DIFFRACTION LOSS CALCULATIONS

The theories developed in Section 4.2 through 4.6 can be applied in a straightforward manner provided sufficient path information is available. A typical path profile derived from topographical maps is shown in Figure 4-39. From this path profile it is readily seen that the propagation (ray) path is a doubly diffracted path. From the great circle distances between terminals and obstacles and the heights of the terminals and obstacles above sea level we can easily determine the diffraction angle at each obstacle. However, the curvature of the crests of the obstacles cannot be accurately determined (only crude estimates are possible) from path profiles such as that of Figure 4-39. In

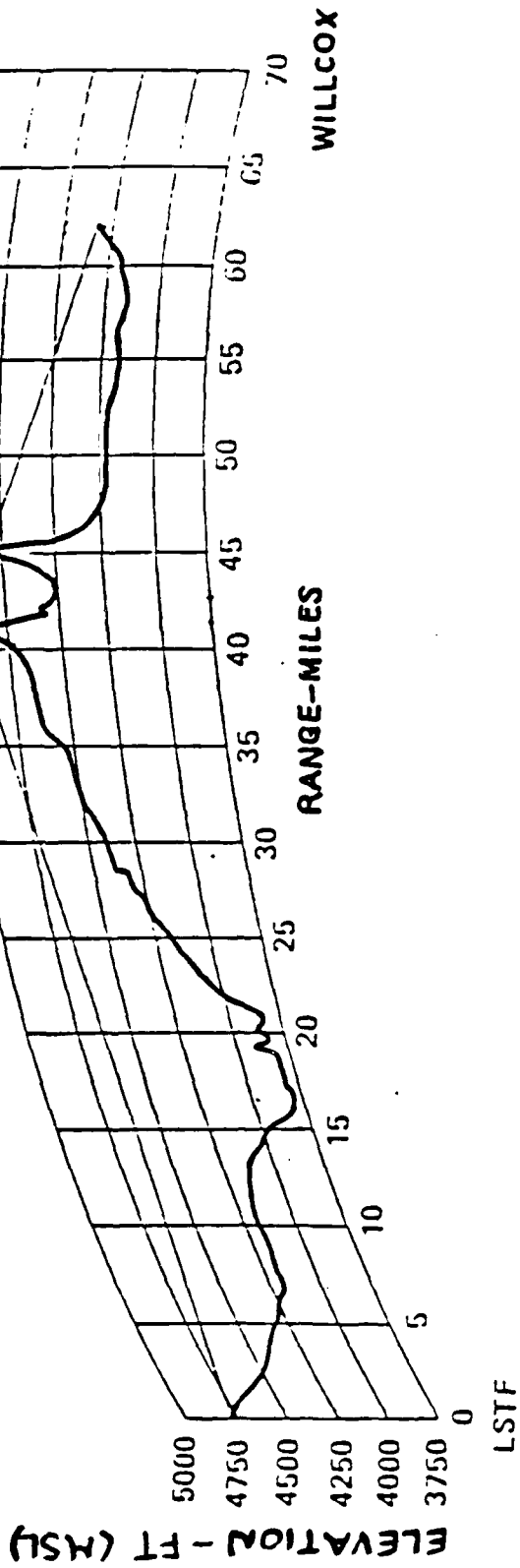


Figure 4-39 Path Profile: LSTF to WILLCOX

order to determine how susceptible the diffraction path loss (transmission loss assuming isotropic antennas) calculation is to the estimates of the edge curvature, we have plotted in Figure 4-40 the path loss (for the path profile of Figure 4-39) for various estimated values of the curvatures of the edges. The curvature of each of the edges was calculated from estimates of the distance d_s , propagated by the ray along the surface of the crest of each obstacle. Each curve in Figure 4-40 corresponds to a pair (one for each obstacle) of estimated distances, d_s . Note that when the distance $d_s = 0$, the obstacle behaves like a knife-edge. The various path loss curves are plotted as a function of the surface refractivity gradient.

For fixed estimates of the curvature of the edges, the path loss is seen to increase as the refractivity gradient increases from its standard value of -40 N-units/km to less negative and even positive values. The reason for the dependence of the diffraction path loss on the refractive index gradient is that the diffraction angle increases proportionally with the refractivity gradient. The increase in the diffraction angle can be explained from the effective earth radius transformation. It is well known that the effects of refractive index gradients on radio wave propagation can be determined by replacing the actual problem of propagation over a spherical earth surrounded by a medium in which the refractive index decreases monotonically with height with one in which the refractive index is constant (so that rays travel in straight lines) but where the radius of the earth is modified. As the refractivity gradient increases and becomes less negative, the effective earth radius becomes smaller and the smaller the effective earth radius becomes the greater the diffraction angle is. Extreme variations in the refractivity gradient from -120 N-units/km to $+20$ N-units/km will result in actual variations in the diffraction path loss of around ± 7 dB about the predicted value for a standard atmosphere (-40 N-units/km). However the predicted path loss for a standard at-

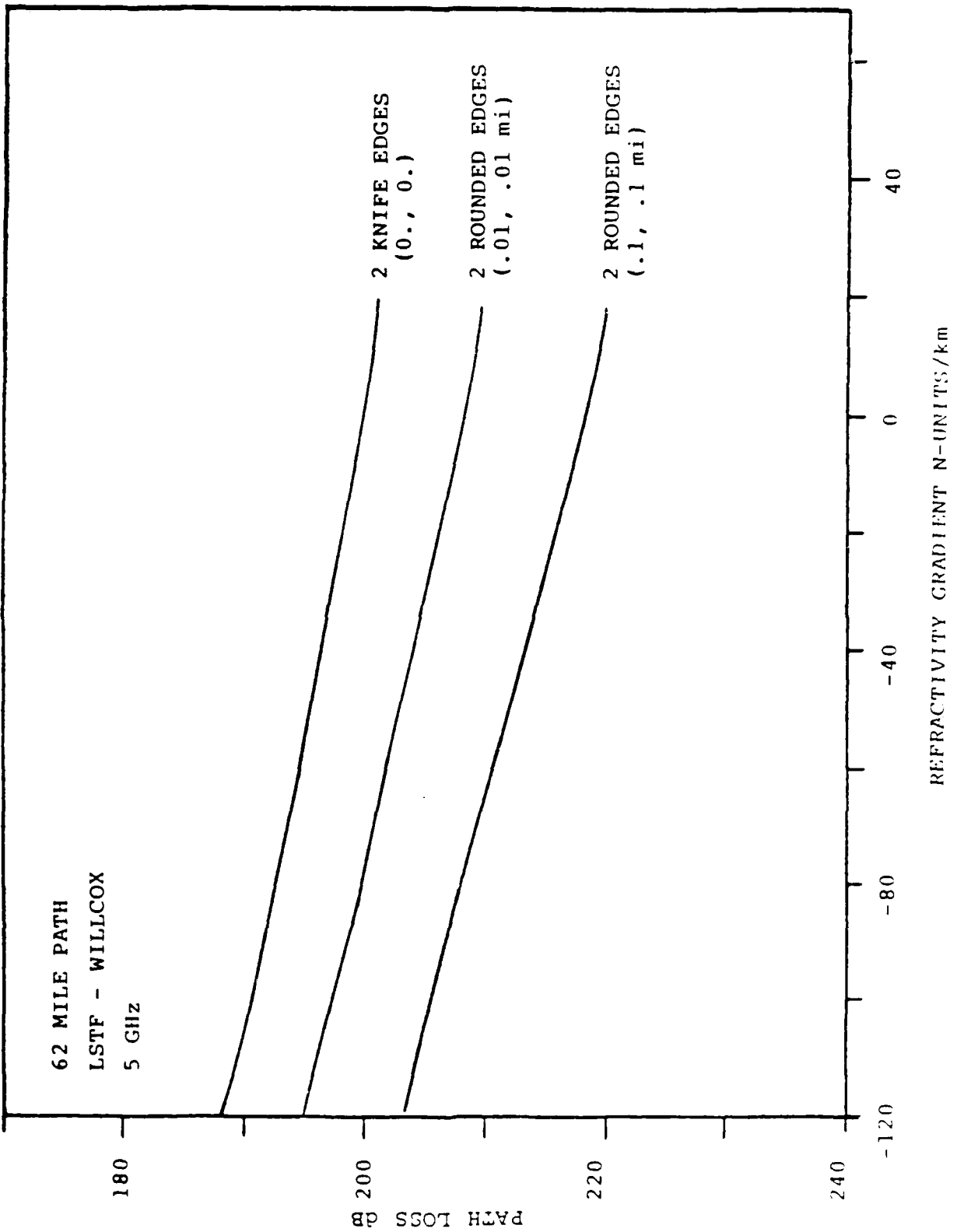


Figure 4-40 Variability in diffraction path loss as a function of refractivity gradient and edge horizontal extents

mosphere may be in error by as much as 15 dB if the diffracting obstacles are treated as knife-edges and they actually behave as rounded edges with horizontal extents (i.e., distance d_g propagated by the ray along the crest of the obstacle) of a tenth of a mile, or vice versa.

From this we may conclude that good estimates of the curvature of the diffracting edges (or their effective horizontal extent) is required in order to obtain a good prediction of the median path loss (path loss exceeded 50% of the time) while knowledge about the variability of the refractivity gradient about its median value is required to predict the temporal variability of the path loss about the median prediction.

SECTION 4
REFERENCES

- Abramowitz, M. and I.A. Stegun (1964), "Handbook of mathematical functions", Washington, DC, Nat. Bureau of Standards.
- Ahluwalia, D.S., R.M. Lewis, and J. Boersma (1968) "Uniform asymptotic theory of diffraction by a plan screen", SIAM J. Appl. Math., Vol. 16, pp. 783-807.
- Aclas of radio wave propagation curves for frequencies between 30 and 10,000 Mc/s. Radio Research Laboratory, Ministry of Postal Services, Tokyo, Japan, pp 172-179, 1957.
- Beckmann, P. and A. Spizzichino, (1963) "The scattering of electromagnetic waves from rough surfaces", Pergamon Press, London.
- Boersma, J., and Y. Rahmat-Samii (1980), Comparison of two leading uniform theories of edge diffraction with the exact uniform asymptotic solution, Radio Sci., 15, 1179-1194.
- Bullington, K. (1974), "Radio propagation at frequencies above 30 megacycles", Proc. IRE, V. 35, No. 10, pp. 1122-1136.
- CCIR (1978), "Propagation by diffraction", Report 715, XIV Plenary Assembly, Kyoto, V5 pp. 36-45.
- Deygout, J. (1966), "Multiple knife-edge diffraction of microwaves", IEEE Trans. Antennas & Prop., V AP-14, No. 4, pp. 480-489.
- Dougherty, H.T. and Maloney, L.J. (1964), "Application of diffraction by convex surfaces to irregular terrain situations", J. NBS, V. 68D, pp. 239-249.
- Dougherty, H.T. and Wilkerson (1967), "Determination of antenna height for protection against microwave diffraction fading", Radio Science, V. 2, pp. 161-165.
- Dougherty, H.T. (1970a). "The application of stationary phase to radio propagation for finite limits of integration", Radio Science, Vol. 5, pp. 1-6.
- Dougherty, H.T. (1970b), "Diffraction by irregular apertures", Radio Science, Vol. 5, pp. 55-60.
- Epstein, J. and Peterson, A.W. (1953), "An experimental study of wave propagation at 850 Mc/s", Proc. IEEE, V. 41, No. 5, pp. 595-611.

SECTION 4
REFERENCES (Continued)

- Fock, V.A. (1946), "Diffraction of radio waves around the earth's surface", Academy of Sciences, USSR.
- Fock, V.A. (1951), "Fresnel diffraction from convex bodies", Uspecki Fiz. Nauk, V. 43, pp. 587-559.
- Haakinson, E.J., Violette, E.J., and Hufford, G.A. (1980), "Propagation effects on an intervisibility measurement system operating in the SHF band", NTIA Report 80-35, U.S. Department of Commerce, NTIA.
- Hacking, K., (1970) "U.H.F. propagation over rounded hills", Proc. IEE., Vol. 117, No. 3.
- James, G.L., (1980), "GTD solution for diffraction by convex corrugated surfaces", IEE Proc., V. 127, Pt. H, No. 5, pp. 257-262.
- Keller, J.B. (1956), "Diffraction by a convex cylinder", IEEE Trans. Antennas & Prop., V. AP-24, pp. 312-321.
- Keller, J.B. (1962), "Geometrical theory of diffraction", J. of Optical Society of America, V. 52, No. 2, pp. 116-130.
- Kouyoumjian, R.G. and Pathak, P.H. (1974), "A uniform geometrical theory of diffraction for an edge in a perfectly conducting surface", Proc. IEEE, V. 62, No 11, pp. 1448-1461.
- Logan, N.A. (1959), "General research in diffraction theory", V. 1-2, LMSD - 288087, Missiles and Space Div., Lockheed Aircraft Corp., Sunnyvale, CA.
- Logan, N.A. and Yee, K.S. (1962), "Electromagnetic waves", Ed. by R.E. Langer, University of Wisconsin press, Madison.
- Malaga, A. (1981), "An empirical path loss model for HF/VHF propagation in urban areas", Radio Science, V. 16, No. 3, pp. 355-364.
- Millington, G., Hewitt, R., and Immirzi, F.S. (1962), "Double knife-edge diffraction in field strength predictions", Proc. IEE, V. 109C, pp. 419-429.
- Millington, G., Hewitt, R., and Immirzi, F.S. (1962), "The fresnel surface integral", Proc. IEE, V. 109C, pp. 430-437.

SECTION 4
REFERENCES (Concluded)

- Okumura, Y., Ohmori, E., Kawano, T., and Fukuda, K. (1968), "Field strength and its variability in VHF and UHF land mobile radio service", Rev. Tokyo Electron. Commun. Lab., V. 16, 825-873.
- Parl, S. and Malaga, A. (1981), "Theoretical analysis of microwave propagation", Interim Report on RADC Contract F19628-80-C-01006.
- Pathak, P.H., Burnside, W.D., and Marhefka, R.J. (1980), "A uniform GTD analysis of the diffraction of EM waves by a smooth convex surface", IEEE Trans. Antenna Prop., V. AP-28, No. 5, pp. 631-642.
- Reudink, D.O., and Wazowicz, M.F., (1973), "Some propagation experiments relating foliage loss and diffraction loss at X-band and UHF frequencies", IEEE Trans. Communications, Vol. COM-21, pp. 1198-1206.
- Rice, S.O. (1954), "Diffraction of plane radio waves by a parabolic cylinder", Bell Syst. Tech. J., V. 33, p. 417.
- Rice, P.L., Longley, A.G., Norton, K.A., and Barsis, A.P. (1967), "Transmission loss predictions for troposcatter communication circuits", NBS Tech. Note 101.
- Sommerfeld, J.W. (1954), "Optics", Academic Press, Inc., New York, p. 249.
- Vogler, L.E., (1982) "An attenuation function for multiple knife-edge diffraction", Radio Science, Vol. 17, No. 6, pp. 1541-1546.
- Wait, J.R., and Conda, A. (1959), "Diffraction of EM waves by smooth obstacles for grazing angles", J. NBS, V. 63D, No. 2, pp. 181-197.

SECTION 5
LINE-OF-SIGHT PROPAGATION

5.1 OVERVIEW

Line-of-sight (LOS) microwave links are among of the most common methods for wireless high data rate communication. The environment can cause deep fades and such fades have been extensively studied in the past. Performance degradation can also be caused by multipath and a large part of this section is devoted to the development and discussion of some new results relative to multipath fading.

Geometrical optics, or ray theory, is usually a good approximation at microwave frequencies. The received signal on a LOS link is in general composed of a specular component which is not fading and a diffuse component with Rayleigh fading. The specular component consists of

1. Direct path
2. Atmospherically refracted multipath rays
3. Ground reflections

The direct path may have phase and amplitude scintillation, as discussed in Section 5.2. The diffuse component can consist of

1. Scatter from atmospheric turbulence
2. Scatter from a rough ground.

Scatter from a rough ground can be modeled by a Rice distribution [Beckmann and Spizzichino, 1963].

Broadband fading (or power fading) implies that the signal is fading completely so frequency diversity is not useful. It

can be caused by atmospheric gradients causing earth bulge or diffraction fading. The computer technique used for the diffraction calculations in this report accounts for a variable constant-gradient refractive index profile using fixed coordinates for the diffraction obstacles. Ducting layers can also cause power fades as can reflecting layers between the terminals. These effects are all difficult to predict, and are usually rare. Rain attenuation is another form of power fading (see Section 2). The large year-to-year variability of the rain rate makes it difficult to predict.

Multipath fading is usually frequency selective, meaning the fading does not occur at all frequencies. A number of empirical models of fading distribution have been developed. For Northwest Europe the probability of a worst month power reduction by a factor of α is [Hall, 1979]

$$P(\alpha) = 1.4 \cdot 10^{-8} \alpha \left(\frac{f}{1\text{GHz}} \right) \left(\frac{d}{1\text{km}} \right)^{3.5} \quad (5.1)$$

Fade duration in the USA has been modeled by

$$\text{median fade duration} = 56.6 \alpha^2 \sqrt{\frac{d/1\text{km}}{f/1\text{GHz}}} \text{ seconds.} \quad (5.2)$$

In Section 5.3 we describe the effects of multipath fading. We show, in particular, that delay spreads are often small but that angle-of-arrival variations can be significant.

5.2 SINGLE RAY PROPAGATION REGIMES

According to the Geometrical Optics (GO) approximation ray tracing is good in a smoothly varying medium when the observation

point is not near a caustic. Caustics are points where the field is focussed and GO predicts an infinite field strength. In a region without caustics random inhomogeneities will affect the ray. The primary effect of a smooth weakly turbulent medium is the change in the phase of the field. Let s denote distance along ray, and let $n(s)$ be the refractive index. The total phase change along the ray is

$$\phi = k \int_0^L n(s) ds \quad ,$$

where $k = 2\pi/\lambda$. The variance of the phase is

$$\begin{aligned} \overline{\phi^2} &= k^2 \int_0^L ds_1 \int_0^L ds_2 \overline{n(s_1)n'(s_2)} \\ &= k^2 L \int_{-\infty}^{\infty} ds \phi_n(s) \end{aligned}$$

where $\phi_n(s)$ is the refractive index correlation function.

For the isotropic von Karman-Kolmogorov spectrum ϕ_n (the Fourier transform of the correlation function ϕ_n)

$$\phi_n(\kappa) = 0.033 C_n^2 \frac{L_0^{11/3}}{(1 + \kappa^2 L_0^2)^{11/6}} \quad (5.3)$$

we have

$$\phi_n(r) = \frac{4\pi}{r} \int_0^{\infty} \kappa \phi_n(\kappa) \sin \kappa r d\kappa$$

or

$$\int_{-\infty}^{\infty} \phi_n(r) dr = 4\pi^2 \int_0^{\infty} \kappa \phi_n(\kappa) d\kappa .$$

Hence

$$\overline{\phi^2} = 0.78 C_n^2 k^2 L L_0^{5/3} . \quad (5.4)$$

This would, of course, be modified by anisotropic turbulence in the buoyancy region.

When GO applies (large scale turbulence) the phase variance is therefore proportional to distance. For smaller turbulence scales the Rytov approximation can be used to calculate both phase and amplitude variation. [Tatarskii, 1971]. It can be shown that if the waveform is written

$$u = u_0 e^{\chi + i\phi} = u_0 e^{\chi}$$

where u_0 is the undisturbed field, χ represents the log amplitude fluctuation and ϕ the phase fluctuations, then the above result is modified to

$$\begin{aligned}
\overline{|X|^2} &= \overline{X^2} + \overline{\phi^2} \\
&= 4\pi^2 k^2 L \int_0^\infty \phi_n(\kappa) \kappa d\kappa \\
&= 0.78 C_n^2 k^2 L L_0^{5/3}.
\end{aligned} \tag{5.5}$$

Comparing this to the GO results we see that in the Rytov approximation $\overline{\phi^2}$ deviates from the GO result exactly by the log-amplitude fluctuation. With the Kolmogorov spectrum the log amplitude fluctuations are [Tatarskii, 1971]

$$\overline{\phi^2} = 0.31 C_n^2 k^{7/6} L^{11/6}. \tag{5.6}$$

This is independent of the outer scale L_0 as long as the Fresnel zone $(\lambda L)^{1/2}$ is much less than L_0 . The phase variance is then

$$\overline{\phi^2} = 0.78 C_n^2 k^2 L L_0^{5/3} \left[1 - 0.40 \left(\frac{L}{kL_0^2} \right)^{5/6} \right].$$

The correction term displays directly the Fresnel condition. Define $\phi = |X^2|$. This parameter characterizes the strength of the turbulence and equals the phase variance in the geometrical optics region. Define also the average Fresnel zone distance

$$l_F = \left(\frac{L}{k} \right)^{1/2}. \tag{5.7}$$

Figure 5-1 shows the regions of turbulence characterized in terms of χ^2 and l_F . In the log-normal region, limited by $\chi^2 < 1$ and $l_F < L_0$, the Rytov approximation above applies. In the Rician regime the small turbulence scatter cause an additive Gaussian component. We now generalize the weak turbulence results for χ^2 and κ^2 to the Rician regime. We have [Tatarski, 1971, §. 47]

$$\begin{aligned} \overline{\chi^2} &= 2\pi^2 k^2 L \int_0^\infty \kappa d\kappa \phi_n(\kappa) \left[1 - \frac{\kappa}{\kappa^2 L} \sin \frac{\kappa^2 L}{\kappa} \right] \\ &= 0.39 C_n^2 L_0^{5/3} H_{11/6} \left(\frac{L}{\kappa L_0^2} \right) \end{aligned} \quad (5.8)$$

where

$$H_\nu(x) = (\nu-1) \int_0^\infty dt \left[1 - \frac{\sin xt}{xt} \right] \frac{1}{(1+t)^\nu} dt . \quad (5.9)$$

This function is difficult to evaluate analytically.

In the Rician region we have

$$\overline{\phi^2} \sim \overline{\chi^2} \sim 0.39 C_n^2 k^2 L L_0^{5/3} = \frac{1}{2} \phi . \quad (5.10)$$

This agrees with (5.8) since $H_\nu(x) \sim 1$ for large x . Figure 5-2 shows the function $H_{11/6}(x)$.

In the lognormal region we can derive (5.6) from (5.8). For small x , H_ν can be evaluated analytically by defining

$$L_\nu = x H_\nu .$$

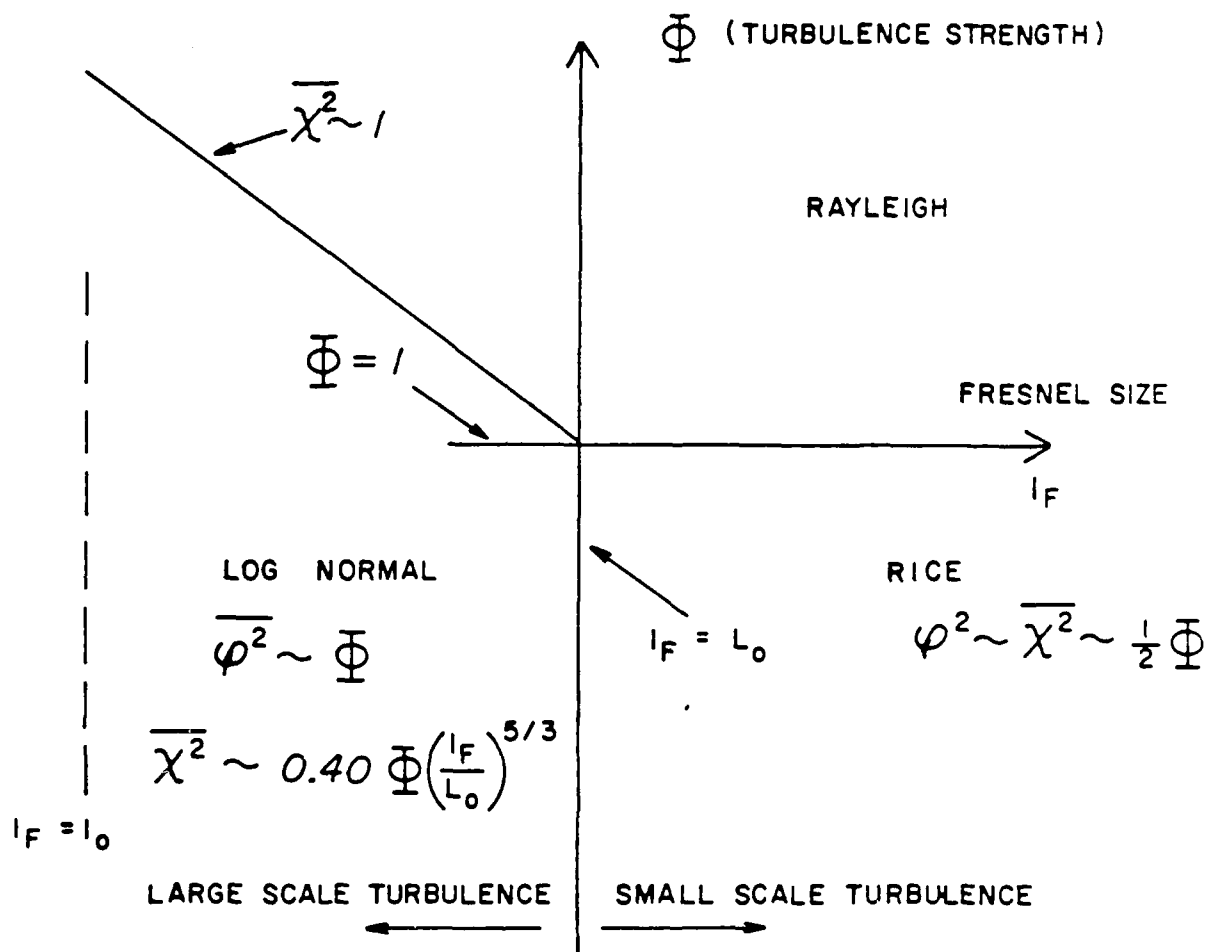


Figure 5-1 Regions of atmospheric turbulence

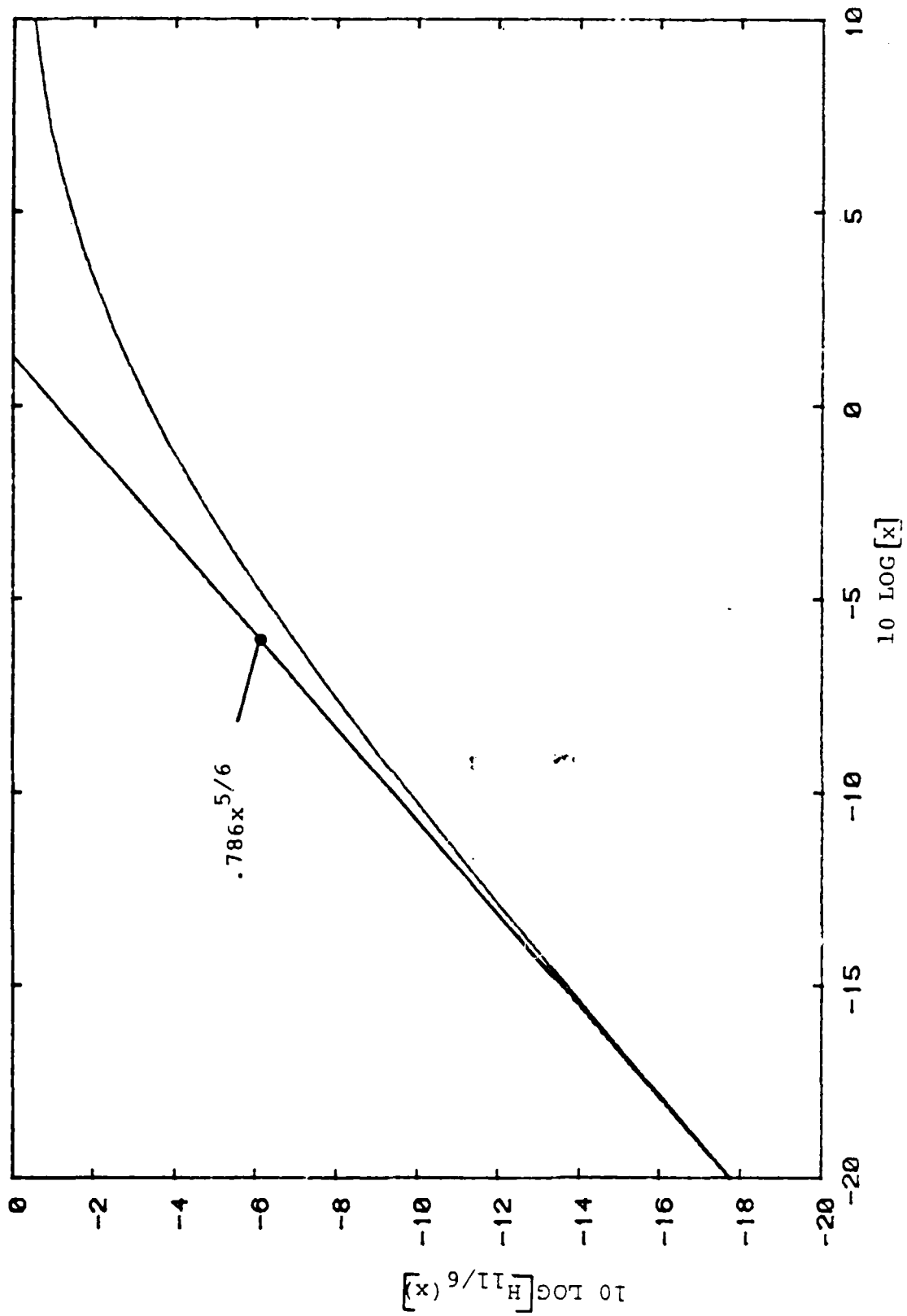


Figure 5-2 The Function $H_{11/6}(x)$

Then

$$\begin{aligned}
 L'_\nu(x) &= \int_0^\infty (1 - \cos xt) \frac{dt}{(1+t)^\nu} \\
 &= \frac{1}{\nu-1} - \operatorname{Re} x e^{i\frac{\pi}{2}(\nu-1)} e^{ix} \Gamma(1-\nu, ix) \\
 &= -\Gamma(1-\nu) \sin\left(x + \frac{\pi\nu}{2}\right) x^{\nu-1} + \Gamma(1-\nu) \sum_{n=1}^{\infty} \frac{(-1)^n x^{2n}}{\Gamma(2-\nu+2n)}.
 \end{aligned}$$

Hence, for small x , we get

$$H_{11/6}(x) \sim \frac{\Gamma(\frac{1}{6})}{11/6} \sin \frac{\pi}{12} x^{5/6} = 0.786 x^{5/6}. \quad (5.11)$$

Inserting this into (5.8) yields (5.6). It is seen from Figure 5-2 that this result is good for $x < 0.1$.

We are now in a position to characterize the turbulence effects on a line-of-sight ray. Typically the outer scale is 100m horizontally and 10m vertically. Using $L_0 = 50\text{m}$ we are in the log-normal region when

$$f > L c / (2\pi L_0^2) = 2.10^4 L.$$

For a 30 km link this requires $f > 600$ MHz. For a 100 km link this requires $f > 2$ GHz. Clearly line-of-sight links can operate right on the boundary between the log-normal region and the Rician region. Since the turbulence is weak either a log-normal

or a Rician distribution represents a good approximation. Figure 5-3 shows the predicted amplitude scintillation in the geometrical optics region. The turbulence may play an important role in modifying the field near a caustic, but we shall not address that question here.

We conclude this section by proposing the following simple model for the distribution of the field:

$$E = me^{j\phi_0} + Y = Ae^{j\phi}$$

where m is constant, ϕ_0 is Gaussian with variance σ_0^2 , and Y is complex Gaussian with variance σ^2 .

For a field of this form we have, assuming weak turbulence, a good approximation to the statistics in the Rician density

$$P(A) = \frac{2A}{\sigma^2} \exp\left(-\frac{A^2 + m^2}{\sigma^2}\right) I_0\left(\frac{2Am}{\sigma^2}\right) \quad (5.12)$$

where

$$m = \exp(-\overline{\chi^2})$$

$$\sigma^2 = 1 - m^2$$

The phase scintillation, which is primarily governed by the large scale turbulence, is approximated by taking

$$\overline{\phi_0^2} = \sigma_0^2 = \overline{|\chi|^2} - \frac{\overline{\chi^2}^2}{2} = -\operatorname{Re} \overline{\chi^2}$$

σ_0^2 is small in the Rician regime. This model should be good also when $l_F \sim L_0$.

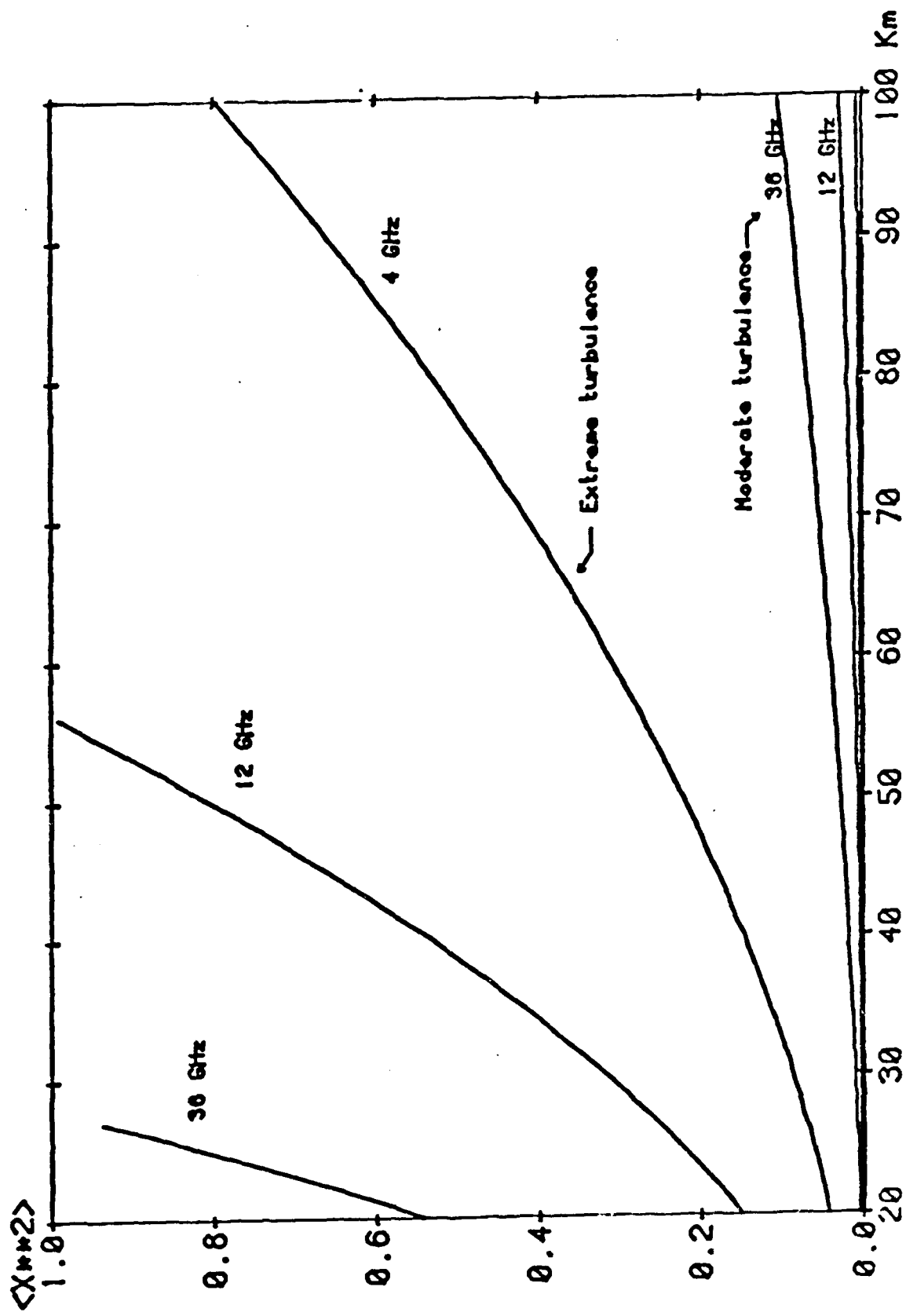


Figure 5-3 LOS Scintillation

AD-A143 762

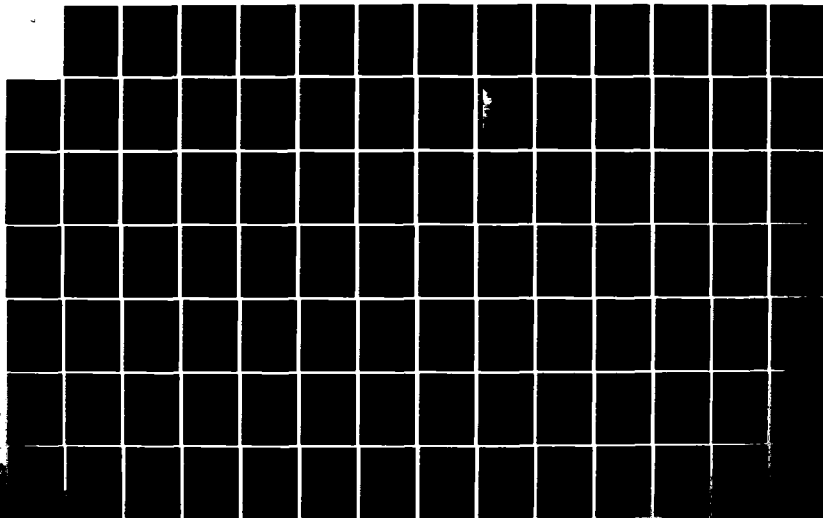
THEORETICAL ANALYSIS OF MICROWAVE PROPAGATION(U)
SIGNATRON INC LEXINGTON MA S PARL ET AL. APR 84
RADC-TR-84-74 F19628-80-C-0106

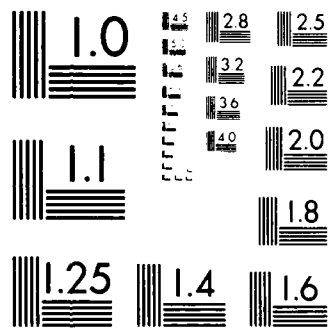
475

UNCLASSIFIED

F/G 20/14

NL





MICROCOPY RESOLUTION TEST CHART
NATIONAL BUREAU OF STANDARDS-1963-A

5.3 MULTIPATH FADING FROM AN ELEVATED DUCT

5.3.1 Introduction

Refractive multipath fading is one of the major sources of degradation of microwave Line-of-Sight (LOS) links. For the design of such links it is important to be able to predict all parameters affecting the performance of the equalizer and diversity combiner subsystems of the radio. For broadband digital radios in particular, the delays, angles of departure and arrival, and amplitudes of the rays are of interest. The model by Rummler [1979] represents the best validated model that includes the selective fading caused by multipath. Recently, more accurate ray tracing analyses have been developed [Pickering and DeRosa, 1979; Sasaki and Akiyama, 1979; Webster, 1982] extending the semiempirical techniques used for flat fading [Barnett, 1972; Vigants, 1971, 1975]. These analyses, together with recent experiments [8-10], [Sandberg, 1980; Webster and Veno, 1980; Webster, 1982] have proved the need for accurate modeling of all of the parameters of interest.

Based on analytical ray tracing, this section develops new results determining conditions for the occurrence of multipath, variations in the angle-of-arrival, and the delay spread. The results are based on a simplified atmospheric model: two stratified layers, of which the lower layer is usually a standard atmosphere (gradient -40 Nu/km) and the upper inversion layer create a ducting medium (gradient steeper than -157 Nu/km). The multipath parameters are first developed assuming an infinitely thick duct model. The effect of finite inversion thickness is considered separately. Throughout this section the height of the layer boundary is considered a variable since such layers are usually seen moving up or down during the day. The ray equations are derived and solved parametrically for the layer height. A sequence of numerical examples illustrate the ray characteristics

and dependence on gradients and layer ducts. It is shown that the number of rays is always odd, and that there exists a layer height with the number of rays of the form $3+4p$ where the integer $p(>0)$ is the number of complete periods and is called the order of the ray. At any given layer height there will be 0, 2, or 4 rays of order p for $p > 0$, 1 or 3 rays of order $p = 0$. Analytic conditions for the existence of rays of order p are derived, leading to a general multipath condition valid for thick inversions (2-layer model of the atmosphere). It is found that the last arriving ray is the strongest. However, in practice, two or more late arriving rays may partially cancel each other and appear as a single ray if the receiver bandwidth is insufficient to resolve the rays.

Expressions for angle-of-arrival variation and for delay spread are derived. The latter are similar to those of Sasaki and Akiyama [1979], showing a cubic distance dependence for small distances and a linear dependence at large distances.

Section 5.3.2 describes the two layer model. The ray solution is described in Section 5.3.3, including techniques for approximate field calculations near a caustic. A number of examples are given in Section 5.3.4 to demonstrate how the different ray solutions are connected. A simple parametric solution of the quartic equation found in Section 5.3.3 is derived in Section 5.3.5. Section 5.3.6 develops some multipath conditions. Section 5.3.7 discusses the angle-of-arrival, the importance of which has often been underestimated [Webster and Veno, 1980; Webster, 1982, 1983]. Section 5.3.8 presents analytical expressions for the delay spread.

5.3.2 Two Layer Refractivity Model

The number of rays is usually a function of the thickness of the elevated ducting layer. By first considering an infi-

nitely thick inversion we can determine the maximum number of rays and then infer the ray structure for finite thickness of the inversion layer. Consider therefore the two-layer model in Figure 5-4 where both layers have a nearly constant refractivity gradient. The gradient in the lower medium is greater than -157 Nu/km while the inversion layer has a gradient less than -157 Nu/km. An earth radius transformation will be used to, in effect, make rays travel in straight lines. The rays are governed by Snell's law,

$$R_0 n(R_0) \cos \theta(R_0) = Rn(R) \cos \theta(R) \quad (5.13)$$

where $\theta(R)$ is the ray elevation angle at radius R from the center of the earth, and R_0 is an arbitrary reference radius.

We wish to express the ray in terms of the polar coordinates (R, ϕ) , where ϕ is the angle of travel in the great circle plane, as shown in Figure 5-5. The equation determining ϕ is

$$Rd\phi = \cot \theta(R) dR . \quad (5.14)$$

Let us postulate a refractive index, $n(R)$, of the form

$$n(R) = n_0 (R_0/R)^Y . \quad (5.15)$$

Then substitution into (5.14) and (5.15) shows that an exact earth radius transformation preserving the angle θ and yielding straight line propagation is

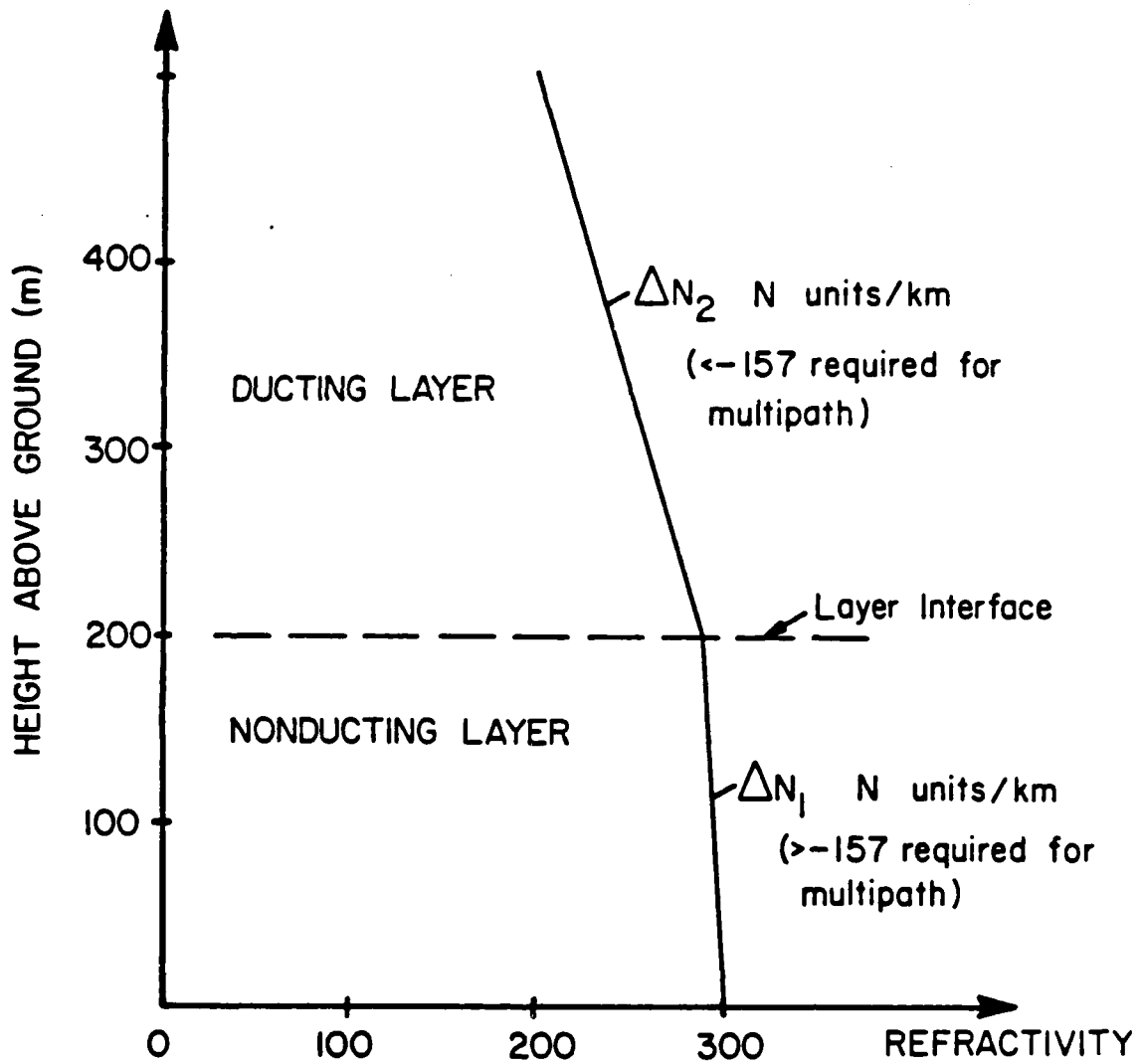


Figure 5-4 Refractivity height profile

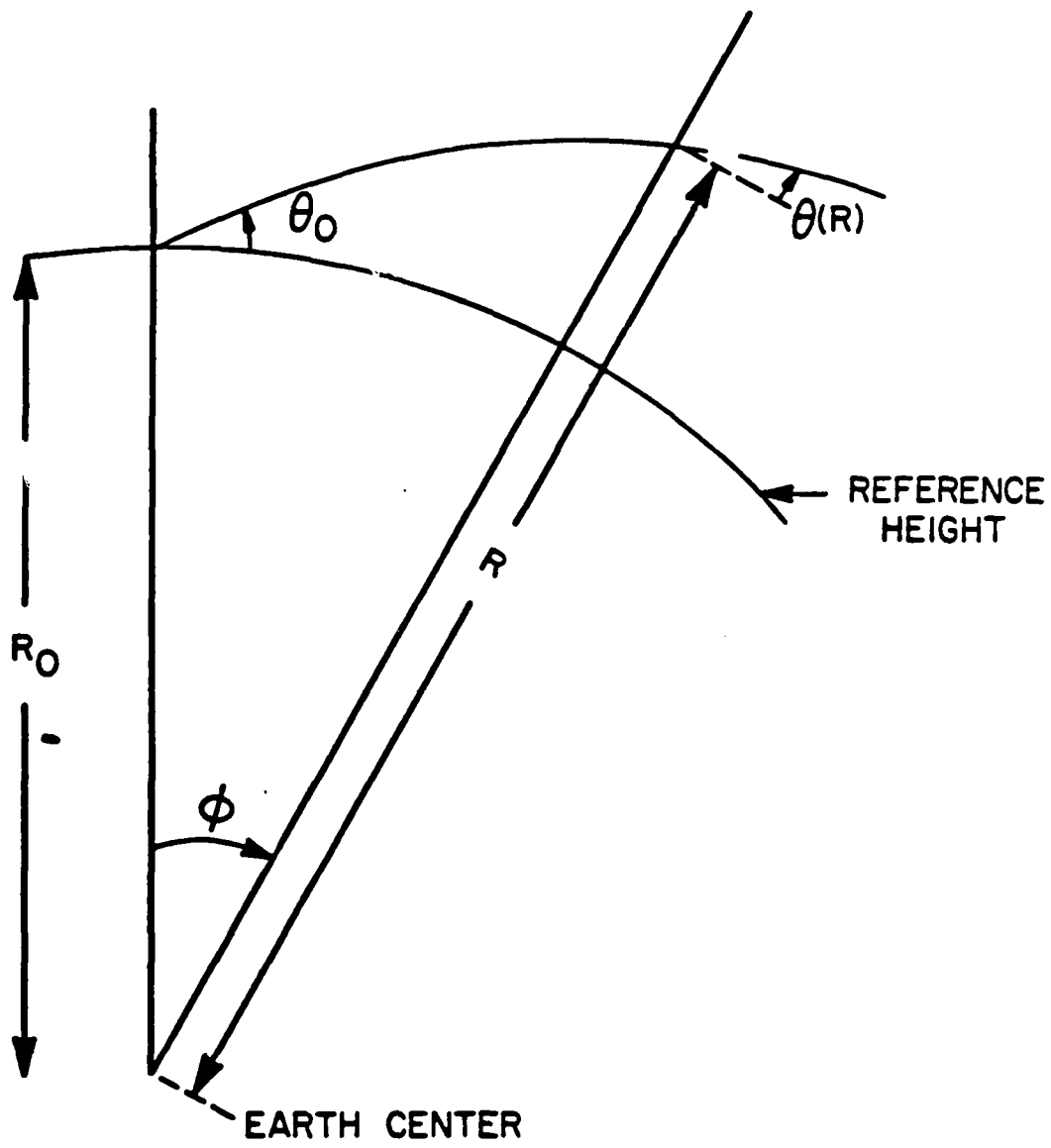


Figure 5-5 Path geometry for refractive path

$$\phi \rightarrow \phi_e = \phi(1-\gamma)$$

$$R \rightarrow R_e = R \left(\frac{R_0}{R} \right)^\gamma / (1-\gamma) . \quad (5.16)$$

This transformation preserves distance at $R=R_0$ and θ at all heights. The atmosphere is generally characterized by the refractivity $N \equiv (n-1) \cdot 10^6$ and the refractivity gradient ΔN , the change in N over a 1 km layer [CCIR, 1978]. In terms of ΔN we have

$$R_e(R_0) = \frac{R_0}{1-\gamma} = \frac{R_0}{1 + R_0 \Delta N 10^{-9}} \quad (5.17)$$

where R_0 is measured in meters. It is seen that the gradient of the profile (5.15) is nearly constant. Constant gradient profiles are commonly used to analyze refractive multipath [Pickering and DeRosa, 1979]. Our motivation for using the profile in (5.15) is that it allows us to obtain equations for the rays which are exact within the geometrical optics approximation. To solve these equations, it is necessary to resort to approximations, however. Another advantage of the model is that the propagation velocity in the transformed coordinates is constant, and equal to the velocity at the reference radius $R=R_0$. The proof of this fact is left to the reader.

The layer model to be used in the following is relative to the earth radius R_B at the layer interface,

$$n(R) = \begin{cases} n_B \left(\frac{R_B}{R} \right)^{\gamma_1} & \text{for } R < R_B \\ n_B \left(\frac{R_B}{R} \right)^{\gamma_2} & \text{for } R > R_B \end{cases} . \quad (5.18)$$

γ_1 and γ_2 are related to the gradients ΔN_1 and ΔN_2 as in (5.17) and the corresponding effective earth radii from (5) are denoted R_{e1} and R_{e2} or more simply R_1 and R_2 . The subscript e denoting the effective earth radius will be dropped in what follows.

5.3.3 Ray Equations

The geometry of a refracted ray in a flat-earth coordinate system is shown in Figure 5-6. This figure defines graphically the key ray parameters. The link is specified by the distance D and the heights h_T and h_R of transmitter and receiver relative to the layer interface. The ray can enter the inversion medium several times. In Appendix A the equations for the rays are determined for all possible configurations of the transmitter and receiver terminal locations relative to the layer interface. It is found that the following exact equations are uniformly valid:

$$D = m \theta_B (R_1 - R_2) - R_T \theta_T - R_R \theta_R, \quad m > 0 \quad (5.19)$$

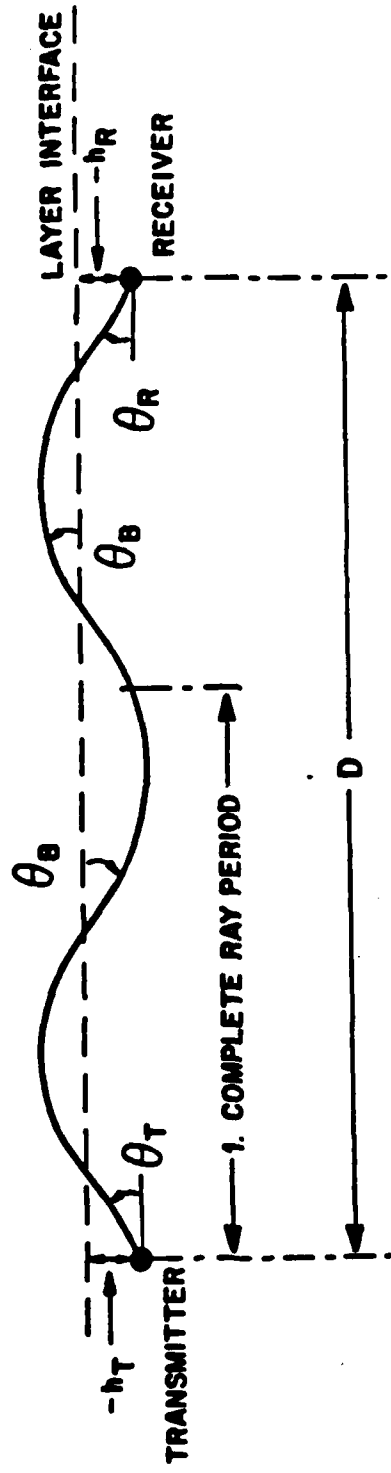
$$\cos \theta_B = \frac{R_T + h_T}{R_T} \cos \theta_T \quad (5.20)$$

$$= \frac{R_R + h_R}{R_R} \cos \theta_R \quad (5.21)$$

where

D = Link distance defined along the layer interface. This parameter is assumed fixed in the following, even when varying the height of the terminals.

UPPER LAYER CHARACTERIZED BY ΔN_2 OR R_2



LOWER LAYER CHARACTERIZED BY ΔN_1 OR R_1

Figure 5-6 Ray Parameters Defined

- R_1 = Effective earth radius just below the interface
 ($R_1 > 0$)
- R_2 = Effective earth radius just above the interface
 ($R_2 < 0$)
- R_T = Effective earth radius in the transmitter medium, i.e.,

$$R_T = \begin{cases} R_1 & \text{for } h_T < 0 \\ R_2 & \text{for } h_T > 0 \end{cases}$$
- R_R = Effective earth radius in the receiver medium,
- h_T = Effective transmitter height
- h_R = Effective receiver height
- m = the number of times the ray crosses the interface.

For each value of m , equations (5.19)-(5.21) must be solved for the unknown ray angles θ_B , θ_T , and θ_R .

In the troposphere, the exact equations (5.20) and (5.21) can be well approximated by assuming small angles. This means that the effective heights are approximately equal to the actual heights, and that (5.20) and (5.21) become

$$\theta_B^2 = \theta_T^2 - 2 \frac{h_T}{R_T} \quad (5.22)$$

$$= \theta_R^2 - 2 \frac{h_R}{R_R} \quad (5.23)$$

Note that we always have $\theta_B^2 > \theta_T^2$ and $\theta_B^2 > \theta_R^2$. By eliminating θ_T and θ_R from (5.19), (5.22), and (5.23) the following quartic equation in θ_B is obtained:

$$\left\{ \left[m \theta_B - \frac{D}{R_1 - R_2} \right]^2 - (\mu_T^2 + \mu_R^2) \theta_B^2 + 2\mu_T^2 \epsilon_T + 2\mu_R^2 \epsilon_R \right\}^2$$

$$= 4\mu_T^2 \mu_R^2 (\theta_B^2 - 2\epsilon_T)(\theta_B^2 - 2\epsilon_R) \quad (5.24)$$

where

$$\mu_{T,R} = \frac{R_{T,R}}{R_1 - R_2}$$

and

$$\epsilon_{T,R} = - \frac{h_{T,R}}{R_{T,R}} .$$

For each value of m , there are at most four real solutions for the rays.

The equations parameterized by m , the number of boundary crossings, are convenient because of their uniform validity. However, the solutions for fixed m do not connect smoothly for smooth variations of the link parameters D , h_T , and h_R , as will be illustrated in Section 5.3.4. Smoothly connecting solutions instead are those which contain the same number, p , of complete periods of the ray. That is, the solutions to (5.24) which satisfy

$$2p \theta_B (R_1 - R_2) < D < 2(p+1) \theta_B (R_1 - R_2), \quad p > 0 \quad (5.25)$$

form a continuous curve as link parameters are varied. This indicates that p is a better parameterization of the solutions than m . We will call p the order of the ray. There can be 1 or 3 rays of order zero, but 0, 2, or 4 rays of any order $p > 0$.

The delay τ of a ray specified by (5.19)-(5.21) is found to be given exactly by

$$\begin{aligned} \tau c = m(R_1 - R_2) \sin \theta_B - R_T \cos \theta_B \tan \theta_T \\ - R_R \sin \theta_B \tan \theta_R, \end{aligned} \quad (5.26)$$

where c is the velocity at the interface. The power focussing gain, G_t , is defined as the ratio of the geometrical optics intensity of the ray relative to a line-of-sight ray in a homogeneous medium. This can also be found exactly:

$$\begin{aligned} G_f = \frac{P}{P_{LOS}} = - \frac{D \cos \theta_T}{\cos \theta_R} \bigg/ \frac{\delta h_R}{\delta \theta_T} \\ = D \cos \theta_T / [m(1-\epsilon_T)(1-\epsilon_R)(R_1-R_2)(\sin \theta_T \sin \theta_R / \sin \theta_B) \\ - (1-\epsilon_T) R_R \sin \theta_T - (1-\epsilon_R) R_T \sin \theta_R] . \end{aligned} \quad (5.27)$$

This geometrical optics solution breaks down near a caustic ($G_f \rightarrow \infty$). A uniform asymptotic solution valid both near a caustic and away from caustics [Ludwig, 1966] is used. Near a caustic, two real rays combine coherently. On the shadow side of the caustic these rays become complex. The uniform asymptotic solution can be applied in the following manner:

1. Solve (5.19)-(5.21) and order all real or complex rays according to increasing delay (real part). There will always be an odd number of rays.
2. Assign the phase shift 0 to the first two rays, $-\pi/2$ to the next two rays, $-\pi$ to rays 5 and 6, etc. In general, a phase shift of $-\pi/2$ is applied each time a ray has been reflected from a caustic.
3. Calculate the field \underline{E}_1 for the first ray using the absolute value of the amplitude found from the geometrical optics equation (5.27).
4. Calculate the field for rays 2 and 3 using the geometrical optics field vectors \underline{E}_2 and \underline{E}_3 (with the phase shifts from step 2) and delays τ_2 and τ_3 in the following expression

$$\underline{E}_{23} = \sqrt{2\pi i} e^{i\theta} \{ \underline{e}_0 \text{Ai}(-t) + i \underline{e}_1 \text{Ai}'(-t) \} \quad (5.28)$$

where $\text{Ai}(z)$ is the Airy function, $\text{Ai}'(z)$ is its derivative, and denoting frequency by f ,

$$\theta = \pi f(\tau_2 + \tau_3)$$

$$\frac{2}{3} t^{3/2} = \pi f(\tau_3 - \tau_2)$$

$$\underline{e}_0 = \frac{t^{1/4}}{\sqrt{2}} [\underline{E}_3 - i \underline{E}_2]$$

$$\underline{e}_1 = \frac{t^{-1/4}}{\sqrt{2}} [\underline{E}_3 + i \underline{E}_2] .$$

5. Repeat steps 4 for rays 4 and 5, 6 and 7, etc., and find the total field

$$\underline{E}_{\text{tot}} = \underline{E}_1 + \underline{E}_{23} + \underline{E}_{45} + \dots$$

The resulting field solution is valid both near to and far from a caustic for sufficiently high frequencies. A more economical representation may sometimes be achieved by using low order modes from the mode expansion to replace the high order rays [Felsen and Ishihara, 1979]. This approach will not be explored here.

We have found that instead of using the correct uniform asymptotic solution, we can approximate the statistics of the total field by adding the amplitudes of the real rays calculated from $|G_f|$ in (5.27) with the phase shifts 0, 0, π , π , 0, 0, While this will not yield the correct field at a given location, the field statistics, in the cases we have examined, have been indistinguishable from the statistics of the field from the more exact solution (5.28).

5.3.4 Examples

Insight into the properties of refractive multipath is best achieved by looking at a few examples. The multipath depends on the relative height of receiver and transmitter,

$$\Delta = h_R - h_T$$

and on the layer height relative to the transmitter ($-h_T$), in addition to the refractivity gradients.

Let us first fix the gradients at -40 Nu/km and -300 Nu/km, and assume $\Delta = 40$ m for a 100 km link. Figure 5-7 shows relative

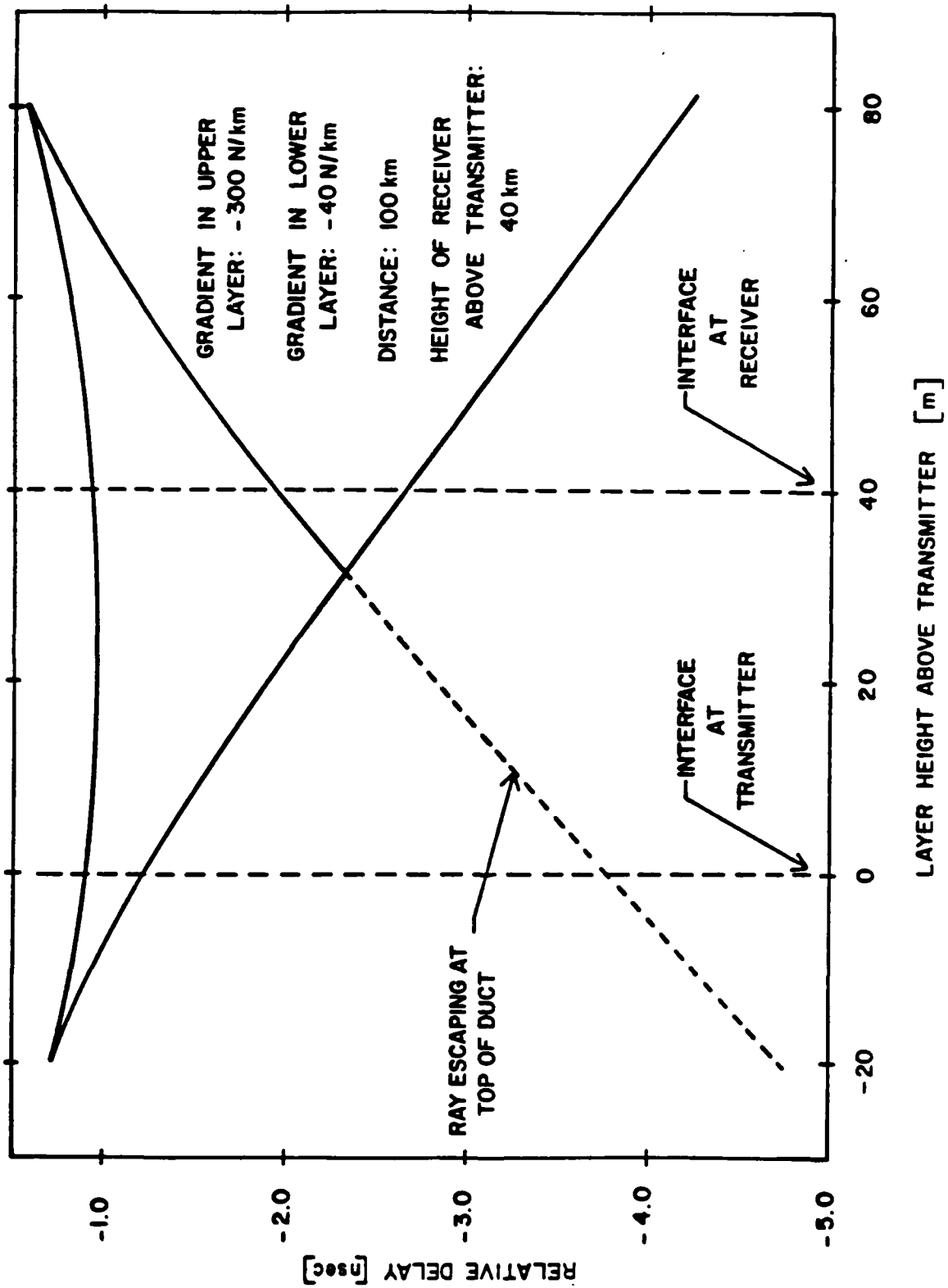
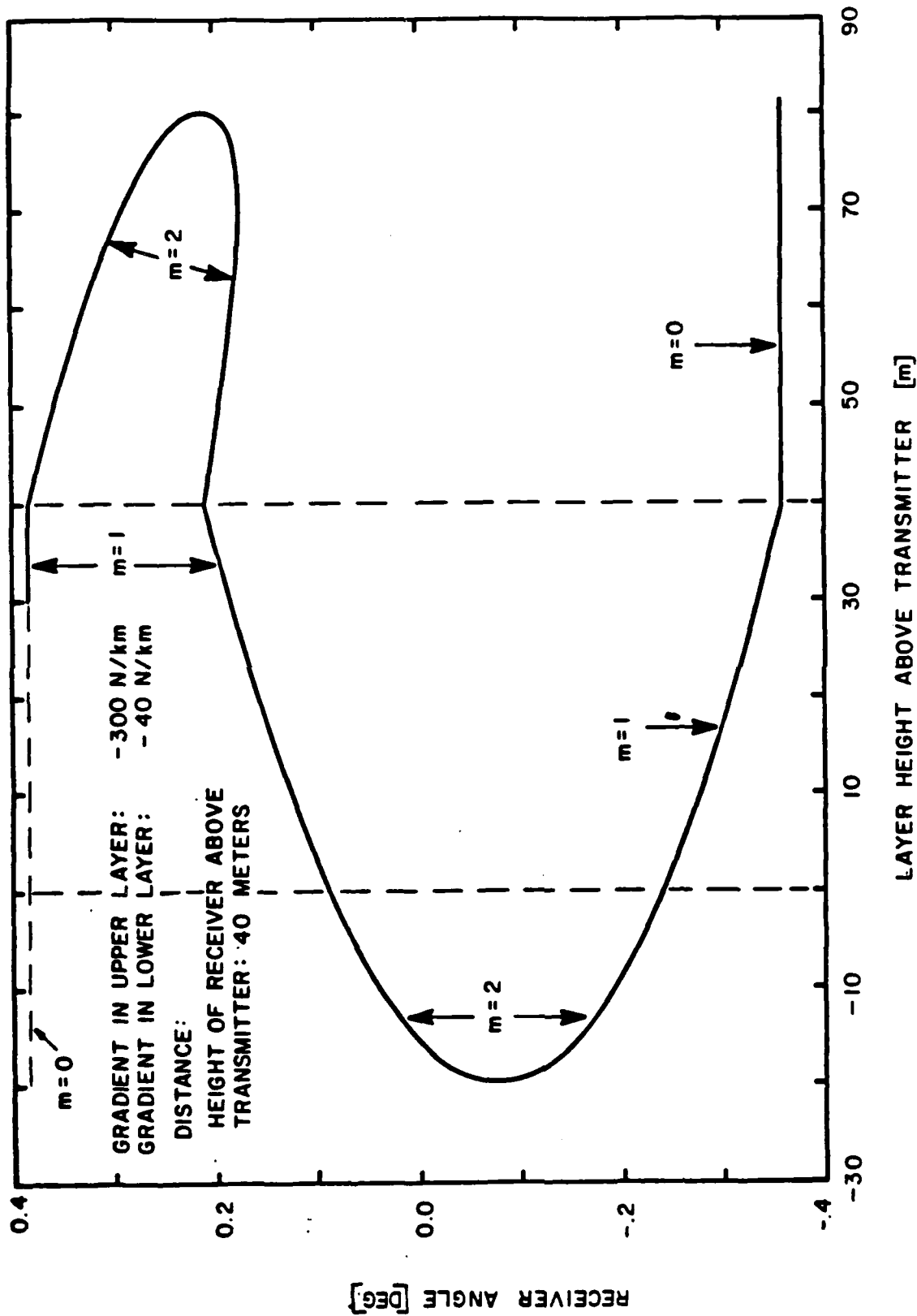


Figure 5-7(a) Example of multipath dependence on layer height



(b) ANGLE - OF - ARRIVAL

Figure 5-7(b) Example of multipath dependence on layer height

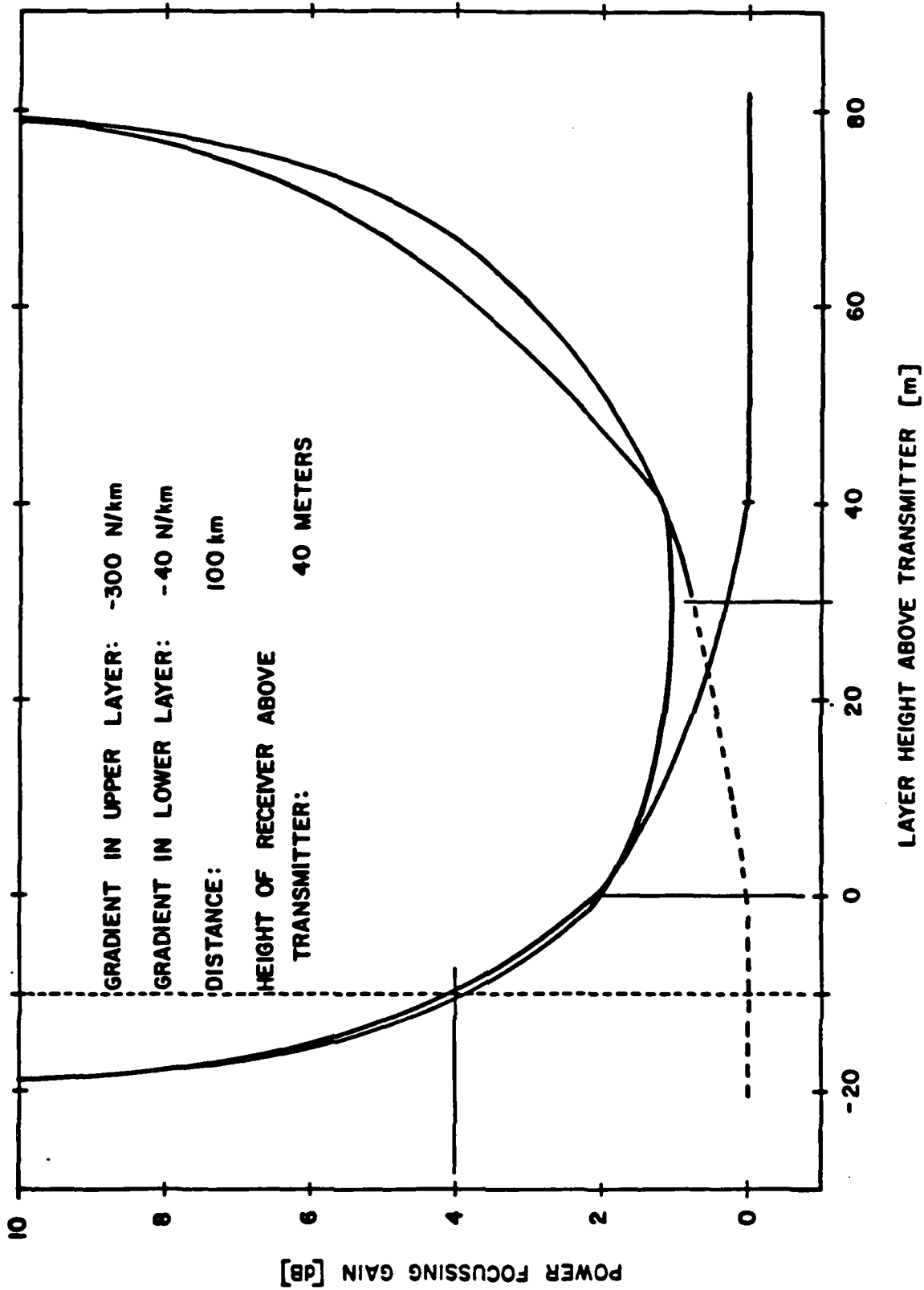


Figure 5-7(c) Example of multipath dependence on layer height

delay (defined as $\tau - D/c$), angles of arrival and power relative to LOS of the rays as a function of layer height. For the layer interface less than 20 m below the transmitter up to 80 m above the transmitter, there are three rays. It can easily be shown that there will always be an odd number of rays. When two rays join and disappear the delay curves meet in a cusp, while the angle curves meet in a parabola segment. This shows that, as we move away from a caustic, such rays faster become resolvable on the basis of angle than on the basis of delay. The example in Figure 5-7 displays a delay spread of 4 nsec and an angle spread of 0.75° . The angle spread shows it is important to model the angle variation for LOS links with narrowbeam antennas. A comparison of Figures 5-7(a) and 5-7(c) shows that the latest arriving ray is the strongest. In practice, the upper ray will exhibit defocusing close to the upper boundary of the finite layer [Webster, 1983]. This effect is not included in Figure 5-7(c).

Figure 5-8 illustrates angle-of-arrival and delay for a 50 km link with the receiver only 1 meter higher than the transmitter. For a -200 Nu/km duct there can be up to 11 rays. The three rays in the large outer diagram define the zero order rays, as defined in (5.25). For a -300 Nu/km duct four more rays (of order 3) are possible. It is characteristic that rays occur in groups of four, and that higher order rays arrive later than lower order rays. The high order rays penetrate less into the duct, skipping in and out many times. These rays are only supported when the layer interface is close to both the terminals. When the gradient is -600 Nu/km (or less) it becomes necessary to consider the finite thickness of the duct. The solid lines are for a duct with a total refractivity change of 50 Nu. Both angle-of-arrival and delay are seen to be strongly dependent on the gradient. Some analytical expressions for these parameters will be presented in Sections 5.3.6 through 5.3.8.

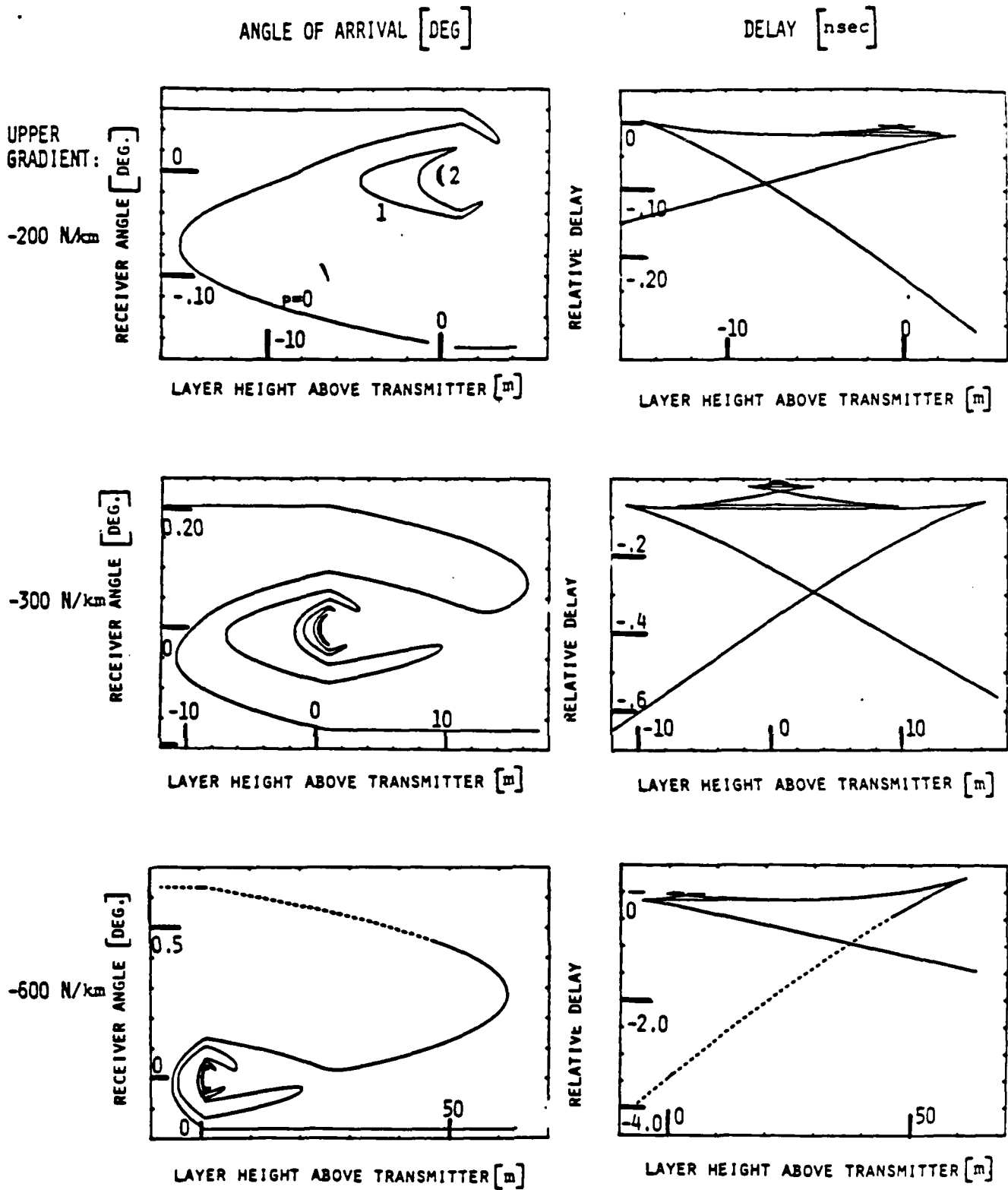


Figure 5-8 Angle-of-arrival and relative delay as a function of layer height above transmitter for different ducting gradient. This link is 50 km, the lower refractivity gradient is -40 Nu/Km and the receiver is 1m above the transmitter. The dashed rays are not supported for ducts with a total refractivity decrease less than 50 Nu.

The inversion layer is often tilted to follow the terrain or the slope of a frontal air mass. Figure 5-9 illustrates the effect of layer slope by considering different relative terminal heights. The figures show angle-of-arrival, delay and the height of the highest point on the ray. This latter parameter is used to determine the effect of the finite duct thickness. When the receiver is much higher than the transmitter relative to the layer interface, no multipath is possible. When both terminals are closer to the layer interface, the number of rays can be 3, 7, 11, ..., etc. For equal height terminals infinitely many rays can exist, as shown in the last row of figures in Figure 5-9. Clearly, there is always an odd number of rays. This holds also for finite thickness ducts, but some of the rays can then have a negligible amplitude.

The power received relative to the predicted line-of-sight (free-space) levels will be called the focussing gain. The focussing gain calculated from the geometrical optics approximation was shown in Figure 5-7(c). It is seen that the infinite gain at caustics occurs where two rays join. The exact theory predicts a finite field strength everywhere. The geometrical optics solution also yields a finite field strength if the two rays near a caustic add with a phase shift of 180° . When this is done at low frequencies, a relatively smoothly varying focussing gain results. Figure 5-10 shows the relative received power as a function of layer height for a terminal height difference of 20 m and for two extreme frequencies, 0 and 100 GHz. The curve for 0Hz is quite smooth, the appearance of caustics almost not noticeable. The rapid oscillations at the high frequency is due to the interaction between the many rays. The focussing gain is mostly positive, with an occasional deep fade. At no point does the field become infinite. Figure 5-11 shows the focussing gain at 4GHz, where the oscillations are less rapid, but the same characteristics are observed.

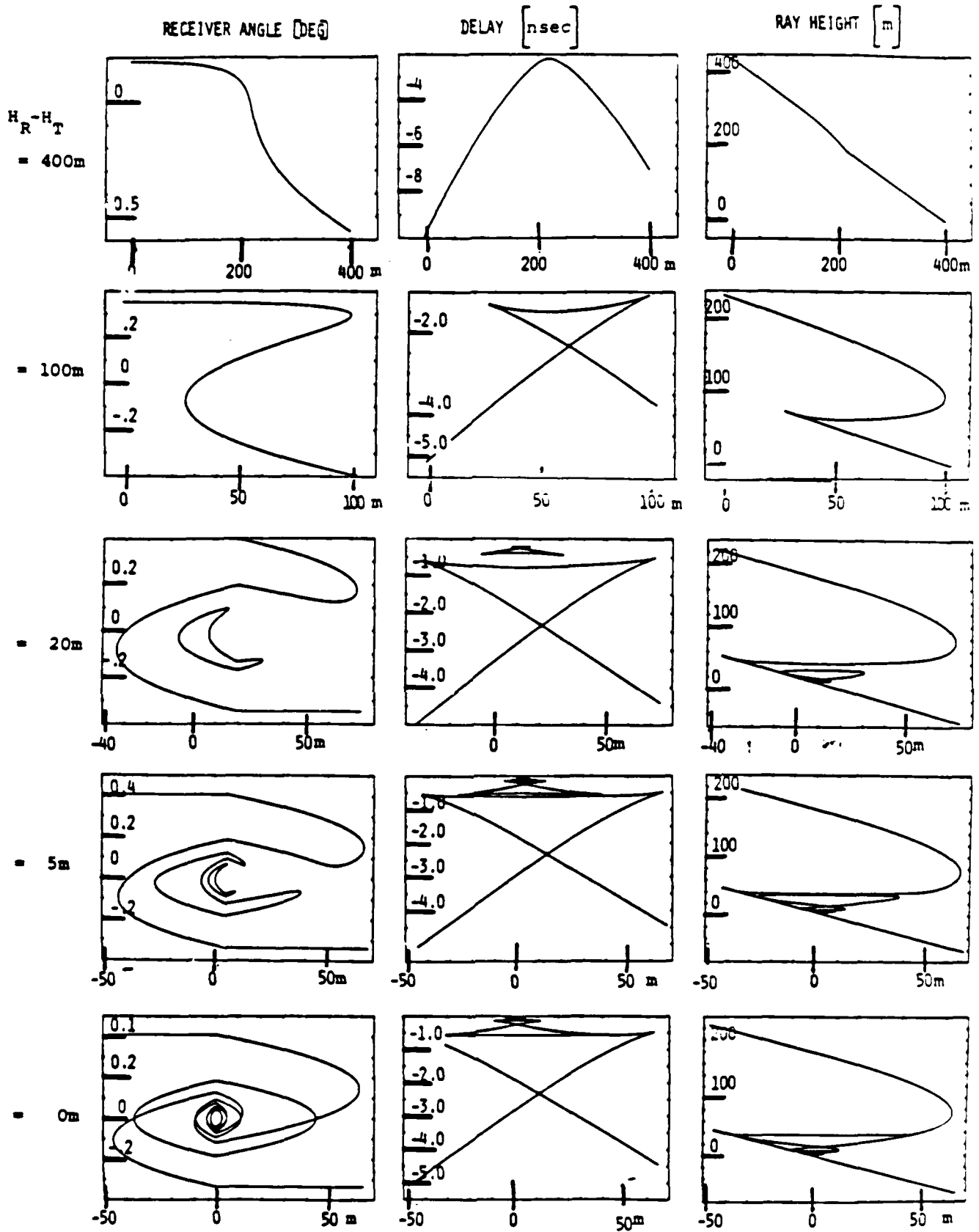


Figure 5-9 Angle-of-arrival, relative delay, and maximum ray height as function of height of layer above transmitter (in meters). The link is 100 km; refractivity gradients are -40 Nu/km below the interface, -300 Nu/km above the interface.

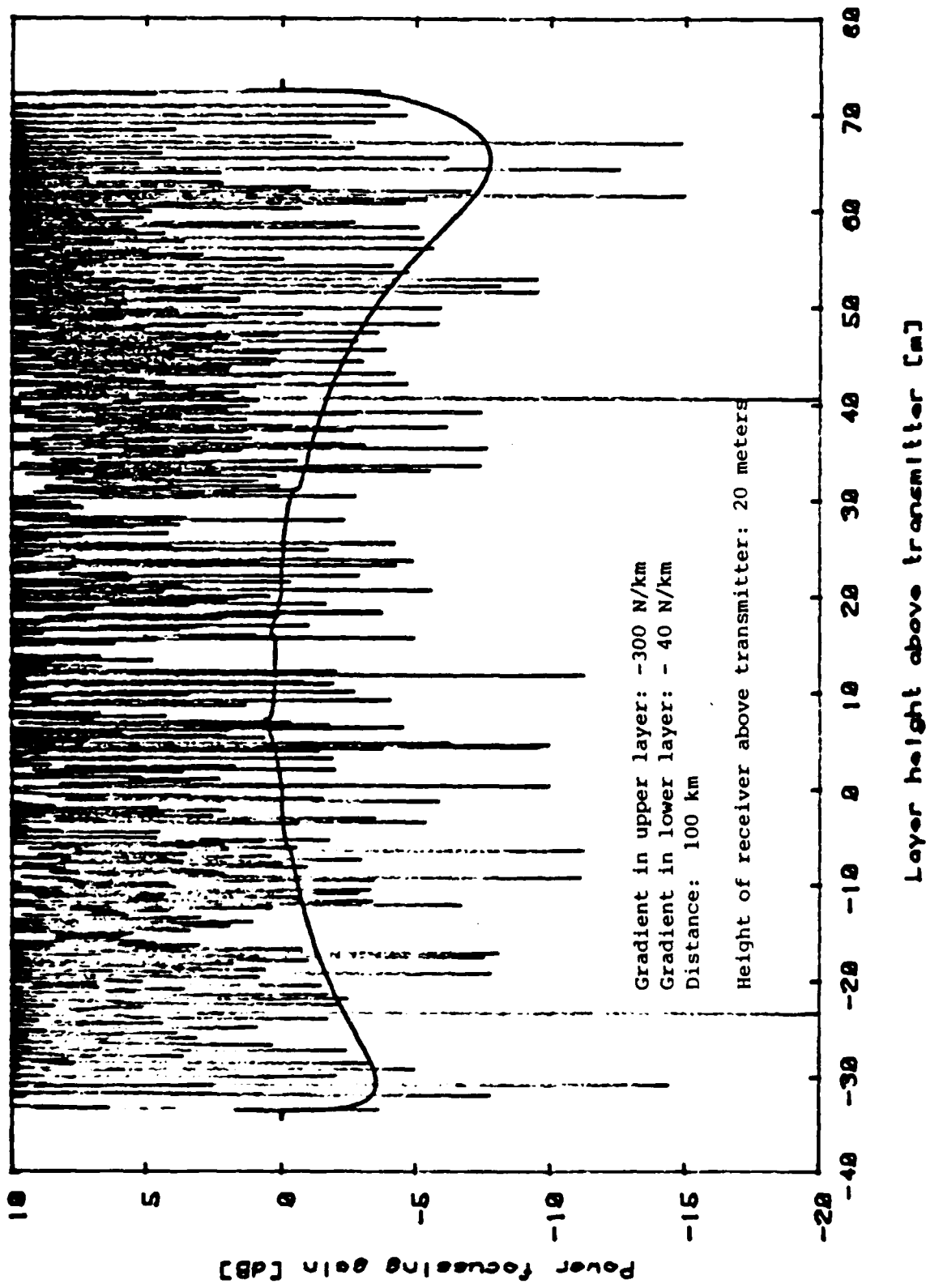
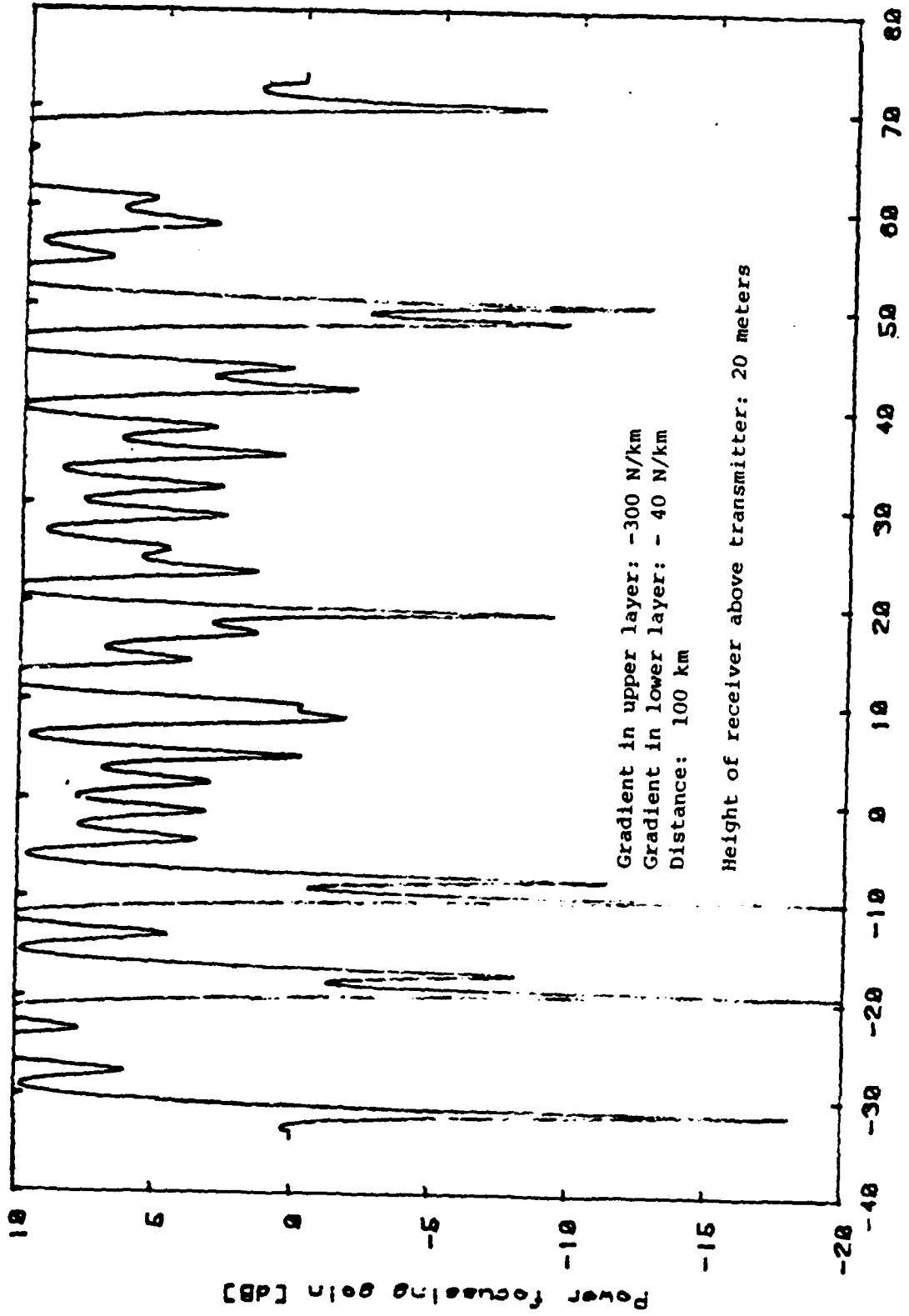


Figure 5-10 Total field strength relative to line-of-sight at low frequencies (smooth curve) and 100 GHz (oscillating curve).



Layer height above transmitter [m]

Figure 5-11 Total Field Strength at 4 GHz.

The approximation used in Figures 5-10 and 5-11 adding rays at a caustic out of phase, does not correspond exactly to the prediction of the full wave theory. Away from a caustic the two approaches yield the same amplitudes but different phases. The ray interference pattern is essentially the same, only the predicted deep fades may be shifted in frequency. Near a caustic, where geometrical optics break down, both methods yield finite results, not drastically different. We therefore conclude that a good picture of the fading mechanisms during refractive multipath conditions can be achieved based on the simpler ray theory.

The fade depth is strongly dependent on the layer height. Figure 5-12 shows the fading vs. frequency for a layer boundary height at 0.2 m intervals near 30 m on a 100 km link with $h_R - h_T = 20\text{m}$.

5.3.5 Solving The Ray Equations (REAL CASE)

The quartic equations (5.24) can be solved numerically or analytically. The analytical solution is particularly simple when

- (i) $h_T = 0$
- (ii) $h_R = 0$
- (iii) $h_T = h_R$

In these cases only quadratics need to be solved. In the general case, instead of solving for the rays of a given layer height, we can solve for the layer height as a function of the boundary angle θ_B . This leads to simpler analytical expressions for the real rays and is useful since θ_B is directly related to the inversion thickness required to support the corresponding ray.

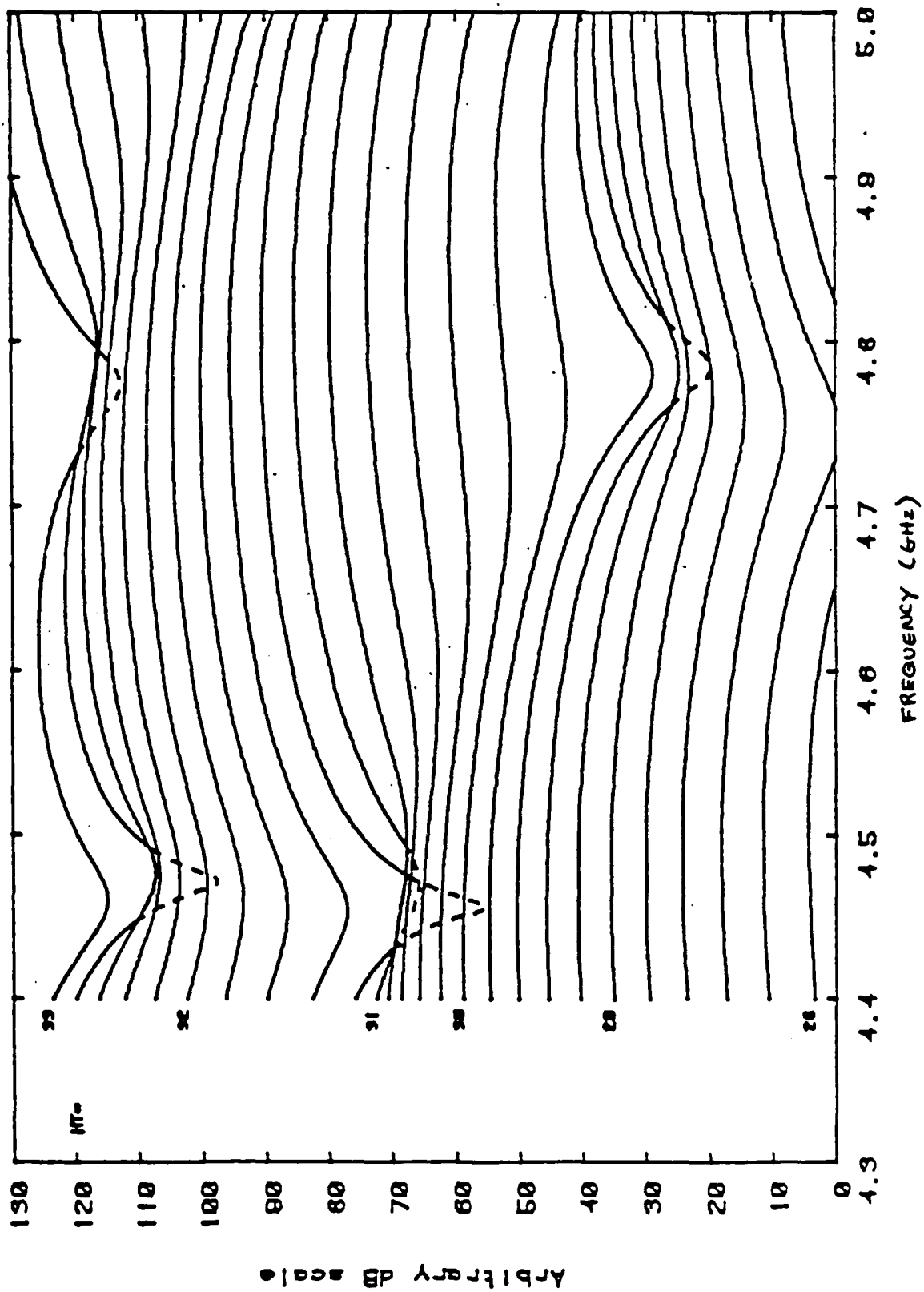


Figure 5-12 Fading vs. Frequency for a Layer Boundary Height at 0.2 m Intervals near 30 m on a 1-0 km Link with $h_R - h_T = 20$ m.

Define

$$\Delta = h_R - h_T$$

and

$$h = h_T + \frac{R_1}{R_1 - R_2} \Delta = h_R + \frac{R_2}{R_1 - R_2} \Delta \quad (5.29)$$

The equations (5.22) and (5.23) become

$$\theta_T^2 = \theta_B^2 + \frac{2h}{R_T} - \frac{2R_1}{R_T} \frac{\Delta}{R_1 - R_2} \quad (5.30)$$

$$\theta_R^2 = \theta_B^2 + \frac{2h}{R_R} - \frac{2R_2}{R_R} \frac{\Delta}{R_1 - R_2} \quad (5.31)$$

By eliminating two variables θ_T and θ_R from these equations, namely, Equation (5.19) (expressed as $R_T \theta_T + R_R \theta_R = W(\theta_B)$), (5.30), and (5.31) one obtains a quadratic equation in h ,

$$A_0 + A_1 h + A_2 h^2 = 0, \quad (5.32)$$

where

$$A_0 = [W^2 - \theta_B^2 (R_T^2 + R_R^2) + 2B(R_1 R_T + R_2 R_R)]^2$$

$$-4R_T^2 R_R^2 \left(\theta_B^2 - \frac{2R_1}{R_T} B \right) \left(\theta_B^2 - \frac{2R_2}{R_R} B \right),$$

$$A_1 = -4(R_T + R_R) [W^2 - \theta_B^2 (R_T - R_R)^2]$$

$$-8B(R_T - R_R) [R_1 R_T - R_2 R_R],$$

$$A_2 = 4(R_T - R_R)^2,$$

and where

$$B = \Delta / (R_1 - R_2),$$

$$W = W(\theta_B) = m(R_1 - R_2) \theta_B - D.$$

We look for solutions for the rays of order p . When the terminals are on opposite sides of the layer interface, this means that $m = 2p+1$, $R_T = R_1$, and $R_R = R_2$ (we assume the receiver is the highest terminal). Defining

$$P(\theta_B) = W^2(\theta_B) - (R_1 - R_2)^2 (\theta_B^2 - 2B),$$

the solution to (5.32) is

$$h = \frac{(R_1 + R_2) P(\theta_B) \pm 2W(\theta_B) \sqrt{R_1 R_2 P(\theta_B)}}{2(R_1 - R_2)^2}, \quad \theta_{B1}(p) < \theta_B < \theta_{B2}(p), \quad (5.33)$$

provided that h corresponds to terminals on opposite sides,

$$R_2 < h(R_1 - R_2)/\Delta < R_1.$$

The interval of validity is determined by the requirement that $P(\theta_B) < 0$, so

$$\theta_{B1}, \theta_{B2} = \frac{\frac{D}{R_1 - R_2} (2p + 1) \mp \left[\left(\frac{D}{R_1 - R_2} \right)^2 - 8 \frac{\Delta}{R_1 - R_2} p(p+1) \right]^{1/2}}{4p(p+1)} \quad (5.34)$$

(minus for θ_{B1} , plus for θ_{B2}).

For $p=0$, we have in particular $\theta_{B2} = \infty$, and

$$\theta_{B1} = \frac{D}{2(R_1 - R_2)} + \frac{\Delta}{D} \quad (5.35)$$

$\theta_B = \theta_{B1}$ is achieved when the terminals are in different layers. Note that for both terminals below the interface and $h_R=0$ we have $\theta_B = -\theta_R = D/(2R_1) + \Delta/D$ which is larger than θ_{B1} in (23) as required. The rays of order p only exist for $\theta_{B1}(p) < \theta_B < \theta_{B2}(p)$. This is consistent with the fact that p denotes the number of completed ray periods on the link (Equation (5.25)).

The conditions (5.34) for a solution of order p hold also when both terminals are on the same side of the layer. In that case, the rays of order p consist of rays that cross the boundary $m = 2p$ or $m = 2p+2$ times. Substituting $R_R = R_T$ in (5.32) yields

$$h = \left[(W^2(\theta_B) - 2R_T^2 \theta_B^2 + 2B R_T(R_1 + R_2)) \right]^2 - 4R_T^2 [R_T \theta_B^2 - 2R_1 B] [R_T \theta_B^2 - 2R_2 B] / 8 R_T W^2(\theta_B) \quad (5.36)$$

This yields two solutions valid for

$$\theta_{B1}(p) < \theta_B < \theta_{B2}(p)$$

by substituting $m = 2p$ and $2p + 2$

and

$$R_T = R_1 \text{ provided } h < \Delta R_2 / (R_1 - R_2)$$

(both terminals in layer 1)

or

$$R_T = R_2 \text{ provided } h > \Delta R_1 / (R_1 - R_2)$$

(both terminals in layer 2) .

It is possible to obtain analytical expressions for the value of θ_B where there is a transition between the solution (5.33) and the solution (5.35). However, these expressions are of less general interest and may easily be derived by the reader by solving analytically for the special cases $h_T = 0$ and $h_R = 0$.

The case of equal height terminals ($h_T = h_R$) is of special interest since it corresponds to the largest delay spread. The solution, from (5.35) consists of four segments:

$$\theta_B = D / [(R_1 - R_2)2p] , \quad (5.37a)$$

$$\theta_B = D / [(R_1 - R_2)(2p + 2)] , \quad (5.37b)$$

and

$$h = \frac{R_T}{2} \left(\left(\frac{W}{2R_T} \right)^2 - \theta_B^2 \right) , \quad m = 2p \text{ and } 2p+2 . \quad (5.37c)$$

In the first two segments ((5.37a), (5.37b)) the height h is constrained only by θ_T^2 and $\theta_R^2 > 0$ in (5.22) and (5.23).

5.3.6 Conditions For Multipath

It is clear from Figure 5-9 that multipath occurs only when the height difference of the terminals is small enough. The exact conditions for the occurrence of higher order rays ($p > 1$) at some layer height can be obtained directly from (5.34). Requiring θ_{B1} and θ_{B2} to be real yields the condition

$$h_R - h_T = \Delta < \frac{D^2}{8 p(p+1)(R_1 - R_2)} . \quad (5.38)$$

The condition for rays of order 0 requires special attention.

Since $\delta h / \delta \theta_B$ is infinite when

$$\theta_B = \theta_{B0} = \frac{1}{2} \frac{D}{(R_1 - R_2)} + \frac{h_R - h_T}{D}$$

(here $h = 0$) multipath occurs if and only if $\delta h / \delta \theta_B = 0$ for some $\theta_B > \theta_{B0}$. By differentiating (5.33) we find that the condition for multipath at some layer height is

$$h_R - h_T < \frac{D^2}{6} \left[\frac{1}{R_1} + \frac{1}{(-R_2)} - \frac{1}{(R_1 - R_2)} \right] . \quad (5.39)$$

This is the theoretical condition assuming infinite layer thickness. With a finite layer thickness (5.39) is only a necessary condition. A condition for strong ducts is found in Section 5.3.8, Equation (5.43). Figure 5-13 illustrates the height difference condition in (5.39).

5.3.7 Angle Of Arrival (AOA)

The AOA of the LOS ray is

$$\theta_R = - \frac{D}{2R_R} - \frac{h_R - h_T}{D} .$$

The maximum angle variation with two thick layers is

$$\Delta \theta = \frac{D}{2} \left(\frac{1}{R_1} - \frac{1}{R_2} \right) = \frac{D}{2 R_0} \frac{\Delta N_1 - \Delta N_2}{157} . \quad (5.40)$$

In practice, the AOA is limited by the ground in the lower medium, and by the duct thickness in the upper medium. The maximum angle-of-arrival is determined from the inversion intensity ΔM [Dougherty and Hart, 1979],

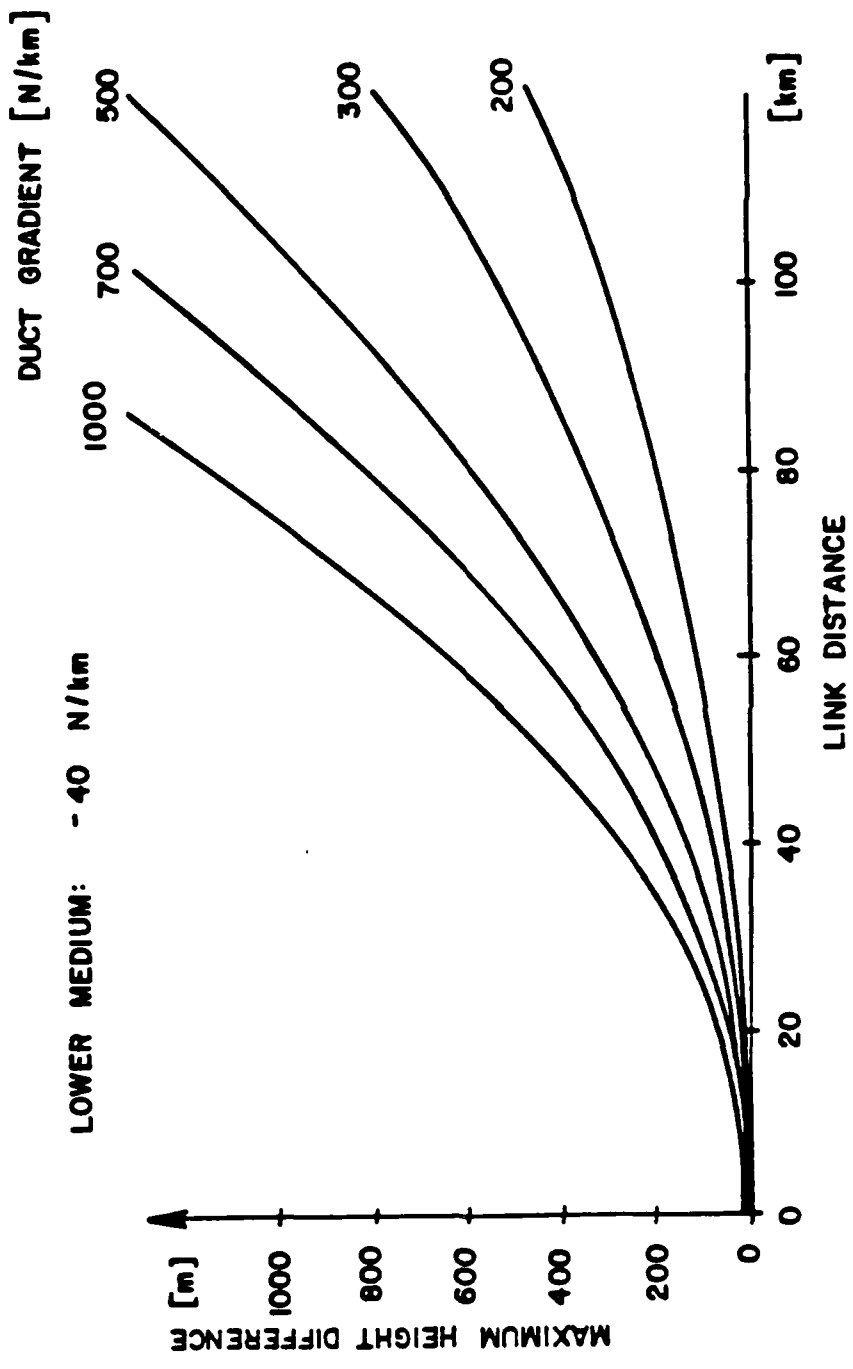


Figure 5-13 The maximum height difference that may support multipath

$$\theta_R < \theta_B < \sqrt{2 \Delta M \cdot 10^{-6}} . \quad (5.41)$$

For $\Delta M < 300$ the maximum angle is 1.4° . For a more realistic value of $\Delta M = 50$ we get a maximum angle of 0.57° . Hence, a beamwidth of at least 1° is required on LOS links to insure that the direct ray remains in the mainlobe even in the absence of multipath [Webster, 1982]. As seen in Figures 5-7 through 5-9 this angle variation also represents the maximum angle spread in the presence of multipath.

5.3.8 Delay Spread With Equal Height Terminals

The largest delay spread occurs when the layer is tilted so that the terminals are at equal height relative to the interface (see Figure 5-9). In this section the delay spread of zero order rays is bounded by considering equal height terminals and the worst case layer height. We assume first that the ducting layer is sufficiently thick so all rays are supported. Only the delay of zero order rays will be considered since the delay of higher order rays is negligible in comparison (see Figures 5-8 and 5-9). It is convenient to define the dimensionless parameters

$$z = - \frac{2 h_T}{R_T} ; \quad x = \frac{D}{2(R_1 - R_2)} ; \quad y = \frac{R_T}{R_1 - R_2} .$$

In terms of these parameters the delay (see Appendix A) can be written

$$\frac{3(D - \tau c)}{(R_1 - R_2)} = X\theta_B^2 - 2ZY\theta_T .$$

For the refracted rays ($m=2$) $\theta_T = (\theta_B - X)/Y$. We find the angle θ_B at the caustic using $dh/d\theta_B = 0$ in (5.37c),

$$\theta_{B, \text{caustic}} = X/(1 - Y^2)$$

and the normalized layer height,

$$z_{\text{caustic}} = X^2/(1 - Y^2) .$$

We are now able to calculate the delay spread at the caustic, e.g., at $h_T = -80\text{m}$ in Figure 5-7(a). The delay of the two rays meeting at the caustic is given by

$$\frac{3(D - \tau_1 c)}{R_1 - R_2} = X^3(1 - 2Y^2)/(1 - Y^2)^2 .$$

At the layer height where this happens the delay of the fixed ray, the LOS ray, is given by

$$\frac{3(D - \tau_2 c)}{R_1 - R_2} = X^3(1 + 2Y^2)/(Y^2 - Y^4) .$$

The difference $\Delta\tau = \tau_1 - \tau_2$ yields the delay spread

$$\Delta\tau = \frac{R_1 - R_2}{3c} \frac{X^3}{Y^2(1 - Y^2)^2} \quad (5.42)$$

Thus when $-R_2 < R_1$ the delay spread is largest when the terminals are in the inversion layer ($R_T = R_2$). When this solution is valid (i.e., the inversion thickness is not a factor) the delay spread is seen to increase with the third power of distance. However, the ducted LOS ray contributing to the large delays in (5.42) may be negligible for practical inversion thicknesses. It is more realistic to use (5.42) with the terminals in the lower medium ($R_T = R_1$).

When the inversion is strong and of finite thickness multipath occurs only when the terminals are below the layer since the highest multipath ray escapes through the duct (extrapolate the results in Figure 5-8 to higher lapse rates). The ray that just grazes the upper boundary of the duct hits the lower boundary with the critical angle $\theta_{BT} = \sqrt{-2T/R_2}$ where T is the inversion thickness. (5.42) is valid when $X < \theta_{BT}(1-Y^2)$. Now suppose that $X > \theta_{BT}(1-Y^2)$. The minimum boundary angle for rays of order zero is X (see Section 5.3.6). Hence, in order for the other refracted ray to exist we must have $\theta_{BT} > X$, or

$$T > \frac{-D^2 R_2}{8(R_1 - R_2)^2} \quad (5.43)$$

For steep gradients ($-R_2$ small), this means that, to see more than one ray of order zero, the inversion intensity (total change in refractivity) must be greater than

minimum duct intensity: $10^6 \frac{D^2}{8 R_1^2}$ (N-units) .

(17 Nu for $D = 100$ km). The terminal height corresponding to θ_{BT} is found from (5.37c), so the delay τ_3 of the refracted ray grazing the upper boundary of the inversion layer is determined from

$$\frac{3(D - c\tau_3)}{(R_1 - R_2)} = X \theta_{BT}^2 - 2(\theta_{BT} - X) \left[\theta_{BT}^2 - \left(\frac{\theta_{BT} - X}{Y} \right)^2 \right] .$$

The LOS ray is characterized by $\theta_T = \theta_R = -D/(2 R_T)$, yielding the delay τ_4 , at the height found above, given by

$$\frac{3(D - c\tau_4)}{(R_1 - R_2)} = X \left\{ (Y^2 - 1) \theta_{BT}^2 + 2 X \theta_{BT} \right\} / Y^2 + 2X \left[\theta_{BT}^2 - \left(\frac{\theta_{BT} - X}{Y} \right)^2 \right] .$$

The delay difference $\Delta\tau = \tau_3 - \tau_4$ is

$$\Delta\tau = \frac{(R_1 - R_2) \theta_{BT}^2}{3c Y^2} [3X - 2 \theta_{BT}(1 - Y^2)] \quad (5.44)$$

$$(\theta_{BT}(1 - Y^2) < X < \theta_{BT})$$

in contrast to (5.42) this increases linearly with distance ($\sim X$). Eq. (5.44) reduces to (30) when $\theta_{BT} > X/(1 - Y^2)$. (5.42) and (5.44) with $Y = R_1/(R_1 - R_2)$ constitute the expression for

the delay spread when an LOS ray in the inversion layer can be neglected (only thick, low intensity ducts can support such a ray). These equations do not consider the usually negligible delays of higher order rays. Note from (5.43) and (5.44) that for $X = \theta_{BT}$ there is a maximum delay spread of zero order rays. When $\theta_{BT} < X$ all but one zero order ray escape from the top of the duct. Setting $\theta_{BT} = X$ we get for a given inversion thickness:

$$\Delta\tau < \frac{(R_1 - R_2)}{3c} \frac{\theta_{BT}^3}{y^2} (1 + 2y^2) . \quad (5.45)$$

The results represent the largest delay spread in the sense that the worst case layer height and layer tilt have been selected. The results are similar to those in [Sasaki and Akiyama, 1974]. At large distances, when $\theta_{BT} < X$, they break down since only one zero order ray is significant and in that case multipath is caused only by higher order rays.

Figure 5-14 illustrates how the delay spread has a cubic distance dependence at small distances and a linear dependence at larger distances.

5.4 ANGLE DIVERSITY FOR LOS MULTIPATH PROTECTION

5.4.1 Introduction

Fading on an LOS link is caused by destructive interference between multiple LOS rays. The multipath condition is associated with the occurrence of elevated ducts near the radio antennas. In the past such fading has been countered by a number of techniques:

1. Requiring a large fade margin,
2. Frequency diversity,
3. Space diversity.

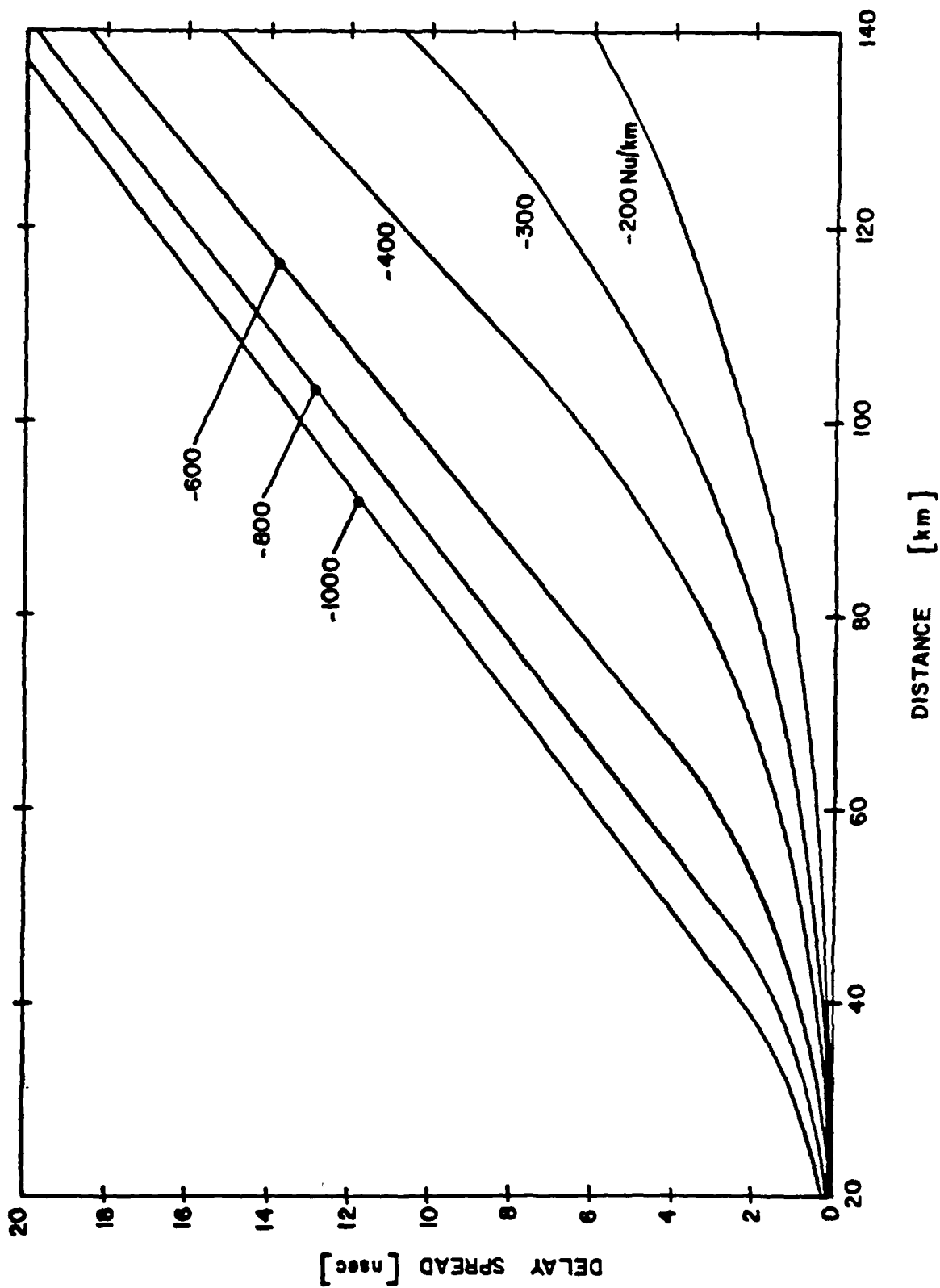


Figure 5-14 Maximum delay spread vs. distance and duct gradient for a duct of intensity $\Delta N = -50$ Nu. Refractivity gradient in lower medium is -40 Nu/km.

Due to the very deep fades that can occur the first approach is extremely wasteful of transmitter power. The diversity techniques have been found effective but have been implemented without regard to the actual structure of the multipath.

The purpose of this section is to demonstrate that the structure of the multipath, as it can be deduced from the propagation theory developed in Section 5.3 suggests an improved multipath combining technique. It is shown in Section 5.3 that LOS multipath exhibits relatively large variations in angle-of-arrival while the multipath delay spread is quite small. This fact shows that frequency diversity, which is based on the delay spread, is less effective than either space- or angle-diversity. It is also demonstrated that the character of the multipath leads to a preference for angle diversity.

The concept of designing the diversity system based on the multipath characteristics is of even greater interest for wide-band LOS systems. The wide arrival angles and small delay spreads indicate that adaptive combining based on angle-of-arrival is superior to adaptive delay equalization. Of course, the combination of these two techniques will yield the best performance, but in most cases equalization is unnecessary.

Figure 5-15 shows the principle of angle diversity. First the extreme angles of arrival are estimated. A multibeam antenna is then designed so that the full range of angles are covered. The individual beams can then discriminate between rays separated by the angular resolution. Table 5-1 shows the angle-of-arrival spread for typical links. It is seen that beamwidth of the order of 0.25° for short links, and 0.5° for long links are required. The technique therefore seems best when solid towers are available preventing significant mast sway.

In the following the details of the analytical results and candidate diversity configuration are presented. Section 5.4.2

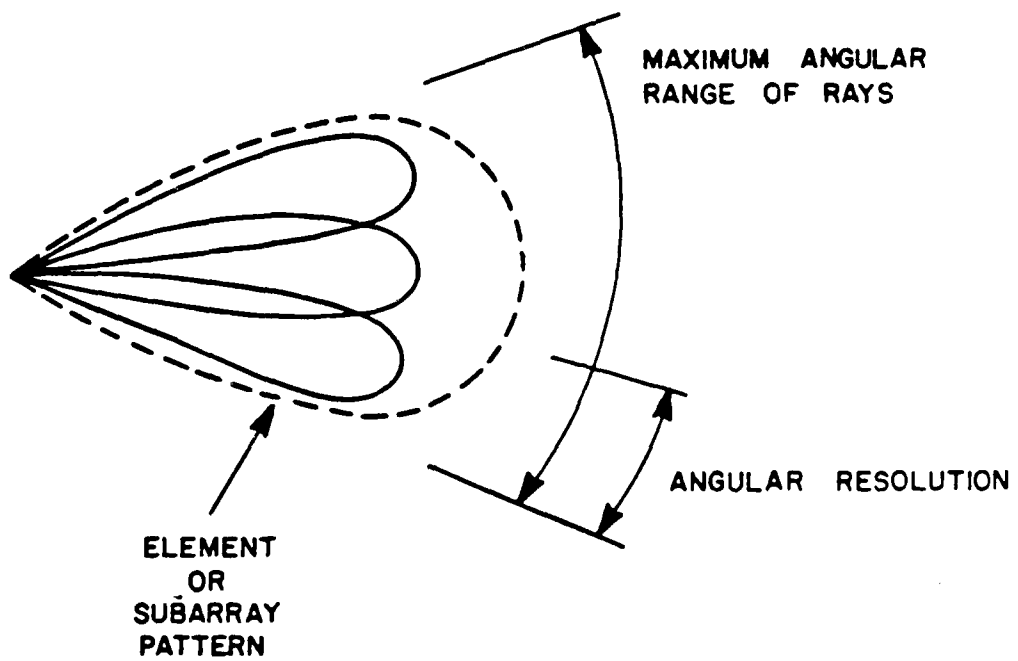


Figure 5-15 Principles of Angle Diversity

TABLE 5-1
 ANGLE SPREAD OF RECEIVED RAYS (DEGREES)
 LOWER LAYER REFRACTIVITY GRADIENT
 -40 Nu/km

UPPER LAYER REFRACTIVITY GRADIENT (NU/KM)	LINK DISTANCE		
	30 KM	50 KM	80 KM
-200	.14 DEG	.23	.36
-400	.31	.51	.82
-600	.48	.80	1.28

describes the fundamentals of diversity combining, summarizing the results of a detailed development in Appendix B. Sections 5.4.3, 5.4.4, and 5.4.5 discuss the merits of frequency diversity, space diversity, and angle diversity. In Section 5.4.5, the performance of a baseline system using adaptive combining and a single antenna with a two-port angle diversity feed approach is discussed. It is seen that the technique using angle diversity feeds has a number of advantages over the one of monopulse or phased array techniques.

The key problems to consider in the diversity system design are:

1. Is the transmitter and receiver beam coverage wide enough to assure sufficient signal during extreme refractive conditions.
2. Is the receiver angular resolution small enough to distinguish the individual rays.

The advantages of the new look at LOS diversity systems in this report are:

1. Use of higher gain antennas saves transmitter power.
2. Longer paths or higher frequencies possible.
3. Lower probability of intercept due to less transmitted power.
4. Less jamming susceptibility due to narrower beams and adaptive combining which can suppress jamming automatically.
5. Less fade margin requirements due to more effective multipath combining.

5.4.2 Diversity Combining

During multipath conditions several rays will be received by each of the diversity antenna ports. The best diversity design is such that deep fades cannot occur simultaneously on all diversity ports. On most frequency and space diversity systems, arbitrarily deep fades are possible even after diversity combining. We analyze in this section an angle diversity combining system based on the following question:

- What propagation condition yields the weakest signal at the output of an optimum diversity combiner, and how weak is the worst signal condition compared to an optimum single ray situation?

Clearly, with only a single antenna port (no diversity) an infinitely deep fade is possible. This is also true for some multiple diversity systems, although the deep fades may only occur with a negligible probability. However, for the purposes of this discussion, we will be looking for 100% availability. To limit the scope of this preliminary analysis only a subclass of propagation conditions are considered.

- Two constant gradient layers, -40 N-units/km in the lower layer, -300 N-units/km in the upper layer.
- Fixed terminal locations with 100 km distance.
- Ray amplitudes calculated from geometrical optics, but with phases assumed unknown.
- Narrow bandwidth.

These conditions are typical and will suffice to illustrate the basic diversity features.

5.4.3 Frequency Diversity Considerations

The use of frequency diversity is undesirable due to spectrum allocation problems. At wide frequency separations the diversities are independent and there is therefore no limit to fade depth possible even with optimum combining. At close frequency separations, the diversities will fade together. This diversity technique therefore does not satisfy the 100% availability condition set out above and will not be considered further.

5.4.4 Space Diversity Considerations

The usual space diversity techniques work well because they rely on the angle-of-arrival of the rays which we have seen is the best way to discriminate the arriving rays. It will be useful to briefly discuss the key operation. Figure 5-16 shows two antennas and two rays arriving at angles θ_1 and θ_2 . We make the simplifying assumption that the angles are the same at both antennas, something which is only true when the spacing is small. However, it is adequate to illustrate the key point. The relative phase shift of ray no. n at antenna no. 2 is

$$k L \sin \theta_n, \quad n = 1, 2 \quad .$$

where L is the antenna separation and $k = 2\pi/\lambda$. When there is a deep fade at antenna 1 (the rays are 180° out of phase) then the rays at antenna 2 have the relative phase shift

$$kL(\sin \theta_1 - \sin \theta_2) \quad .$$

If this is a multiple of 2π a deep fade will exist at antenna 2 as well. To avoid this, L must be smaller than

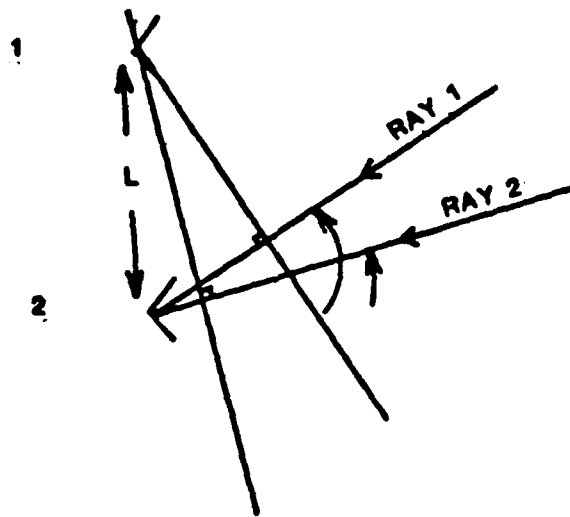


Figure 5-16 Geometry for Dual Space Diversity with Two Rays

$$L < \frac{c}{f \Delta\theta} = \frac{\lambda}{\Delta\theta}$$

where $\Delta\theta$ is the maximum angle variation.

At 8GHz and with $\Delta\theta=2^\circ$ this yields $L < 1m$. Since LOS antenna spacings are typically much larger than this, it appears that complete fades can occur at both antennas simultaneously. The most effective way of achieving the closer spacing required is to use angle diversity instead of space diversity.

5.4.5 A Baseline Angle Diversity Multipath Protection System

Figure 5-17 shows an angle diversity system with a dual horn feed on a paraboloid antenna. The system must be capable of both vertical and horizontal polarization. The upper and lower beams are combined so that the sum beam is twice as broad in elevation as each of the individual beams. While this means a 3dB loss in antenna gain it guarantees that the signal will be transmitted through the main beam even under extreme propagation conditions. The reference to the adaptive combiner may be decision directed, transmitted at a low duty cycle, or incoherent power maximization. The latter approach only applies to narrow-band links.

In order to analyze this system consider a 100 km link such as the one leading to the multipath diagrams in Figure 5-7 and use an optimum combiner with worst case ray phases as described in Appendix B. We assume the ideal antenna patterns

Transmitter

$$g_T(\theta) = \frac{\sin\left(\frac{\pi A}{2\lambda} \theta\right)}{\frac{\pi A}{2\lambda} \theta}$$

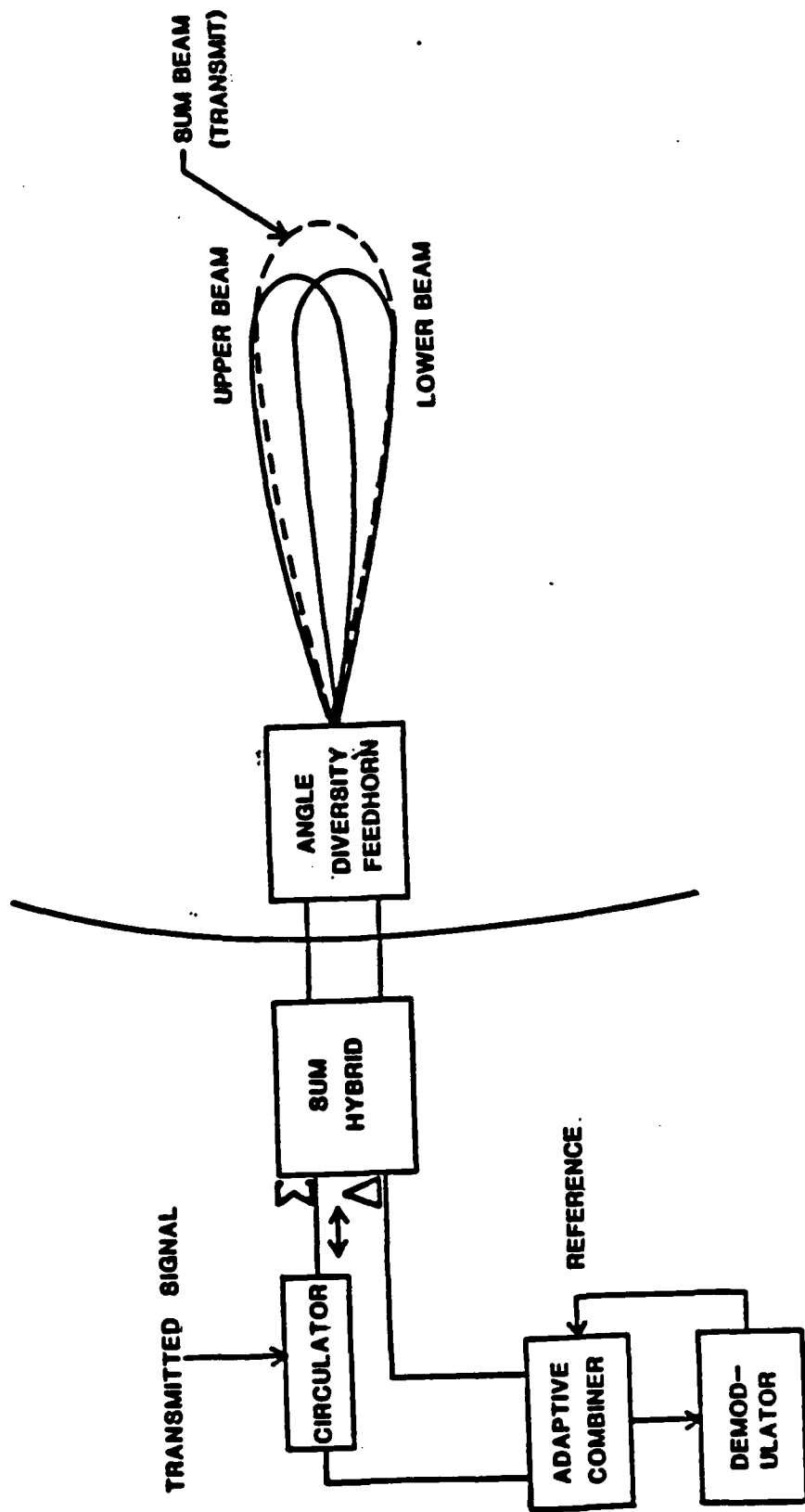


Figure 5-17 Angle Diversity System Configuration

Upper Receiving Beam

$$g_{Ru}(\theta) = \frac{\sin\left[\frac{\pi A}{\lambda}\left(\theta - \frac{\lambda}{2A}\right)\right]}{\frac{\pi A}{\lambda}\left(\theta - \frac{\lambda}{2A}\right)}$$

Lower Receiving Beam

$$g_{Rl}(\theta) = \frac{\sin\left[\frac{\pi A}{\lambda}\left(\theta + \frac{\lambda}{2A}\right)\right]}{\frac{\pi A}{\lambda}\left(\theta + \frac{\lambda}{2A}\right)}$$

Note that $g_T(\theta)$ is twice as broad as $g_{Ru}(\theta)$ and $g_{Rl}(\theta)$. The antenna boresight is aimed horizontally; no attempt is made to optimize the pointing angles of either transmit or receive antenna.

In the following calculations, the frequency is assumed to be 11 GHz. For each height of the ducting layer the angles-of-arrival and ray amplitude are calculated by ray tracing. The optimum diversity combiner and worst case ray phase length is then calculated as outlined in Appendix B. The results are shown in Figures 5-18 and 5-19. Figure 5-18 shows the effective path antenna gain as a function of layer height. The path antenna gain includes nominal antenna gains at both ends and worst case fade at the output of the adaptive combiner. The performance improves with increasing antenna size up to about 2m due to the improved antenna gains. For the 4m antenna, a 12 dB fade occurs near one of the caustics. In this case, some of the rays are in the sidelobes. Note that the signal at the combiner output, does not fade much even with the worst phases associated with each ray. For smaller antennas, deeper fades are possible due to the lower angular resolution. Figure 5-19 shows the fade

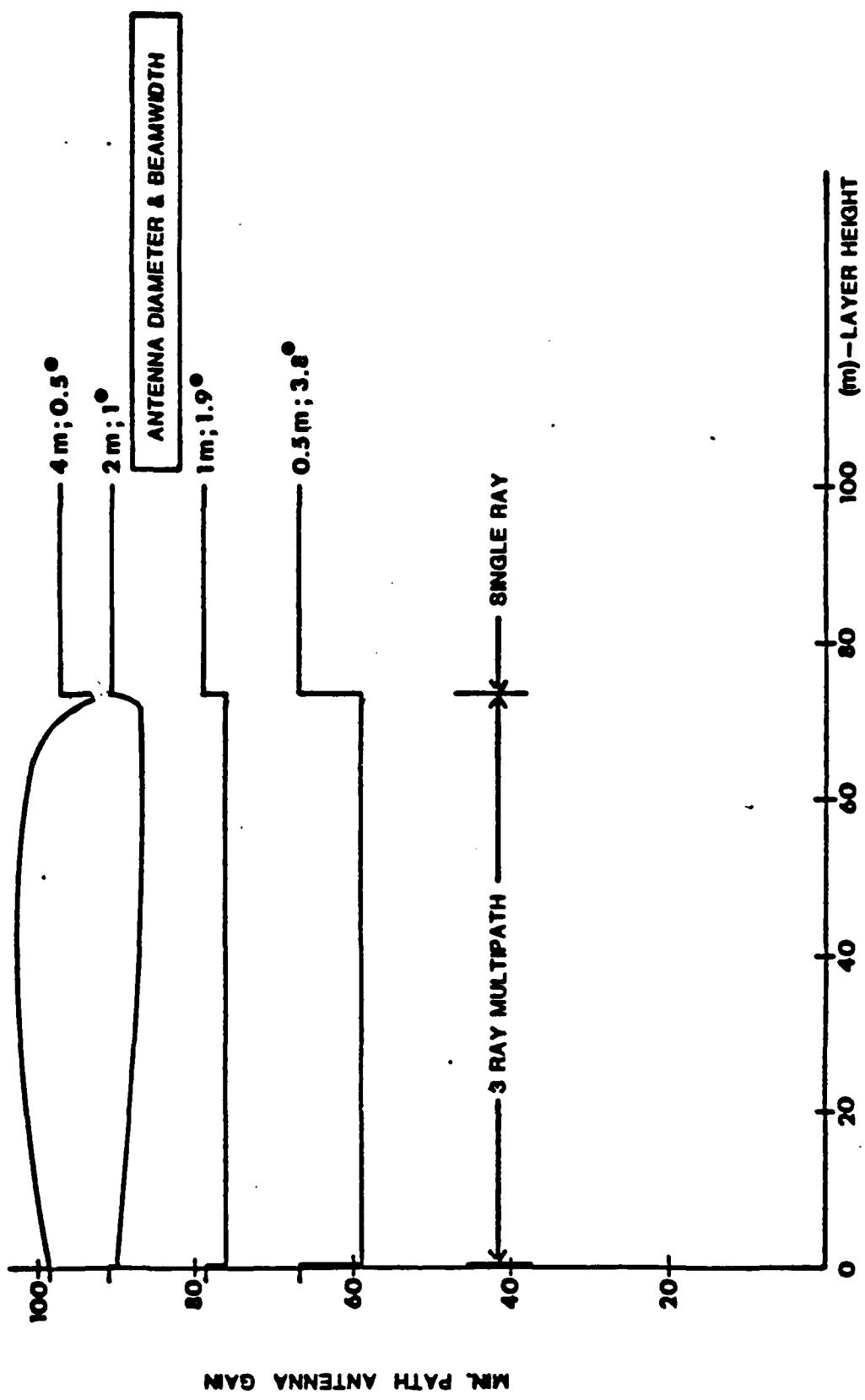


Figure 5-18 Performance as a Function of Height of Duct

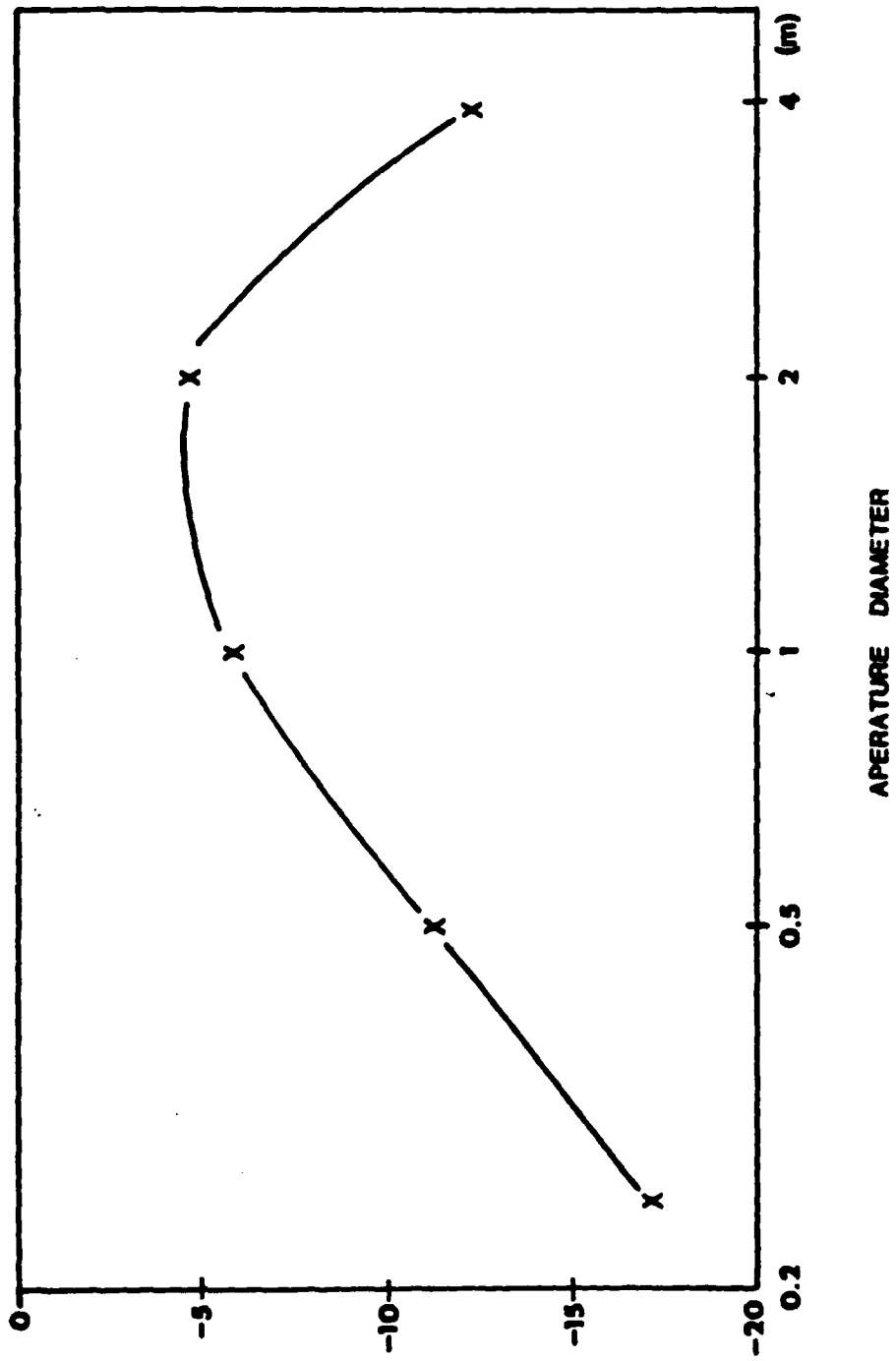


Figure 5-19 Worst Fade Depth with Optimum Combiner

depth as a function of antenna diameter. There is a relatively broad maximum near 1-2 meters where at most a 5dB degradation is possible.

The 2-meter antenna clearly gives the best results. The receive beamwidth is 1° while the transmit beamwidth is 2° . According to the calculations in this section this is adequate to cover even the most extreme ray angles.

Due to the angle variations possible, the best antenna size is independent of link distance.

In broadband systems, intersymbol interference is automatically eliminated. By synchronizing the local reference with one of the rays the other rays will be suppressed. This also improves combining by automatically using the delay information available to discriminate between the rays. Therefore only a single tap is required in the combiner (i.e., no equalization), but a delay-locked loop should be used to synchronize the reference. This may mean time-sharing the adaptation between two or three different delays and using the best for forming the combiner output. Care must be taken to avoid sudden loss of sync when the ray that is synchronized disappears. This can be achieved by using a long time constant in the delay tracking loop with only a small performance degradation when rays disappear near a caustic.

5.4.6 Conclusions

Angle diversity can eliminate fading almost completely. For space diversity to work best the antennas should be separated sufficiently to minimize the chance of multipath fading at both antennas simultaneously. Table 5-2 shows the probability that both antennas have multipath. A key advantage of angle diversity is therefore that a compact antenna configuration can be used (smaller towers). Another advantage is that deep fades often are

TABLE 5-2
 Probability that Both Receivers see Multipath
 Given that One Does

UPPER LAYER REFRACTIVITY GRADIENT (Nu/km)	5m Separation			10 m Separation		
	LINK DISTANCE (km)			LINK DISTANCE (km)		
	30	50	80	30	50	80
-200	.04	.45	.86	0	.17	.72
-400	.34	.82	.95	.07	.64	.89
-600	.60	.91	.97	.33	.82	.94

not possible on angle diversity system while they can occur on space diversity systems where the spacing is not large enough. Figure 5-20 shows the effect - space diversity has a smaller probability of fades in the range of 0-18 dB than does angle diversity. However, for fades greater than 18 dB angle diversity is vastly superior - they simply do not occur.

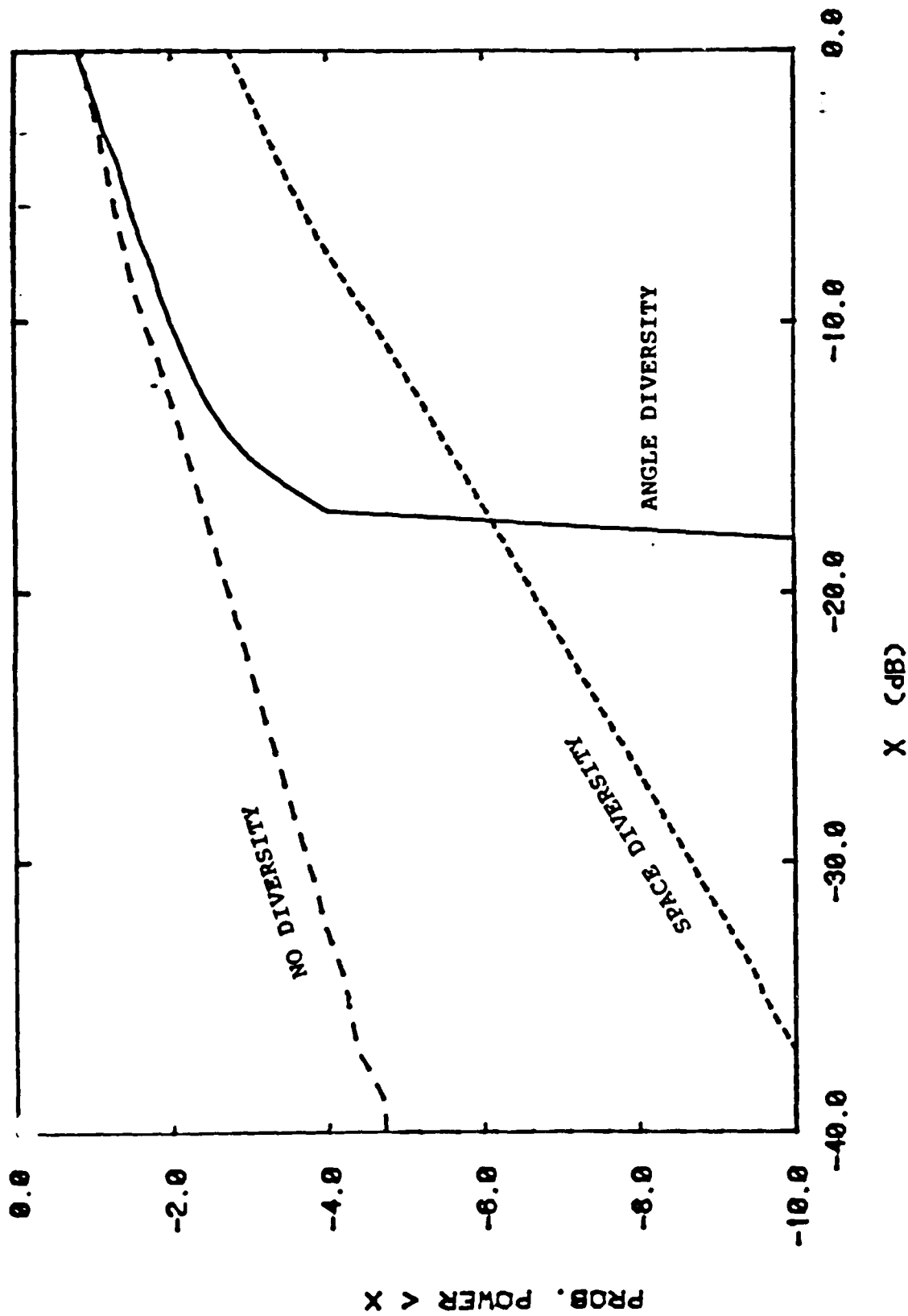


Figure 5-20 Typical Angle Diversity Performance; Link Distance 50 km,
Gradient -200 Nu/km in Upper Layer

SECTION 5
REFERENCES

- W.T. Barnett (1972), "Multipath propagation at 4, 6, and 11 GHz," BSTJ, Vol. 51, pp. 321-361.
- CCIR (1978), XIV'th Plenary Assembly, Kyoto 1978, Volume V: Propagation in non-ionized media. Recommendation 453, Report 563-1, pp. 69-89, Geneva.
- H.T. Dougherty and B.A.Hart (1979), "Recent progress in duct propagation predictions", IEEE Trans. Antennas Propagat., Volume AP-27, pp. 542-548.
- L.B. Felsen and T. Ishihara (1979), "Hybrid ray-model formulation of ducted propagation", J. Acoust. Soc. Amer., Vol. 65, pp. 595-607.
- D. Ludwig (1966), "Uniform asymptotic expansion at a caustic," Communications on Pure and Applied Mathematics, Vol. 19, pp. 215-250.
- L.W. Pickering and J.K. DeRosa (1979), "Refractive multipath model for microwave line-of-sight links," IEEE Trans. Commun., Vol. COM-27, pp. 1174-82.
- W.D. Rummler (1979), "A new selective fading model: application to propagation data," BSTJ, Vol. 58, pp. 1037-1071.
- J. Sandberg (1980), "Extraction of multipath parameters from swept measurements on a line-of-sight path," IEEE Trans. Antennas Propagat., Vol. AP-28, pp. 743-750.
- O. Sasaki and T. Akiyama (1979), "Multipath delay characteristics on line-of-sight microwave radio system," IEEE Trans. Commun., Vol. COM-27, pp. 1876-1886.
- Tatarskii, V.I. (1971), The effects of the turbulent atmosphere on wave propagation, US Department of Commerce, NTIS, Springfield, VA.
- A. Vigants (1975), "Space diversity engineering," BSTJ, Vol. 54, pp. 103-142.
- A. Vigants (1971), "Number and duration of fades at 6 and 4 GHz," BSTJ, Vol. 50, pp. 815-841.

SECTION 5
REFERENCES (Concluded)

- A.R. Webster (1983), "Angle-of-arrival and delay times on terrestrial line-of-sight microwave links", IEEE Trans. Antennas Propagat., Vol. AP-31, pp. 12-17.
- A.R. Webster (1982), "Angle-of-arrival considerations in microwave communications systems," IEEE Trans. Antennas Propagat., Vol. AP-30, pp. 800-802.
- A.R. Webster (1982), "Raypath parameters in tropospheric multipath propagation," IEEE Trans. Antennas Propagat., Vol. AP-30, pp. 786-800.
- A.R. Webster and I. Ueno (1980), "Tropospheric microwave propagation - an X-band diagnostic system," IEEE Trans. Antennas Propagat., Vol. AP-28, pp. 693-699.

APPENDIX A
DERIVATION OF LOS RAY PARAMETERS

In this appendix we find the equations for the rays that can exist between two LOS terminals in the presence of an elevated ducting layer. The derivation is based on the exact effective earth radius transformation developed in Section 5.3.2. A single set of equations is found to govern the propagation for all values of layer and terminal heights.

A.1 RAYS CROSSING THE BOUNDARY TWICE

The ray in Figure 5-6 may consist of several periods i.e., it may enter and leave the ducting layer more than once. Each time the boundary is crossed, the same angle, θ_B , is found between the ray and the boundary. Let us first consider the properties of the ray in the lower medium. This is shown in Figure A-1. X_ℓ is the length of the ray below the boundary, while S_ℓ is the distance along the boundary. From the effective center of the earth the angular distance is

$$\phi_e = S_\ell / R_{e1} .$$

Elementary geometric considerations show that

$$\theta_B = \phi_e / 2$$

so that

$$S_\ell = 2R_{e1} \theta_B , \quad (A.1)$$

where θ_B , as defined in Figure 5-6, is always positive, as is R_{e1} , so the distance S_ℓ is guaranteed to be positive. We also have the ray length

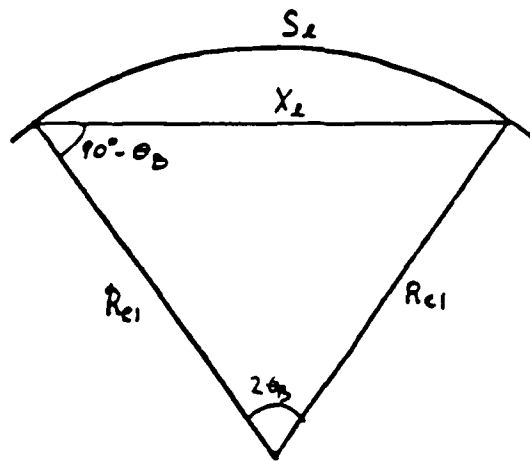


Figure A-1 Ray Crossing Lower Medium

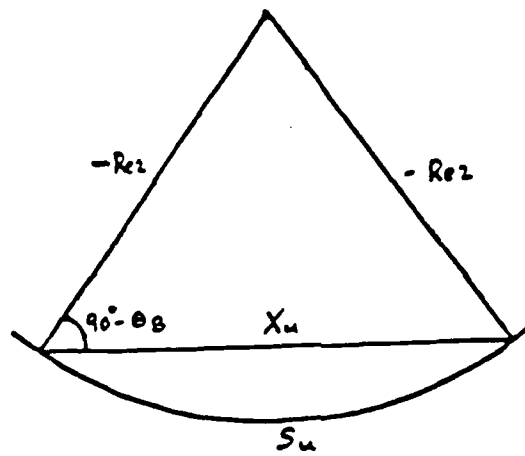


Figure A-2 Ray Crossing Upper Medium

$$X_l = 2R_{e1} \sin \theta_B . \quad (A.2)$$

Hence the delay along this segment of the ray is

$$\tau_l = X_l/c = 2 \frac{R_{e1}}{c} \sin \theta_B \quad (A.3)$$

where c is the velocity of light at the interface.

Consider next the segment above the layer interface. Figure A-2 shows the geometry after the effective earth radius transformation. Since ducting is assumed the radius involved is $-R_{e2}$. As above, we find

$$S_u = -2 R_{e2} \theta_B \quad (A.4)$$

and

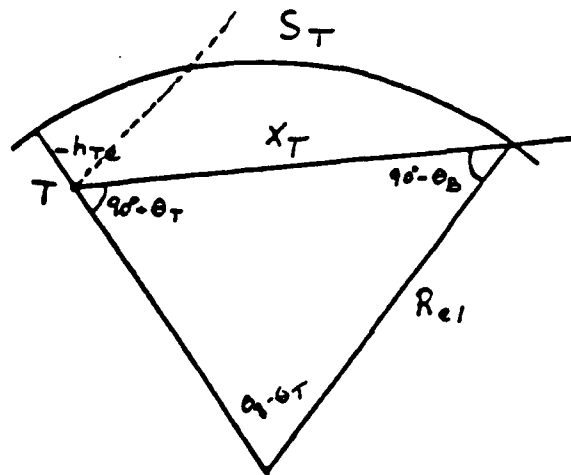
$$X_u = -2 R_{e2} \sin \theta_B, \quad (A.5)$$

$$\tau_u = X_u/c. \quad (A.6)$$

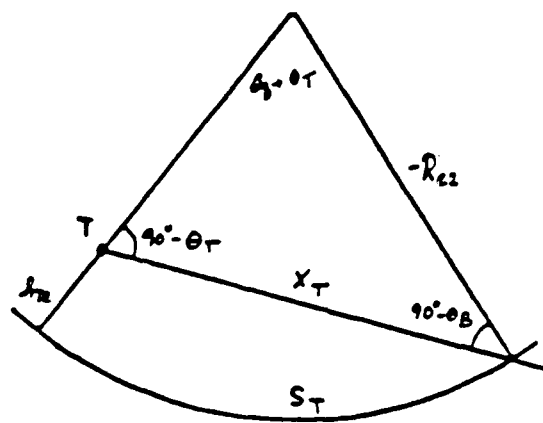
A.2 RAYS FROM THE TRANSMITTER

Equations (A.1)-(A.6) describe the complete arcs of the ray above and below the layer boundary in Figure 5-6. We now derive the equations describing the ray between the transmitter and the layer boundary. Figure A-3(a) shows the geometry when the transmitter is below the boundary. The height, h_{Te} , is measured positive above the boundary, and hence is negative in this case. Figure A-3(a) shows that

$$\cos \theta_B = \cos(\theta_T) \frac{R_{e1} + h_{Te}}{R_{e1}} = \rho_T \cos \theta_T \quad (A.7a)$$



(a) Transmitter Below Boundary



(b) Transmitter Above Boundary

Figure A-3 Ray Geometry Near the Transmitter

where we define

$$\rho_T = \frac{\Delta}{R_{e1} + h_{Te}} / R_{e1} \quad (\text{A.8a})$$

Given θ_B the magnitude of the elevation angle θ_T at the transmitter can be found. The distance to the boundary is then

$$X_T = R_{e1} \frac{\sin(\theta_B - \theta_T)}{\cos \theta_T} \quad (\text{A.9a})$$

$$= (R_{e1} + h_{Te}) \frac{\sin(\theta_B - \theta_T)}{\cos \theta_B} \quad (\text{A.10a})$$

When the transmitter is above the boundary we use Figure A-3(b) to calculate the distances and angles involved. We get

$$X_T = \sin(\theta_T + \theta_B) \frac{-R_{e2} - h_{Te}}{\cos \theta_B} \quad (\text{A.10b})$$

$$= \sin(\theta_T + \theta_B) \frac{-R_{e2}}{\cos \theta_T} \quad (\text{A.9b})$$

and hence

$$\cos \theta_B = \rho_T \cos \theta_T \quad (\text{A.7b})$$

where

$$\rho_T = \frac{R_{e2} + h_{Te}}{R_{e2}} \quad . \quad (A.8b)$$

Note that the only formal difference between case (a) and (b) is the sign of θ_B .

We can combine the two results by defining

$$R_{eT} = \begin{cases} R_{e1} & \text{for transmitter in layer 1} \\ R_{e2} & \text{for transmitter in layer 2} \end{cases}$$

so that

$$\rho_T = (R_{eT} + h_{Te})/R_{eT} \quad . \quad (A.8c)$$

Also define

$$\theta_{BT} = \begin{cases} \theta_B (>0) & \text{for transmitter in layer 1} \\ -\theta_B (<0) & \text{for transmitter in layer 2} \end{cases}$$

so we get

$$\cos \theta_B = \cos \theta_{BT} = \rho_T \cos \theta_T \quad (\text{A.7c})$$

$$X_T = R_{eT} \sin(\theta_{BT} - \theta_T) / \cos \theta_T \quad (\text{A.9c})$$

$$= (R_{eT} + h_{Te}) \sin(\theta_{BT} - \theta_T) / \cos \theta_B \quad (\text{A.10c})$$

and, for the projected distance along the boundary,

$$S_T = R_{eT}(\theta_{BT} - \theta_T) = \left| R_{eT} \theta_B \right| - R_{eT} \theta_T \quad (\text{A.11})$$

A.3 RAYS AT THE RECEIVER

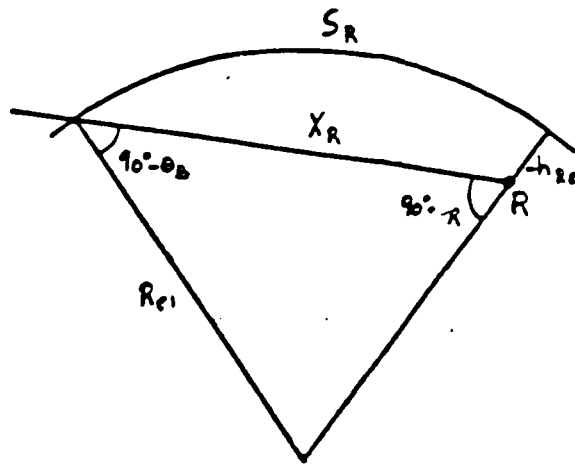
At the receiver, we clearly will get analogous equations. The results derived from Figure A-4 are

$$\cos \theta_B = \rho_R \cos \theta_R \quad (\text{A.12})$$

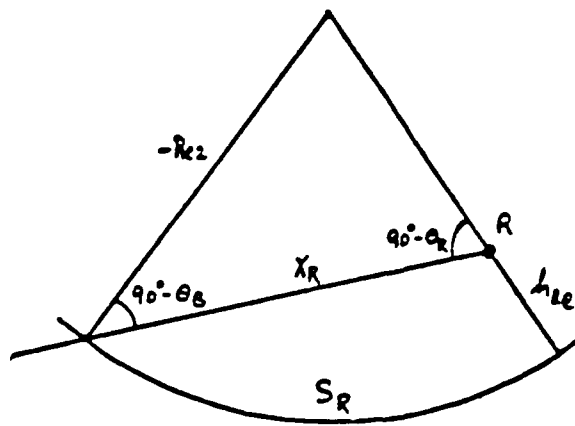
where

$$\rho_R = \frac{R_{eR} + h_{Re}}{R_e} \quad (\text{A.13})$$

is evaluated in the medium where the receiver is located.



(a) Receiver Below Boundary



(b) Receiver Above Boundary

Figure A-4 Ray Geometry Near the Receiver

Also,

$$X_R = (R_{eR} + h_{Re}) \frac{\sin(\theta_{BR} - \theta_R)}{\cos \theta_B} \quad (\text{A.14})$$

$$= R_{eR} \frac{\sin(\theta_{BR} - \theta_R)}{\cos \theta_R} . \quad (\text{A.15})$$

We also have

$$S_R = R_{eR}(\theta_{BR} - \theta_R) . \quad (\text{A.16})$$

θ_{BR} is defined as

$$\theta_{BR} = \theta_B \text{ sign}(R_{eR}) .$$

A.4 COMBINING THE RESULTS TO YIELD THE GENERAL EQUATIONS

For the overall link the distance must be the sum of the distances found in (A.1), (A.4), (A.11), and (A.16). Let us consider each of the four cases separately, and let k denote the number of complete periods between the first and the last boundary crossings.

A. Both terminals in lower layer

$$\begin{aligned} D &= S_T + S_u + k(S_l + S_u) + S_R \\ &= R_{e1}(\theta_B - \theta_T) - 2R_{e2}\theta_B + 2k(R_{e1} - R_{e2})\theta_B + R_{e1}(\theta_B - \theta_R) \\ &= (2k+2)(R_{e1} - R_{e2})\theta_B - R_{e1}\theta_T - R_{e1}\theta_R \end{aligned}$$

$k > 0$.

B. Transmitter in upper layer, receiver in lower layer

$$\begin{aligned} D &= -R_{e2}(\theta_B + \theta_T) + 2k(R_{e1} - R_{e2})\theta_B + R_{e1}(\theta_B - \theta_R) \\ &= (2k+1)(R_{e1} - R_{e2})\theta_B - R_{e2}\theta_T - R_{e1}\theta_R \end{aligned}$$

$k > 0$.

C. Transmitter in lower layer, receiver in upper layer

$$\begin{aligned} D &= R_{e1}(\theta_B - \theta_T) + 2k(R_{e1} - R_{e2})\theta_B - R_{e2}(\theta_B + \theta_R) \\ &= (2k+1)(R_{e1} - R_{e2})\theta_B - R_{e1}\theta_T - R_{e2}\theta_R \end{aligned}$$

$k > 0$.

D. Both terminals in upper layer

$$\begin{aligned} D &= -R_{e2}(\theta_B + \theta_T) + 2R_{e1}\theta_B + 2k(R_{e1} - R_{e2})\theta_B - R_{e2}(\theta_B + \theta_B) \\ &= (2k+2)(R_{e1} - R_{e2})\theta_B - R_{e2}\theta_T - R_{e2}\theta_R \end{aligned}$$

$$k > 0 .$$

Inspection of these four cases shows that the equation can be written compactly as

$$D = m\theta_B(R_{e1} - R_{e2}) - R_{eT}\theta_T - R_{eR}\theta_R \quad (\text{A.17})$$

where, again, R_{eT} is the effective earth radius in the layer of the transmitter and R_{eR} is the effective earth radius in the layer of the receiver. m is a positive integer which can be interpreted as the number of times the ray crosses the boundary between the two layers. We will show later that this interpretation extends to include the line-of-sight ray by allowing $m=0$ when the terminals are located in the same layer.

In addition to (A.17) we have, from (A.7) and (A.12)

$$\cos \theta_B = \rho_T \cos \theta_T \quad (\text{A.18})$$

$$= \rho_R \cos \theta_R \quad (\text{A.19})$$

where

$$\rho_T = (R_{eT} + h_{Te})/R_{eT} \quad (\text{A.20})$$

and

$$\rho_R = (R_{eR} + h_{Re})/R_{eR} \quad . \quad (A.21)$$

The expressions in (A.17)-(A.21) are the general equations to be solved in order to find the rays connecting the two terminals.

A.5 THE EXPRESSION FOR DELAY

Consider again each of the four cases separately (c denotes the propagation velocity at the boundary):

A. Both terminals in lower layer

$$\begin{aligned} \tau c &= X_T + X_U + 2k(X_L + X_U) + X_R \\ &= R_{e1} \frac{\sin(\theta_B - \theta_T)}{\cos \theta_T} - 2 R_{e2} \sin \theta_B + 2k(R_{e1} - R_{e2}) \sin \theta_B \\ &\quad + R_{e1} \frac{\sin(\theta_B - \theta_R)}{\cos \theta_R} \\ &= (2k+2) \sin \theta_B - R_{e1} \cos \theta_B \tan \theta_T \\ &\quad - R_{e1} \cos \theta_T \tan \theta_R . \end{aligned}$$

B. Transmitter in upper layer, receiver in lower layer

$$\begin{aligned} \tau_c &= -R_{e2} \frac{\sin(\theta_B + \theta_T)}{\cos \theta_T} + 2k(R_{e1} - R_{e2}) \sin \theta_B \\ &\quad + R_{e1} \frac{\sin(\theta_B - \theta_R)}{\cos \theta_R} \\ &= (2k+1)(R_{e1} - R_{e2}) \sin \theta_B - R_{e2} \cos \theta_B \tan \theta_T \\ &\quad - R_{e1} \cos \theta_B \tan \theta_R . \end{aligned}$$

C. Transmitter in lower layer, receiver in upper layer

$$\begin{aligned} \tau_c &= R_{e1} \frac{\sin(\theta_B - \theta_T)}{\cos \theta_T} + 2k(R_{e1} - R_{e2}) \sin \theta_B \\ &\quad - R_{e2} \frac{\sin(\theta_B + \theta_R)}{\cos \theta_R} \\ &= (2k+1)(R_{e1} - R_{e2}) \sin \theta_B - R_{e1} \cos \theta_B \tan \theta_T \\ &\quad - R_{e2} \cos \theta_B \tan \theta_R . \end{aligned}$$

D. Both terminals in upper layer

$$\begin{aligned}
 \tau_c &= -R_{e2} \frac{\sin(\theta_B + \theta_T)}{\cos \theta_T} + 2k(R_{e1} - R_{e2}) \sin \theta_B \\
 &\quad - R_{e2} \frac{\sin(\theta_B + \theta_R)}{\cos \theta_R} \\
 &= (2k+2)(R_{e1} - R_{e2}) \sin \theta_B - R_{e2} \cos \theta_B \tan \theta_T \\
 &\quad - R_{e2} \cos \theta_B \tan \theta_R .
 \end{aligned}$$

Combining these four separate cases yields the following expression for delay valid in all regions

$$\tau_c = m(R_{e1} - R_{e2}) \sin \theta_B - R_{eT} \cos \theta_B \tan \theta_T - R_{eR} \cos \theta_B \tan \theta_R \tag{A.22}$$

For small angles a Taylor series expansion yields the delay relative to the path along the boundary,

$$\begin{aligned}
\tau_{C-D} &= -m(R_{e1} - R_{e2}) \theta_B^3/6 \\
&\quad - R_{eT} \theta_T (\theta_T^2/3 - \theta_B^2/2) \\
&\quad - R_{eR} \theta_R (\theta_R^2/3 - \theta_B^2/2) \\
&= -(D\theta_B^2 + 4\theta_T h_{Te} + 4\theta_R h_{Re})/6 .
\end{aligned} \tag{A.23}$$

The relative delay is seen to be proportional to the third power of distance if the terminal height difference is assumed proportional to distance.

A.6 THE RECEIVED POWER

Let us now consider the evaluation of the intensity at the receiver due to a particular ray where take-off angle θ_{Te} is obtained by solving (A.17)-(A.21). Consider a pencil beam at the transmitter with azimuth beamwidth $\delta\phi$ and elevation beamwidth $\delta\theta_{T0}$. We wish to calculate the area intersected in a vertical plane at the receiver. The azimuth width of that area will be $D\delta\phi$. Consider a range of elevation angles at the transmitter,

$$\theta_{T1} = \theta_T + \delta\theta_T, \quad |\delta\theta_T| < \frac{1}{2} \delta\theta_{T0} . \tag{A.24}$$

From (A.18) we get the range of angles at the boundary,

$$\theta_{B1} = \theta_B + \rho_T \frac{\sin \theta_T}{\sin \theta_B} \delta\theta_T$$

or a beamwidth of

$$\delta\theta_{B0} = \rho_T \frac{\sin \theta_T}{\sin \theta_B} \delta\theta_{T0} . \quad (\text{A.25})$$

From (A.17) we get the beamwidth at the receiver,

$$\delta\theta_{R0} = \left[m(R_{e1} - R_{e2}) \delta\theta_{B0} - R_{eT} \delta\theta_{T0} \right] / R_{eR} \quad (\text{A.26})$$

$$\delta\theta_{R0} = \left[m\rho_T \frac{R_{e1} - R_{e2}}{R_{eR}} \frac{\sin \theta_T}{\sin \theta_B} - \frac{R_{eT}}{R_{eR}} \right] \delta\theta_{T0} .$$

From (A.19) and (A.21) we then find the change in height at the receiver,

$$\cos \theta_R \delta h_{Re} = (R_{eR} + h_{Re}) \sin \theta_R \delta\theta_{R0} - R_{eR} \sin \theta_B \delta\theta_{B0} .$$

This yields

$$\begin{aligned} \frac{\cos \theta_R \delta h_{Re}}{\delta \theta_{T0}} &= m \rho_T \frac{(R_{e1} - R_{e2})(R_{eR} + h_{Re})}{R_{eR}} \frac{\sin \theta_T \sin \theta_R}{\sin \theta_B} \\ &\quad - \frac{R_{eT}(R_{eR} + h_{Re})}{R_{eR}} \sin \theta_R \\ &\quad - \rho_T R_{eR} \sin \theta_T \end{aligned}$$

or,

$$\begin{aligned} \cos \theta_R \frac{\delta h_{Re}}{\delta \theta_{T0}} &= m \rho_T \rho_R (R_{e1} - R_{e2}) \frac{\sin \theta_T \sin \theta_R}{\sin \theta_B} \\ &\quad - R_{eT} \rho_R \sin \theta_R - R_{eR} \rho_T \sin \theta_T . \quad (A.27) \end{aligned}$$

The total area intersected by the pencil beam, a plane normal to the beam, is

$$A = \left| D \delta \phi \delta h_{Re} \cos \theta_R \right| .$$

For a line-of-sight ray in a homogeneous medium, we would have

$$A_{LOS} = \left| (D \cos \theta_T \delta \phi)(D \delta \theta_{T0}) \right| .$$

Hence, the intensity received relative to an LOS ray is, from (A.27)

$$\begin{aligned}
 P &= \frac{A_{\text{LOS}}}{A} = \left| \frac{\cos \theta_T}{D \cos \theta_R} \frac{\delta \theta_{T0}}{\delta h_{Re}} \right| \\
 &= \cos \theta_T \left[\frac{m \rho_T \rho_R (R_{e1} - R_{e2})}{D} \frac{\sin \theta_T \sin \theta_R}{\sin \theta_B} - \frac{\rho_T R_{eR}}{D} \sin \theta_T \right. \\
 &\quad \left. - \frac{\rho_R R_{eT}}{D} \sin \theta_R \right]^{-1} \quad (\text{A.28})
 \end{aligned}$$

A.7 THE LOS RAY

So far, we have only considered the rays crossing the layer boundary. When the two terminals are on the same side there is also a direct line-of-sight ray. We consider these two cases separately.

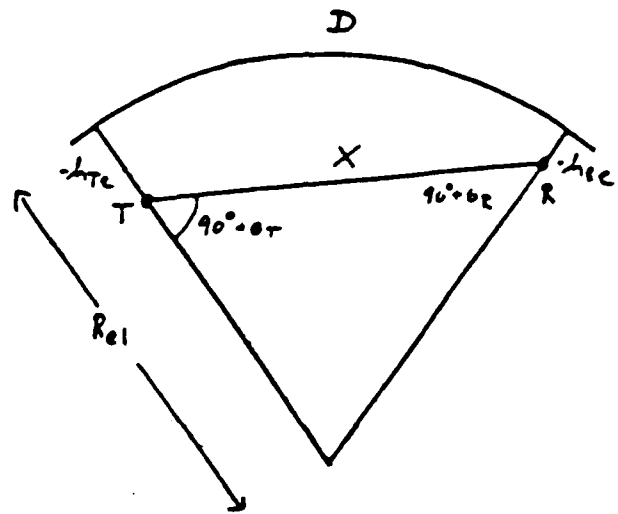
Both terminals in lower layer

We have from the geometry (Fig. A-5(a))

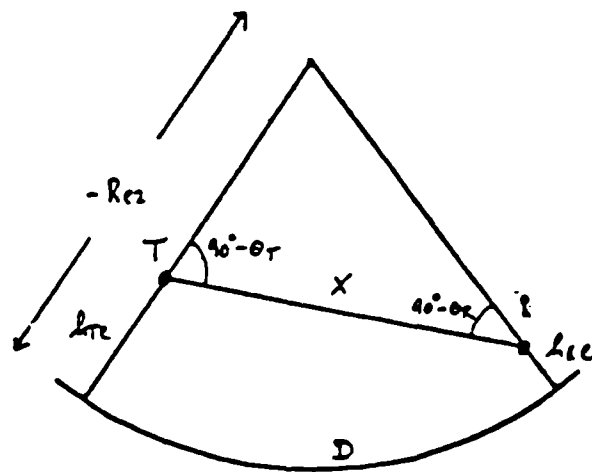
$$D = R_{e1} (-\theta_T - \theta_R) .$$

This is simply equation (A.17) with $m=0$. We also have

$$\rho_T \cos \theta_T = \rho_R \cos \theta_R (= \cos \theta_B) .$$



(a) Terminal Below Boundary



(b) Terminal Above Boundary

Figure A-5 LOS Ray Geometry

This is the same as equations (A.18) and (A.19), except that the angle θ_B is not needed. However, it is useful to include it in the equations since it allows us to get a set of equations describing all rays independent of where the terminals are located.

The delay is

$$\begin{aligned}
 c\tau &= X = \frac{-\sin(\theta_T + \theta_R)}{\cos \theta_T} (R_{e1} + h_{eR}) \\
 &= -R_{e1} \rho_R (\tan \theta_T \cos \theta_R + \sin \theta_R) \\
 &= -R_{e1} \tan \theta_T \cos \theta_B - R_{e1} \tan \theta_R \cos \theta_B
 \end{aligned}$$

which is simply (A.22) with $m=0$.

Both terminals above boundary

From Figure A-5(b) we get

$$D = (-R_{e2})(\theta_T + \theta_R),$$

which again is equivalent to (A.17) with $m=0$. We still have

$$\rho_T \cos \theta_T = \rho_R \cos \theta_R (= \cos \theta_B)$$

so (A.17)-(A.21) are valid in general for $m > 0$. The equation for the delay is

$$\begin{aligned}
 c\tau &= X = \frac{\sin(\theta_T + \theta_R)}{\cos \theta_T} (-R_{e2} - h_{eR}) \\
 &= -R_{e2} \rho_R (\tan \theta_T \cos \theta_R + \sin \theta_R) \\
 &= -R_{e2} \tan \theta_T \cos \theta_B - R_{e2} \tan \theta_R \cos \theta_B,
 \end{aligned}$$

which also reduces to (A.22) for $m=0$.

Hence, our equations are valid in general. The solutions for $m > 0$, m even for terminal in same layer, m odd for terminal in opposite layers, describe all possible rays satisfying the laws of geometrical optics.

A.8 THE EQUATION FOR θ_T FROM THE SMALL ANGLE APPROXIMATION

When the angles are small and the heights h_{Te} , h_{Re} are much smaller than the earth radius, we can derive a quartic equation for θ_T . For convenience define the small dimension-less height parameters

$$\epsilon_T = 1 - \rho_T = -h_{Te}/R_{eT} \quad (\text{A.29})$$

and

$$\epsilon_R = 1 - \rho_R = -h_{Re}/R_{eR}. \quad (\text{A.30})$$

These quantities are always positive.

Expanding (A.18) and (A.19) now results in the approximations:

$$\theta_B^2 = \theta_T^2 + 2\epsilon_T \quad (\text{A.31})$$

$$= \theta_R^2 + 2\epsilon_R. \quad (\text{A.32})$$

Define

$$k_{12} = (R_{e1} - R_{e2})/R_0$$

$$k_T = R_{eT}/R_0$$

$$k_R = R_{eR}/R_0$$

and

$$\phi = D/R_0.$$

Squaring (A.17) and using (A.32) we get also that

$$\begin{aligned} m^2 k_{12}^2 \theta_B^2 &= [D/R_0 + k_T \theta_T + k_R \theta_R]^2 \\ &= \phi^2 + k_T^2 \theta_T^2 + k_R^2 \theta_R^2 + 2k_T \phi \theta_T + 2k_R \phi \theta_R + 2k_T k_R \theta_T \theta_R \\ &= \phi^2 + k_T^2 \theta_T^2 + k_R^2 (\theta_T^2 + 2\epsilon_T - 2\epsilon_R) + 2k_T \phi \theta_T + 2k_R (\phi + k_T \theta_T) \theta_R. \end{aligned}$$

Combining with (A.31) and collecting the terms independent of θ_R at the left yields the equation:

$$a_1 \theta_T^2 + b_1 \theta_T \phi + c_1 \phi^2 = 2k_R (\phi + k_T \theta_T) \theta_R \quad (\text{A.33})$$

where

$$a_1 = m^2 k_{12}^2 - k_T^2 - k_R^2$$

$$b_1 = -2k_T$$

$$c_1 = (2m^2 k_{12}^2 \epsilon_T - 2k_R^2 (\epsilon_T - \epsilon_R)) / \phi^2 - 1 .$$

Squaring (A.33) and using (A.32) yields,

$$\begin{aligned} a_1^2 \theta_T^4 + 2a_1 b_1 \phi \theta_T^3 + (b_1^2 + 2a_1 c_1) \phi^2 \theta_T^2 + 2b_1 c_1 \phi^3 \theta_T + c_1^2 \phi^4 \\ = 4k_R^2 (\phi^2 + k_T^2 \theta_T^2 + 2k_T \phi \theta_T) (\theta_T^2 + 2\epsilon_T - 2\epsilon_R) \\ = a_2 \theta_T^4 + b_2 \phi \theta_T^3 + c_2 \phi^2 \theta_T^2 + d_2 \phi^3 \theta_T + e_2 \end{aligned} \quad (\text{A.34})$$

where

$$\begin{aligned}a_2 &= 4k_R^2 k_T^2 \\b_2 &= 8k_T k_R^2 \\c_2 &= 4k_R^2 + 8k_T^2 k_R^2 (\epsilon_T - \epsilon_R) / \phi^2 \\d_2 &= 16k_T k_R^2 (\epsilon_T - \epsilon_R) / \phi^2 \\e_2 &= 8k_R^2 (\epsilon_T - \epsilon_R) / \phi^2 .\end{aligned}$$

Combining (A.33) and (A.34) we get the quartic equation in $x = \theta_T / \phi$,

(A.35)

$$\begin{aligned}(a_1^2 - a_2)x^4 + (2a_1 b_1 - b_2)x^3 + (b_1^2 + 2a_1 c_1 - c_2)x^2 + (2b_1 c_1 - d_2)x \\+ c_1^2 - e_2 = 0\end{aligned}$$

For small angles specific cases of this equation can be identified with that of Pickering and DeRosa [1979]. Their equation is in terms of $\sin\theta$ rather than θ , and does not include all terminal locations.

APPENDIX B
DIVERSITY COMBINER PERFORMANCE

The multipath rays in an LOS link can be calculated from geometrical optics. Near caustics, the amplitude of the individual rays is inaccurate, but it turns out that if the rays are combined with a proper phase then the total field is finite and an approximation to the total field found from a more exact analysis. The following approach can then be used to evaluate the worst case performance:

1. Find all eigenrays and evaluate their amplitudes and delays using geometrical optics. Assume the phases are unknown.
2. Find the optimum diversity combining of all antenna ports coupled to the electromagnetic field. This will depend on the phase of the incoming rays.
3. Select the phases of all the rays to yield the deepest fade at the output of the combiner. Strong rays will tend to cancel thus avoiding problems with infinite fields near caustics.

Let N_R be the number of rays. The amplitude of the n 'th ray is A_n , and is calculated using geometrical optics. Let ϕ_n be the unknown phase of the n 'th ray, and let θ_{Tn} and θ_{Rn} be the calculated takeoff and arrival angles of the n 'th ray. Let N_A be the number of apertures at the receiving site, and assume that each ray has the same amplitude, angle-of-arrival and phase at each aperture. This is exact for angle diversity applications and reasonably accurate for space diversity applications if equivalent beam patterns are defined. Let $g_m(\theta)$ be the amplitude gain pattern of the m 'th receiving antenna port and let $g_0(\theta)$ be the transmitter antenna pattern. The signal received at the m 'th antenna port is then

$$\sum_{n=1}^{N_R} A_n g_0(\theta_{Tn}) g_m(\theta_{Rn}) e^{j\phi_n} .$$

The amplitudes A_n are real, but can be negative for some rays. The SNR at the output of an optimum diversity combiner is proportional to

$$\rho = \sum_{m=1}^{N_A} \left| \sum_{n=1}^{N_R} A_n g_0(\theta_{Tn}) g_m(\theta_{Rn}) e^{j\phi_n} \right|^2 .$$

The deepest fade (worst case) is achieved for the ray phases which minimize ρ ,

$$\rho_0 = \min_{\{\phi_n\}_{n=1}^{N_R}} \rho .$$

ρ can be written in the form

$$\rho = \sum_{n_1=1}^{N_R} \sum_{n_2=1}^{N_R} e^{j(\phi_{n_1} - \phi_{n_2})} B(n_1, n_2)$$

where

$$B(n_1, n_2) = \left[\sum_{m=1}^{N_A} g_m(\theta_{Rn_1}) g_m^*(\theta_{Rn_2}) \right] g_0(\theta_{Tn_1}) g_0^*(\theta_{Tn_2}) A_{n_1} A_{n_2} .$$

The average SNR, which is sometimes of interest, is

$$\rho_{AV} = \sum_{n=1}^{N_R} B(n, n) .$$

The minimization over the phases ϕ_n can be solved analytically in a few specific cases. The two cases most of interest are $N_R=1$ (no multipath) and $N_R=3$ (typical multipath condition). When $N_R=1$ ρ is independent of the phase. We now consider the case $N_R=3$ in detail.

The Worst-Case Phases for the case $N_R=3$

Assume three rays, with the phase of the first ray being zero. Then,

$$\rho = \sum_{n=1}^3 B(n, n) + 2B_{12} \cos \phi_2 + 2B_{13} \cos \phi_3 + 2B_{23} \cos(\phi_2 - \phi_3) .$$

A necessary condition for the minimum SNR is

$$\frac{\delta \rho}{\delta \phi_2} = -2B_{12} \sin \phi_2 - 2B_{23} \sin(\phi_2 - \phi_3) = 0$$

and

$$\frac{\delta \rho}{\delta \phi_3} = -2B_{13} \sin \phi_3 + 2B_{23} \sin(\phi_2 - \phi_3) = 0 .$$

We immediately see four possible solutions:

$$\begin{aligned} \phi_2 &= 0, & \phi_3 &= 0 \\ \phi_2 &= 0, & \phi_3 &= \pi \\ \phi_2 &= \pi, & \phi_3 &= 0 \\ \phi_2 &= \pi, & \phi_3 &= \pi . \end{aligned}$$

For additional solutions, we must have

$$\sin \phi_3 = \frac{B_{12}}{B_{13}} \sin \phi_2$$

and

$$\begin{aligned} \sin \phi_3 &= \frac{B_{23}}{B_{13}} (\sin \phi_2 \cos \phi_3 - \sin \phi_3 \cos \phi_2) \\ &= -\frac{B_{23}}{B_{12}} \sin \phi_3 \cos \phi_3 - \frac{B_{23}}{B_{13}} \sin \phi_2 \cos \phi_2 \end{aligned}$$

or

$$-1 = \frac{B_{23}}{B_{12}} \cos \phi_3 + \frac{B_{23}}{B_{13}} \cos \phi_2 .$$

Hence,

$$\left(1 + \frac{B_{23}}{B_{12}} \cos \phi_3\right)^2 = \frac{B_{23}^2}{B_{13}^2} \left(1 - \frac{B_{13}^2}{B_{12}^2} (1 - \cos^2 \phi_3)\right)$$

which leads to

$$\cos \phi_3 = \frac{B_{12}}{2B_{23}} \left\{ \frac{B_{23}^2}{B_{13}^2} - \frac{B_{23}^2}{B_{12}^2} - 1 \right\} = \frac{1}{2} \left[\frac{B_{23}}{B_{12}} \cdot \frac{B_{12}}{B_{13}} - \frac{B_{23}}{B_{12}} - \frac{B_{12}}{B_{23}} \right]$$

similarly we get

$$\begin{aligned} \cos \phi_2 &= \frac{B_{13}}{2B_{23}} \left\{ \frac{B_{23}^2}{B_{12}^2} - \frac{B_{23}^2}{B_{13}^2} - 1 \right\} \\ &= \frac{1}{2} \left[\frac{B_{23}}{B_{12}} \cdot \frac{B_{13}}{B_{12}} - \frac{B_{23}}{B_{13}} - \frac{B_{13}}{B_{23}} \right] \end{aligned}$$

and

$$\cos(\phi_2 - \phi_3) = \frac{1}{2} \left[\frac{B_{12}B_{13}}{B_{23}^2} - \frac{B_{13}}{B_{12}} - \frac{B_{12}}{B_{13}} \right]$$

For this solution to be valid we must have the expressions for $\cos\phi_2$, $\cos\phi_3$, and $\cos(\phi_2-\phi_3)$ lie between -1 and 1. If, for instance, $|B_{23}|$ is smaller than $|B_{12}|$ and $|B_{13}|$ this leads to the condition

$$\left| \frac{B_{23}}{B_{12}} \right| + \left| \frac{B_{23}}{B_{13}} \right| > 1 .$$

This condition is called the triangle condition. For the case of a single antenna, it is the condition on the amplitudes of the three rays that can form the three sides of a triangle resulting in an infinitely deep null. By substituting the above results into the expression of ρ we find

1) Triangle Condition:

$$\frac{1}{|B_{12}|} + \frac{1}{|B_{13}|} + \frac{1}{|B_{23}|} > 2 \max\left(\frac{1}{|B_{12}|}, \frac{1}{|B_{13}|}, \frac{1}{|B_{23}|}\right)$$

yields the potential minimum

$$\rho = B_{11} + B_{22} + B_{33} - \frac{B_{13}B_{23}}{B_{12}} - \frac{B_{12}B_{13}}{B_{23}} - \frac{B_{12}B_{23}}{B_{13}}$$

Other potential minima are:

$$2) \quad \rho = B_{11} + B_{22} + B_{23} + 2(B_{12} + B_{13} + B_{23}).$$

$$3) \quad \rho = B_{11} + B_{22} + B_{33} + 2(-B_{12} + B_{13} - B_{23}).$$

$$4) \quad \rho = B_{11} + B_{22} + B_{33} + 2(B_{12} - B_{13} - B_{23}).$$

$$5) \quad \rho = B_{11} + B_{22} + B_{33} + 2(-B_{12} - B_{13} + B_{23}).$$

The smallest of the solutions, 1)-5) corresponds to the deepest fade possible with the given 3 ray amplitudes and the specified diversity configuration.

APPENDIX C
DERIVATION OF THE SCATTER EQUATION

Consider the geometry in Figure C-1. The distances to the transmitter and receiver terminals from a variable scattering point in the troposphere are R_T and R_R . The corresponding vectors are denoted \underline{R}_T and \underline{R}_R . We also will use the unit vectors defined by

$$\underline{e}_T = \underline{R}_T/R_T$$

and

$$\underline{e}_R = \underline{R}_R/R_R .$$

The total electromagnetic field at a point \underline{r} is denoted \underline{E} (or $\underline{E}(\underline{r})$) and is assumed to be composed of a direct field \underline{E}_0 and a scattered field \underline{E}_S . The field satisfies Maxwells equations:

$$\begin{aligned} \underline{\nabla} \cdot (\epsilon \underline{E}) &= 0 & ; & \quad \underline{\nabla} \cdot \underline{H} = 0 \\ \underline{\nabla} \times \underline{E} &= -j\omega\mu_0 \underline{H} & ; & \quad \underline{\nabla} \times \underline{H} = j\omega\epsilon \underline{E} \end{aligned} \tag{C-1}$$

where $\underline{\nabla}$ is the usual differential operator. The dielectric constant ϵ is of the form

$$\epsilon = \epsilon_0(1 + \epsilon_1) \quad ,$$

where in the atmosphere ϵ_1 is on the order of 10^{-5} . We will assume the dielectric constant ϵ is varying slowly with time, so that the turbulence can be assumed to be frozen in the calculation of the field. Tatarskii [1971] show that this assumption is justified when the wind velocity v satisfies

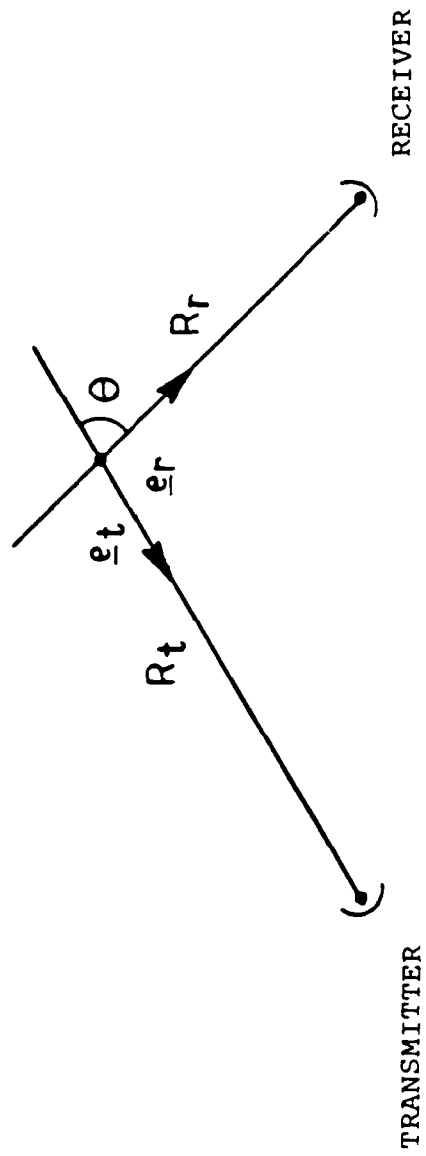


Figure C-1 Scatter Geometry

$$v/c \ll \epsilon ,$$

where c is the velocity of light.

Since we can assume the turbulence is frozen, we can use the relationship

$$\underline{\nabla} \times \underline{\nabla} \times \underline{E} = -\nabla^2 \underline{E} + \underline{\nabla}(\underline{\nabla} \cdot \underline{E}) \quad (C-2)$$

to get

$$\begin{aligned} -\nabla^2 \underline{E} + \underline{\nabla}(\underline{\nabla} \cdot \underline{E}) &= \omega^2 \mu_0 \epsilon \underline{E} \\ &= k^2 (1 + \epsilon_1) \underline{E} \quad . \end{aligned} \quad (C-3)$$

where ∇^2 is the Laplacian operator $\nabla^2 = (\underline{\nabla} \cdot \underline{\nabla})$. From Maxwell's equations we also have

$$0 = \underline{\nabla} \cdot (\epsilon \underline{E}) = \epsilon \underline{\nabla} \cdot \underline{E} + (\underline{\nabla} \epsilon) \cdot \underline{E} \quad . \quad (C-4)$$

Using (C-4) in (C-3) we get

$$\nabla^2 \underline{E} + k^2 (1 + \epsilon_1) \underline{E} + \underline{\nabla}(\underline{\nabla} \ln(\epsilon) \cdot \underline{E}) = 0 \quad . \quad (C-5)$$

Since ϵ_1 is small we have

$$\underline{\nabla} \ln \epsilon = \frac{1}{1 + \epsilon_1} \underline{\nabla} \epsilon_1 \sim \underline{\nabla} \epsilon_1 \quad . \quad (C-6)$$

Now, writing the field in \underline{E} in terms of the direct \underline{E}_0 and the scattered field \underline{E}_S we get

$$\begin{aligned} \nabla^2 \underline{E}_0 + k^2 \underline{E}_0 + k^2 \epsilon_1 \underline{E}_0 + \nabla(\nabla \epsilon_1 \cdot \underline{E}_0) + \nabla^2 \underline{E}_S + k^2 \underline{E}_S = \\ - k^2 \epsilon_1 \underline{E}_S - \nabla(\nabla \epsilon_1 \cdot \underline{E}_S) \end{aligned}$$

The field \underline{E}_0 is defined as the field that would exist if $\epsilon_1=0$, so we have that $\nabla^2 \underline{E}_0 + k^2 \underline{E}_0 = 0$. \underline{E}_0 is the first term in the asymptotic expansion of the field. The second term is found by neglecting the higher order terms involving both ϵ_1 and \underline{E}_S . Hence we get

$$\nabla^2 \underline{E}_S + k^2 \underline{E}_S = -k^2 \epsilon_1 \underline{E}_0 + \nabla(\nabla \epsilon_1 \cdot \underline{E}_0) \quad (C-7)$$

This result is valid asymptotically for sufficiently small ϵ_1 . Since ϵ_1 is extremely small in the atmosphere, the validity of (C-7) is unquestioned. The solution to (C-7), with no boundary conditions except at infinity, is known:

$$\underline{E}_S = \frac{1}{4\pi} \int_V \frac{e^{-jkR_R}}{R_R} [k^2 \epsilon_1(\underline{r}) \underline{E}_0(\underline{r}) + \nabla(\nabla \epsilon_1 \cdot \underline{E}_0)(\underline{r})] d^3 \underline{r} \quad (C-8)$$

where the integral is over all scatterers in the common volume. \underline{E}_S in (C-8) is the scattered field at the receiver with an incident field $\underline{E}_0(\underline{r})$ in the common volume.

This integral can be rewritten using the Gauss integral formula:

$$\int_V dV \underline{\nabla} = \int_S dS \underline{n} \quad (C-9)$$

where S is the surface around the volume V and \underline{n} is the surface normal. The volume in (C-8) can be assumed sufficiently large so that contributions from the surface integral can be ignored. To rewrite the expression we therefore need to rewrite the last integrand in (C-8) in terms of a divergence. Define

$$u = e^{-jkR_R} / R_R .$$

The second term in (C-8) is then

$$T_2 = u \underline{\nabla} (\underline{\nabla} \epsilon_1 \cdot \underline{E}_0) .$$

Using the Leibnitz rule for the differential operator $\underline{\nabla}$ we get

$$T_2 = \underline{\nabla} (u \underline{\nabla} \epsilon_1 \cdot \underline{E}_0) - \underline{\nabla} u \underline{\nabla} \epsilon_1 \cdot \underline{E}_0 .$$

The first term only yields a surface integral (C-9), and can be ignored. Define therefore

$$T_2' = - \nabla u (\nabla \epsilon_1 \cdot \underline{E}_0) .$$

Using the Leibnitz rule again twice yields

$$T_2' = - \nabla \cdot (\epsilon_1 \underline{E}_0 \nabla u) + (\nabla \cdot \underline{E}_0) \epsilon_1 \nabla u \\ + \epsilon_1 \underline{E}_0 \cdot \nabla (\nabla u) .$$

The second term vanishes everywhere (Maxwell's equations) and the first term is again a divergence expression which only contributes to the surface integral and hence can be ignored. We now have reduced the second term in the integrand of (C-8) to

$$T_2'' = \epsilon_1 \underline{E}_0 \cdot \nabla \nabla \frac{e^{-jkR_R}}{R_R} .$$

The evaluation of this proceeds in a straightforward manner using that $\underline{\nabla} R_R = -\underline{R}/R_R = -\underline{e}_R$:

$$\begin{aligned} \underline{\nabla} \underline{\nabla} \frac{e^{-jkR_R}}{R_R} &= -\underline{\nabla} \left[\left(-\frac{jk}{R_R} - \frac{1}{R_R^2} \right) e^{-jkR_R} \frac{R_R}{R_R} \right] \\ &= \left[\frac{-jk}{R_R^2} - \frac{1}{R_R^3} \right] e^{-jkR_R} (-\underline{\nabla} R_R) \\ &\quad + \left[\frac{k^2}{R_R^2} - \frac{3jk}{R_R^3} - \frac{3}{R_R^4} \right] e^{-jkR_R} (\underline{\nabla} R_R) \underline{R}_R . \end{aligned}$$

Since $-\underline{\nabla} R_R$ is the identity matrix the first term above is on the order of R_R^{-2} . In the far field only the term on the order of R_R^{-1} need to be retained, so we get

$$\underline{T}_2'' = -\epsilon_1 k^2 \underline{E}_0 \cdot \frac{R_R}{R_R^3} e^{-jkR_R} .$$

Using this as the second term of the integrand in (C-8) yields

$$\underline{E}_S = \frac{1}{4\pi} \int_V dV k^2 \epsilon_1 \frac{e^{-jkR_R}}{R_R} [\underline{E}_0 - (\underline{E}_0 \cdot \underline{e}_R) \underline{e}_R] . \quad (C-10)$$

This is the basic equation for the scattered electromagnetic field. Instead of the relative dielectric constant ϵ_1 it is convenient in the following to use the relative index of refraction, n_1 . They are related by

$$n = 1 - n_1 = \sqrt{1 + \epsilon_1} \quad ,$$

or

$$n_1 \sim 0.5\epsilon_1 \quad . \quad (C-11)$$

The incident field \underline{E}_0 is a spherically spreading wave of the form

$$\underline{E}_0 = \underline{A}_0 (\underline{R}_T) e^{-jkR_T} \quad . \quad (C-12)$$

The amplitude vector \underline{A}_0 , which varies slowly with distance is perpendicular to the direction of propagation ($-\underline{e}_T$), and depends on transmit power and antenna gain in addition to the $1/R_T$ spherical spreading loss. We have that

$$|\underline{A}_0|^2 = \frac{30 P_T G_T}{R_T^2(\underline{e}_T)} |g_T(\underline{e}_T)|^2$$

where G_T is the gain of the transmitting antenna and $g_T(\underline{e}_T)$ is the normalized voltage pattern in the direction of the scattering point. So far we have only assumed that the terminals are in the far field. We now assume that the scattering angle is small, so that \underline{E}_0 is nearly perpendicular to the direction vector \underline{e}_R to the receiver. Hence we get

$$\underline{E}_0 - (\underline{E}_0 \cdot \underline{e}_R) \underline{e}_R \sim \underline{E}_0 = \underline{A}_0 e^{-jkR_T} .$$

Inserting this in (C-10), and using (C-11), yields

$$\underline{E}_S = \frac{k^2}{2\pi} \int_V dV \frac{\underline{A}_0}{R_R} e^{-jk(R_T+R_R)} \underline{n}_1 . \quad (C-14)$$

The average field on a receiving aperture A is

$$\underline{E}_R = \frac{1}{A_R} \int_{A_R} dA \underline{E}_S . \quad (C-15)$$

For small apertures ($A_R \ll \lambda R_R$) this becomes

$$\underline{E}_R = \frac{k^2}{2\pi} \int_V dV \frac{\underline{A}_0 g_R}{R_R} e^{-jk(R_T+R_R)} \underline{n}_1 \quad (C-16)$$

where g_R is the normalized voltage of the receiving aperture.
The received power is

$$\begin{aligned}
 P_R &= A_R |\underline{E}_R|^2 / (120\pi) \\
 &= \frac{G_R}{120k^2} |\underline{E}_R|^2 \\
 &= \frac{G_R k^2}{16\pi^2} P_T G_T \int_V dV' \int_V dV'' \frac{g_T(\underline{e}'_T) g_T^*(\underline{e}''_T)}{R_T(\underline{e}'_T) R_T(\underline{e}''_T)} \\
 &\quad \cdot \frac{g_R(\underline{e}'_R) g_R^*(\underline{e}''_R)}{R_R(\underline{e}'_R) R_R(\underline{e}''_R)} \frac{1}{n_1' n_1''^*} \\
 &\quad \cdot \exp[-jk(R_T(\underline{e}'_T) + R_R(\underline{e}'_R) - R_T(\underline{e}''_T) - R_R(\underline{e}''_R))] .
 \end{aligned} \tag{C.17}$$

The asterisk denotes complex conjugation. This relatively formidable expression is simplified by noting that the refractive index is uncorrelated for points \underline{r}' and \underline{r}'' in the common volume which are separated by more than the outer scale L_0 . Hence we can assume that (outside of the complex exponent)

$$R_T(\underline{e}'_T) = R_T(\underline{e}''_T)$$

and

$$R_R(\underline{e}'_R) = R_R(\underline{e}''_R)$$

AD-A143 762

THEORETICAL ANALYSIS OF MICROWAVE PROPAGATION(U)
SIGNATRON INC LEXINGTON MA S PARL ET AL. APR 84
RADC-TR-84-74 F19628-88-C-0186

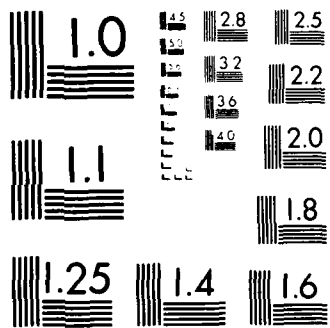
5/5

UNCLASSIFIED

F/G 28/14

NL





MICROCOPY RESOLUTION TEST CHART
NATIONAL BUREAU OF STANDARDS 1963-A

and that

$$g_T(\underline{e}'_T) = g_T(\underline{e}''_T) ,$$

$$g_R(\underline{e}'_R) = g_R(\underline{e}''_R) .$$

The correlation function of the refractive index is taken to be homogeneous. We do not assume isotropy at this period. We define the correlation function

$$\rho(\underline{r}' - \underline{r}'') = \overline{n_1(\underline{r}') n_1^*(\underline{r}'')} . \quad (C-18)$$

Inserting this in (C-17) together with the assumptions above yields

$$P_R = \frac{P_T G_T G_R k^2}{16\pi^2} \int_V d^3\underline{r}' \int_V d^3\underline{r}'' \frac{|g_T|^2 |g_R|^2}{R_T^2 R_R^2} \rho(\underline{r}' - \underline{r}'') e^{-jk\psi} \quad (C-19)$$

where the phase term ψ is

$$\psi = R_T(\underline{e}'_T) + R_R(\underline{e}'_R) - R_T(\underline{e}''_T) - R_R(\underline{e}''_R) . \quad (C-20)$$

Tatarskii [1971] simplifies the result further by using an approximation of ψ which is valid when the Fresnel conditions

$$L_0^2 \ll \lambda R_T, \lambda R_R \quad (C-21)$$

are satisfied. These conditions will be violated at the high end of the microwave spectrum. The conditions reflect the fact that at high frequencies the scale of the turbulence is large compared to the wavelength (or rather, the Fresnel distance $(\lambda R)^{1/2}$) so that scattering is negligible. At these extremely high frequencies the effect of the atmosphere is primarily refraction (Geometrical optics region). In the derivation below we show that the condition (C-21) can be slightly relaxed, a fact that has significant impact on the possible use of troposcatter systems at high microwave frequencies and at millimeter wave frequencies. To derive the simpler expression the integral (C-19) is transformed so that $\underline{r}' - \underline{r}''$ is a direct integration variable:

$$\underline{r}' = \underline{r}_0 + \underline{r}_1/2$$

$$\underline{r}'' = \underline{r}_0 - \underline{r}_1/2 .$$

Let $\underline{R}_{T0}(\underline{r}_0)$ be the vector to the transmitter from the point \underline{r}_0 . The vector from the origin to the transmitter is then

$$\underline{R}_{T1} \triangleq \underline{r}_0 + \underline{R}_{T0}(\underline{r}_0) .$$

Then

$$R_T(\underline{r}') = |\underline{R}_{T1} - \underline{r}_0 - \underline{r}_1/2|$$

and

$$R_T(\underline{r}'') = |\underline{R}_{T1} - \underline{r}_0 + \underline{r}_1/2| .$$

Similarly we have that

$$R_R(\underline{r}') = \left| \underline{R}_{R1} - \underline{r}_0 - \underline{r}_1/2 \right|$$

and

$$R_R(\underline{r}'') = \left| \underline{R}_{R1} - \underline{r}_0 + \underline{r}_1/2 \right| .$$

Assume $|\underline{r}_1|$ is small relative to $R_{T0}(\underline{r}_0)$ and $R_{R0}(\underline{r}_0)$. Exactly what this implies will be determined later. We can then expand R_T and R_R in a Taylor series in r_1 . Maintaining terms up to order 3 we find that

$$\begin{aligned} R_T(\underline{r}') - R_T(\underline{r}'') &= \left| \underline{R}_{T0} - \underline{r}_1/2 \right| - \left| \underline{R}_{R0} + \underline{r}_1/2 \right| \\ &= - \frac{\underline{R}_{T0} \cdot \underline{r}_1}{R_{T0}} \\ &\quad + \frac{\underline{R}_{T0} \cdot \underline{r}_1}{8 R_{T0}^5} \left[R_{T0}^2 r_1^2 - \left| \underline{R}_{T0} \cdot r_1 \right|^2 \right] \\ &\quad + o\left(\frac{r_1^5}{R_{T0}^4} \right) , \end{aligned} \tag{C-22}$$

where the symbol o stands for "order of", i.e., $o(X) \sim CX$ for small X where C is a constant. Using the analogous result for the receiving end we get the following approximation to the phase term Ψ :

$$\begin{aligned}
\psi &= - \underline{r}_1 \cdot \left(\frac{\underline{R}_{T0}}{R_{T0}} + \frac{\underline{R}_{R0}}{R_{R0}} \right) \\
&+ \frac{\underline{R}_{T0} \cdot \underline{r}_1}{8 R_{T0}^5} [R_{T0}^2 r_1^2 - |\underline{R}_{T0} \cdot \underline{r}_1|^2] \\
&+ \frac{\underline{R}_{R0} \cdot \underline{r}_1}{8 R_{R0}^5} [R_{R0}^2 r_1^2 - |\underline{R}_{R0} \cdot \underline{r}_1|^2] \\
&+ 0 \left(\frac{r_1^5}{R_{T0}^4}, \frac{r_1^5}{R_{R0}^4} \right) \\
&= - \underline{r}_1 \cdot [\underline{e}_{T0} + \underline{e}_{R0}] + \epsilon
\end{aligned} \tag{C-23}$$

where we have defined the unit vectors \underline{e}_{T0} and \underline{e}_{R0} , and the correction term ϵ . Assuming that $r_1 \ll L_0$ we have that

$$\epsilon < \frac{L_0^3}{16} \left(\frac{1}{R_{T0}^2} + \frac{1}{R_{R0}^2} \right) + 0 \left(\frac{L_0^5}{R_{T0}^4}, \frac{L_0^5}{R_{R0}^4} \right) . \tag{C-24}$$

The correction term ϵ can be ignored only if $k\epsilon < \pi/8$, or

$$L_0^3 \left(\frac{1}{R_{T0}^2} + \frac{1}{R_{R0}^2} \right) < \lambda . \tag{C-25}$$

This is the basic condition required for the further simplification of the expression for the received power (C-19). As a numerical example, take $R_{T0} - R_{R0} = 50$ km and $L_0 = 50$ m (typical), then (C-25) yields

$$\lambda > .0001 \text{ meters,}$$

or

$$f < 3000 \text{ GHz.}$$

This shows that the theory should be valid for higher frequencies than would be expected from the condition derived by Tatarskii [1971]. That condition states

$$\lambda \gg L_0^2/R ,$$

which for the above numerical values translates to

$$\lambda \gg 0.05 \text{ meters}$$

or

$$f \ll 6 \text{ GHz .}$$

We now proceed to the derivation of the simplified scattering equations. The first term of Ψ in (C-23) can be written

$$\Psi = - \underline{r}_1 \cdot \underline{e}_S \tag{C-26}$$

when

$$\underline{e}_S = \underline{e}_{T0} + \underline{e}_{R0} \tag{C-27}$$

\underline{e}_S is typically pointing straight up so that only the vertical scale influence ψ .

We have that

$$e_S = |\underline{e}_S| = 2 \sin (\theta/2) \quad (C-28)$$

where θ is the scattering angle at the given point in the common volume. Inserting this in (C-19) yields

$$P_R = \frac{P_T G_T G_R k^2}{16\pi^2} \int_{V_0} d^3 \underline{r}_0 \frac{|g_T(\underline{r}_0)|^2 |g_R(\underline{r}_0)|^2}{R_{T0}^2(\underline{r}_0) R_R^2(\underline{r}_0)} \int_{V_1} d^3 \underline{r}_1 \rho(\underline{r}_1) e^{+jk\underline{r}_1 \cdot \underline{e}_S} \quad (C-29)$$

If the common volume is large compared to the scale of the turbulence in all directions we can assume that $V_0 \sim V$, and that

$$\begin{aligned} & \int_{V_1} d^3 \underline{r}_1 \rho(\underline{r}_1) e^{+jk\underline{r}_1 \cdot \underline{e}_S} \\ & \sim \int_{-\infty}^{\infty} d^3 \underline{r}_1 \rho(\underline{r}_1) e^{+jk\underline{r}_1 \cdot \underline{e}_S} \\ & = (2\pi)^3 \phi(k \underline{e}_S) \end{aligned}$$

where ϕ is the wave number spectrum of the refractive index. For simplicity we now assume isotropy so the result is independent of the direction of \underline{e}_S . The case of anisotropic turbulence will be considered in the main part of the text. Using (C-28) and (C-30) in (C-29) results in

$$P_R = P_T G_T G_R \frac{\pi}{2} k^2 \int_V dV \frac{g_T^2}{R_T^2} \frac{g_R^2}{R_R^2} \phi (2k \sin(\theta/2)) \quad (C-31)$$

Based on this expression we can interpret each infinitesimal part of dV of the volume as an individual scatterer. The cross section σ_C , as usually defined in the radar context, is found by comparison of (C-31) with

$$P_R = P_T \cdot \frac{G_T}{4\pi R_T^2} \cdot \frac{\sigma_C}{4\pi R_R^2} \cdot \frac{\lambda^2 G_R}{4\pi} \quad (C-32)$$

so that (setting $g_T = g_R = 1$ for the purpose of defining σ_C)

$$\sigma_C = 8\pi^2 k^4 \phi (2k \sin \frac{\theta}{2}) dV \quad (C-33)$$

Equation (C-31) is the desired scattering equation. We briefly summarize the conditions for the validity of (C-31):

1. The atmosphere can be considered frozen:

$$v/c \ll n_1 ;$$

2. The terminals are in the far field:

$$k R_T, k R_R \gg 1 ;$$

3. The scattering volume is much larger than a correlation cell:

$$V \gg L_0^3 ;$$

4. The scattering volume is in the far field of the antennas:

$$A_T/R_T, A_R/R_R \ll \lambda ;$$

5. The Fresnel zone condition:

$$2L_0^3/\lambda < R_{T0}^2, R_{R0}^2 .$$



MISSION
of
Rome Air Development Center

RADC plans and executes research, development, test and selected acquisition programs in support of Command, Control Communications and Intelligence (C³I) activities. Technical and engineering support within areas of technical competence is provided to ESD Program Offices (POs) and other ESD elements. The principal technical mission areas are communications, electromagnetic guidance and control, surveillance of ground and aerospace objects, intelligence data collection and handling, information system technology, ionospheric propagation, solid state sciences, microwave physics and electronic reliability, maintainability and compatibility.

END

FILMED

DTIC